AN ISOTHERMAL EXPERIMENTAL STUDY OF THE UNSTEADY FLUID MECHANICS OF GAS TURBINE FUEL INJECTOR FLOWFIELDS

Kristofer Midgley

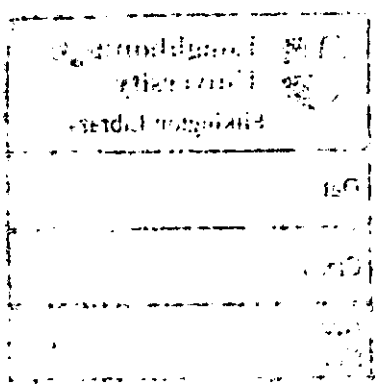

Submitted in partial fulfilment of the requirements for the award of
Doctor of Philosophy of Loughborough University
Department of Aeronautical and Automotive Engineering
June 2005

Abstract

Low-emissions combustor design is crucially important to gas turbine engine manufacturers. Unfortunately, many designs are susceptible to unsteady oscillations that can result in structural fatigue and increased noise. Computational approaches that resolve flow unsteadiness, for example Large Eddy Simulation (LES), are being explored as one avenue to help understand such phenomena. However, in order to quantify the accuracy of LES predictions, benchmark validation data in suitably chosen test cases are required. Comprehensive experimental data covering both time-averaged and time-resolved features are currently scarce. It was the aim of this thesis, therefore, to provide such data in a configuration representing the near-field of a typical gas turbine fuel injector. It was decided to focus on the fuel injector since many unsteady events are believed to originate because of the transient interactions between the fuel injector flow and the main combustor flow. A radial fed two-stream fuel injector, based on a pre-existing industrial gas-turbine Turbomeca design was used, since this geometry was known to be susceptible to unsteadiness. The fuel injector was investigated under isothermal conditions to place emphasis on the fluid mechanical behaviour of the fuel injector, including detailed capture of any unsteady phenomena present.

Light Sheet Imaging (LSI) systems were used as the primary experimental technique to provide high quality spatially and temporally resolved instantaneous velocity and scalar field information in 2D planes (using Particle Image Velocimetry (PIV) and Planar Laser-Induced Fluorescence (PLIF) techniques). Several methods were employed to extract information quantifying the flow unsteadiness and improve visualisation of time-dependent large-scale turbulent structures. Proper Orthogonal Decomposition (POD) analysis enabled clear identification of the dominant modes of energy containing structures. The results indicated that periodic high-energy containing vortex structures occurred in the swirl stream shear layer, emerging from the fuel injector. These formed a two-strong two-weak rotating vortex pattern which propagated down the main duct flow path. The formation of these vortices was found to be a function of the swirl number and originated due to an interaction between the forward moving swirl flow and the furthest upstream penetration point of the recirculation zone present in the main duct flow.

Dependent on the magnitude of the swirl number (influencing the swirl stream cone angle) and the geometry of the fuel injector, the vortex formation point was sometimes found inside the fuel injector itself. If the vortices originated inside the fuel injector they appeared much more coherent in space and time and of higher energy. A second unsteady high energy containing phenomenon was also identified, namely a Precessing Vortex Core (PVC), which was damped out if the fuel injector contained a central jet. The dynamics of the PVC interacted with the dynamics of the swirl stream shear layer vortices to reduce there strength. Transient scalar measurements indicated that there was a clear connection between the unsteady vortex pattern and the rate of mixing, resulting in bursts of high heat release and is therefore identified as one source of combustor oscillations. Future fuel injector designs need to pay close attention to these unsteady features in selecting swirl number and internal geometry parameters.

Keywords: Gas Turbine Fuel Injectors, Flow Instabilities, Vortices, Precessing Vortex Core, Particle Image Velocimetry, Planar Laser-Induced Fluorescence.

Acknowledgements

Thanks to all the members of the Rolls-Royce UTC, my friends and my family.

Dedication

This thesis is dedicated to the Space terrace in Ibiza

Contents

List of Figures

Nomenclature

Symbols

a	acceleration
a_k	temporal coefficient
A	area, efficiency parameter
b_0	side width at image plane
B_0	side width at object plane
c	constant
C	concentration
C_d	discharge coefficient
d_r	pixel width
d_f	diffusion coefficient
dx (dy)	interrogation cell width
D	diameter
E	energy
f	frequency
f#	f-number
F_s	fan speed
I	intensity of incident light
k	turbulent kinetic energy
L_{11}	longitudinal integral length scale
L_η	Kolmogorov length-scale
M	momentum, magnification, Mach number
$\dot{m}$	mass flow rate
N	number of samples
N_I	number of particles per interrogation cell
p	static pressure
P	total pressure, wetted perimeter
$\dot{Q}$	volumetric flow rate
q	scatter light intensity
r	separation vector, radius
R	characteristic radius, correlation function
R_0	Universal gas constant
Re	Reynolds number
s	time separation
S	species concentration
Sn	Swirl number
Sc	Schmidt number
St	Strouhal number
T	temperature
t	time
v	fluctuating velocity
v′	RMS velocity
V	instantaneous velocity
$\overline{V}$	time-average of V
$\langle V \rangle$	ensemble average of V
V_p	velocity lag
x, r, θ	cylindrical polar coordinates

z	confidence band
z_0	focal length
Δt	inter-frame time (for PIV measurements)
ΔZ_0	camera depth-of-field

Greek Symbols

Δ	separation, determinant
Φ	quantum efficiency
α	angle
ε	error, extinction coefficient, dissipation rate
ϕ_{pz}	primary zone equivalence ratio
φ	spatial coefficients
γ	surface roughness
λ	wavelength, eigenvalue, coefficient of friction
λ_{ci}	swirling strength
μ	viscosity
ν	kinematic viscosity
ρ	density
τ	integral time-scale
τ_p	particle response time
τ_η	Kolmogorov timescale

Subscripts

e	effective
ex	dump area expansion duct
h	hydraulic
i, j, (k)	in-plane (out-of-plane) motions
j	jet stream
max	maximum
p	particle
r	quantity at x/D_s=-1.0
ref	reference
s	swirl stream
x, r, t	cylindrical polar component direction
1	radial slot
2	fuel injector inner body
3	fuel injector outer body

Superscripts

^	peak

Abbreviations

ACF	Auto-Correlation Function
AOI	Area of Interest
CAEP	Committee on Aviation Environmental Protection
CCF	Cross Correlation Function
CFD	Computational Fluid Dynamics
CW	Continuous Wave (Laser)

DNS	Direct Numerical Simulation
EPA	Environmental Protection Agency
FAR	Fuel Air Ratio
FFT	Fast Fourier Transform
FoV	Field of View
FZC	First Zero Crossing
HP	High Pressure
HS	High Speed
HWA	Hotwire Anemometry
ICAO	International Civil Aviation Organisation
IPCC	Intergovernmental Panel on Climate Change
LDA	Laser Doppler Anemometry
LES	Large Eddy Simulation
LHS	Left Hand Side
LP	Low Pressure
LPP	Lean Premixed Pre-vaporised
LS	Low Speed
LSI	Light Sheet Imaging
LSV	Laser Speckle Velocimetry
LTO	Landing Takeoff Cycle
MOLECULES	Modelling of Low Emission Combustors Using Large Eddy Simulations
Nd:YAG	Neodym Yttrium Aluminium Garnet (laser)
Nd:YLF	
NO_x	Nitrogen Oxides
PDF	Probability Density Function
PIV	Particle Image Velocimetry
PLIF	Planar Laser Induced Fluorescence
POD	Proper Orthogonal Decomposition
PTU	Programmable Timing Unit
PTV	Particle Tracking Velocimetry
PVC	Precessing Vortex Core
RANS	Reynolds-Averaged Navier-Stokes
RHS	Right Hand Side
RMS	Root Mean Square
RQL	Rich-burn Quick-quench Lean-burn
SNR	Signal to Noise Ratio
SVD	Singular Value Decomposition
UHC	Unburned Hydrocarbons
UNFCCC	United Nations Framework Convention on Climate Change

1 INTRODUCTION

Gas turbines produce emissions that are similar to the emissions resulting from any fossil fuel combustion. However, aircraft emissions are unique in the sense that a significant proportion is emitted at altitude. These emissions give rise to important environmental issues regarding their impact on global climate and local air quality. As demand for air travel continues to rise these effects are causing increasing concern and as a result, legislation limiting aircraft engine emissions are becoming increasingly stringent. However, it is unlikely that conventional combustor designs will be able to meet many further restrictions, especially proposals for the limitation of nitrogen oxides at altitude. The gas turbine emissions challenge is amplified in aero applications by the continual drive to reduce size and weight through shorter length combustors. At present the development of new combustors is hindered by the use of empirically based design rules and the need for extremely expensive and time-consuming testing on high pressure and temperature test rigs. Clearly flow modelling and simulation via Computational Fluid Dynamics (CFD) has an increasingly important role. However, for computational models to be used effectively, they have to predict the flowfield sufficiently well for designers to have confidence in the predicted effects of design changes. At present steady-state CFD models struggle to cope with the complex unsteady flowfields created within combustors. Large Eddy Simulation (LES) can often improve predictions by modelling the dynamics of the large-scale time-dependent turbulent motions of the flowfield. For LES codes to be validated they require high quality spatially and temporally resolved experimental data in combustor relevant test cases. It is the generation of appropriate benchmark LES validation data relevant to gas turbine combustion system development that has motivated the research reported in this thesis.

1.1 The Global Impact of Gas Turbines

Between 1960 and 1999 worldwide scheduled passenger air traffic has grown from 109 billion to 2.8 trillion passenger kilometres, corresponding to a growth rate of nearly 9% per annum year, Jamin (2004). The Intergovernmental Panel on Climate Change (IPCC) predicts that over the next 20 years there will be a further growth of 3.1% per annum until 2050, IPCC (1999). This ever increasing demand for air travel is largely due to the superiority of the gas turbine over the piston engine as a power source for aircraft in terms of range, speed and fuel economy. However, along with the obvious social and

economic benefits provided by gas turbine technology, there are also negative affects, namely noise pollution and engine emissions.

1.2 Gas Turbine Pollutant Emissions

The main emissions from gas turbine combustion are water vapour, carbon dioxide (CO_2) unburned hydrocarbons (UHC), particulate matter (mainly carbon), nitrogen oxides (NO_x) and carbon monoxide (CO). The emissions that impact on the local air quality are, CO, UHC, particulate matter and NO_x. CO reduces the capacity of blood to absorb oxygen and in high concentrations may even cause death. UHC's, are both toxic and combine with NO_x to form toxic ozone and aldehydes known as photochemical smog. Particulate matter has been linked to asthma and other respiratory diseases, Seaton *et al* (1995) and NO_x emissions not only add to photochemical smog, but also cause damage to plant life and react with hydroxyl radicals in the atmosphere to form acid rain (HNO_3). As a result these emissions are limited within a prescribed Landing Take-Off (LTO) cycle.

1.2.1 Emissions Producing Climate Change

The aircraft emissions that are believed to produce changes in climate are water vapour, CO_2, and NO_x. Water vapour from gas turbines may lead to cirrus cloud formation in both the troposphere and stratosphere, which could have a large radiative effect on climate. The effect of CO_2 on climate change is direct and depends simply on its atmospheric concentration. CO_2 molecules add to the greenhouse effect by absorbing outgoing infrared radiation emitted by the Earth's surface and the lower atmosphere. The transport mechanisms of all CO_2 molecules emitted into the atmosphere follow similar pathways; thus CO_2 emitted from aircraft becomes well mixed and indistinguishable from other anthropogenic CO_2 sources. Whilst improvements in overall engine efficiency and airframe design have lead to a drop in CO_2 and water production per kilometre, the increase in the number of flights has offset this reduction; in fact the amounts of CO_2 and water vapour produced by aircraft continues to rise. This is unavoidable until the type of fuel used is changed. NO_x are influential on atmospheric ozone (O_3) concentrations, an effect that differs with location and season. In the upper troposphere and lower stratosphere, where subsonic passenger aircraft operate, NO_x emissions have increased ozone amounts by up to 6% through the oxidation of CO

molecules; these increases tend to warm the surface of the earth and hence contribute to the greenhouse effect, Schumann (2000).

1.2.2 Emissions Contributing to Stratospheric Ozone Depletion

At altitudes of 18km or above, where supersonic aircraft operate, ozone exists which helps to shield the earth from harmful ultraviolet (UV) radiation. However, NO_x emissions in this region tend to *decrease* ozone by catalytically converting it into oxygen. Whilst the temperature of the troposphere tends to reduce with altitude, resulting in an amplification of the vertical turbulent motion, the temperature in the stratosphere generally increases with altitude and, as a result, the region is stratified (hence the name) with little or no vertical turbulent motion. This means that NO_x molecules have extremely long residence times (ranging from months to years) and one molecule of NO_x can destroy many molecules of ozone. NO_x is however, not the only cause of ozone depletion in the stratosphere, industrial and domestic production of chlorine and bromine compounds (mainly chlorofluorocarbons) also act as catalysts to stratospheric ozone destruction.

1.2.3 Global Emissions Legislation

On a global scale, emissions causing climate change fall under the broad international agreements created by the United Nations Framework Convention on Climate Change (UNFCCC). More than 170 countries are members to this Convention and, in 1997, the Kyoto Protocol was agreed. This required developed countries to reduce their total national greenhouse gas emissions levels (from all sources) by an average of 5% per year for the years 2008–2012 compared with 1990 levels. Notably the United States pulled out of the treaty in 2001 claiming it to be "unfair" as it did not include the "population centres" of India or China. This despite the fact that, on a per person basis, the total emissions from India and China are far less than the United States, who contribute 20-25% of the world's carbon dioxide emissions for just 5% of the world's population. However, in 2004 Russia unilaterally decided to ratify the treaty, increasing the support of the global population to 55%.

The emissions contributing to stratospheric ozone depletion are controlled by the Vienna Convention for the Protection of the Ozone Layer. In 2002 it seemed that the Protocol

was working as, according to NASA, the hole in the ozone layer above the Antarctic had shrunk to a relative low of 8.1 million square miles. However, in 2003 the area of the hole had increased again to 10.9 million square miles, the second largest recorded. The apparent reduction the year before was attributed to warmer than normal stratospheric temperature patterns above Antarctica.

1.2.4 Aero Gas Turbine Emissions Legislation

Legislation aimed directly at limiting aircraft engine emissions are controlled by the International Civil Aviation Organisation (ICAO) and have been in place (for new engines) since 1986. At the present time the ICAO concentrates only on protecting local air quality through limiting aircraft emissions in a prescribed Landing Take-Off (LTO) cycle. This is achieved by recognising four operating modes; approach (below 914m or 3000ft), taxi/idle, take-off and climb-out (to 914m). The climb-out mode also imposes an indirect limitation on emissions at altitude.

The Committee on Aviation Environmental Protection (CAEP) is responsible for ongoing revision of the ICAO emissions legislation. For NO_x production the CAEP/2 standard became effective for all new aircraft types in 1996 and for all aircraft in 2000, IPCC (1999). In 1998 CAEP/4 set new standards, which came into force for new aircraft types in 2004 and will affect all aircraft after 2008. In general, due to improved engine cycle efficiencies and combustor design the emissions are usually kept well within the limits. However, in 2004 CAEP/6 decided to limit NO_x emissions by a further 12% relative to the CAEP/4 standard *and* will also include a flight phase, directly restricting emissions at altitude. These restrictions are expected to come into force for new aircraft types in 2010. It is these further restrictions, especially the flight phase restrictions, that will provide the greatest challenge for combustor designers. In fact, it is questionable whether CAEP/6 targets can be achieved using conventional (single annular) combustors as shown graphically in Figure 1.1 with regards to NO_X emissions. The reasons for this are discussed in the following section.

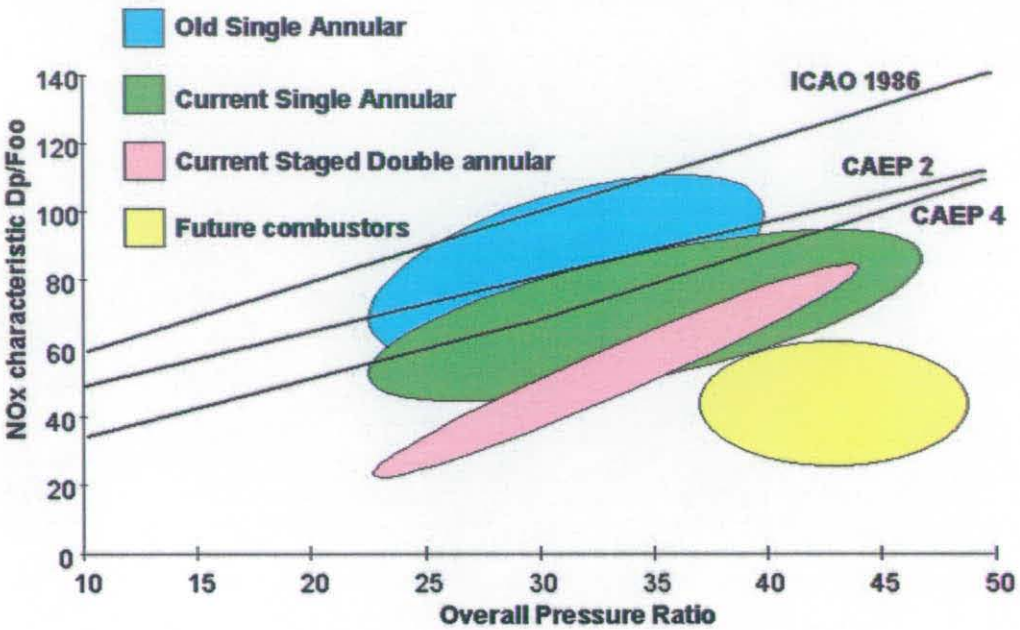

Figure 1.1. Variation of NO_x Characteristics with Engine Pressure Ratio, Birch (2000)

1.3 Conventional Combustor Design

Despite the obvious significance of the combustor to the emissions characteristics of a gas turbine the overall combustor geometry has seen only gradual change over the past 30 years. Figure 1.2 shows a typical (single annular) combustor configuration.

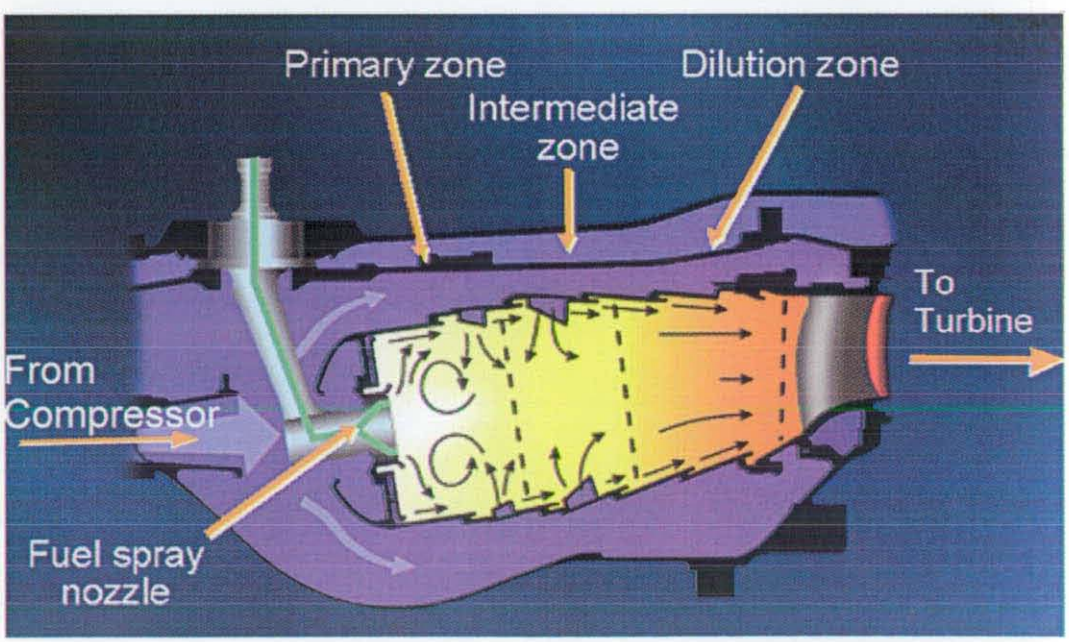

Figure 1.2. Annular Combustor, Rolls Royce (1995)

As Figure 1.2 shows, high-velocity delivery air passes into the combustor from the HP compressor. In order to reduce the air velocity it passes through a pre-diffuser and into a dump diffuser. In conventional combustors approximately 20% of the air then passes through the fuel injector, where a strong swirl component is usually imparted to the flow. A strongly swirling flow aids the mixing of fuel-spray and air and creates a primary zone re-circulation (see Section 1.7). Gupta (1984) states that the presence of a swirl induced re-circulation zone helps to meet many of the combustor performance requirements by:-

i. a reduction in combustor length, due to higher rates of mixing close to the injector nozzle and near re-circulation boundaries.
ii. improved flame stability, due to the presence of a central re-circulation zone which acts like an aerodynamic blockage, providing a region of low speed flow near the eye of the re-circulation.
iii. minimising maintenance and extending life of equipment, since the blockage is aerodynamic and flame impingement on solid surfaces (with high heat transfer and carbon deposition problems) is minimised.

The remaining 80% of the air flows around the flame tube head and into the annular gap between the liner and combustor casing and into the flame tube through ports. Since kerosene will only burn efficiently at Fuel Air Ratios (FAR) of approximately 1:15, Rolls-Royce (1995), the airflow split between the primary and dilution port rows is set such that the primary zone operates within the flame stability limits for the whole range of engine power settings. The flow through the liner ports also aids mixing and helps provide a favourable temperature profile for the Nozzle Guide Vanes and turbine rotors. The geometry and basic layout of this design has proved extremely successful, especially as high pressures and temperatures ensure near 100% combustion efficiency.

The improvements in the performance of combustors over the past 30 years (as indicated in Figure 1.1) are therefore attributable to small changes in the detailed design; including the optimisation of the flow splits into various sections of the liner, the fuel injector design and the diffuser design. Unfortunately, further modifications to existing combustor geometries will be unlikely to meet CAEP/6 especially with regards to NO_x

emissions. Therefore the development of low-emissions (low-NO_x) combustors has become central to realising the full potential of global aviation growth.

1.4 Low-Emissions Combustors

The challenge of reducing emissions in conventional combustor designs is not trivial, due primarily to the separate admission of fuel and air (diffusion flame combustion) and the fixed air percentage introduced into the primary zone. This results in a wide range of primary zone equivalence ratios, ϕ_{pz} during an aircraft operating cycle:-

$$\phi_{pz} = \frac{FAR_{actual}}{FAR_{stoichiometric}}$$

At low power settings, such as idle, the primary zone is designed such that the equivalence ratio is just above the lean blow-out value, since primary zone temperatures are low, NO_x production is negligible. However, as primary fuel breakdown reaction rates are slow, CO and UHC levels may be significant. As the power setting increases towards maximum take-off power, primary zone equivalence ratios move towards stoichiometric ($\phi_{pz} \approx 1$) and the flame temperature rapidly increases; the increased reaction rates suppress CO and UHC levels, but atmospheric nitrogen no longer remains inert and NO_x production increases exponentially, smoke may also start to form in any fuel rich regions of the flame. Figure 1.3 shows combustor emissions as a function of the primary zone equivalence ratio.

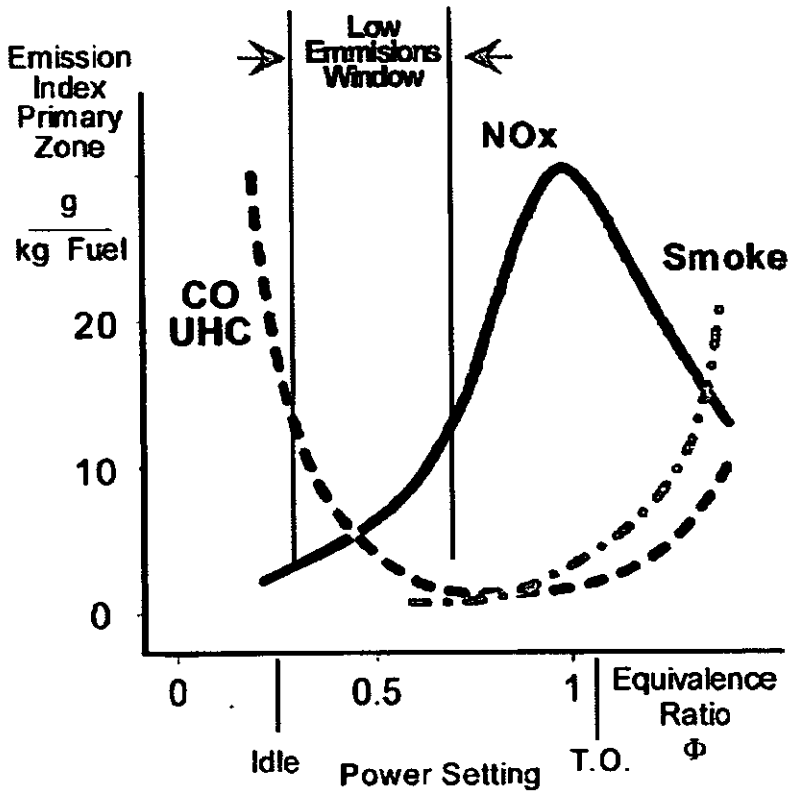

Figure 1.3. Combustor Emissions as a Function of Primary Zone Equivalence Ratio, Wulff and Hourmouziadis (1997)

As shown, emissions are minimised when the primary zone equivalence ratio is close to 0.5. The ideal solution to the emissions problem would therefore be to have a variable primary port geometry (flow area) or fuel injector such that the proportion of air entering the primary zone could be altered to maintain $\phi_{pz} \approx 0.5$ at all power settings. However, weight penalties and satisfactory reliability with such a complex system under the high temperatures of a combustor primary zone has prevented any serious developments in this area.

As an alternative, Pratt and Whitney (Koff (1994)) developed a two-staged (double annular) combustor using "pilot" and "main" zones. The pilot zone is used at idle and, as the power is increased, combustion in the main zone is initiated. When combined, the pilot and the main zones provide high power setting conditions with lean equivalence ratios, this resulted in a 40% drop in LTO cycle NO_x emissions and a 50% reduction at cruise compared to a conventional combustor design. However, there are several disadvantages to a double annular configuration, including increased design complexities of the fuel management system, more fuel injectors and additional length or bulk,

depending on whether the combustor is axially or radially staged, in addition an increased liner wall surface area demands more cooling air.

Another possibility is the Rich-burn, Quick-quench, Lean-burn (RQL) combustor design that utilises initially the low flame temperature created by high equivalence ratios ($1.2<\phi_{pz}<1.6$) achieved when only a small fraction of compressor air is introduced into the primary zone. After the rich-burn zone the flow is rapidly mixed with more air in the quenching region to reduce the temperature and create a final lean-burn zone. Again there are several problems associated with the application of this configuration, large pressure drops are required to provide the rapid mixing and to minimise residence times at or near stoichiometric, also film cooling cannot be used as it would produce locally stoichiometric conditions increasing flame temperatures and NO_x production. This cooling problem is exacerbated by the large amount of soot created in the rich zone which radiates an increased level of heat from the flame to the walls. Further complications arise when RQL is applied to aero engines as the correct flow split between rich and lean burn zones may be hard to achieve for the whole range of engine power settings, Wulff and Hourmouziadis (1997).

Bearing in mind the complications involved in novel low-emissions combustor geometries attention has instead turned to improved methods of fuel preparation, whilst maintaining a more conventional combustor layout.

"When faced with new and challenging problems, the combustion engineer has traditionally looked to the fuel injector to provide a solution. This is not merely a pious hope, because in the past more than one problem that appeared at first sight to constitute a fundamental barrier to further progress in combustion performance was solved either by modifications to existing fuel injector designs or by the introduction of new and sometimes revolutionary atomiser concepts" Lefebvre (1995)

In conventional combustors fuel is typically injected directly into the primary zone by air-blast atomisers, where a thin continuous sheet of fuel is passed into (or sandwiched between) high velocity swirling air streams. However, if the mixing is poor (and the mean fuel droplet diameter is large) then even if the overall equivalence ratio is low, NO_x

may still be produced in high quantities as "envelope" flames at near stoichiometric conditions are created, Rink and Lefebvre (1989). Hence, an obvious way of meeting future NO_x legislation is to improve the mixing of fuel and air and minimise spray drop sizes. If the mixing is sufficiently good that a close to homogeneous mixture of fuel and air is achieved then the lean blow-out equivalence ratio of the system can be reduced, allowing for an increase in the fraction of air into the primary zone, thus suppressing NO_x emissions at high power settings. Unfortunately, combustors with high airflow fuel injectors or very lean burn primary zones are susceptible to combustion induced thermo-acoustic instabilities generating pressure and velocity fluctuations so intense that they can cause structural damage and high noise levels, Dowling and Hubbard (2000) and Anacleto *et al* (2001). In order to avoid such undesirable instabilities careful design and development is required.

1.5 Combustor Design and Development

Traditionally the design and development of combustors, even for small changes to meet a specific engine requirement, has relied heavily on extensive "cut-and-try" rig testing programmes based on empirical design methods which are both time-consuming and expensive. In order to reduce the development costs there is a desire to use Computational Fluid Dynamic (CFD) modelling. However, traditional CFD codes, based on the steady-state Reynolds Averaged Navier-Stokes (RANS) approach cannot resolve time-dependent flow instabilities. Thus the effectiveness of the RANS approach for flow predictions in the design and development of low-emissions combustors may be limited. However, a computational approach that may be able to resolve time-dependent flow instabilities is the Large Eddy Simulation (LES) approach where numerically resolved calculations predict the dynamics of the largest-scales of the flow and only the smaller scales (too small for the grid to resolve) are modelled using a sub-grid scale turbulence model. As it is the unsteadiness of the largest-scale motions that will influence combustion induced thermo-acoustic instabilities, LES should provide an improved design tool over RANS methods. At present LES in applications with complex geometries (such as combustors) is still in its infancy and requires high quality benchmark validation data to quantify its accuracy.

1.6 Benchmark Validation Data

Combustor representative benchmark validation data sets, in addition to the expected reacting flow test cases often utilise isothermal test conditions and focus on individual components of a combustor rather than on the whole combustor geometry. This allows for the fluid mechanical behaviour of the combustor flows to be isolated and understood, without the complex interactions that will occur in reacting flow. Isothermal test conditions also allow for much less complex experimental facilities, often with far superior optical access relative to combusting experiments. This allows for comprehensive data sets to be gathered, both improving our fundamental knowledge of the flow physics and also providing excellent validation data. Such benchmark data are extremely important for CFD development as they provide a "first-step" before variable density combustion models are included.

As discussed previously, one component that will play a crucial role in the development of low-NO_x combustors is the fuel injector. Under isothermal conditions benchmark validation data-sets have previously been collected in flows representative of the fuel injector by Dellenback *et al* (1988), Kihm *et al* (1988), Ahmed (1998) and Solero and Coghe (2002). However, all of the above mentioned investigations were tailored for RANS validation and as a result, reported only time-averaged flowfield statistics. Whilst time-averaged statistics are still useful, to fully validate an LES prediction information pertaining to the large-scale time-dependent structures is also required. This is especially true in fuel injector flowfields where the high levels of swirl imparted on the flow are known to induce several forms of flow instability, as discussed in the following section.

1.7 Strongly Swirling Flows

Gupta (1984) states that swirling flows "*always possess a central core of solid body rotation [forced vortex], outside the central region free [potential] vortex conditions may prevail*". A solid body rotation implies a linear increase of circumferential velocity with increasing radius from the swirl centre, i.e. $V_t \alpha cr$ (where c is a constant dependant on the flow conditions). Unlike a forced vortex, a potential vortex is irrotational in its flow (its vorticity is zero), this implies that the circumferential velocity component is given by:-

$$V_t = \frac{c}{r}$$

Therefore, a swirling flow exhibiting both central solid body rotation and outer free vortex conditions may be represented as a function of radius by a combined (Rankine) vortex relationship:-

$$V_t = \frac{c}{r}\left[1 - \exp\left(-\frac{r^2}{R^2}\right)\right]$$

Where R is a characteristic radius. The boundary between the solid body rotation and the free vortex is defined by the radius, r at which the peak circumferential velocity occurs. A Rankine vortex profile is shown in Figure 1.4.

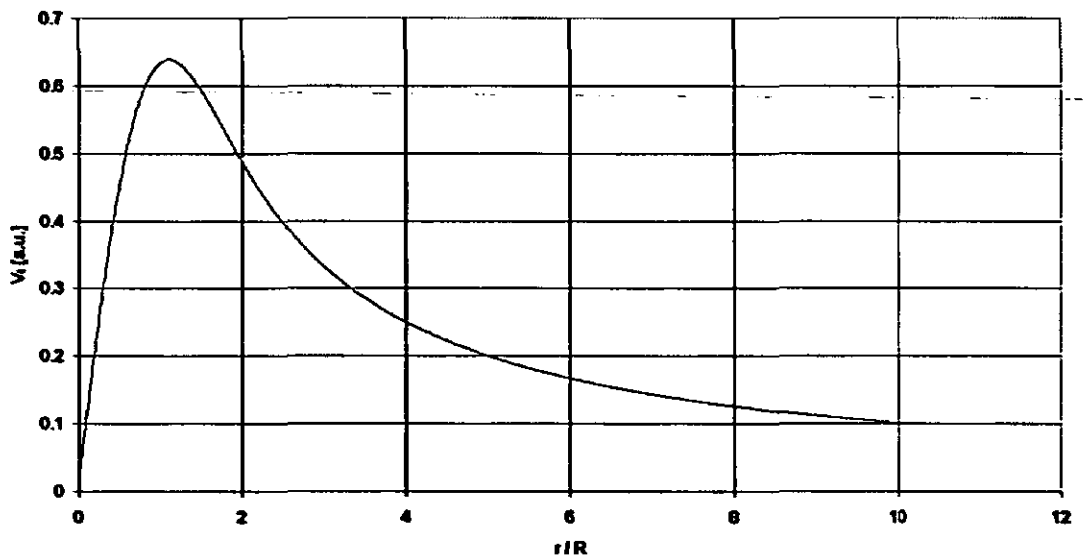

Figure 1.4. Circumferential Velocity in Rankine Vortex

In a simple swirling flow radial pressure gradients are formed to balance the centripetal acceleration:-

$$\frac{dp}{dr} = -\rho\frac{V_t^2}{r}$$

Hence, in the core of a Rankine vortex the pressure increases proportionally with the square of the radius and in the free vortex region the radial pressure distribution is hyperbolic. For a given fuel injector design the radial pressure gradient will be greatest at the exit to the nozzle where circumferential velocities will be largest; since the level of swirl decays due to mixing with non-swirl fluid, the radial pressure gradient will start to reduce forming an adverse axial pressure gradient (dp/dx). The level of swirl that a flow contains is assessed via the non-dimensional parameter, the Swirl number, Sn. This is defined as the axial flux of swirl momentum divided by the axial flux of axial momentum times a characteristic radius, R, Chigier and Beer (1964) (for axi-symmetric flows):-

$$Sn = \frac{G_\phi}{G_x.R}$$

where

$$G_t = 2\pi\int_0^\infty \rho\overline{V_x}\,\overline{V_t}r^2dr$$

$$G_x = 2\pi\int_0^\infty \rho\overline{V_x}^2 rdr + 2\pi\int_0^\infty prdr$$

The overbars denote time-averaged quantities. The axial flux of axial momentum (G_x) relies on knowledge of the pressure field, something that is very difficult to measure without disturbing the flowfield. Therefore Kerr and Fraser (1965) proposed a modified Swirl number that assumed no density variation and a negligible pressure contribution. This equation has widely been used by fuel injector designers:-

$$Sn = \frac{\int_0^R \overline{V_x}\,\overline{V_t}r^2dr}{R\int_0^R \overline{V_x^2}rdr}$$

When the swirl number is sufficiently high, the forward momentum of the flow is insufficient to overcome the axial pressure gradient and flow reversal occurs. The transition from weakly swirling flow with no flow reversal to strongly swirling flow that

exhibits re-circulation zones is often known as vortex breakdown, which is discussed below.

1.7.1 Vortex Breakdown

The term vortex breakdown refers to an *"abrupt and drastic change in flow structure which is characterised by a sudden axial deceleration that occurs above a certain level of swirl, leading to the formation of a free stagnation point followed by a separation region with turbulence behind it"* Wang and Rusak (1997).

Vortex breakdown was observed by Peckham and Atkinson (1957) in the vortices created at the leading edge of a delta wing at an angle of attack and was consequently found to aid stability and increase lift. The importance of vortex breakdown to wing aerodynamics and to the mixing properties and flame stabilisation in the primary zone of gas turbine combustors has lead to many investigations into its cause. Benjamin (1962, 1967) states that the phenomenon is associated with the existence of a "critical state" which separates a sub-critical from a super-critical flow state. In a sub-critical flow disturbances can propagate both upstream and downstream and standing waves are supported, whereas in a super-critical flow only downstream propagation is possible. Hall (1967) suggested that the initiation of vortex breakdown is analogous to boundary layer separation under the influence of an adverse pressure gradient. Finally, Howard and Gupta (1962) and Leibovich and Stewartson (1983) deduced that vortex breakdown was connected to the size of the vortex core. This was based on the work of Rayleigh (1916) who stated that for swirling flow to be stable the angular momentum has to increase with radius. However, there is still no general theory of vortex breakdown nor agreement on its fundamental nature. Comprehensive reviews of the literature available on vortex breakdown are given by Hall (1972), Escudier (1988) and, more recently, by Lucca-Negro and O'Doherty (2001).

Experimentally Sarpkaya (1971, 1972) and Leibovich (1978) discovered seven distinct types of vortex breakdown, however, in turbulent flows only two; the spiral and bubble modes were identified. Sarpkaya (1971) showed that there is a progression of breakdown types such that the bubble mode always evolves from the spiral mode, as swirl strength is increased. Further increases in the swirl number resulted in the bubble becoming

increasingly stable with the point of vortex breakdown moving further upstream until the boundary of the equipment was reached. Yet further increases in the swirl number resulted in the formation of a long columnar vortex with backflow along the axis, Escudier and Zehnder (1982). Sarpkaya (1971) showed that the effect of an adverse axial pressure gradient was to move the vortex breakdown further upstream, or if extreme enough, even to initiate it.

Gupta (1984) states that in a gas turbine combustor application, generally a stable re-circulation bubble will be established if the swirl number is greater than 0.6 (Sn>0.6) and the Reynolds number is greater than 1.8×10^4 ($Re>1.8\times10^4$). Further increases in Reynolds number yield no significant change in the flowfield, as shown by Li and Tomita (1994) and Dellenback *et al* (1988). Both these investigations found that non-dimensionalised mean velocities measured at several nozzle diameters downstream of an angled vane flow swirler collapsed onto single curves for Reynolds numbers ranging from 3.0×10^4-1.0×10^5. The Reynolds number is defined as:-

$$Re = \frac{\rho D_{ref} V_{x,ref}}{\mu}$$

Where the reference length-scale is the swirler diameter and the reference velocity scale is the bulk average axial velocity at the swirler exit plane. Figure 1.5 shows a time-averaged streamline plot for a high Reynolds number strongly swirling flowfield, typical of that induced by a gas turbine fuel injector. In this case the swirl was imparted on the flow by angled vanes providing a Swirl number of 1.57.

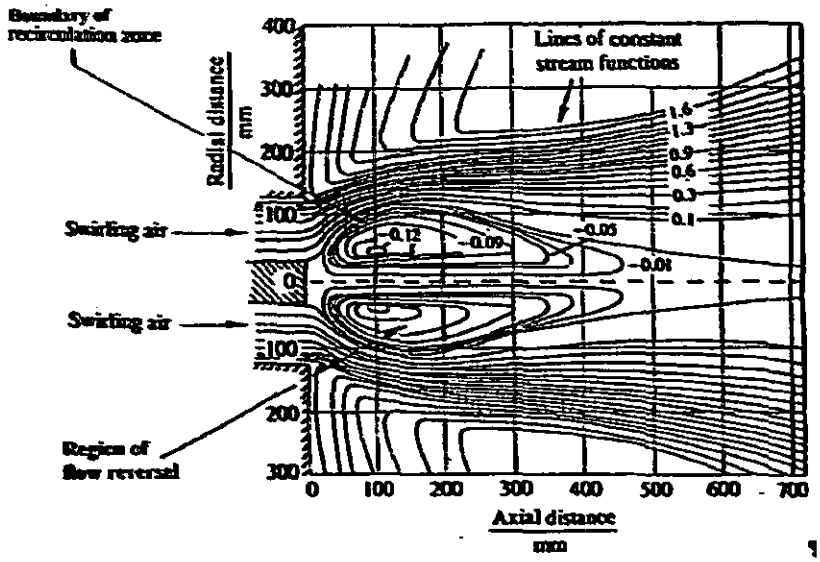

Figure 1.5. Streamlines of Re-Circulation Eddy in an Unconfined Swirling Jet Flow (Sn=1.57), Chigier & Beer (1972)

As can be seen, the high level of swirl and large adverse axial pressure gradient caused by the sudden area expansion have resulted in vortex breakdown as far upstream as the fuel injector exit plane (x=0mm). A bubble type breakdown can be observed, characterised by a stagnation point on the centreline followed by an axi-symmetric parcel of re-circulating fluid, which Harvey (1962) described as *"giving the impression that an imaginary spherical body has been placed on the axis of the vortex, around which the fluid is obliged to flow. In practice the imaginary object takes the form of a slightly elongated sphere of stagnant fluid"*. This re-circulating region of fluid has been shown by Sarpkaya (1972) continually to exchange fluid with its surroundings, a property that is crucial to combustor performance. The re-circulation zone boundary is defined by the radial positions at which the axial velocity changes from forward flow to reverse flow, Gupta (1984).

Measurements in a vortex breakdown relevant to combustor applications have been carried out by Dellenback *et al* (1988), Kihm *et al* (1988), Ahmed (1998), Khezzar (1997) and Zhou *et al* (2000), all using the non-intrusive optical measurement LDA technique. These results showed turbulence intensities to be highly anisotropic and reach extremely high levels within the shear layer between the forward and reverse flows. Compared to a jet (with no swirl) Ahmed (1997) found normal and shear stresses were also increased by up to an order of magnitude.

1.7.2 Precessing Vortex Core

Whilst time-averaged measurements in strongly swirling flows indicate axi-symmetric breakdown such as that shown in Figure 1.5, there is a tendency for the central solid body region of the flow to become unstable and precess about the axis of symmetry. This large-scale time-dependant oscillation is known as a Precessing Vortex Core (PVC) and is shown in Figure 1.6 by an instantaneous streamline plot deduced from PIV data in a confined pipe flow, Grosjean *et al* (1997). The red cross signifies the geometrical pipe centre.

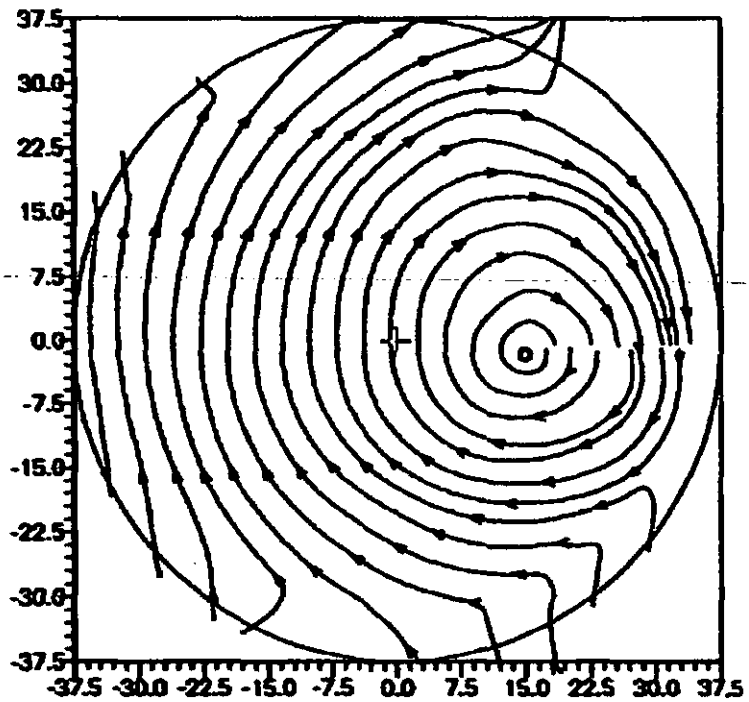

Figure 1.6. Instantaneous Streamlines Showing a Precessing Vortex Core, Grosjean *et al* (1997)

The geometric centre is clearly not consistent with the swirl centre; at other instants of time, the location of the swirl centre moves circumferentially around the geometric centre. The rotation of the PVC tends to have a regular frequency and amplitude directly proportional to the flow rate and is also a function of the system configuration and the Swirl number. Using previous work by Claypole and Syred (1980), Syred *et al* (1994) plotted a non-dimensional frequency parameter (the Strouhal number) of the PVC

periodic motion as a function of the Reynolds number and Swirl number as shown in Figure 1.7. The Strouhal number, St, is usually defined as:-

$$St = \frac{fD_{ref}}{V_{ref}}$$

Where f is the PVC precession frequency (in this case deduced from LDA measurements), D_{ref} is the diameter of the duct and V_{ref} is the bulk average axial velocity. This definition is used in throughout this thesis. However, the Strouhal number defined by Syred *et al* (1994) was based on the volumetric flow rate, $\dot{Q}$ and is a factor of $\pi/4$ less than the above definition:-

$$St_{\dot{Q}} = \frac{fD_{ref}^3}{\dot{Q}} = \frac{\pi}{4} St$$

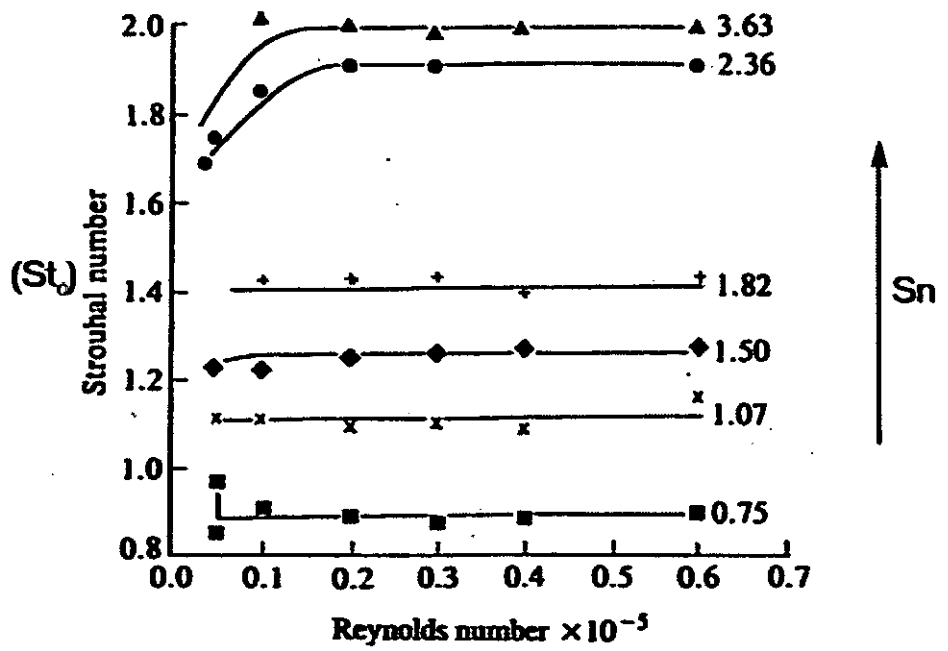

Figure 1.7 Variation of Strouhal Number as a Function of Swirl Number and Reynolds Number, Syred *et al* (1994)

Figure 1.7 shows that the PVC precession Strouhal number increases with increasing Swirl number but is independent of Reynolds numbers at values greater than 1.5×10^4.

Similar measurements were carried out by Yazdabadi *et al* (1994) using Hotwire Anemometry (HWA) on a tangential inlet cyclone dust separator; the data again showed the tendency for the Strouhal number to reach an asymptotic value with increasing Reynolds number. Froud *et al* (1995) used the PVC periodicity in a tangential entry swirl burner to trigger a three-component LDA system such that a phase-locked representation of the flowfield could be calculated. In this case, phase-locking was a method whereby data was collected only when the PVC centre was at a particular angular location in its periodic motion, hence one measurement per PVC rotational cycle. This work showed that the mean radial displacement of the PVC vortex core from the geometric centreline was approximately 3.5% of the duct diameter.

1.8 Project Objectives

It was the overall aim of this project to create a high quality single-phase isothermal benchmark data set in a strongly swirling flow induced by a low-emissions type fuel injector for the validation of LES codes. The fuel injector that was selected was based on a current low-emissions industrial application fuel injector supplied by Turbomeca as part of a joint EU Framework 5 project known as MOLECULES (See Appendix 1). The Turbomeca fuel injector design (described in detail in Chapter 2) was particularly suitable for LES validation research as engine tests had showed it to cause, or be one of the main contributors to undesirable combustor oscillations under certain conditions, Lartigue *et al* (2004).

The data set was to be gathered with emphasis on:-

i. Providing a geometrically repeatable problem relevant to near-field fuel injector aerodynamics.
ii. Gathering data including the measurement of appropriate and complete inlet and exit conditions for CFD calculation boundary conditions.
iii. Documenting the data in a manner appropriate for the validation of LES results, i.e. with particular focus on time-resolved flow features.
iv. Analysis of the data to improve understanding of unsteady high swirl phenomena such as vortex breakdown and PVC effects.

The non-intrusive, spatially and temporally resolved measurement techniques primarily to be used are described collectively as Light Sheet Imaging (LSI) techniques. LSI techniques such as Particle Image Velocimetry (PIV) measurements to resolve the velocity field and Planar Laser-Induced Fluorescence (PLIF) to resolve the scalar field were to be considered. Data analysis methods were applied with particular attention to analysis of time-dependent flow structures. If required, alternative experimental techniques such as HWA and LDA should be considered for PIV validation purposes and to provide higher rates of temporal resolution at desired points than is possible using LSI systems. The combined application of these measurement and analysis techniques was to be used to help improve understanding of the flow physics typical of a low-emissions combustor.

1.9 Thesis Structure

This thesis will be separated into the following sections:

i. Chapter 2 details the design and commissioning of the experimental facilities, including details of the fuel injector and the choice of test conditions.
ii. Chapter 3 provides a description of the LSI experimental configuration, and the optimisation and data collection methodologies adopted for PIV and PLIF measurement techniques, plus descriptions of the HWA and LDA systems.
iii. Chapter 4 describes the data reduction methods used, for the evaluation of time-averaged statistics and identification and assessment of instantaneous flow structures.
iv. Chapter 5 describes the results.
v. Chapter 6 provides a summary, conclusions and recommendations for further work.

2 EXPERIMENTAL FACILITIES

As described in the previous chapter, a swirling flowfield was created using a fuel injector based on a current low-emissions Turbomeca design. The original Turbomeca design and the modifications introduced for this study are described in Section 2.1. In order to assess the impact of the swirl stream passage definition and slot angle on the flowfield a second modular swirler design was also manufactured, this is described in Section 2.2.

The fuel injector and swirler flowfields were investigated in both water flow and airflow rigs, where the choice of working fluid was based on the suitability to the measurement technique. Water was used for Light Sheet Imaging (LSI) measurement techniques as it allowed for full system optimisation, which was not possible in the airflow rig. However the airflow rig allowed for the used for Hotwire Anemometry (HWA) which enabled for measurements with temporal resolutions higher than possible with the LSI systems. A pre-existing water flow rig and the modifications required for the measurements of this thesis are described in Section 2.3; the design of the airflow rig is described in Section 2.4.

The test conditions in both air and water flows were based on matching, as close as possible, combusting experiments carried out as part of the same MOLECULES work package at Darmstadt University (Janus *et al* (2004)). The test condition is described in Section 2.5. This section also presents a selection of measurements used to commission the experimental facilities and demonstrate the comparability of data taken on both airflow and water flow test rigs.

2.1 Datum Fuel Injector

The fuel injector design was based on an industrial application low-emissions fuel injector. Good mixing between the gaseous fuel and air was achieved by premixing within the radial feed slots that imparted swirl onto the flow. A central jet of air was also injected directly into the combustion zone for control of the primary zone re-circulation, as shown in Figure 2.1.

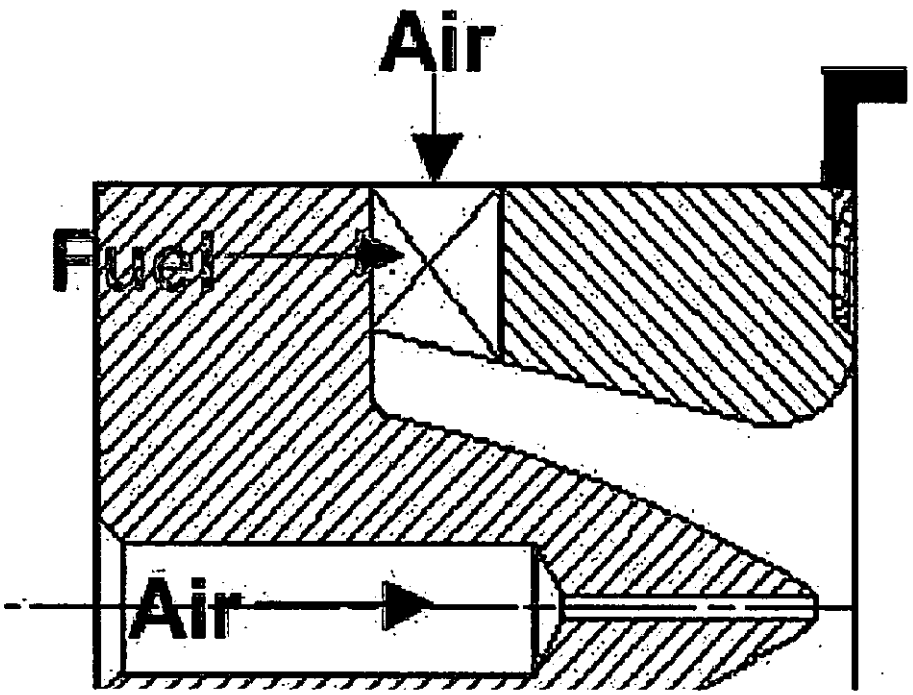

Figure 2.1. Turbomeca Low Emissions Fuel Injector, Lartigue *et al* (2004)

The radial entry slots were at an angle, α_1=30° and are shown in Figure 2.2.

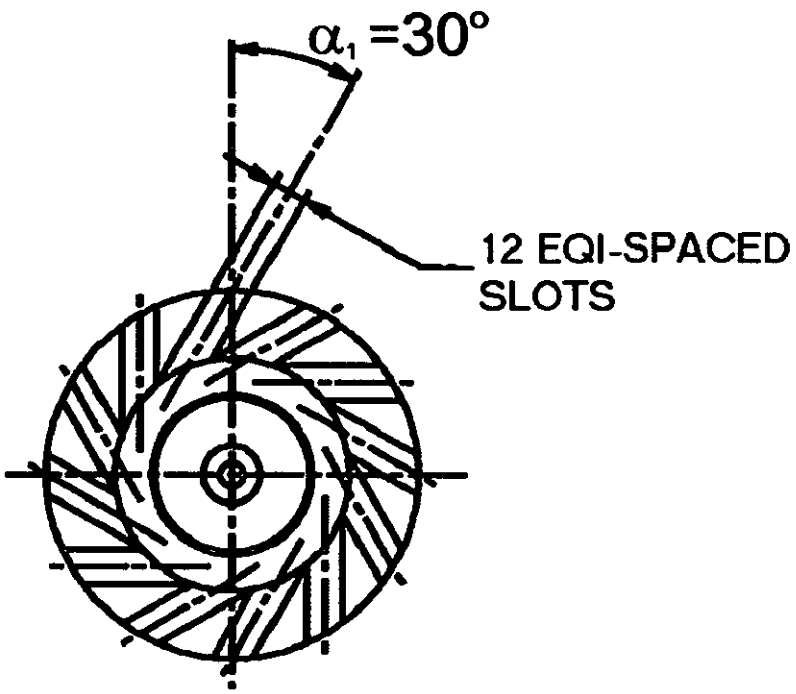

Figure 2.2. Turbomeca Fuel Injector Radial Entry Swirl Slots

By agreement of all MOLECULES partners, the internal geometry of the fuel injector was simplified such that it could be easily reproduced using block-structured computational meshes. The swirl stream passage shape inner wall was defined with a constant half angle of 17° all the way to the nozzle exit plane, and an outer wall with a constant half angle of 12.5° until 10mm from the exit plane, after which the radius of the outer wall remained constant. This replaced the flare on the swirler passage outer wall with a discontinuous wall gradient (i.e. a corner) and made the central jet and swirler passage duct co-planar at exit. For the MOLECULES combusting measurements, the premixing slots were not used, instead fuel (methane) was passed through the central jet shown in Figure 2.3.

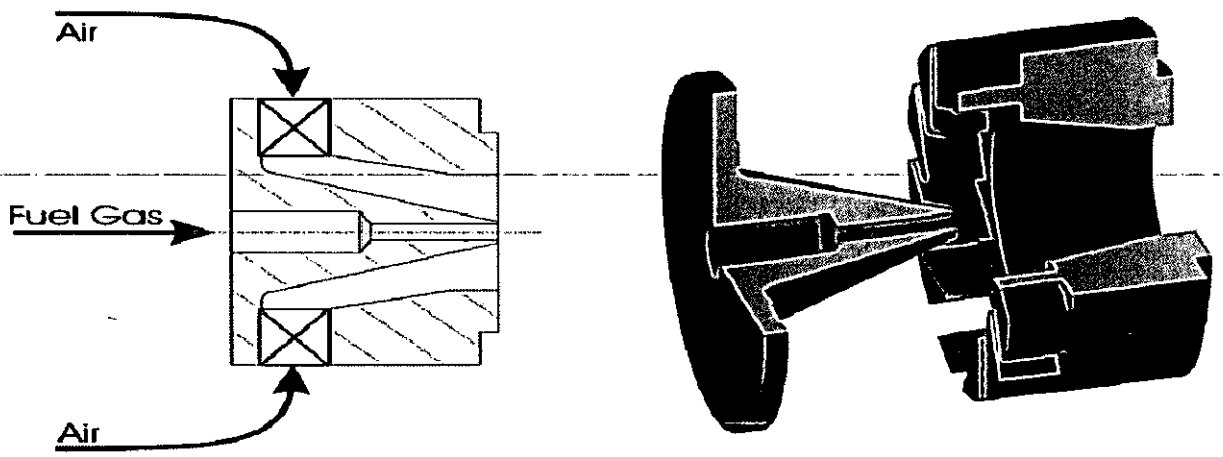

Figure 2.3. Fuel Injector used for Combusting Measurements in MOLECULES Project, Janus *et al* (2004)

For the isothermal measurements of this thesis, the generic design shown in Figure 2.3 was maintained. However, the size of the fuel injector was scaled (for both water and airflow rigs) to maintain a similar ratio of swirl stream geometric exit area, A_s to dump area expansion chamber, A_{ex}, (A_s/A_{ex}). This lead to a scale factor of 1.35 with a fuel injector exit (outer wall) diameter of 37.63mm. The scaled fuel injector, denoted throughout this thesis as the datum fuel injector, is shown in Figure 2.4, held in situ by a spigotted flange common to both airflow or water flow rigs.

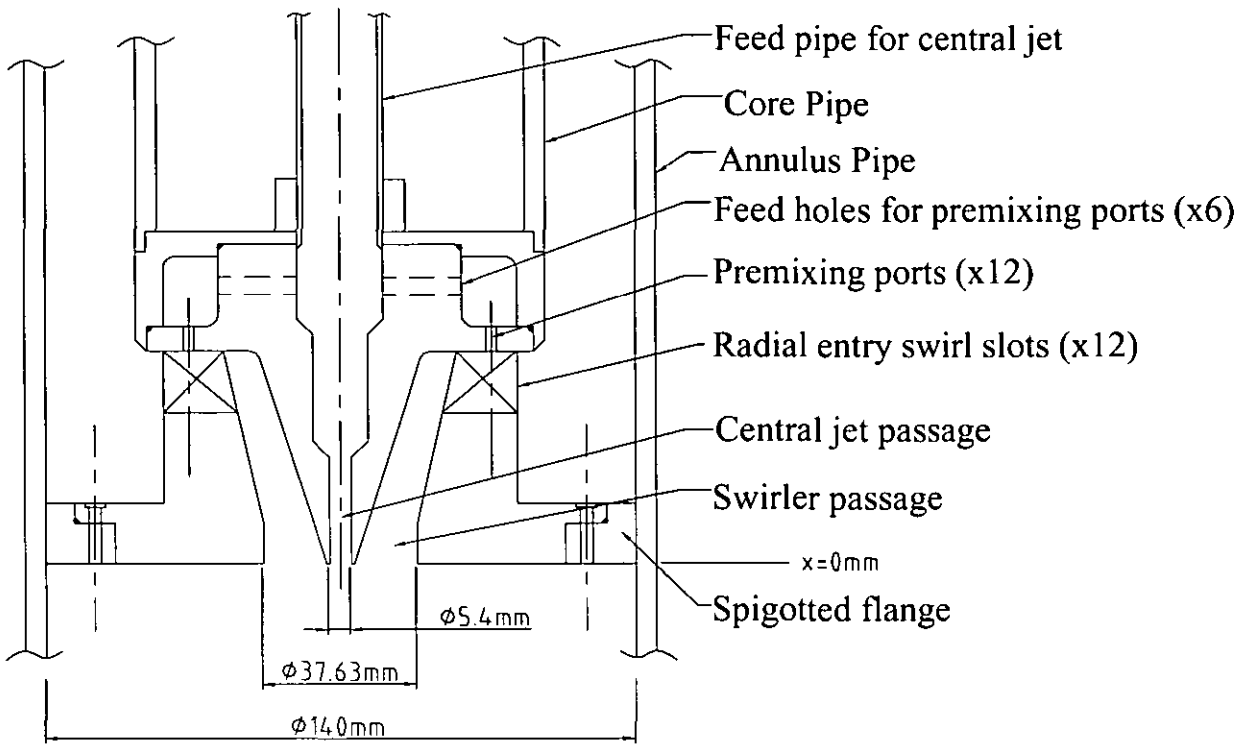

Figure 2.4 Datum Fuel Injector Design

The fuel injector was manufactured from translucent cast Acrylic to provide excellent optical access into the swirl flow passage. The premixing slots were included in the design, however, they were not used as part of the work presented here. For detailed drawings of the datum fuel injector, see Appendix 2. For simplicity some frequently used dimensions and geometrical areas are listed in Table 2.1. The subscripts s and j denote the swirl stream and central jet stream exit planes (values at x=0mm) respectively:-

Swirl stream outer diameter, D_s	37.63×10^{-3} m
Swirl stream inner diameter	6.76×10^{-3} m
Swirl stream geometrical area, A_s	1.08×10^{-3} m^2
Central jet diameter, D_j	5.40×10^{-3} m
Central jet geometrical area, A_j	2.29×10^{-5} m^2
Dump expansion chamber diameter, D_{ex}	1.40×10^{-2} m^2

Table 2.1. Exit Plane Dimensions for Datum Fuel Injector.

2.2 Modular Swirler Design

To assess the affects of the swirl passage shape and the swirler slot angle on the flowfield a modular swirler was designed based on the datum fuel injector geometry but with no central jet. An exploded view is shown in Figure 2.5, once again to allow for good optical access this swirler was manufactured from translucent cast Acrylic.

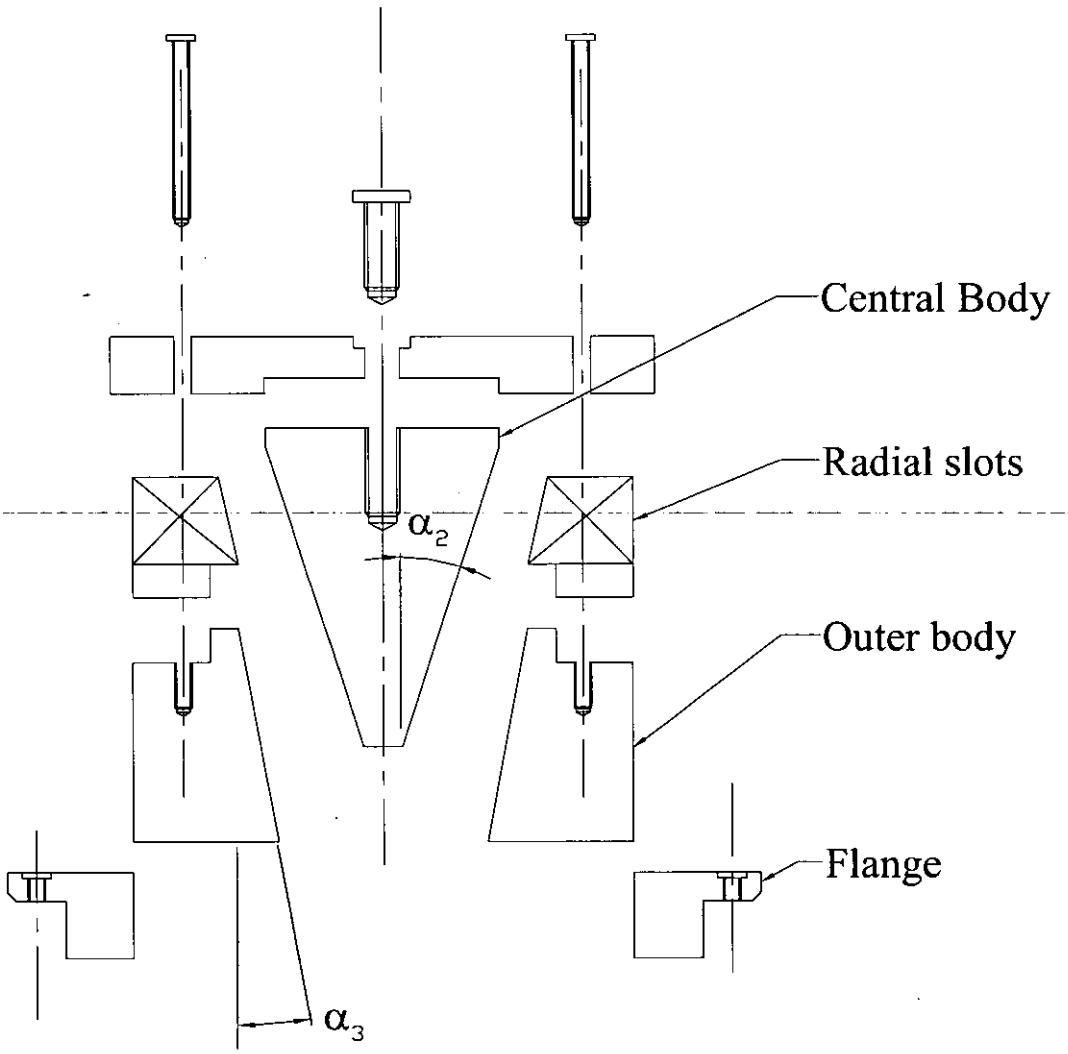

Figure 2.5. Exploded View of Modular Swirler

In this design, the central and outer bodies could be exchanged in order to modify the swirl passage internal geometry. By selecting a central body with a wall angle of α_2=17° and an outer body with a wall angle of α_3=9.5°, the datum fuel injector and modular swirler inlet (denoted by subscript the r) and exit plane bulk average axial and circumferential velocities remained similar, as shown in Figure 2.6 and Figure 2.7

respectively. The bulk averaged tangential velocity was calculated from an area weighted moment, M_θ defined by Scott and Bartlett (1976) assuming the conservation of angular momentum:-

$$M_\theta = 2\pi \int_{R_0}^{R_1} V_t r^2 dr \Big/ 2\pi \int_{R_0}^{R_1} r dr$$

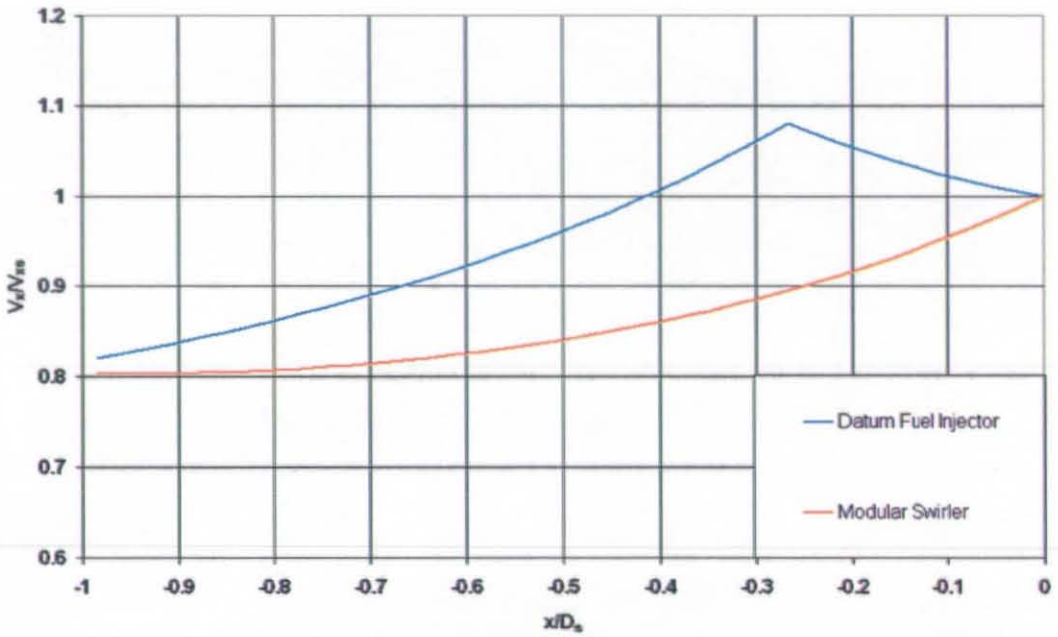

Figure 2.6. Swirl Stream Passage Bulk Average Axial Velocity Variation for the Datum Fuel Injector and the Modular Swirler (α_2=17° and α_3=9.5°)

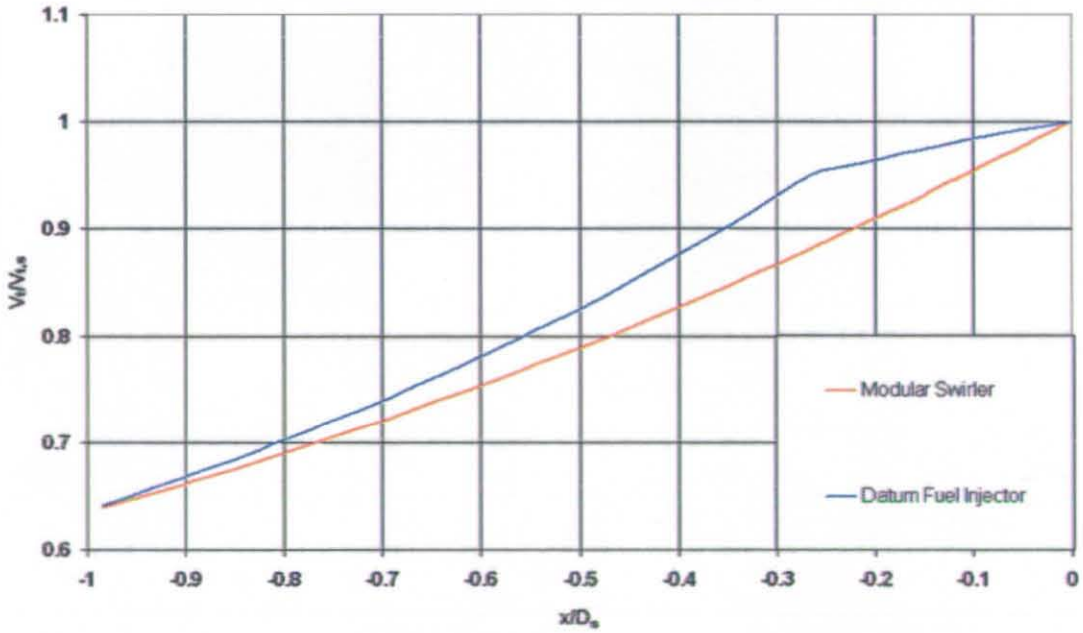

Figure 2.7. Swirl Stream Passage Bulk Average Tangential Velocity Variation for Datum Fuel Injector and Modular Swirler (α_2=17° and α_3=9.5°)

By using this swirl passage geometrical definition (α_2=17° and α_3=9.5°) as a "base" case, the effects of the internal corner present in the datum fuel injector could be assessed. By then using inner body modules with walls angles of α_2 = 13.5° and 20.5°, and outer body modules with wall angles of α_3 = 8.5° and 11.5°, the effects of varying the bulk average axial velocity ratio ($V_{x,s}/V_{x,r}$) or the bulk average tangential velocity ratio ($V_{t,s}/V_{t,r}$) could be assessed. Table 2.2 below details the swirl stream geometric definitions used in this thesis. To provide a parametric study, only the axial or circumferential velocity ratio was varied relative to the base case. In Table 2.2 the values in red highlight configurations with a similar bulk average axial velocity ratio and the values in blue highlight configurations with a similar circumferential velocity ratio to the base case.

	α_2	α_3	$V_{x,s}/V_{x,r}$	$V_{t,s}/V_{t,r}$
Base case	17°	9.5°	1.25	1.56
Reduced $V_{x,s}/V_{x,r}$ (const $V_{t,s}/V_{t,r}$)	20.5°	8.5°	1.13	1.56
Increased $V_{x,s}/V_{x,r}$ (const $V_{t,s}/V_{t,r}$)	13.5°	11.5°	1.43	1.56
Increased $V_{t,s}/V_{,r}$ (const $V_{x,s}/V_{x,r}$)	13.5°	8.5°	1.29	1.65
Reduced $V_{t,s}/V_{t,r}$ (const $V_{x,s}/V_{x,r}$)	20.5°	11.5°	1.21	1.43

Table 2.2. Modular Swirler Flow Path Definitions

A central body module with a constant radius of 14mm (α_2=0°) and an outer body module set at a constant radius of 25mm (α_3=0°) was also used. This provided a parallel wall configuration with axial and circumferential velocity ratios of unity. In order to assess the impact of the swirl slot angle on the flowfield, five radial slot modules, with slot angles of α_1=30°, 25°, 20°, 15°, 10° and 0° were used. In conjunction with the various swirl stream passage internal geometry definitions, a total of 36 modular swirler configurations were tested.

2.3 The Water Flow Test Rig

The vertical standing water flow rig test rig used for this investigation is a well-established facility that over the past six years has contributed to experimental work in two PhD theses, namely Spencer (1998) and Hollis (2004). Several journal papers have also been written, including Hollis *et al* (2001), Spencer and McGuirk (2001), and more recently, based on the work of this thesis, Midgley *et al* (2004).

Originally the water rig was designed to investigate multiple impinging jets in a confined cross flow, analogous to primary and dilution liner port flows of a gas turbine combustor. The achieve this flow pattern a 90mm ID core pipe (representing the liner) contained the ports and was concentrically mounted within an 140mm ID annulus pipe (representing the casing of the combustor). Both pipes were 5mm thick and made from cast Acrylic. A schematic diagram of the water flow test rig is shown in Figure 2.8.

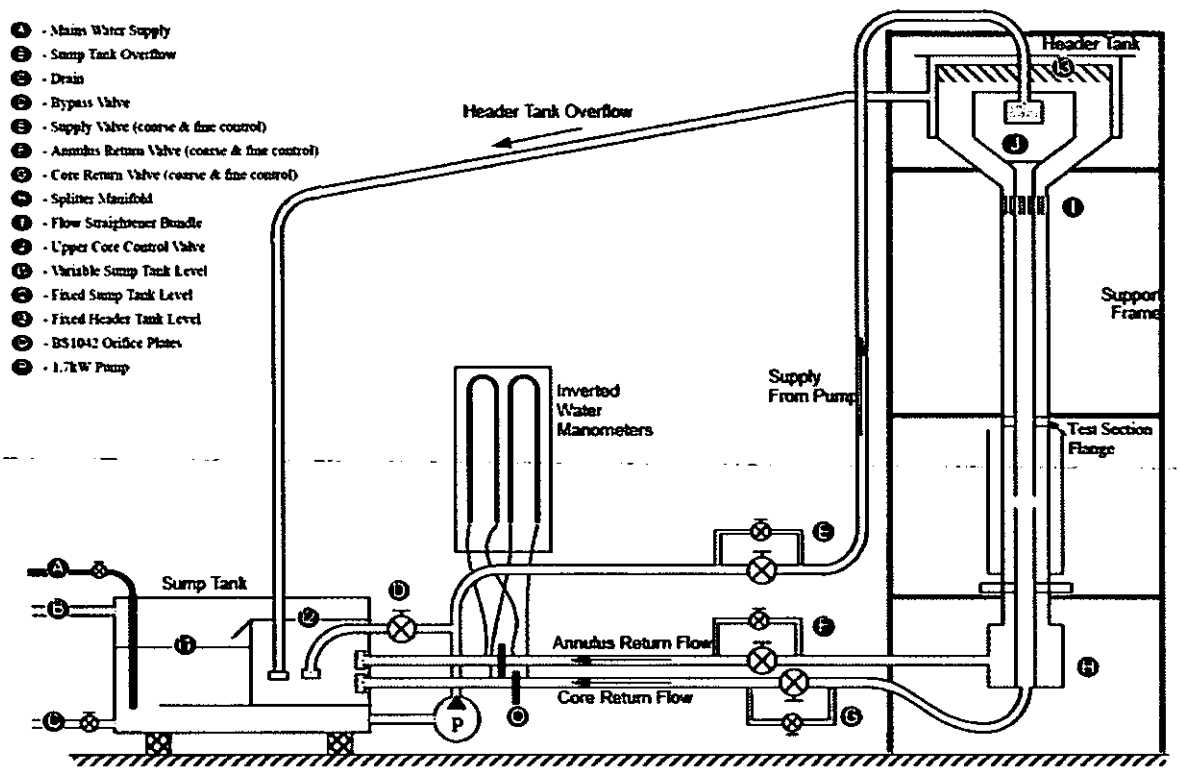

Figure 2.8. Schematic of the Vertical Flow Water Flow Test Rig, Spencer (1998)

The test facility creates a closed-loop circuit that uses a 1.7kW pump (P) to fill the header tank from a sump tank. By ensuring the pump delivered a slightly higher mass flow rate to the header tank than was required through the test section the header tank experienced a surplus of water inflow, this excess water was returned to the sump tank via the header tank overflow, maintaining a constant level of water within the header tank and therefore a constant driving force through the test section. Flow straighteners were included in both core and annulus streams at inlet to remove any swirl components in the flow. The mass flow rates through the test section were controlled by flow valves in the annulus and core return flow pipes and measured using BS1042 orifice plates connected to

manometers. The performance of these orifice plates and manometers was assessed by Hollis (2004) by comparing the manometer based results to inlet mass flow rates calculated from area integration of profiles measured in the core and annulus using the PIV technique:-

$$\dot{m} = 2\pi\rho\int_{r_0}^{r_1} \overline{V_x} r dr$$

Where in the core r_0=0mm and r_1=45mm and in the annulus r_0=50mm and r_1=70mm. The results are shown in Figure 2.9.

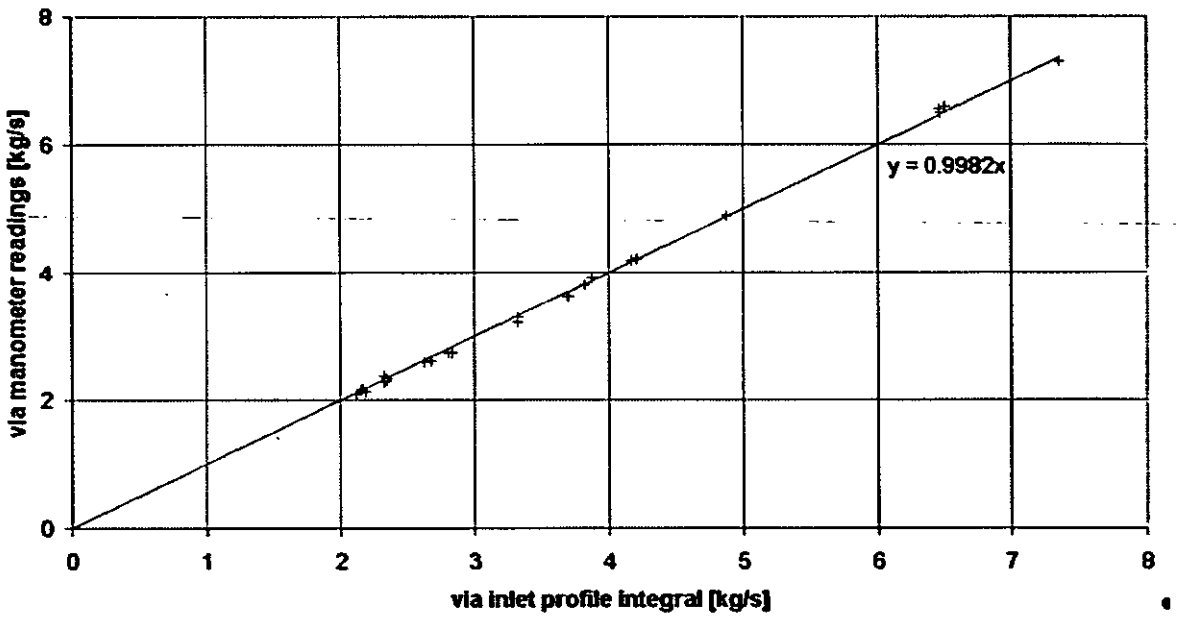

Figure 2.9. Comparison of Inlet and Outlet Mass Flow Rates, Hollis (2004)

As would be expected a linear relationship with a gradient of 1 exists, the very small amount of scatter of data points suggests that the mass flow values calculated from the manometers are repeatable and of high accuracy.

2.3.1 Modified Test Section

In order to make the water flow rig suitable for the investigation of the datum fuel injector and modular swirler, several modifications were necessary in order to:-

i. feed (and isolate) the central jet flow.
ii. control and condition inlet flow paths to both radial swirler stream and central jet.
iii. dictate the length of the dump area expansion chamber.
iv. allow for optical access to both axial-radial and radial-circumferential planes.
v. exhaust the water from the test section without biasing the upstream flowfield.

To meet all of these requirements a new test section and a separate feed flow for the central jet were required, these are shown in Figure 2.10. The following sub-sections describe in detail the important aspects on the modified test rig.

In common with the pre-existing test section, a square-section water jacket was used to encase the annulus pipe across the area of interest. This ensured that the refraction of light at the curved surface of the test section wall was minimised due to a similar density water/acrylic/water interface. The distortion across an axial-radial plane (x-r) including the test section centreline was assessed by identifying the spatial locations of accurately drawn crosses equi-spaced at 3mm on a laminated calibration plate and comparing them to their expected positions using a "distortion correction" algorithm in the Davis v6.2 PIV evaluation software, LaVision (2001). It was found that the distortion across the vast majority of the plane was negligible, however in the near wall regions (<1mm) the algorithm failed due to the relatively coarse resolution of the crosses (required by the algorithm).

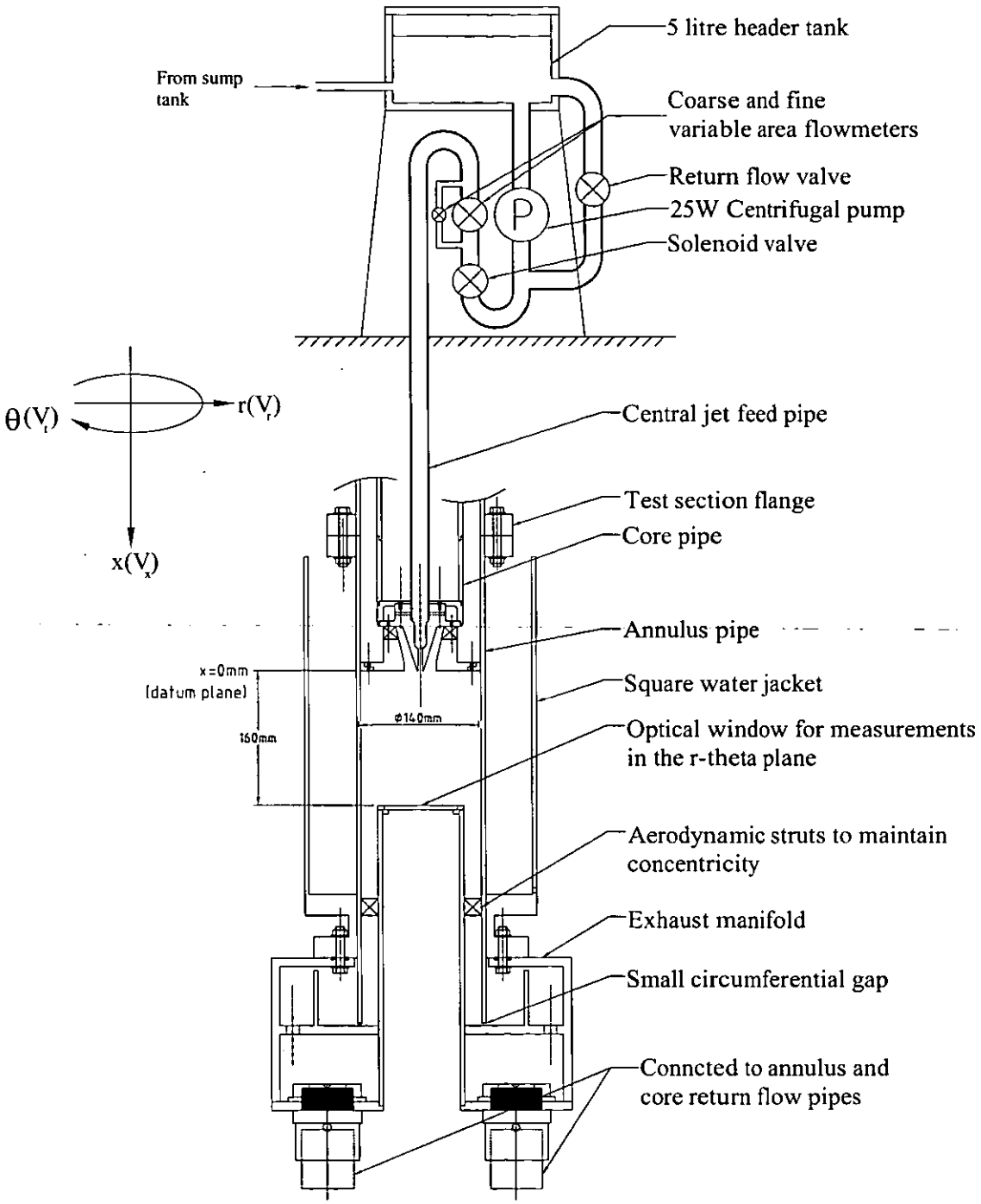

Figure 2.10. Modified Test Section

2.3.1.1 Central Jet Feed Flow Path

In order to control the mass flow rate through the central jet (for both PIV and PLIF measurements) and allow dyed fluid to be used (for PLIF measurements) an isolated central jet feed flow path was necessary. This isolated flow path was created by using a 5-litre header tank positioned directly above the original header tank (header tank (2), Figure 2.10). A 25W DC centrifugal pump was used to provide a constant driving force through the 12mm ID pipe network. The mass flow rate was controlled by two flow-meters with variable area valves operating in parallel, a "coarse" flow-meter with measurable increments of $3.33\times10^{-3}kgs^{-1}$ and a "fine" control with incremental steps of $4.16\times10^{-4}kgs^{-1}$. As the centrifugal pump operated at a constant power, a return flow pipe with a variable area valve was added such that the mass flow rate through the central jet feed pipe could be controlled without overloading the pump.

As this isolated feed system was not closed loop and it had a finite operating time. Therefore a solenoid valve was employed, which when closed allowed flow only through the return flow pipe (creating a closed loop), when required this valve was opened allowing flow though the both. When the solenoid valve was open the maximum rig operating time was 46 seconds with the required central jet mass flow rate of $0.11kgs^{-1}$ (see Section 2.5). This was sufficient for the longest time-history of data taken of 43 seconds. The header tank was refilled with either particulate seeded water (for PIV measurements) or dyed water (for PLIF measurements) by a dedicated 30 litre sump tank at ground level using a 60W centrifugal pump. The variable area flow-meters were calibrated by exhausting the flow through the central jet feed pipe into a measuring jug over a period of one minute. Comparison of the flow-meter reading (input) and the mass flow rate calculated from the volume of water collected in the measuring jug (output) is shown in Figure 2.11.

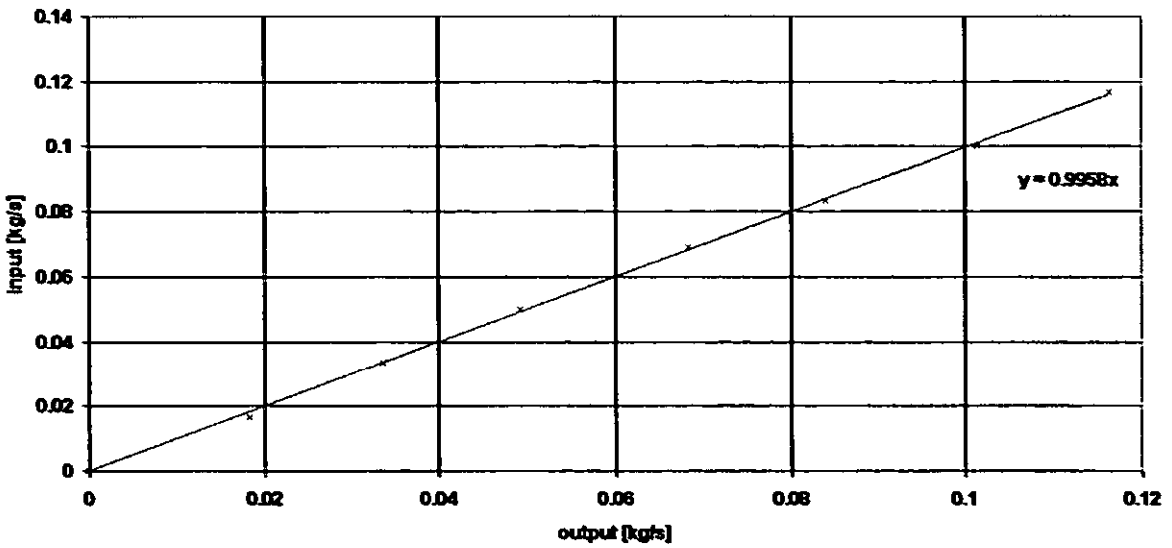

Figure 2.11. Calibration of Flow-meters Upstream of the Central Feed Pipe

The excellent agreement of this data indicates that the flow-meters could be used directly for accurate control of the mass flow rate through the central jet passage. It should be noted that as adjustment of the mass flow rate through the jet affected the total mass flow rate through the rig and visa versa; an iterative approach of increasingly fine adjustments was necessary until both the total mass flow rate and the central jet mass flow rate were as required.

2.3.1.2 Conditioning of Inlet Flow Paths

Well defined inlet conditions to the swirl and central jet passages were essential for both repeatable measurements and CFD boundary condition definition. Fully developed pipe flow data suggests that if Re>4000 the flow will be fully developed after around 20 pipe diameters, however for 2100<Re<4000 a transition zone exists whereby the flow may take up to 100 pipe diameters to become fully developed. The central jet feed pipe of 12mm ID had an axial length of 166 pipe diameters and would therefore be expected to be fully developed for mass flow rates greater than $0.02kgs^{-1}$ (Re>2100). However, the 20mm annular gap used to feed the swirl stream was only 74 pipe diameters length. By measuring the axial velocity inlet profile 100mm upstream of the fuel injector exit plane (x=-100mm) in the annular swirl stream feed passage using the PIV technique, the mass

flow rate to peak velocity ratio ($\dot{m}/\hat{V}_x$) was assessed for a range of annulus Reynolds numbers 1800>Re>7200. The Reynolds number is defined as:-

$$Re = \frac{\rho D_{ref} V_{x,ref}}{\mu}$$

Where the annular gap height of 20mm was used as the reference length-scale and the bulk average axial velocity was taken as the reference velocity scale. The effect of the Reynolds number on this ratio is shown in Figure 2.12.

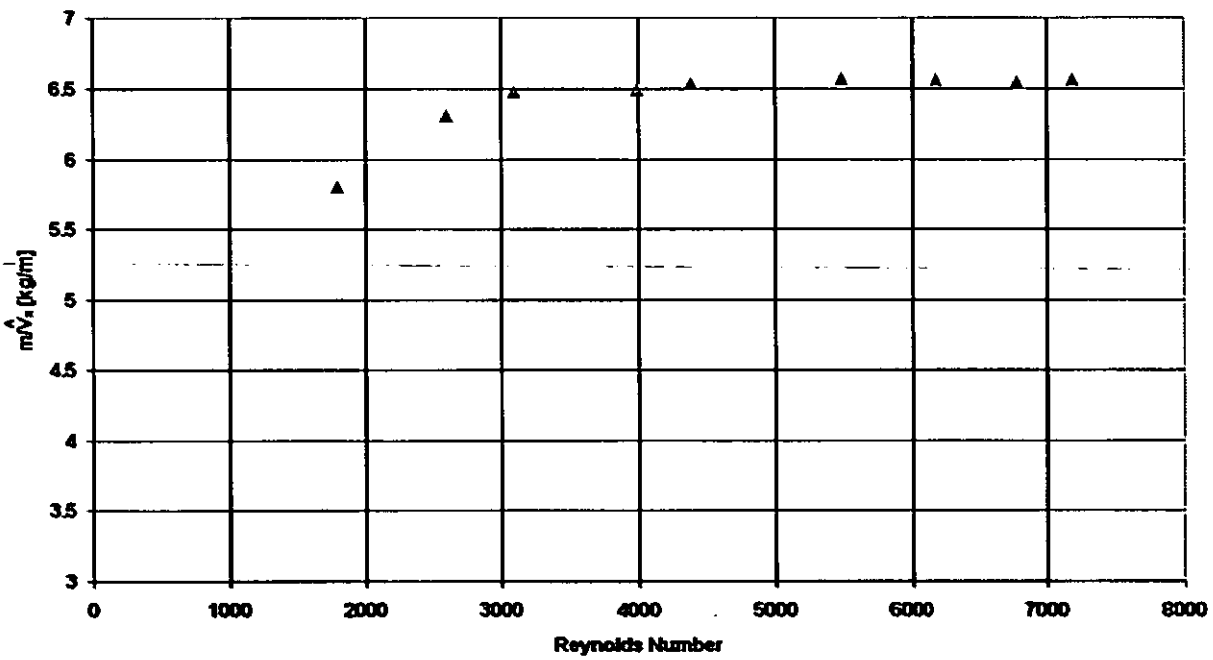

Figure 2.12 Mass Flow Rate to Peak Velocity Ratio as a Function of Reynolds Number in the Annular Swirl Stream Feed Path (x=-100mm)

It can be seen that $\dot{m}/\hat{V}_x$ becomes approximately constant at Re>3000 ($\dot{m} > 1.13 kgs^{-1}$) indicating that beyond this value the flow was fully developed. All water flow rig measurements reported in this thesis were conducted using annulus mass flow rates above this value.

2.3.1.3 Axial Length of Dump Area Expansion Chamber

In a strongly swirling flow exhausting into a dump expansion chamber there is a tendency for a long stable backflow region to occur (see Section 1.7). Forward flow across the central portion of the chamber will only be re-established when the radial pressure gradient (which scales on the square of the swirl velocity component) equalises and the resultant adverse axial pressure gradient diminishes in strength sufficiently enough that it can be overcome by the forward momentum of the flow. Reader-Harris (1994) showed that the rate of circumferential velocity reduction in a swirling pipe-flow was approximately proportional to the skin friction coefficient of the pipe, λ, which can estimated from the Colebrooke (1938) equation:-

$$\frac{1}{\sqrt{\lambda}} = -2.0\log_{10}\left[\left(\frac{2.51}{\mathrm{Re}\sqrt{\lambda}}\right)+\left(\frac{\gamma/\mathrm{D_{ref}}}{3.72}\right)\right]$$

This equation shows that λ reduces with larger Reynolds numbers and smaller relative surface roughness, γ/D_{ref}, where γ is the average height of the surface irregularities and D_{ref} is the pipe diameter. For the water flow rig tests the Reynolds number was calculated to be of order $Re=2\times10^4$ in the dump expansion chamber. The surface roughness γ is approximately 2μm for Acrylic pipe, hence λ was estimated at 0.025. Reader-Harris (1994) predicted that for $Re=1\times10^4$ and $\lambda=0.032$ the swirl velocity would decay by only 10.75% over 65 pipe diameters. The maximum possible length of the test section was approximately 10 pipe diameters.

In practical gas turbine combustion systems the length of the swirl-induced re-circulation zone is controlled by the radial impinging jets from primary ports which act as an aerodynamic blockage. This mixing of non-swirling fluid from both primary and dilution ports also reduces the level of swirl. Finally, the acceleration of the axial velocity in the combustor exit nozzle means that the swirl velocity will reduce even further. Hence in an isolated fuel injector experiment, as designed here, without the addition of impinging jets a long backflow region may be expected, as observed by Gouldin (1985) and Hughes (2003). As it is was not feasible to provide a row of impinging jets into the test section it was decided that the position of pressure recovery would have to be physically imposed onto the flow. This was achieved by using a circular-sectioned concentrically mounted

downstream blockage. In order to decide on the most appropriate axial location of the downstream blockage, preliminary measurements using the PIV technique were taken in a flowfield induced by a pre-existing three-stream axially fed swirler as shown in Figure 2.13. For further details on this swirler see Hughes (2003).

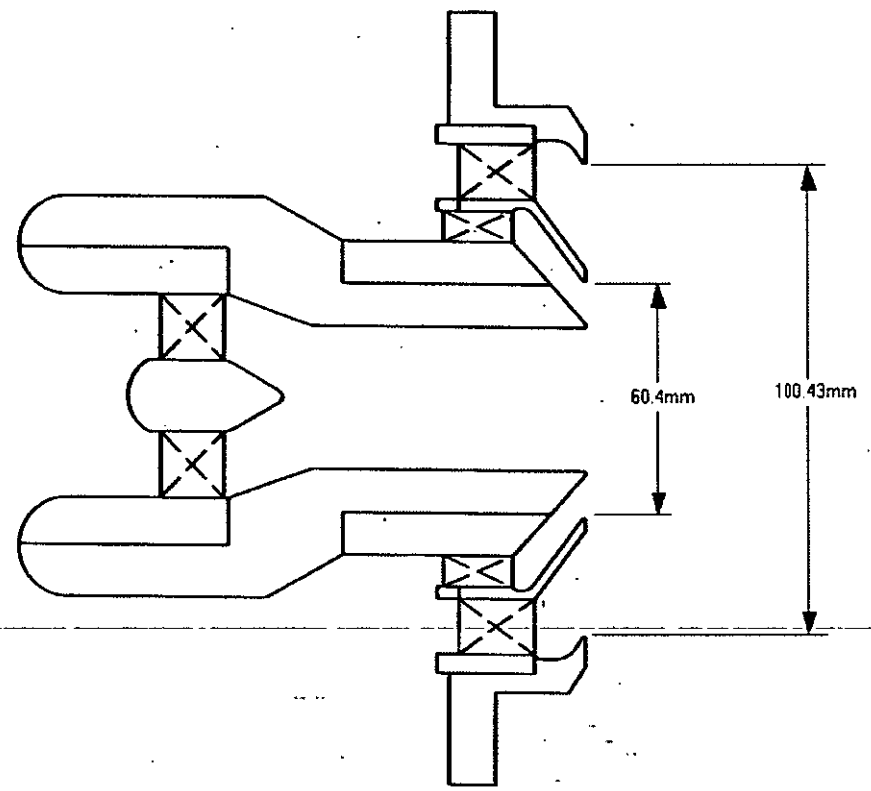

Figure 2.13. Three-Stream Axially Fed Swirler, Hughes (2003)

This three-stream swirler model was mounted in the un-modified water rig using a bracket attached to the test section flange as shown in Figure 2.14 and a variable length 90mm diameter cylinder was used to create a downstream blockage. With the three-stream swirler having an outer exit diameter of 100.43mm the area ratio was sufficiently high (A_s/A_{ex}= 0.51) that the flowfield would be affected by the confinement of the outer duct wall, Gupta (1984). To make the flowfield more representative to that of the datum fuel injector the outer ring of the swirler was removed and only the inner and core swirlers were used. This created a fuel injector with an outer exit diameter of 60.40mm and an area ratio of 0.186. This was much closer to the value of 0.072 of the datum fuel injector and considered sufficient for the preliminary tests.

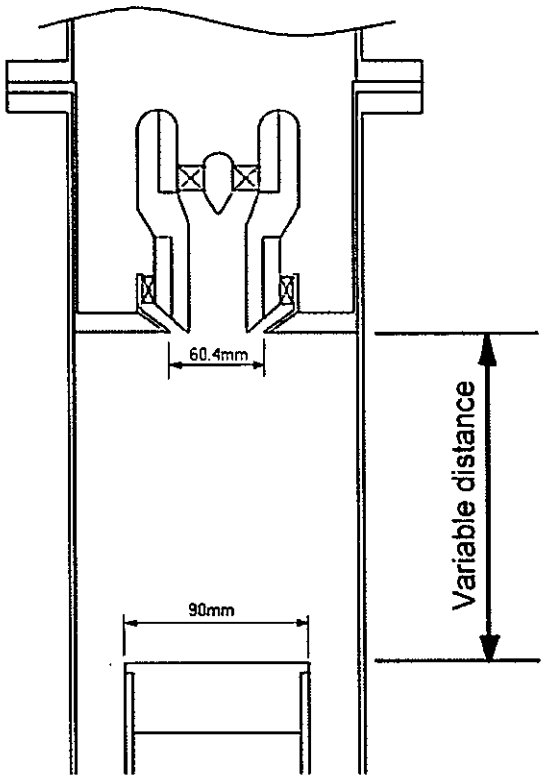

Figure 2.14. Water Flow Rig Configuration for Three Stream Swirler Tests

Typically, the location of the primary port row is 1-2 fuel injector diameters downstream of the fuel injector exit plane, as shown in Figure 2.15 for the Rolls-Royce Tay annular combustor.

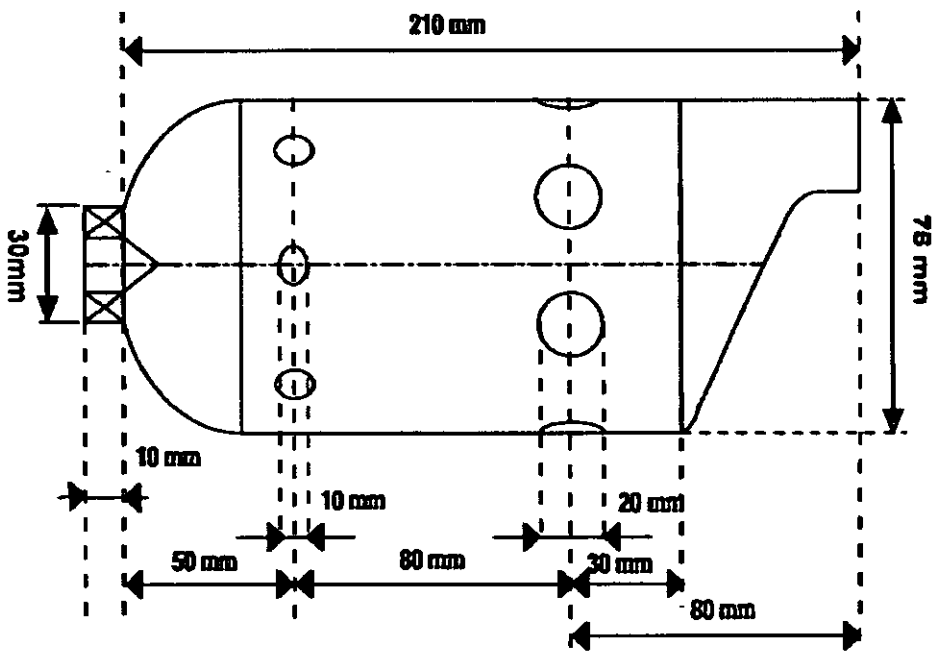

Figure 2.15. Rolls Royce Tay Combustor, di Mare *et al* (2004)

However the preliminary measurements indicated that placing the blockage less than 3 fuel injector diameters downstream would affect the flowfield, most notably by damping any precession of the vortex core. Therefore, it was decided that rather than provide a re-circulation zone length comparable to that of an actual combustor, it was more important to ensure that the aerodynamic characteristics of the flowfield, particularly any flow instabilities, were not influenced by the location of the downstream blockage. Therefore, the downstream blockage was finally placed (for all data presented in this thesis) at an axial distance of 160mm (or 4.25 fuel injector exit diameters) downstream of the fuel injector exit plane. A similar strategy was employed by Khezzar (1997) who placed a baffle plate 5.4 swirl passage diameters downstream of a radially fed swirler.

2.3.1.4 Optical Access to Radial-Circumferential Plane

As several of the aerodynamic characteristics of a strongly swirling flow are influenced by the swirl velocity it was essential to capture PIV data in the radial-circumferential (r-θ) plane. However, with the available LSI systems this would require optical access viewing along the fuel injector centreline. As it was unfeasible to have optical mountings above any r-θ plane of interest, i.e. within the feed flow paths, this optical access had to be from below. For this purpose the downstream blockage discussed in the previous section provided a convenient solution. Whilst it would have been possible to mount an angled mirror in an optically transparent downstream blockage with the camera positioned to the side of the test section, the optical path from the plane of interest to the camera would be complex, with several additional curved Acrylic surfaces. A much simpler optical path was established by locating the camera inside a hollow downstream blockage, such that the camera could be oriented along the fuel injector centreline. As the camera would be placed perpendicular to the flat blockage top there would be no image distortion.

2.3.1.5 Exhausting the Test Section Flow

Once the flow had past the downstream blockage a method had to be found to exhaust it without biasing the flow in the test section. In order to achieve this, a small circumferential gap between the bottom of the test rig and the annulus pipe was used (see Figure 2.10). This allowed water to exit in all theta directions into an enclosing box. The

circumferential gap was designed to provide an effective area slightly larger than the effective area of the fuel injector exit; this ensured that the pressure drop across the fuel injector would be higher than that across the circumferential exit gap. Therefore, the flow through the fuel injector should not be influenced by the downstream conditions. The original idea was that the flow would then be carried away via four return flow pipes located one on each of the four sides of the manifold, choosing large enough diameter return flow pipes such that the pressure drop across the circumferential gap would be higher than that across the return flow pipes. The four return flow pipes would then connect into a second manifold arrangement and exhaust via the pre-existing return flow pipes. However, the lack of space available for the pipe network resulted in an alternative approach. Rather than four return flow pipes an arrangement was designed such that the flow travelled up through a second circumferential gap, after this the flow passed through 12 holes into a lower section of the exhaust manifold and into the return flow pipes (see Figure 2.10) At each stage the effective area was designed to be slightly greater than the previous stage such that the pressure drops across each stage reduced and flow effects within the manifold would be isolated from the test section.

2.4 The Airflow Rig

In order to provide good commonality with the above described water flow rig, several of the design features were maintained for the airflow rig. These similarities were:-

1. The use of a concentric pipe inlet arrangement to feed the swirl flow, the length of the pipes being sufficient to ensure a fully developed flow
2. The use of a downstream blockage to control the length of the re-circulation zone and provide controlled exit conditions.
3. The use of a circumferential gap and manifold arrangement to isolate the test section and exhaust system flows.

However, as PLIF measurements were not to be taken in airflow, an isolated flow path to the central feed pipe was not necessary. Therefore both swirl and central jet streams were fed from a single intake and the mass flow split was fixed by a throttle plate in the concentric pipe arrangement feeding the swirl stream. A diagram of the airflow rig is shown in Figure 2.16.

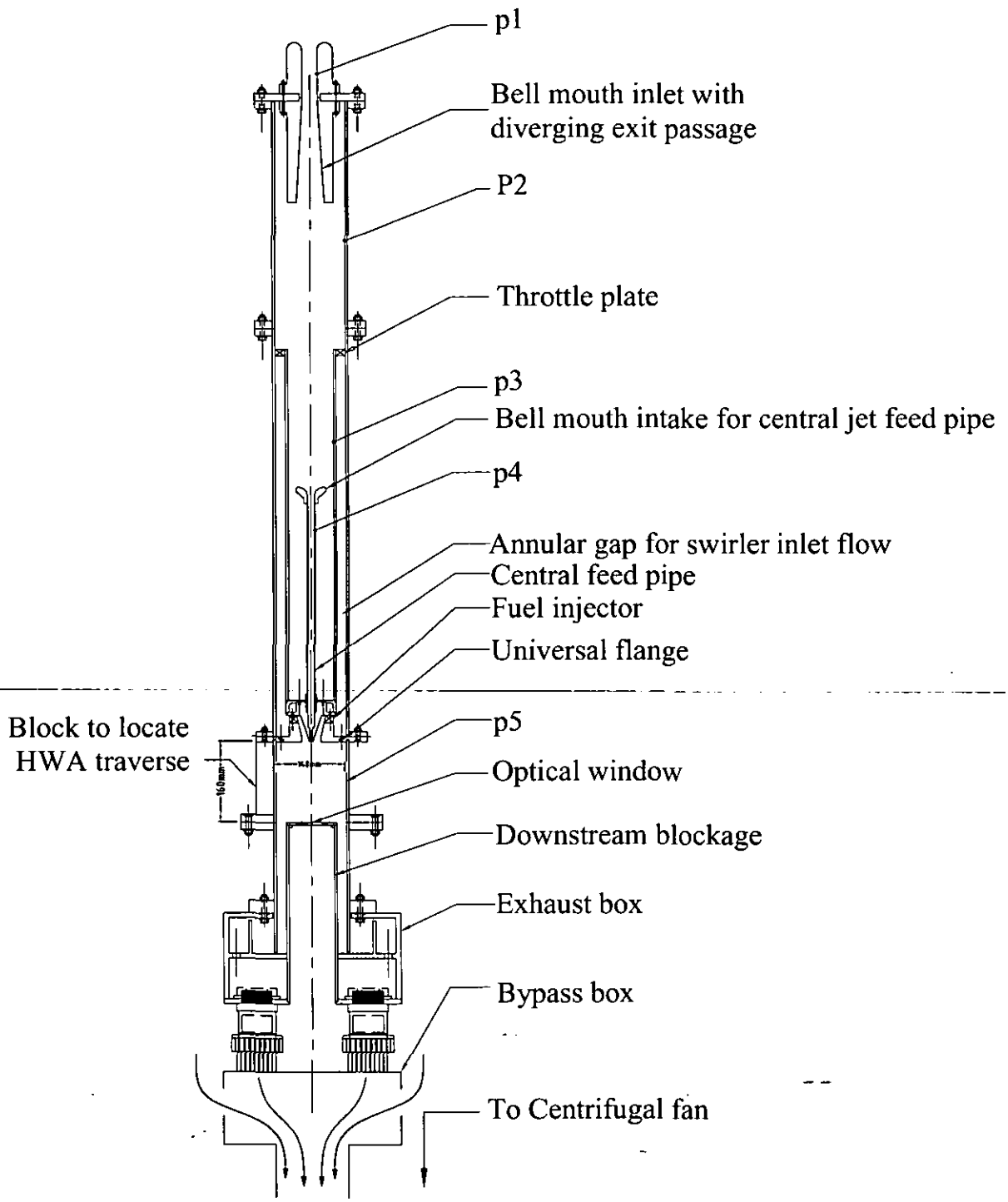

Figure 2.16. Diagram of the Airflow Rig*

* In practice the airflow rig was mounted horizontally

Air was drawn into the rig (by a downstream centrifugal fan) through a smooth bell mouth intake containing a static pressure tapping p_1 whereby the dynamic head and hence the mass flow rate could be calculated by knowing the ambient pressure, P_0 from:-

$$\dot{m} = \sqrt{2\rho(P_0 - p_1)}.C_d A$$

Where the discharge coefficient, C_d is defined as the ratio of the geometrical area to the effective area:-

$$C_d = \frac{A_e}{A}$$

Where the subscript e denotes an effective area. As a result of the low inlet Mach number used (M<0.12) the discharge coefficient for the aforementioned bell mouth inlet could be taken as 1.0, McGreeham and Schotsch (1987). Due to the low volume flow rates required through the rig (approximately $0.04m^3/s$, see Section 2.5) the inlet diameter of the bell mouth was set to 30mm in order to provide an adequate static pressure drop (dynamic head) such that errors in pressure transducer readings were minimised. The majority of this dynamic head was then recovered via a diffuser of area ratio 3.3 and half angle 7° after which the flow was dumped into a pipe of 10 diffuser exit diameters length to allow for the recovery of the radial pressure gradients before entry to the concentrically mounted test section feed pipes.

A central pipe of similar dimensions to the core pipe of the water flow rig was used to create the 20mm annular gap for the swirl stream feed flow. To ensure a fully developed flow into the swirl stream (of length 50 annular gap heights) a mass flow rate greater than $27.14\times10^{-3}kgs^{-1}$ (Re>4000) was required. To feed to the central jet, a 12mm ID central feed pipe was used (of length 36 diameters) in which fully developed flow could be assumed with a mass flow rate of $6.14\times10^{-4}kgs^{-1}$ (Re>4000). The central feed pipe also provided a sufficiently large static pressure drop for the accurate calculation of the jet mass flow rate via an upstream static pressure tapping (p_3) (assuming that the dynamic head at p_3 was negligible, $p_3 = P_3$) and the feed pipe static pressure (p_4).

Because of the large pressure drop across the fuel injector, the available centrifugal fan operated at an off-design condition to provide the required volumetric flow, resulting in blade stall. In order to remove this problem (and avoid any dominant frequencies associated with this unsteadiness propagating upstream into the test section) a bypass flow was included downstream of the test section exhaust box (but upstream of the fan) as shown in Figure 2.16 and also schematically in Figure 2.17.

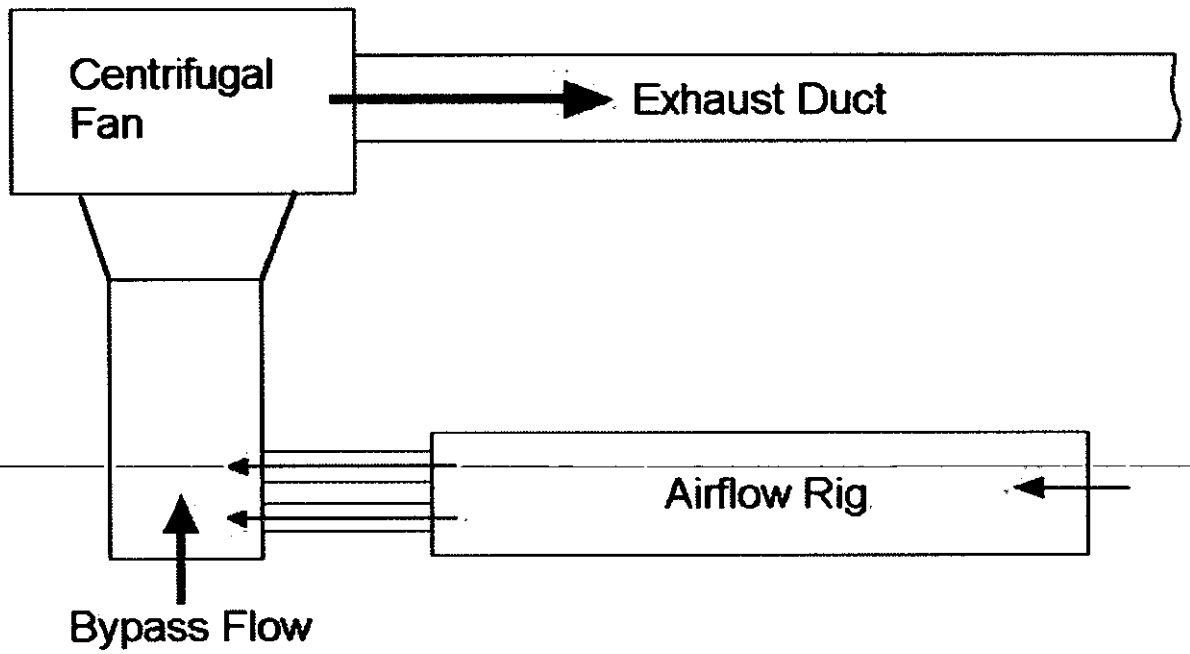

Figure 2.17. Schematic of the Airflow Rig Layout Including Bypass Flow

The effect of the addition of the bypass flow on the centrifugal fan operating point (for the required mass flow rate through the test section) is shown in Figure 2.18 on the fan characteristic plot.

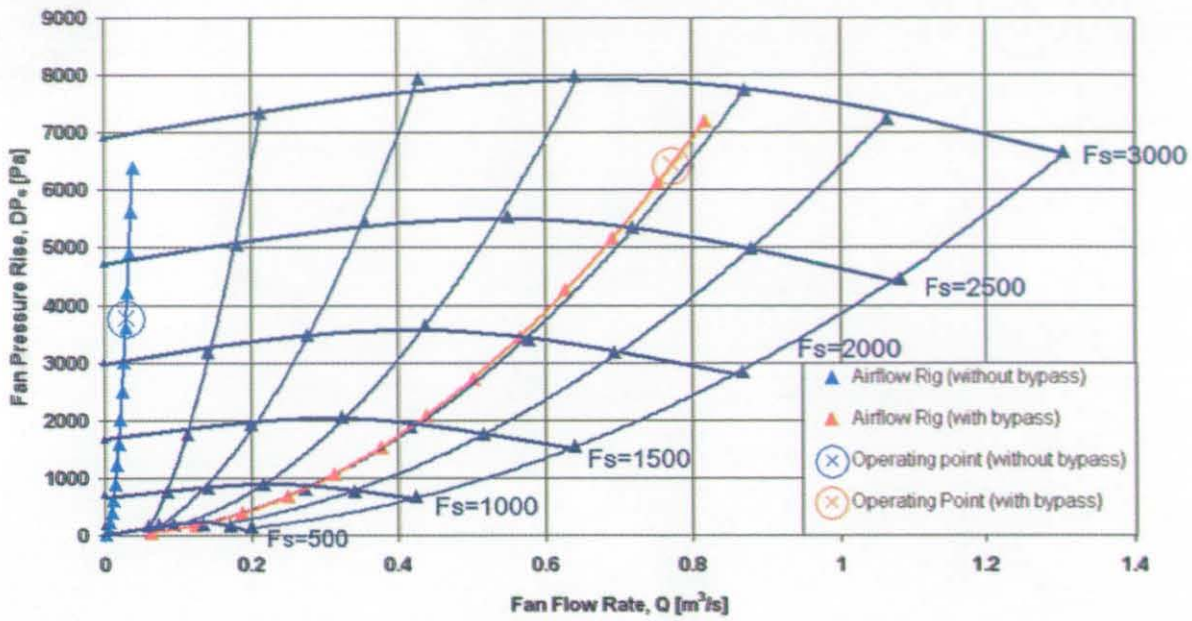

Figure 2.18. Effect of Bypass Flow on Volumetric Flow Rate into Centrifugal Fan (for Fixed Fuel Injector Flow Rate) Superimposed on the Fan Characteristic

As can be seen the inclusion of the bypass duct results in an operating point where the fan characteristic gradient is positive ($dDP_s/dQ>0$), this ensures a stable fan operation. Figure 2.19 shows a photograph of the airflow rig including the bypass duct; the location of the radial traverse for a HWA profile can also be seen, positioned perpendicular to the curved surface of the dump area expansion duct by a location block. In Figure 2.19 the axial location of the HWA traverse is $x/D_s=0.27$.

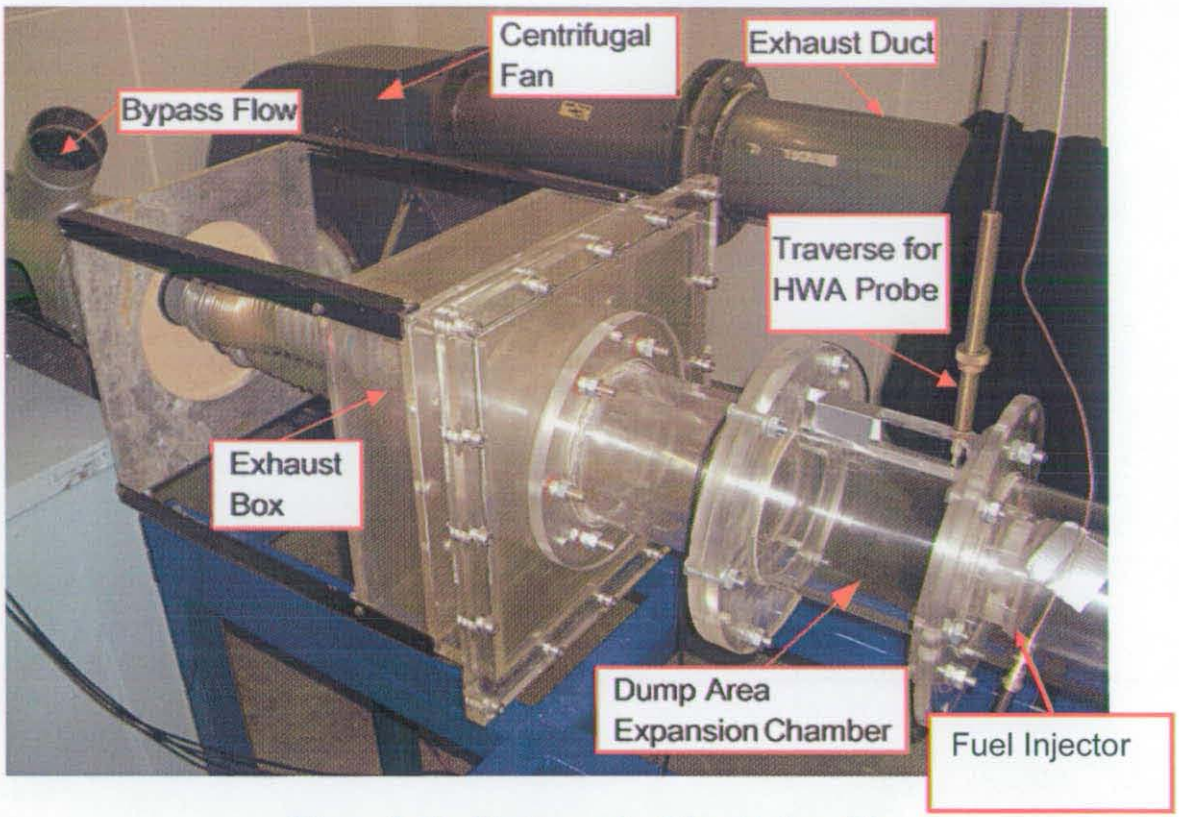

Figure 2.19. Photograph of the Airflow Rig

2.5 Experimental Test Conditions

The test conditions used in this thesis were selected by matching the isothermal flow parameters as closely as possible to the combusting conditions of the MOLECULES project, which used a similar (but different scale) fuel injector, as described by Janus *et al* (2004). Section 2.5.1 provides a description of this combusting test condition. Section 2.5.2 then outlines the methodology used to match the combusting conditions in the current isothermal test case. Section 2.5.3 then examines the Reynolds number independence of the flow (within the range used) and compares the test conditions in water and airflows to demonstrate the good similarity.

2.5.1 Combusting Test Case

The combusting test case used a central jet of methane and an electrically heated airflow through the radial entry swirl slots. The mass flow rates were based on a fuel injector pressure drop of 3%, a value typical of the liner pressure drop in an actual combustor. The combusting test conditions are detailed in Table 2.3.

Swirl stream mass flow rate (air)	$25\times10^{-3}kgs^{-1}$
Swirl stream temperature	623K
Swirl stream pressure	$2\times10^{5}Pa$
Central (fuel ((CH_4)) jet temperature	298K
Central (fuel) jet pressure	$2\times10^{5}Pa$
Equivalence ratio	0.95

Table 2.3. Combusting Test Conditions, Janus *et al* (2004)

From this data the Reynolds numbers, density, velocity and momentum flow rates may be calculated. Density is defined as:-

$$\rho = \frac{p}{R_0 T}$$

Where R_0 is the Gas Constant, which for air is R_0=286.8J/kg.K and for CH_4 is 518.1J/kg.K, hence ρ_s=1.12kgs^{-1} and ρ_j=1.30kgm^{-3} and the density ratio between jet and swirl flows was:-

$$\frac{\rho_j}{\rho_s} = 1.16$$

The reference velocity scales were calculated from the geometrical areas:-

$$V_{x,ref} = \frac{\dot{m}}{\rho A}$$

The swirl stream inner and outer exit radii in combusting experiment of Janus *et al* (2004) were 2.5mm and 13.93mm respectively, therefore $A_s = 5.90\times10^{-4}m^2$ and $V_{x,s}$=37.86ms^{-1}. In order to calculate the central jet reference velocity the fuel mass flow rate had to be calculated, this was found via knowledge of the stoichiometric FAR found from a simple chemical equation for complete combustion of methane in air to produce CO_2, water and N_2.

$$CH_4 + 2O_2 + 7.52N_2 \rightarrow CO_2 + 2H_2O + 7.52N_2$$

Thus 0.275kg of air was required to burn 1.60×10^{-2}kg of methane, and the stoichiometric FAR is 5.82×10^{-2}. From the equivalence ratio of 0.95 the actual FAR is calculated as 5.53×10^{-2}, hence the fuel mass flow rate is 1.38×10^{-3}kg/s. Since the central jet ID was 4mm in the Darmstadt experiments, $A_j=12.57\times10^{-6}m^2$ and $V_{x,j}=84.91ms^{-1}$. Therefore the reference velocity ratio was:-

$$\frac{V_{x,j}}{V_{x,s}} = 2.24$$

The axial-momentum flow rate in either stream can be characterised by:-

$$M_x = \rho A V_{ref}^{\ 2}$$

Therefore at the combusting conditions:-

$$M_{x,j} = 1.17\times10^{-1}\text{kgms}^{-2}$$

$$M_{x,s} = 9.46\times10^{-1}\text{kgms}^{-2}$$

And the axial momentum flow rate ratio was:-

$$\frac{M_{x,j}}{M_{x,s}} = 1.24\times10^{-1}$$

The swirl and jet stream Reynolds numbers may then be found using:-

$$Re = \frac{\rho D_{ref} V_{x,ref}}{\mu}$$

Where the most appropriate reference length scale at the fuel injector exit plane was considered as the hydraulic diameter, D_h of each passage defined as:-

$$D_h = \frac{4A}{P}$$

Where P is the wetted perimeter, which simplifies to $D_{h,j}=D_j=4mm$ for the central jet and $D_{h,s}=D_s-D_j=23.85mm$ for the swirl stream. The viscosity, μ of air at 623K is 3.10×10^{-5}Pas, and 1.02×10^{-5}Pas for methane at 298K. Therefore:-

$$Re_s=2.91\times10^4$$

$$Re_j=3.33\times10^4$$

2.5.2 Matching Combusting Test Case for Isothermal Conditions

Whilst the velocity ratio itself could have been replicated it was decided that matching the axial momentum flow rate ratio, $M_{x,j}/M_{x,s}$ would provide the most suitable match, ensuring a similar central jet penetration to the combusting case and similar mixing properties. Matching the axial momentum flow rate ratio is denoted as the "main" test condition for the rest of this thesis. Table 2.4 shows this main test condition in airflow (assuming an air density of $1.19kgm^{-3}$).

	$V_{x,ref}$ [m/s]	$\dot{m}$ [kgs^{-1}]	Re
Jet stream	65.58	17.90×10^{-4}	2.34×10^{4}
Swirl stream	27.19	34.81×10^{-3}	5.79×10^{4}
Ratio	2.41	5.14×10^{-2}	

Table 2.4. Main Test Condition in Airflow

By matching the axial momentum flow rate ratio, not only would the jet penetration be most accurately represented but, as shown in Table 2.4, the velocity ratio would be comparable to the combusting case and the exit plane Reynolds numbers would be of a similar order of magnitude. The above deduced mass flow rates resulted in a swirl stream annulus Reynolds number of $Re>1\times10^{4}$ and a central jet feed pipe Reynolds number of $Re>0.5\times10^{4}$, therefore the inlet feed flows in the airflow rig could be assumed to be fully developed. Table 2.5 shows the axial momentum flow rate ratio matched test conditions in water (assuming a density of 998.2kgm^{-3}).

	$V_{x,ref}$ [m/s]	$\dot{m}$ [kgs^{-1}]	Re
Central jet stream	2.26	5.18×10^{-2}	1.22×10^{4}
Swirl stream	9.39×10^{-1}	1.01	3.02×10^{4}
Ratio	2.41	5.14×10^{-2}	

Table 2.5. Axial Momentum Matched Condition in Water flow

As discussed previously in Section 2.3.1.2, the swirl stream annular feed path in the water flow rig required a mass flow rate greater than 1.13kgs^{-1} ($Re>3\times10^{3}$) to ensure a fully developed profile. However, the momentum matched condition required a mass flow rate of only 1.01kgs^{-1} ($Re=2.67\times10^{3}$). The solution to this was to increase both mass flow rates in the water flow experiments, whilst maintaining the momentum flow rate ratio. Gupta (1984) states that beyond a critical nozzle exit Reynolds number of approximately 1.80×10^{4} a swirler flow field remains largely independent of the Reynolds number; hence this increase in the mass flow rate would not be expected to have an effect on the observed flow field (investigated below in Section 2.5.3.1). The factor used was 2.12 resulting in a swirl stream feed path Reynolds number of $Re=5.67\times10^{3}$ and a central jet feed pipe Reynolds number of $Re=11.66\times10^{3}$ thus ensuring both inlet flows would be

fully developed. The scaling factor of 2.12 was chosen (providing a mass flow rate close to the water flow rigs maximum mass flow rate) as it provided the most comparable fuel injector exit plane Reynolds numbers to both the airflow experiments and the combusting experiment. Table 2.6 shows the factored test conditions. This condition is denoted as the main test condition for the water flow rig tests.

	$V_{x,ref}$ [m/s]	$\dot{m}$ [kg.s^{-1}]	Re
Central jet stream	4.81	0.11	2.59×10^4
Swirl stream	1.99	2.14	7.48×10^4
Ratio	2.41	5.14×10^{-2}	

Table 2.6. Main Test Condition in Water

To assess its influence, the central jet could be switched off whilst maintaining the swirl stream mass flow rate. This test condition was denoted as the "no-jet" test condition. The no-jet test condition was also used to investigate the modular swirler. PLIF measurements were taken (only in water) at the main test condition.

2.5.3 Validation of Test Conditions

In order to show that the flowfield was independent of Reynolds number, as has been assumed in the above discussion, and that operation at the same axial momentum flow rates would provide comparable flowfields in both air and water, data sets were captured using the PIV measurement technique.

2.5.3.1 Reynolds Number Independence of Flowfield

A comparison of the mean velocity vectors superimposed on axial RMS velocity contours for the main test condition ($Re_s=7.48\times10^4$) and at half the Reynolds number ($Re_s=3.74\times10^4$) is shown in Figure 2.20. Both measurements were taken in water flow with the correct momentum flow rate ratio, $M_{x,j}/M_{x,s}=0.124$. Note that both the mean velocity vectors and the RMS turbulence levels have been non-dimensionalised by the appropriate swirl stream exit plane axial velocity, $V_{x,s}$.

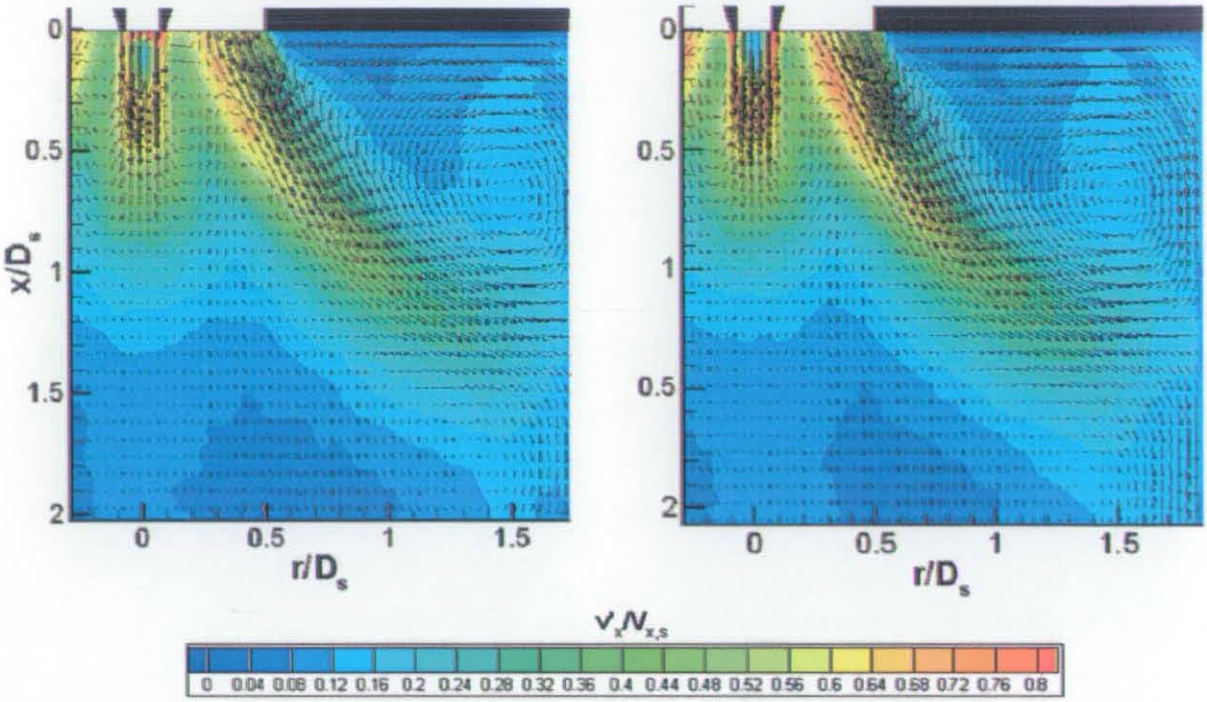

Figure 2.20 Mean Velocity Vectors Superimposed on Axial RMS Velocity Contours for $Re_s=7.48\times10^4$ [left] and $Re_s=3.74\times10^4$ [right] in Water Flow

As can be seen, there is excellent agreement between both the mean velocity field and the turbulence intensity field, as represented by the axial RMS contours. Further evidence of this agreement is found by comparison of radial profiles of mean and RMS circumferential velocity, as shown in Figure 2.21 and Figure 2.22 for axial measurement locations $x/D_s=0.27$ and $x/D_s=0.53$ respectively.

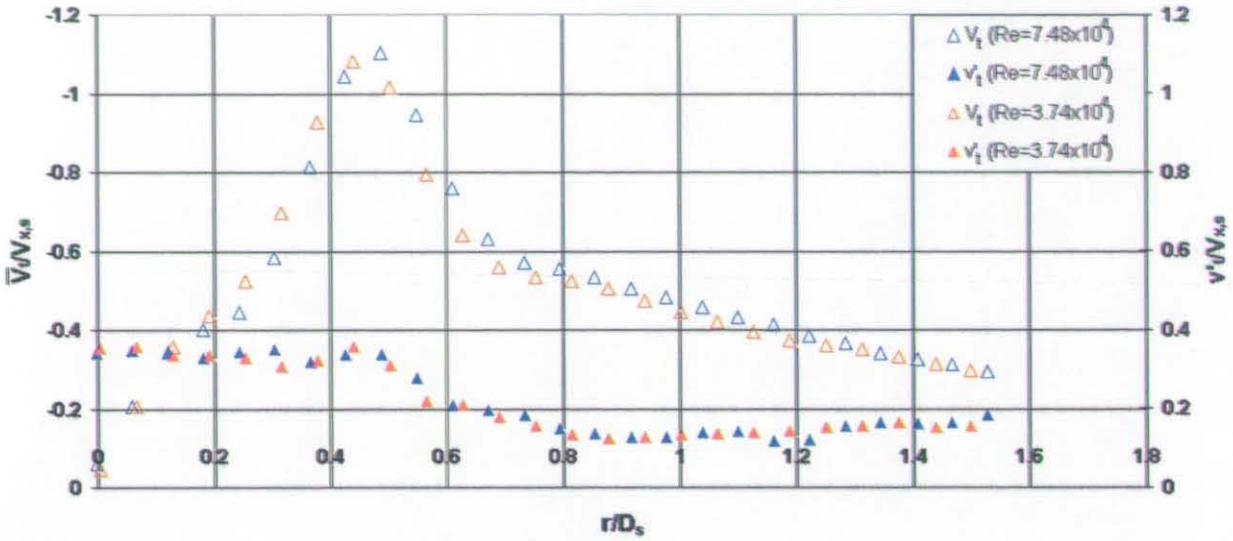

Figure 2.21 Mean and RMS Circumferential Velocity Profiles at x/D_s=0.27 in Water Flow

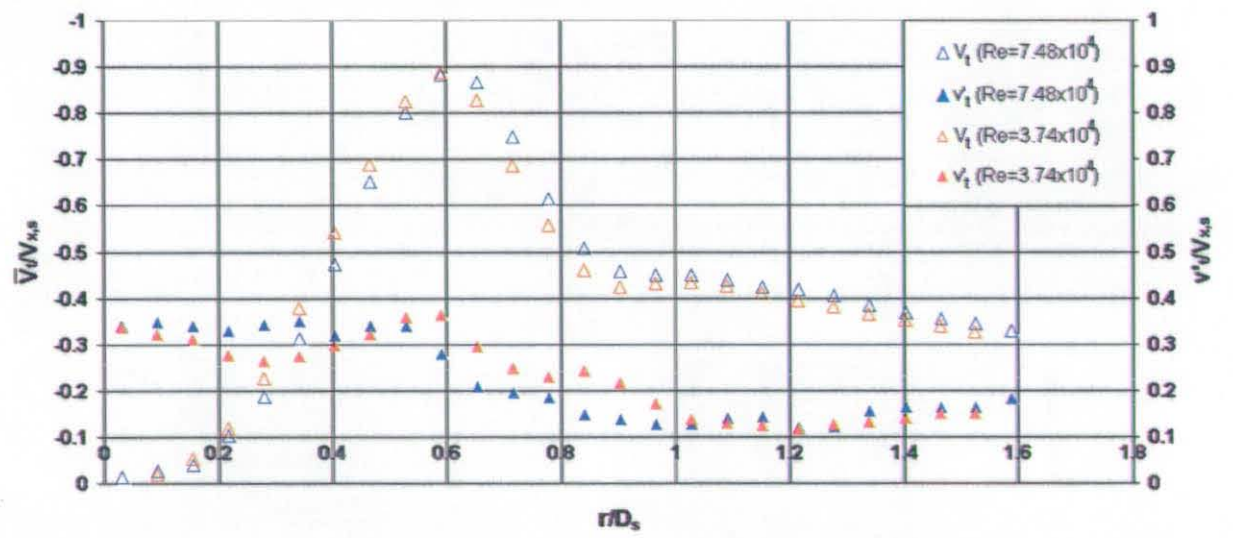

Figure 2.22 Mean and RMS Circumferential Velocity Profiles at x/D_s=0.53 in Water Flow

From the data presented it is clear that, as expected, the non-dimensional flowfield shows Reynolds number independence within the range used and the (factored) main test condition used in water is still clearly representative of the axial momentum flow rate matched test condition.

2.5.3.2 Comparison of Measurements in Water Flow and Airflow

Figure 2.23 shows a comparison of the (non-dimensional) mean velocity vectors superimposed in axial velocity contours for the main test condition in the water flow rig ($Re_s=7.79\times10^{-4}$) and in the airflow rig ($Re_s=5.79\times10^{4}$) using the PIV measurement technique.

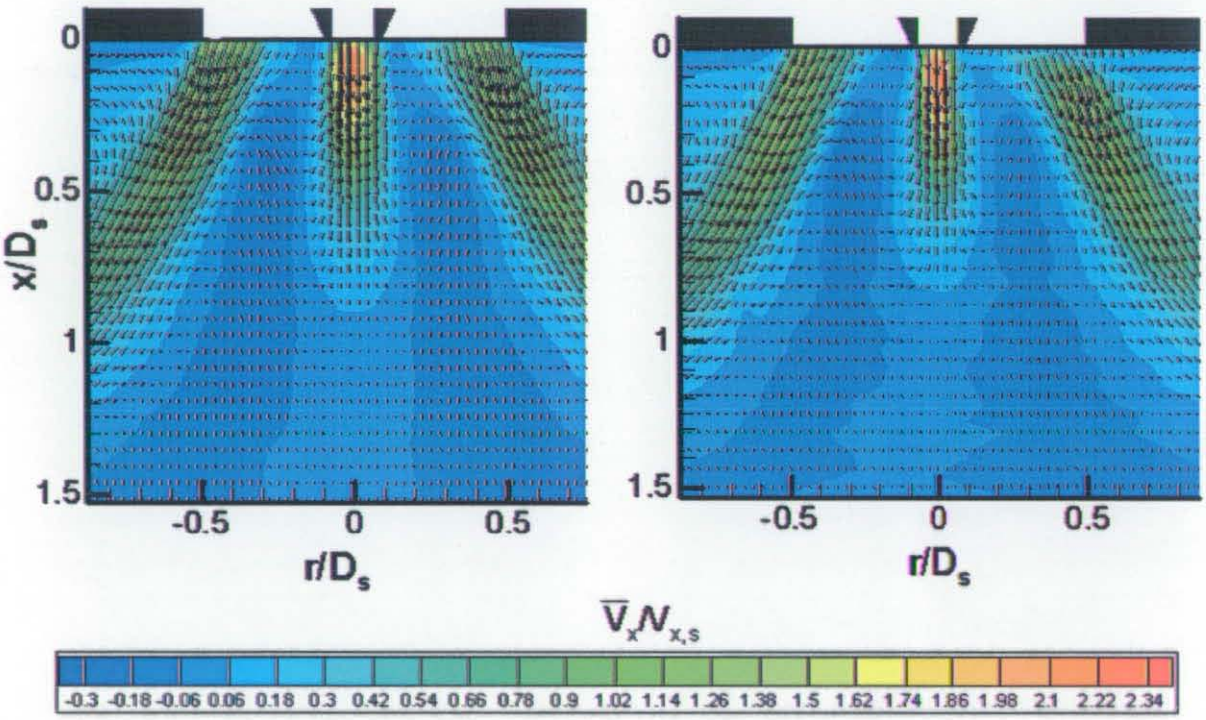

Figure 2.23. Comparison of Mean Velocity Vectors Superimposed on Mean Axial Velocity Contours in Water Flow [left] and Airflow [right] for Main Test Condition

Once again there is excellent agreement between the airflow and water flow results where the mean velocity field is clearly in good agreement. Further evidence of similarity is provided by comparison of (non-dimensional) radial profiles of mean and RMS circumferential velocity, as shown in Figure 2.24 at $x/D_s=0.27$.

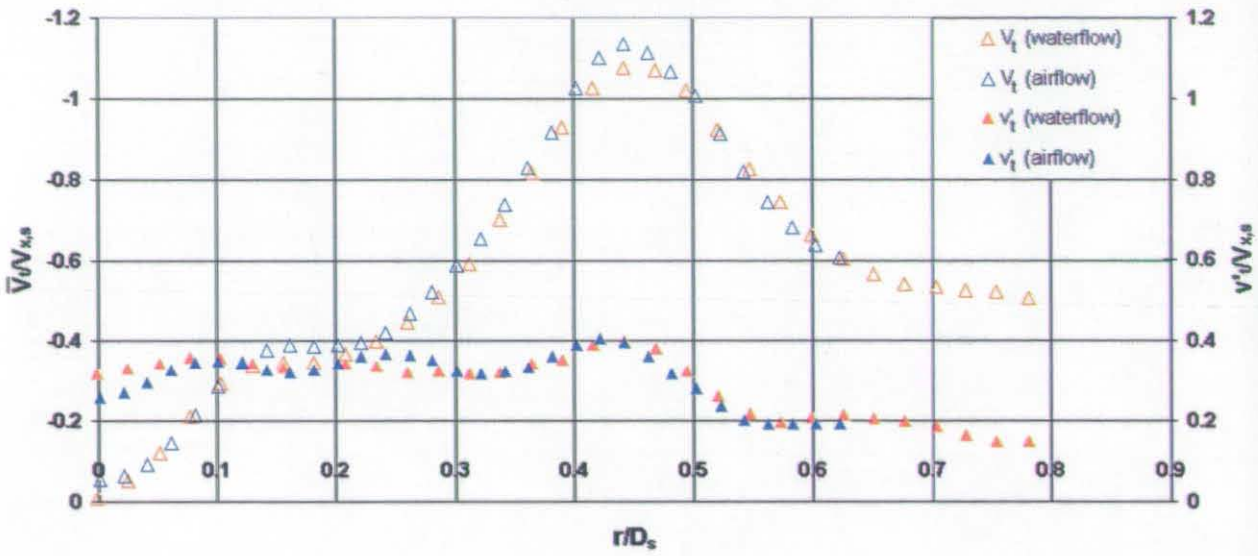

Figure 2.24 Mean and RMS Circumferential Velocity Profiles at x/D_s=0.27 for Main Test Condition

The excellent agreement shows that non-dimensional comparison between water flow and airflow data at the main test condition can be used with confidence.

2.6 Closure

In this chapter the Turbomeca low-emissions radial fed single stream fuel injector has been described as have the modification necessary for the measurements within the MOLECULES project. A modular swirler has also been described based on this datum design, to be used for assessing the impact of the swirl flow slot angle and passage shape on the flowfield.

To best suit the measurement techniques used, the fuel injector flowfields were to be investigated in both water and airflow rigs. For water flow measurements a pre-existing vertically flowing test rig was used. The modifications required in order to make it suitable for this investigation included the isolation, control and conditioning of the feed flow paths to both streams, improving the optical access (especially to the r-θ plane), determining the length of the dump area expansion chamber and providing an even distribution of the exit flow. The design of an airflow rig was then described which incorporated a high degree of commonality with the modified water rig.

Finally, the methodology for calculating the test conditions for the water and airflow rigs was described which was based on matching the axial momentum flow rate ratio to that of the MOLECULES (Darmstadt University) combusting test case. The test conditions were then shown to be Reynolds number independent (which the range of Reynolds numbers used) and to provide comparable non-dimensional time-averaged mean and turbulence flow fields in both water and airflows.

3 MEASUREMENT TECHNIQUES

In this chapter the LDA system and HWA systems applied in the present experiments are briefly described in Sections 3.1 and 3.2 respectively. The primary measurement technique, described collectively as Light Sheet Imaging (LSI) is described in Section 3.3. Sections 3.4 and 3.5 then describe the operation of an LSI system for capture of the velocity fields via Particle Image Velocimetry (PIV) and the scalar field via Planar Laser-Induced Fluorescence (PLIF).

3.1 Laser Doppler Anemometry System

LDA is a highly accurate and well-established measurement technique that *"measures the velocity of a moving object by illuminating it using laser light and measuring the Doppler shift of the light scattered by the moving object"* Fingerson and Menon (1998).

For a comprehensive description of the LDA measurement technique see Durst *et al* (1981). The single-component LDA system employed comprised of a Helium-Neon (He-Ne) 20mW laser and a Dantec photo-multiplier, for further details of the system see Spencer (1998). In the current work it was operated in a forward scatter mode at a fixed data rate of 1kHz. The laser and photo-multiplier were rigidly connected to a traversing mechanism so that the LDA measuring volume could be moved without the need to realign and refocus the photo-multiplier. Digital position indicators allowed the measuring volume to be positioned with ±0.1mm in the axial direction of the flow and a mechanical indicator on the radial traverse allowed accuracy of ±0.25mm. A summary of the LDA system details are provided in Table 3.1.

LDA System	
Photo-Multiplier	Dantec 55X
Processor	TSI IFA550
Software	ZECH Electronic 1400A
LDA Laser	
Type	Helium-Neon
Power output	20mW
Wavelength	632.8nm
Diameter of Beam at $1/e^2$	0.68mm
Beam half angle	5.53°
Fringe spacing	3.28μm
Number of fringes	46
Frequency shift	0.80MHz
Minor axis of control volume	0.30mm
Major axis of control volume	3.12mm

Table 3.1. LDA System

3.2 Hotwire Anemometry System

The Hotwire Anemometry system used operated by placing a 5μm wire (usually tungsten) of known temperature and resistance into the flow at a point of interest. As flow passes over the wire it is cooled by an amount that is related to the velocity of the air. The cooling of the wire causes the wire resistance to decrease, so a greater voltage is required to maintain its temperature. The resolution of these fine voltage adjustments is inversely proportional to the sampling frequency. In this thesis the system was operated at up to 25kHz. For a comprehensive description of the Hotwire Anemometry measurement technique see Gad-el-Hak (1998)

A Dantec 55P11 miniature single wire was used in conjunction with the Dantec Streamline hotwire system with data acquisition controlled by Dantec Streamware software, for further details on the system see Dantec (1996). A manual traverse was used to produce radial traverses of hotwire data to an accuracy of ±0.1mm, for a picture of the radial traverse see Figure 2.19.

3.3 Light Sheet Imaging System

There are three main components to an LSI system, the flow seeding, the light source and the image recording device; the type of flow seeding used determines the measurement technique. A basic description of an LSI system is that the light source (laser) is used to illuminate a 2D plane of interest (AOI). The incident light is scattered by particulate seeding (PIV) or absorbed and emitted as fluorescence by molecular seeding (PLIF). The scattered/emitted light is focused through a lens onto the image plane of the recording device which is arranged parallel to the plane of the light-sheet. The light source and recording devise are synchronised by a programmable timing unit (PTU) within the system PC. The LSI arrangement is shown in Figure 3.1. A picture of the LSI system, measuring in an x-r plane of the water flow rig is shown in Figure 3.2.

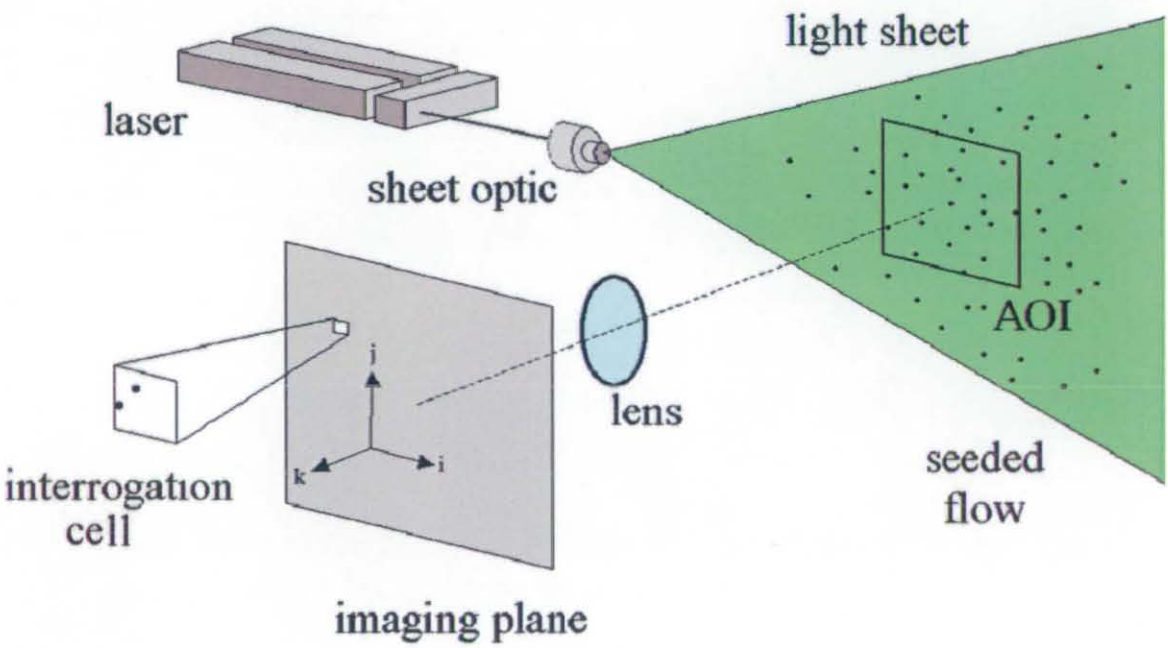

Figure 3.1 Typical Arrangement of a Light Sheet Imaging System, La-Vision (2001)

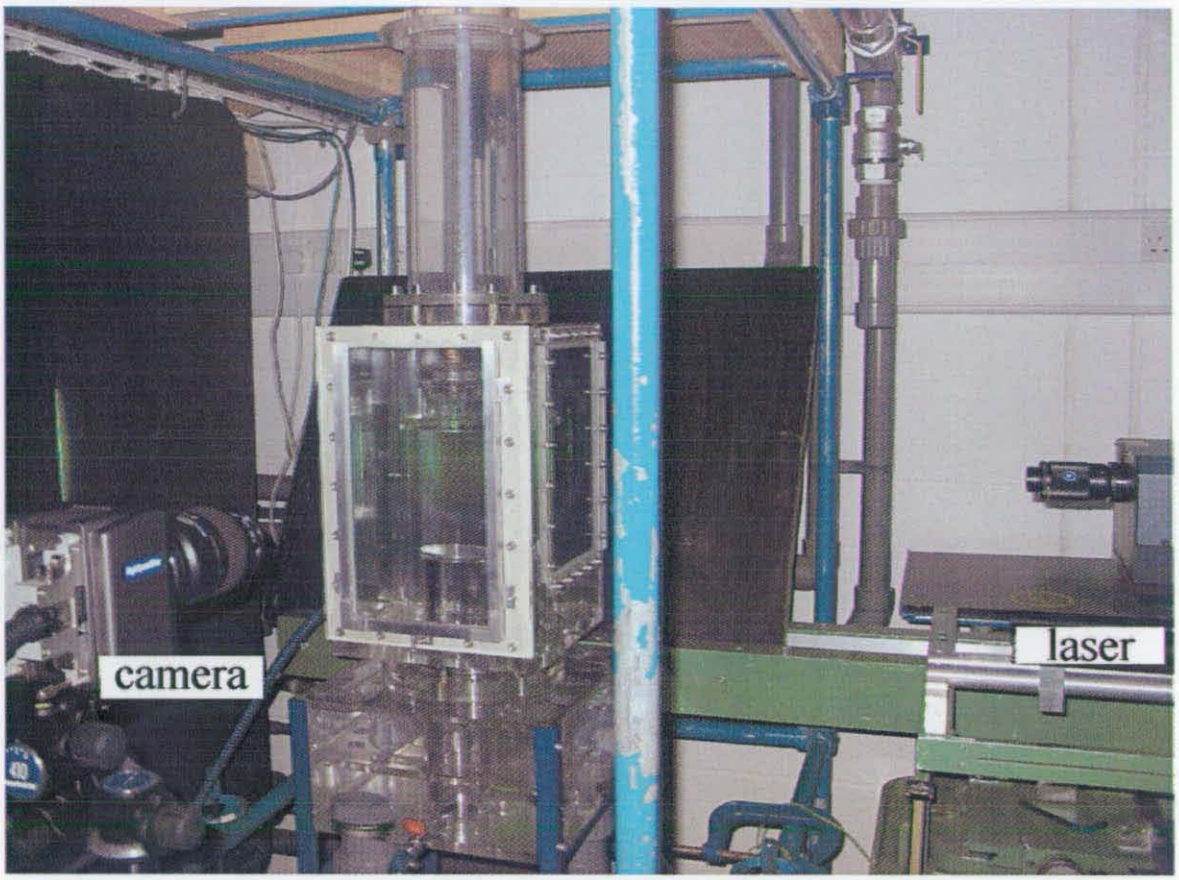

Figure 3.2. Photograph of Light Sheet Imaging Set up for Water Flow Test Rig

The following two sections describe the flow illumination (Section 3.3.1) and image recording hardware (Section 3.3.2). Since the type of flow seeding defines the measurement technique these are described separately within the sections describing PIV (Section 3.4) and PLIF (Section 3.5) techniques.

3.3.1 Flow Illumination

In LSI applications pulsed lasers are almost always used; this is because they allow energy to build up within capacitor banks before a "Q-switch" opens, providing a short burst of high intensity monochromatic light at desired intervals with a pulse duration of order a few nanoseconds. As the energy of the laser capacitor banks is transmitted only when required, the energy density achieved by pulsed lasers is much higher than the equivalent continuous wave (CW) unit. A typical 2.5W argon-ion CW laser has a power density of order $1x10^{6}W/m^{2}$ whereas a 50mJ pulsed laser with a pulse length of 9ns has a power density of $5.7x10^{11}W/m^{2}$, five orders of magnitude greater, Shan *et al* (2004). As the pulse length is so short it also produces a close to "frozen" image of the flowfield, this

property is fundamental to LSI techniques as it allows for crisp images of the flow to be taken despite the relatively long exposure times of current CCD cameras (compared to the smallest timescales of the flow). If a more detailed description of the physics of pulsed lasers is required see Raffel *et al* (1998)

From the unfocused laser beam a light sheet is created by combination of two spherical lenses and one cylindrical lens. The cylindrical lens spreads out the beam (in one direction only) and the separation of the spherical lenses controls the beam thickness, as shown in Figure 3.3. The divergence of the light sheet is dependant on the focal length of the cylindrical lens (quoted as a negative number to signify divergence) where the larger the negative value the less the beam divergence.

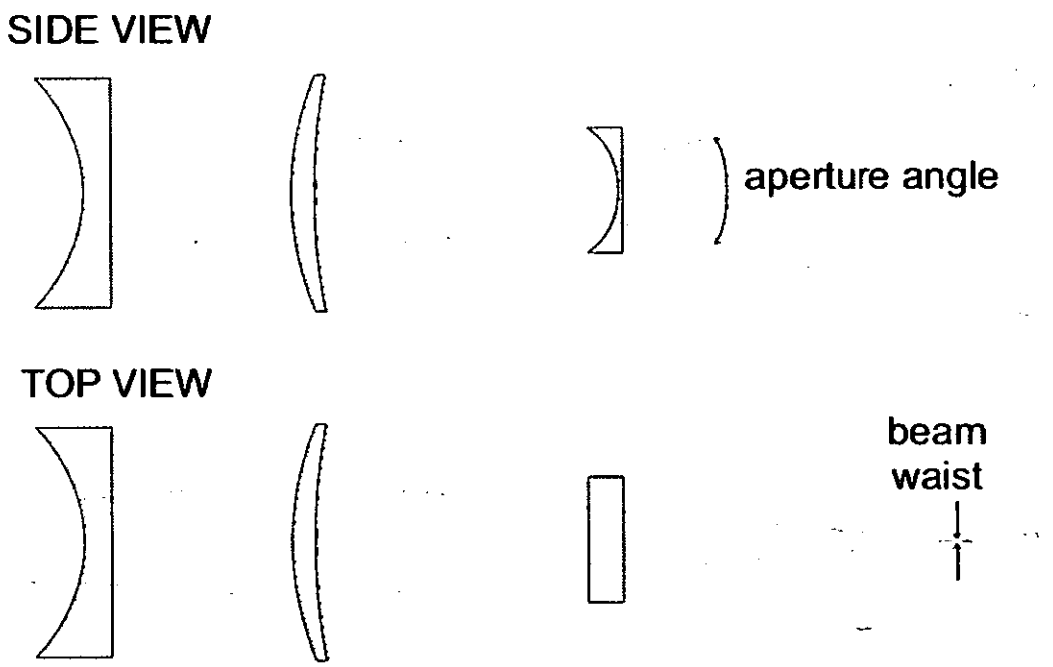

Figure 3.3. Creation of a Light Sheet

A close-up photograph of the light sheet illuminating water flow containing 20μm polyamide particulate seeding (for PIV measurements) in an x-r plane (including the centreline) of the water flow test rig is shown in Figure 3.4.

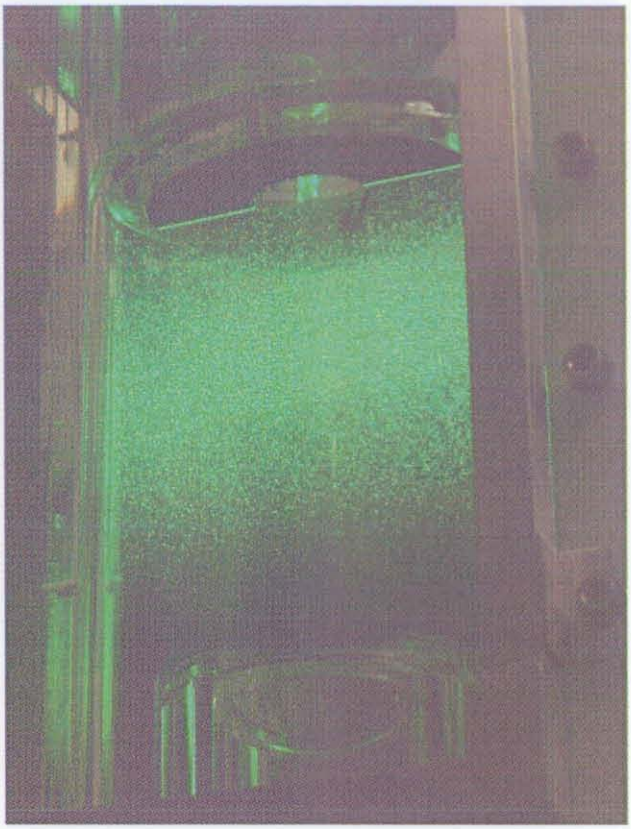

Figure 3.4. Photograph of the Light Sheet Illuminating an x-r Plane (Including the Centreline) of the Water Flow Rig Test Section Containing 20μm Polyamide Particulate Seeding

3.3.2 Recording Device

The recording devices widely used in LSI applications are Charged Coupled Device (CCD) cameras. This is due to their ability to transfer rapidly digital intensity images of the incident light intensity to PC memory allowing for much faster repetition rates and drastically reduced processing times compared to the use of traditional silver-nitrate films. Whilst film offers several orders of magnitude greater spatial resolution than a current 1000×1000 pixel CCD chip, Westerweel (1997) found that there was no difference in the accuracy of results observed from CCD and film based PIV. The CCD spatial resolution also provides acceptable resolution for PLIF measurements, as described below in Section 3.5.2. For more details on the physics of a CCD array see Beynon (1976).

The spatial resolution of an LSI measurement is directly proportional to the image magnification. The magnification, M is defined by the ratio of the image distance (focal length) z_0 to the object distance, Z_0, or alternatively as the ratio of the side dimension of

the CCD chip (b_0) to the side dimension of the flow region imaged at the image plane (B_0), known as the Field-of-View (FoV).

$$M = \frac{z_0}{Z_0} = \frac{b_0}{B_0}$$

These dimensions are shown graphically in Figure 3.5.

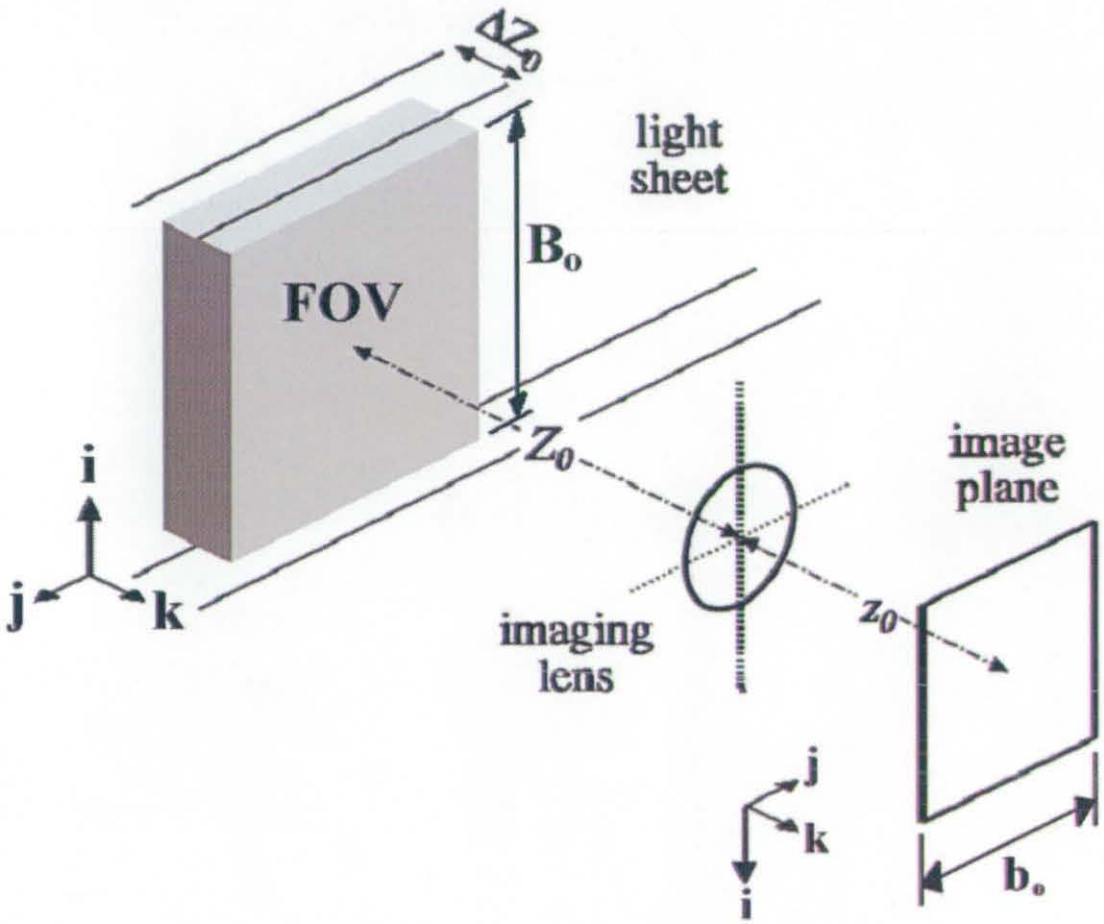

Figure 3.5. PIV Imaging Set-up, Westerveel (1997)

In Figure 3.5, ΔZ_0 denotes the camera depth-of-field which is discussed below. With the usable range of object distances between the camera imaging lens and the test section centreline (Z_0) being of order 150-500mm (the minimum distance of 150mm was due to the width of the water jacket) Nikon Nikkor macro lenses with focal lengths (z_o) ranging from 24mm (wide-angle) to 105mm gave the range of possible image magnifications shown in Figure 3.6.

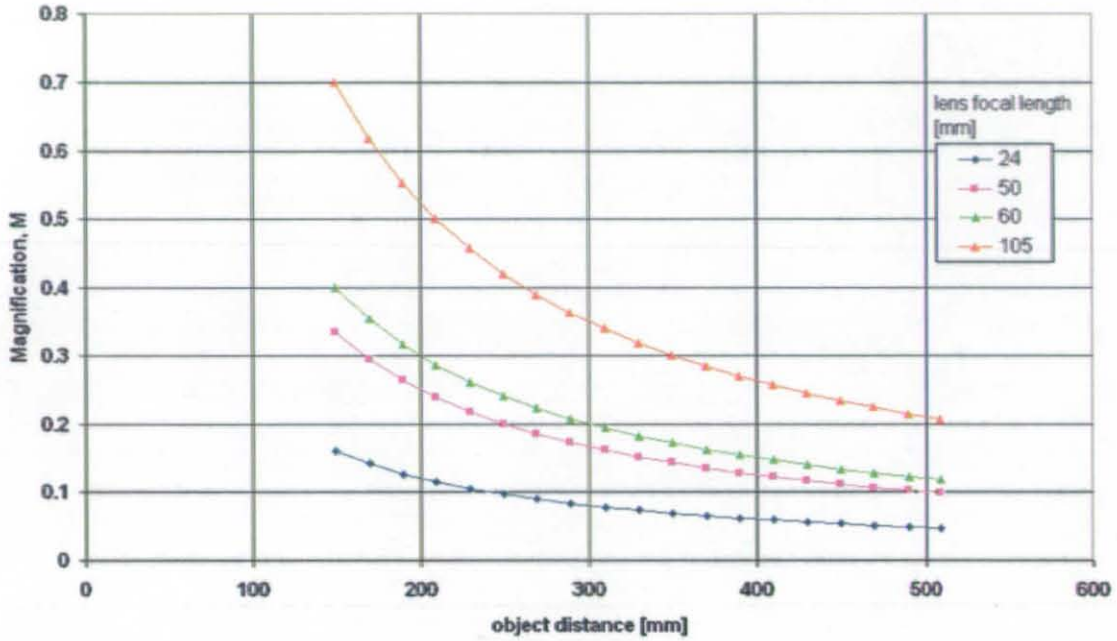

Figure 3.6. Image Magnification as Function of Focal Length and Object Distance

The camera depth-of-field is calculated from the image magnification, the wavelength of the laser, λ and the ratio of the focal length to aperture diameter known as the f-number, f#:-

$$\Delta Z_0 = 4(1 + M^{-1})^2 f\#^2 \lambda$$

For image magnifications of M=0.06-0.5 and f-numbers of f#=1.8–4 the camera depth-of-field is shown in Figure 3.7.

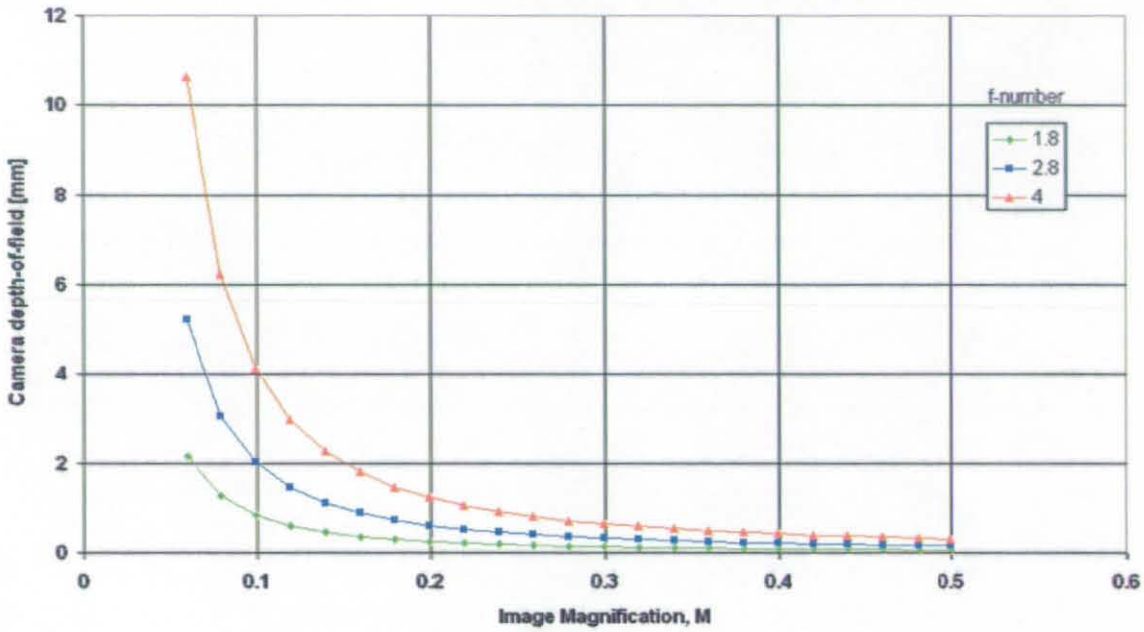

Figure 3.7. Camera Depth of Field as Function of Image Magnification and f-number.

For planar data large camera depth-of-fields are undesirable, however by careful selection of the magnification and the f-number the camera-depth-of-field was maintained <1mm for all optimised PIV and PLIF measurements presented below.

3.3.3 Light Sheet Imaging System Details

Two LSI systems were used in this experiment, a "low-speed" system (LS-LSI) with a temporal resolution of 15Hz and a "high-speed" system (HS-LSI) with maximum temporal resolution of 1kHz. Table 3.2 provides details of the illumination systems, the recording devises and the system computers.

	Low-speed system	High-speed system
Illumination	**Dual head New Wave Solo Nd:YAG**	**Dual head New Wave Nd:YLF**
Wavelength (λ)	532nm (green)	527nm (green)
Pulse length	9ns	135ns
Max. Repetition rate	18Hz	10kHz
Max. Energy	50mJ	10mJ @ 1kHz
Light Sheet Optics		
Cylindrical lens focal length	-3.5mm, -6mm ,-10mm, -20mm	
Beam divergence	60° 30° 20° 10°	
Beam thickness	0.5-2.5mm	
Working distance	300-2000mm	
Recording	**Kodak Megaplus E.S. 1.0**	**High Speed Star 4**
CCD	8-bit monochrome	10-bit monochrome
CCD size	$9mm^2$	$17.5mm^2$
Resolution	1008 × 976	1024 × 1024
Pixel width (d_r)	9μm	17μm
Max. frame rate	30Hz	2kHz @ max resolution
Min. inter-frame time	1μs	4μs
camera memory	none	8GBytes
Lenses	**Nikon Nikkor Macro**	
Focal lengths	24mm, 50mm, 60mm, 105mm	
System Computer		
Processor	Dual 800MHz, Pentium III	Dual 2.8GHz Pentium IV
Memory	2GBytes	4GBytes
Storage	70GBytes + CD-RW	120GBytes + DVD-RW
Max. No Samples (N)	650	3072

Table 3.2. Light Sheet Imaging System Parameters.

The following sections describe the use of the LSI systems for PIV and PLIF measurements respectively.

3.4 Particle Image Velocimetry

PIV allows for the construction of instantaneous 2D planar velocity fields by capturing the movement of particulate markers over two image exposures with a known time separation. The velocity at any point in the plane at the time instant, t (mid-way between the two exposures) can be calculated by:-

$$V(x,t) = \frac{\Delta x(x,t)}{\Delta t}$$

Whilst the pulse separation Δt is known (set by the PTU) the accuracy of the displacement vector, Δx is dependent on the choice of flow seeding, seeding density and the method chosen to calculate it.

3.4.1 Flow Seeding

The choice of flow seeding is of great importance to the accuracy of PIV as ultimately it is the motion of the seeding particles that determines the accuracy of the returned flow velocity vector. For a seeding particle to be suitable for PIV it must be able to follow the flow and efficiently scatter the illuminating light. The ability of a particle to follow the flow is dependant on two parameters, the velocity lag and the particle response time, both of which are proportional to the density difference between a seeding particle and a fluid particle and proportional to the square of the particle diameter, D_p. The velocity lag, V_p of a particle is a measure of its ability to precisely match the acceleration of a fluid particle when experiencing a constant acceleration, a and can be calculated from Stokes law:-

$$V_p = D_p^2 \frac{(\rho_p - \rho)}{18\mu} a$$

In a swirling flow seeding particles are subject to large centripetal accelerations proportional to V_t^2/r. This produced maximum accelerations >2200m^2/s within the swirl stream of the fuel injector body, which would result in significant particle slip over time. Therefore a neutrally buoyant seeding was chosen (ρ_p=ρ) which eliminated velocity slip. Unfortunately materials with similar densities usually have similar refractive indices; to

combat this problem neutrally buoyant seeding particles often utilise larger diameters (relative to different-density seeding particles) as the scattered light from a seeding particle, q increases proportional to the square of the particle diameter, D_p, Raffel *et al* (1998).

$$q = \left(\frac{\pi D_p}{\lambda} \right)^2$$

The disadvantage of larger diameter seeding particles is that the particle response time (to a step input) also increases proportionally to D_p^2, as described by Elghobashi (1994):-

$$\tau_p = D_p^2 \frac{\rho_p}{18\mu}$$

The 20μm neutrally buoyant polyamide particle, used for all water flow measurements in the thesis, therfore had a response time of 19.5μs (in water at 298K, $\mu = 1 \times 10^{-3}$ m^2/s). For a particle to respond to all of the turbulent motions of a high Reynolds number flow the particle response time should be smaller than the smallest timescales of the flow i.e. the Kolmogorov timescales. Figure 3.8 shows the Kolmogorov timescale contours calculated from axial and radial velocities within the dump area expansion chamber at the main test condition using LS-PIV data. The methodology for calculating Kolmogorov timescales directly from PIV data sets is described in Chapter 4.

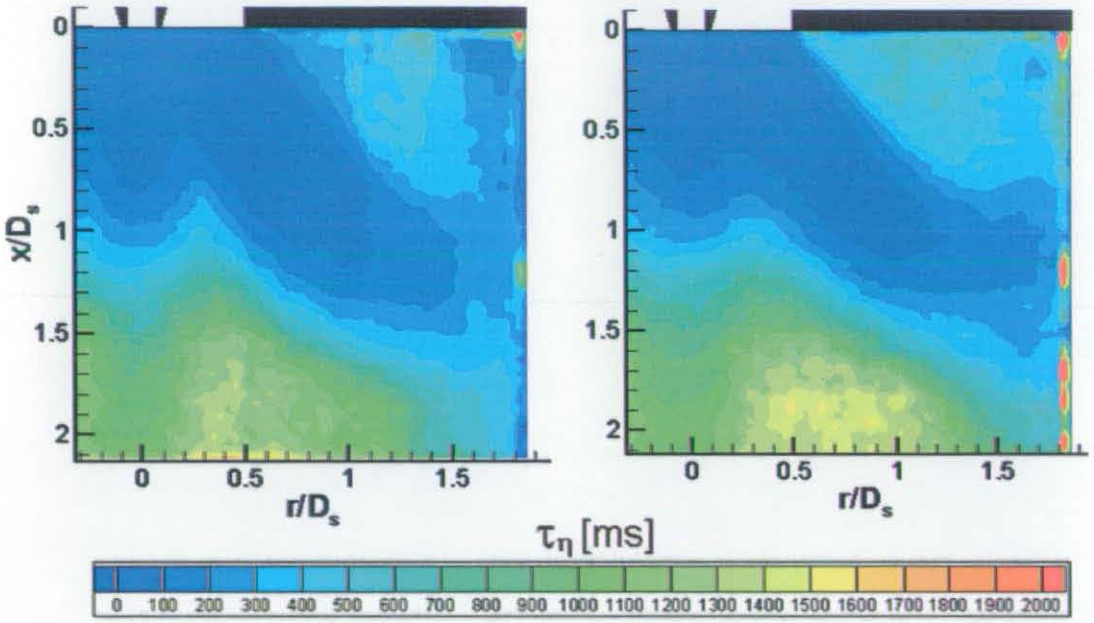

Figure 3.8. Axial [left] and Radial [right] Kolmogorov Timescales in Water Flow (Main Test Condition)

As can be seen, the smallest Kolmogorov timescale was approximately 40μs, therefore the particular seeding was deemed suitable for accurate measurements.

3.4.2 Seeding Density

If the seeding density is low, then the mean number of particulate markers per interrogation cell, N_I, is small. Therefore sequential exposures (at a suitable time interval) produce particle displacements that are small compared to the mean distance between the particles. In this case individual particles can be traced (provided out-of-plane motion, V_k, does not move the tracer particle out of the incident light sheet); this technique is known as low-density PIV, or Particle Tracking Velocimetry (PTV). PTV is clearly a direct progression from flow visualisation methods. The main disadvantage of PTV is that by definition the data density is low; also the velocity vectors calculated are located randomly throughout the plane.

Alternatively, at concentrations of tracer particles so high that the particle images overlap each other on the image plane, the random phase differences between the images creates an interference pattern known as laser speckle from which the velocity can be found by measuring the speckle displacement. This technique is known as Laser Speckle Velocimetry (LSV). Unlike PTV, manual analysis of a double exposed "specklegram" is

not possible and a technique known as a Young's fringe method of interrogation is required, Pickering and Halliwell (1984). LSV is widely used in solid mechanics where the speckle interference pattern produced when a coherent light source reflects from an optically rough surface is used to measure surface distortions. Whilst LSV can be used as a method for investigating fluid flows, light sheet attenuation may become significant and in most cases it is not practical and is usually too expensive to create high enough seeding densities.

Therefore, the natural technique to select bearing in mind the limitations of both PTV and LSV in fluid flows, is to operate with particle concentrations large enough to ensure that every measurement region contains several particle images but with no overlapping; this is known as high-density PIV. By definition the probability that high-density PIV measurement regions contain several particles is high, making it difficult to track individual particles. Therefore instead of determining the displacement of individual particles, high-density PIV (from now on stated simply as PIV) relies on the use of a correlation approach to determine a displacement vector.

3.4.3 Displacement Vector Calculation

In the early stages of PIV development, when silver-nitrate film was used, only single-frame/double-exposures were possible, where the camera shutter stayed open during the time that two laser pulses occurred. The film was then digitised and intensity patterns produced by the light scatter on the frame were evaluated via spatial auto-correlation. A typical auto-correlation function for an interrogation cell of size dx×dy is shown in Figure 3.9.

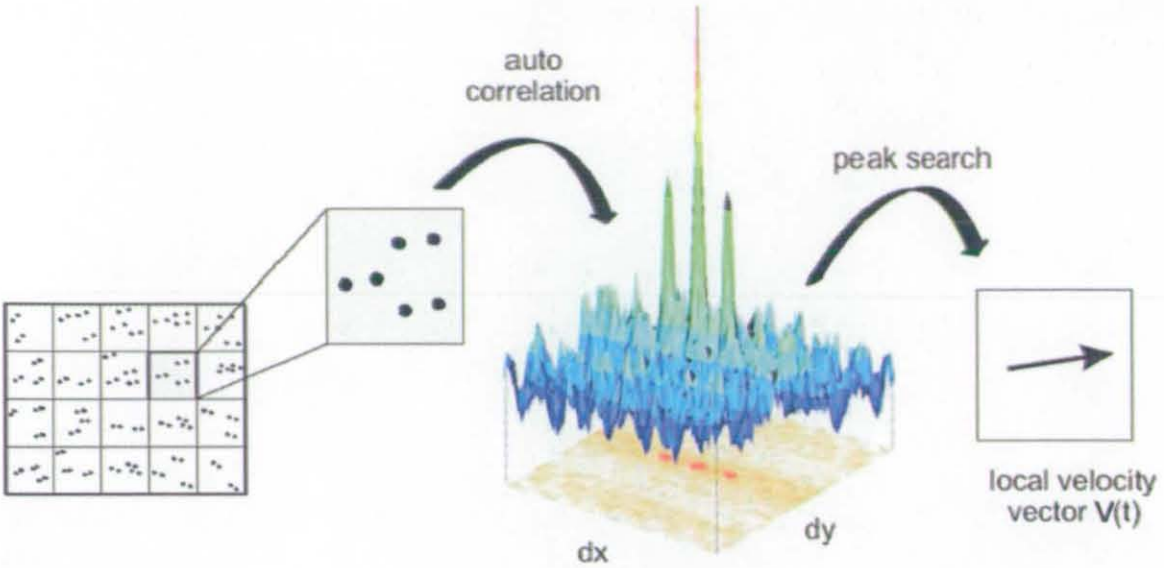

Figure 3.9. Calculation of Velocity Vector in an Interrogation Cell Using Auto-Correlation, La-Vision (2001)

The main disadvantage of this technique is that the auto-correlation function produces a rotationally symmetric auto-correlation plane, where a signal peak at (x,y) is replicated at (-x,-y), leading to directional ambiguity. Whilst in certain cases this ambiguity can be ignored though a priori knowledge of the flowfield it has remained the limiting factor of the single-frame/double-exposure methodology. However, the advent of fast-transfer CCD chip cameras has allowed for the use of double-frame/single-exposures with small enough inter-frame times that Cross-Correlation Functions (CCF) could be used of the general form:-

$$CCF(m,n) = \sum_{i}\sum_{j} f(i,j) \times g(i+m, j+n)$$

Where f(i,j) and g(i,j) denote the CCD image intensity distribution of the first and second exposures (frames). The two in-plane directions are denoted i, and j, and m, and n, are the pixel offsets (between the two images). An example of a cross-correlation map is shown in Figure 3.10.

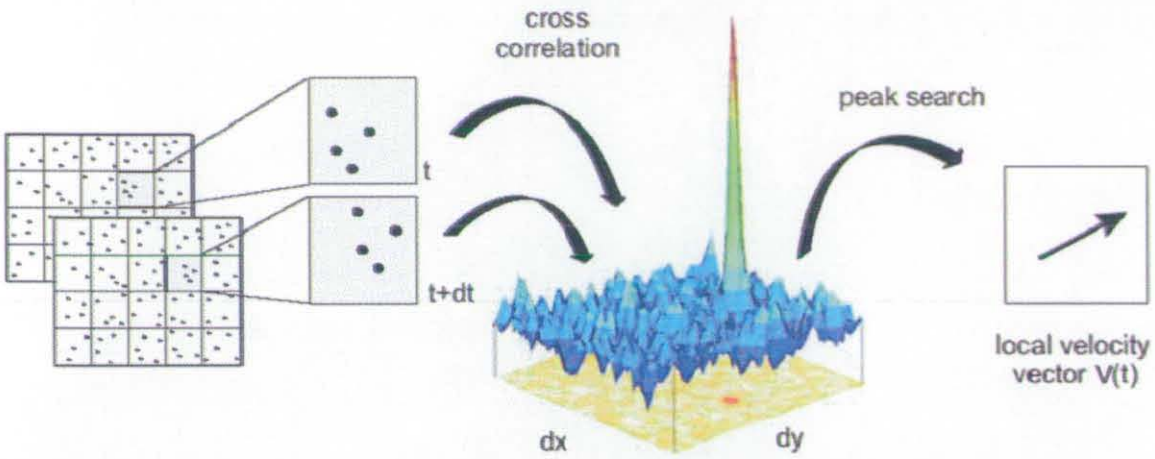

Figure 3.10 Calculation of Velocity Vector in an Interrogation Cell Using Cross-Correlation, La Vision (2001)

Hence, the pixel offset (m,n) which represents the most common (or modal) particle displacement within the interrogation region creates the highest correlation peak and thus is chosen as the displacement vector. The i and j components of the displacement vector are then calculated as $\Delta x_i = m d_r / M$ and $\Delta x_j = n d_r / M$ (where M is the image magnification and d_r is the pixel width) thus, the i and j velocities are $V_i = \Delta x_i / \Delta t$ and $V_j = \Delta x_j / \Delta t$ (where Δt is the inter-frame time, the optimisation of which is discussed in Section 3.4.5).

According to Prassad (2000), the advantages of the cross-correlation technique over the auto-correlation technique are as follows:-

i. it produces only one correlation peak thus removing directional ambiguity
ii. it can measure zero displacements
iii. relative to auto-correlations the signal to noise ratio (SNR) is increased, where the higher the SNR the higher the probability of the detection of the correct correlation peak

In order to reduce computational speeds the CCF is calculated by means of a Fast-Fourier Transform (FFT). All the PIV measurements reported in this thesis used a La Vision FFT CCF algorithm as part of the Davis v6.2 software, for further details see La Vision (2001).

3.4.4 System Synchronisation

The sequence of events necessary for a double-frame/single-exposure recording using a (duel head) pulsed laser and a fast transfer CCD chip both synchronised by the PTU, is as follows:-

i. The camera shutter opens and the PTU triggers the first laser Q-switch
ii. an intensity image of the scattered light from first pulse is captured (1^{st}-frame)
iii. the first-frame is rapidly transferred to a non light-sensitive buffer
iv. after the desired inter-frame time the camera shutter re-opens and the PTU triggers the second laser Q-switch
v. an intensity image of the scattered light from second pulse is captured (2^{nd}-frame) whilst the 1^{st}-frame is transferred from the temporary buffer to memory
vi. the second image transferred to memory

This sequence is shown schematically in Figure 3.11.

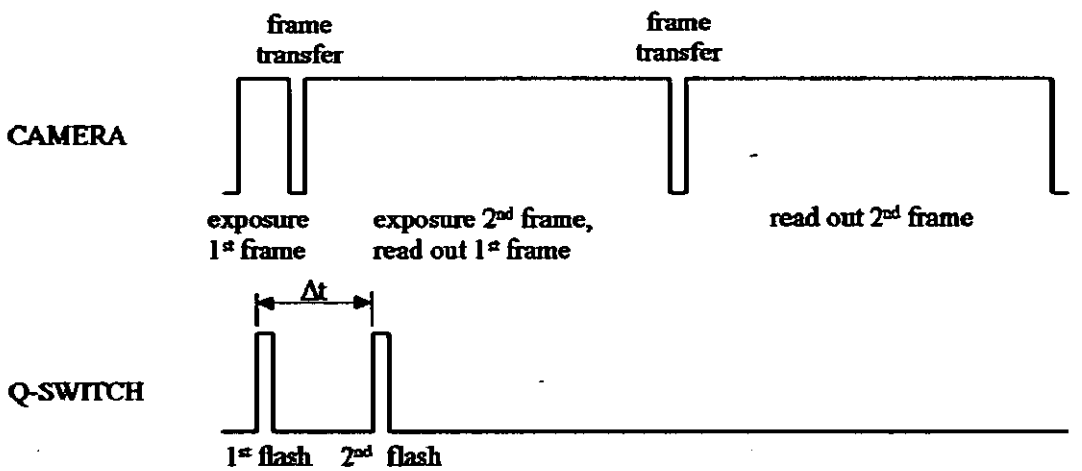

Figure 3.11. Synchronisation of Lasers and Camera for Cross-Correlation

As Figure 3.11 shows, the duration of the second exposure is much greater than the first; this is because the second exposure time is a function of the time it takes for the first image to be "read-out" of the buffer and into the memory. The inter-frame time, Δt is controlled through the PTU board, the value chosen for the inter-frame time is crucial to the optimisation and hence quality of the returned velocity, and is discussed in detail below in Section 3.4.5. Whilst the sequence is similar for LS-PIV and HS-PIV and the

1st-frame transfer rate (to the buffer) is of the order 300ns for both, it is the read-out time that is significantly different. The read-out time effectively acts as a system bottleneck allowing the maximum double-frame/single-exposure capture rate of 15Hz for LS-PIV and 1kHz for HS-PIV.

3.4.5 Optimisation of PIV System Parameters

Whilst the return of a spatially resolved velocity field via the cross-correlation of a double-frame/single-exposed image pair may be relatively simple to achieve (using an arbitrarily small inter-frame time) careful optimisation of the PIV system parameters is required if associated errors are to be minimised. The errors associated with PIV are classified in Table 3.3. Each is then discussed in detail below.

Error	Cause	Effect
PIV system errors	Related to the hardware of the PIV system	Directly affects the instantaneous velocity
Dynamic Averaging	Incurred by using Eulerian velocities to approximate Lagrangian particle displacements.	Loss of fluctuating data
Detection errors	Error incurred by not identifying the correct correlation peak in the correlation plane.	Increases the percentage of spurious data
Precision errors	Error associated with the sub-pixel interpolation used to identify the location of the correlation peak.	Increases the recorded RMS (via increased data variance)

Table 3.3. Errors Associated with PIV Technique

System errors are incurred due to image aberrations, incorrect assessment of the fields of view (FoV) and tracking errors (due to seeding particles not accurately following the flow). Image aberrations were avoided by using high-quality Nikon macro lenses and by encasing the AOI in a square-section water jacket to minimise distortion across the curved surfaces of the test section (for further details see Section 2.2). Errors in the FoV dimensions were minimised by using a calibration plate, placed across the test section centreline with equi-spaced 10mm crosses on it. This also allowed for the exact spatial location on the FoV to be ascertained. Tracking errors were minimised by the use of neutrally buoyant 20μm polyamide seeding particles as described in Section 3.4.1.

The effect of dynamic averaging is shown in Figure 3.12.

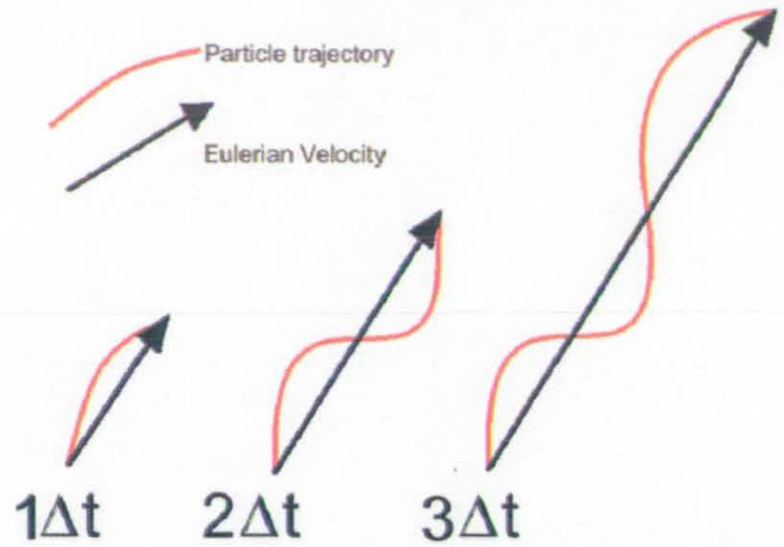

Figure 3.12. Effect of Inter-Frame Time on Dynamic Averaging

To minimise dynamic averaging the inter-frame time must be smaller than the Kolmogorov timescale ($\tau_\eta > \Delta t$). The Kolmogorov timescales for the main test section (in water flow) have been previously shown in Figure 3.8. This indicates maximum inter-frame times as low as 40μs in the very near-field of the fuel injector, however this rapidly increases and by the far-field ($x/D_s > 1$) inter-frames times of over to 1000μs could be used with confidence.

The dynamic averaging consideration points to the use of small inter-frame times, this would also result in strong correlation peaks as particles would be less likely to move out of the interrogation cell over the two frames. However, the minimum inter-frame time for optimised data collection is also constrained. This is because the Davis v6.2 software locates the correlation peak by fitting a three-point Gaussian curve to the data, this process has a maximum precision of $\pm 0.1 d_r$ (where d_r denotes the pixel width). If the inter-frame time was set such that the in-plane displacement was small, say 1 pixel ($MV_i \Delta t = d_r$) then the *relative* precision error on the displacement vector would be ±10%.

Therefore, for optimised data collection, the inter-frame time has to be increased (within the upper constraint of $\tau_\eta > \Delta t$) to minimise the precision error, but without incurring large detection errors. This was achieved by adhering to the non-dimensional parameters listed in Table 3.5 (and discussed in detail below). For further details, see Adrian (1991),

Keane and Adrian (1990, 1991, 1992), Westerveel (1994, 1997) Raffel *et al* (1998) and Prassad (2000).

Description	Optimisation parameter
Number of particles per interrogation cell	$N_I>10$
In-plane particle image displacement	$MV_i\Delta t<0.25Mdx$
Out-of-plane displacement	$V_k\Delta t<0.25\Delta Z_0$
Particle image diameter	$MD_p=2d_r$
In-plane displacement variation	$M\Delta V_i\Delta t<MD_p$

Table 3.4. Non-Dimensional Optimisation Parameters for PIV

Where the velocity component subscripts i (or j) denote in-plane velocities and k denotes an out-of-plane velocity (for definition of the i, j, k notation see Figure 3.5). MD_p is the particle *image* diameter and ΔV_i is the in-plane velocity variation across a cell as is discussed in detail further in this section.

The seeding density requirement of $N_I>10$, helps to maintain a strong correlation and hence a high SNR, thus reducing detection error. In the water facility it was found that within the range of magnifications used, this constraint meant that the smallest usable interrogation cell size was 32×32 pixels ($dx=32d_r/M$). Any further reduction would have required excessive seeding of the flow. A grid size of 32×32 pixels resulted in a data resolution of 31×30=930 vectors.

To set the inter-frame time (within the limit $\tau_\eta>\Delta t$) the "quarter" rule was applied to both in-plane ($MV_i\Delta t<0.25Mdx$) and out-of-plane ($V_k\Delta t<0.25\Delta Z_0$) velocity components and is essentially a compromise between the conflicting requirements of minimising the relative precision error whilst avoiding significant detection errors. In flows with strong out-of-plane motions the quarter rule can only be adhered to for in-plane motions (without significant out-of-plane loss of particle pairs) by increasing the image magnification. The inter-frame times selected for the water flow rig PIV measurements based on the quarter-rule criteria are detailed below in Table 3.5.

The precision errors are then minimised by optimising the particle image diameter and controlling the in-plane displacement variation. The particle image diameter is optimised for PIV at 2 pixels ($MD_p/d_r=2$) the reason for this is that the Davis v6.2 software locates

the particle image centres using a Gaussian intensity fit. If $MD_p/d_r<2$ the Gaussian fit becomes biased towards the nearest integer value, this is known as "peak locking" with the net effect of broadening the correlation peak (hence increased the precision error). The effect of particle image diameter on peak-locking is shown in Figure 3.13 for a particle image with a diameter of (a) $MD_p/d_r>2$, where peak-locking is not present, and (b) $MD_p/d_r<2$, where the particle image centre is "locked" to the nearest integer value.

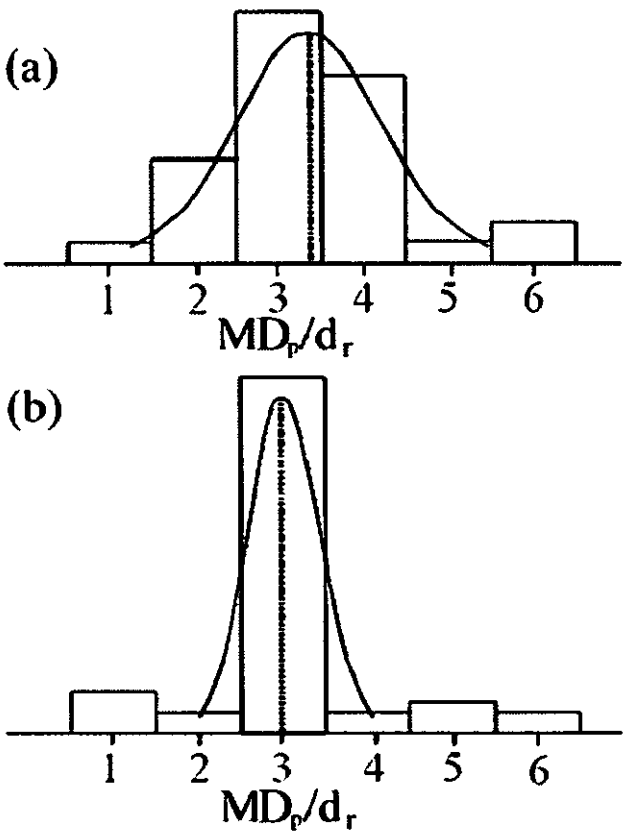

Figure 3.13. Effect of Particle Image Diameter on Sub-Pixel Interpolation Accuracy

Whilst it may seem from Figure 3.13 that increasing MD_p/d_r past 2 would increase further the sub-pixel accuracy in locating a particle image centre, this in fact is not the case. As MD_p/d_r increases past 2 the uncertainty in locating the particle image centre increases, and random error increases, Raffel *et al* (1998). The overall effect of the particle image diameter on the precision error (shown as a manifested increase in RMS) is shown in Figure 3.14

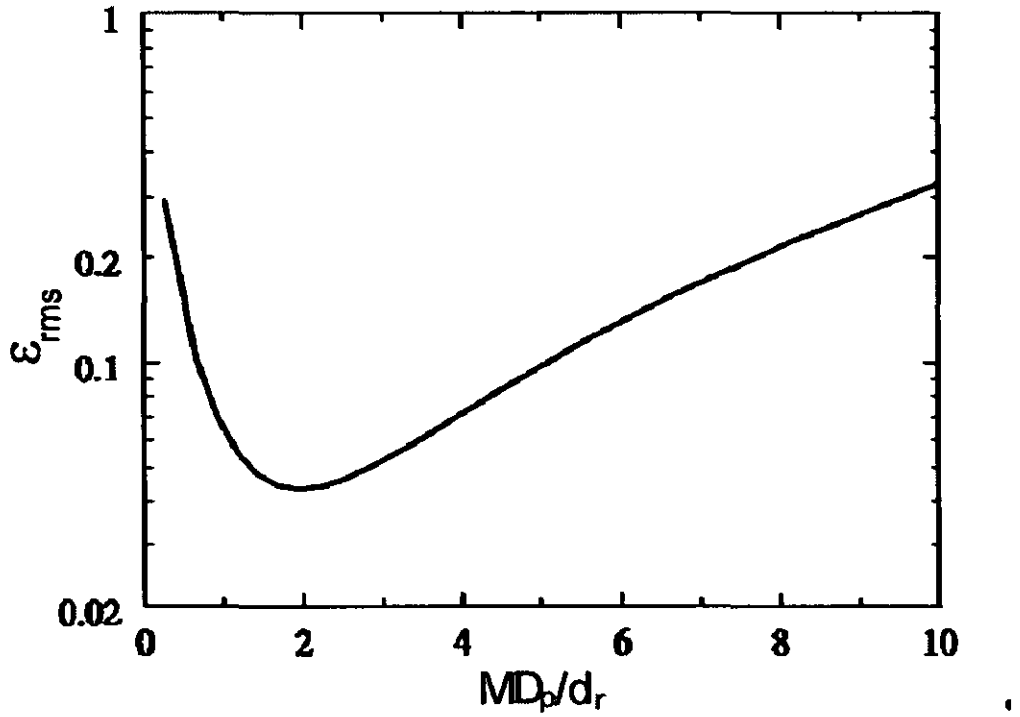

Figure 3.14. RMS Error (Precision Error) as a Function of Particle Image Diameter, Raffel *et al* (1998)

In the water rig using the range of magnifications available it was possible to achieve $MD_p/d_r=2$ for a range of magnifications 0.1-0.45 in conjunction with modifying the incident laser power.

To calculate the in-plane displacement variation ($M\Delta V_i\Delta t$) one requires knowledge of the in-plane velocity variation, ΔV_i across the interrogation cell, defined by Bolinder (1999) as:-

$$\Delta V_i = |\overline{\nabla V_i}|\, dx$$

Where $|\overline{\nabla V_i}|$ is the magnitude of the time-average of the instantaneous velocity gradient across an interrogation cell in either in-plane direction:-

$$|\overline{\nabla V_i}| = \sqrt{\left(\frac{dV_i}{dx}\right)^2 + \left(\frac{dV_i}{dy}\right)^2}$$

The terms $\frac{dV_i}{dx}$ and $\frac{dV_i}{dy}$ were calculated using a central differencing scheme across each interrogation cell. Clearly increasing the magnification reduces the in-plane velocity variation by reducing dx and dy. Maintaining the in-plane displacement variation across an interrogation cell less than the particle image diameter ($M\Delta V_i\Delta t<MD_p$) minimises the correlation peak width, hence minimising precision error. If the flow was completely homogeneous, then there would be a zero displacement variation ($\Delta V_i=0$). As PIV returns only one velocity vector per interrogation cell, anything less than a completely homogeneous flow will result in spatial filtering of particle displacements other than the modal displacement. Spatial filtering is discussed in Section 3.4.10.2.

3.4.6 Advanced Processing Methods

To improve the data quality further advanced processing methods, available within the Davis v6.2 software were employed. Firstly adaptive multi-pass grids were used whereby large interrogation cell sizes were used to calculate an initial low-resolution displacement vector field. The vector field was then recalculated using smaller interrogation cells but with the initial low resolution vector field used as a reference interrogation cell shift between the two frames. Adaptive grids therefore improve the SNR (and hence the probability of valid detection) by reducing the likelihood of in-plane loss of particle pairs.

The multi-pass grid was applied using a 50% data overlap (where the velocity field was recalculated with final interrogation cells overlapping by 50%) thus improving the data density by a factor of 4. For the 930 velocity vectors calculated using a final cell size of $32d_r/M$ this resulted in 3721 (63×61) vectors. It must be stressed that this is only a perceived increase in spatial resolution; smaller scales of the flow will not be resolved as the final cell size is still 32dr/M.

On each pass of the adaptive grid a cell deformation was applied whereby the originally square interrogation cells were deformed according to the velocity gradient across the cell. The velocity gradients were calculated from a central differencing scheme; the velocities on each side of an interrogation cell were known from the 50% overlap. The deformed grid was then used on the second pass with a resulting reduced in-plane loss of

particles within the cell. A bilinear interpolation was then used to relocate the calculated velocity vector from the centre of the deformed grid back to the centre of the non-deformed grid. This method is described in detail by Fincham and Delerce (2000).

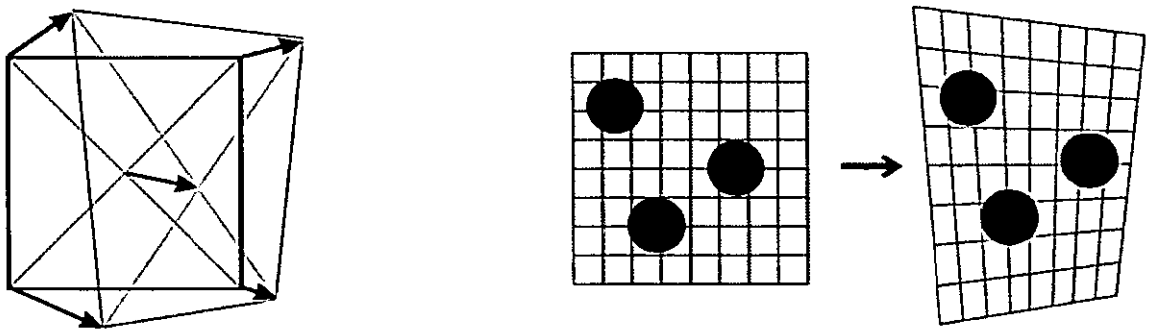

Figure 3.15. Interrogation Cell Deformation, La Vision (2004)

Correlation Based Correction (CBC) as proposed by Hart (2000) was used as a method of further increasing the SNR. CBC achieves this by multiplying (element-by-element) the correlation map of one interrogation cell with a correlation map of an adjacent interrogation cell that overlaps the first by 50%. As a result, correlation peaks that do not occur in both correlation maps are eliminated from this second order correlation map, thus amplifying the true correlation and suppressing noise peaks. Figure 3.16 shows an example of noisy correlations at spatial location (a) and at the 50% overlap position (b), the second order correlation map is shown in (c).

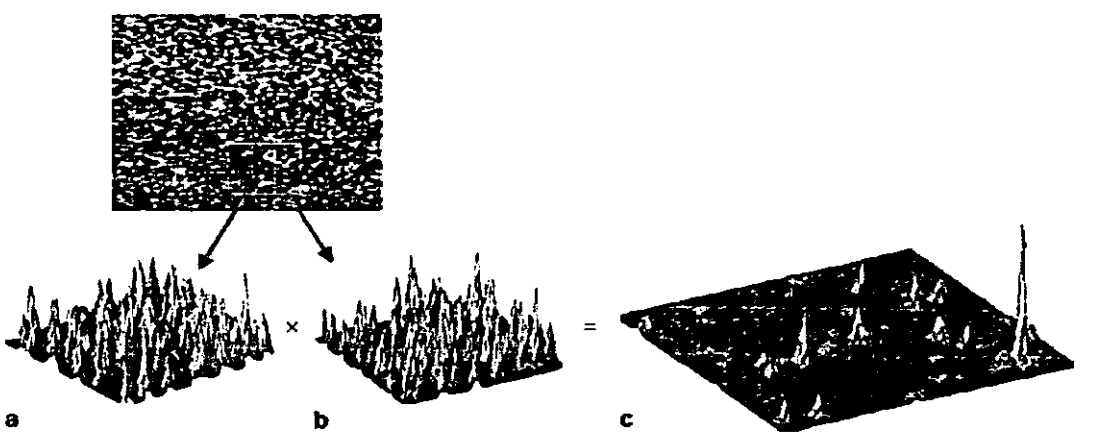

Figure 3.16 Effect of CBC on Eliminating Noise and Amplifying the True Correlation Peak, Hart (2000)

Assuming there is a linear relationship between the vectors at positions (a) and (b), then the displacement vector and hence the velocity half way between the centre of the two interrogation cells can be calculated (v_0 in Figure 3.17). The CBC also helps minimise precision error by reducing the width of the correlation peak on the CBC correlation map, also shown in Figure 3.17.

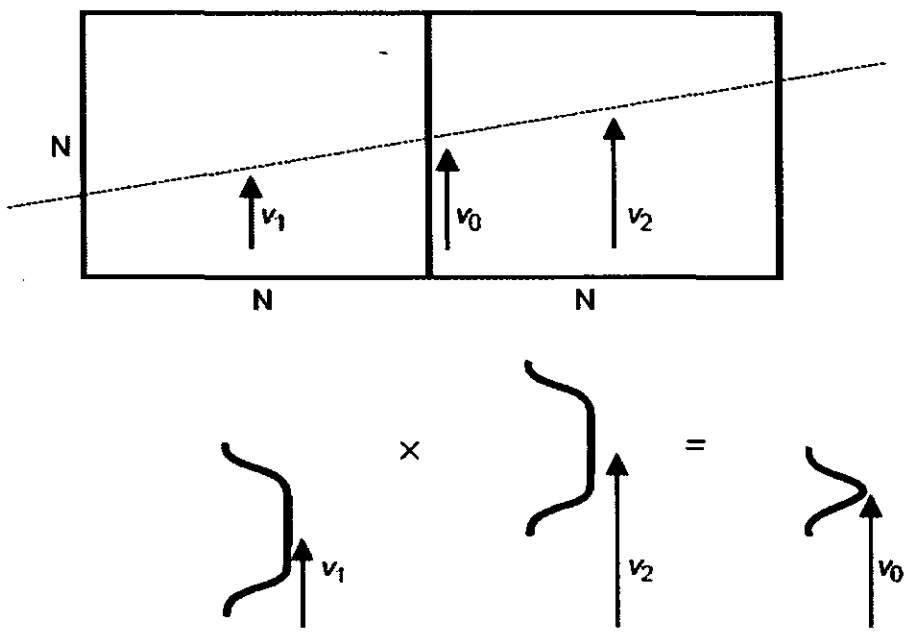

Figure 3.17. Effect of the CBC on the Correlation Peak Width, Hart (2000)

3.4.7 Post Processing

The main objective of post-processing is to assess critically the returned vector field and remove and replace vectors that appear to be spurious; the amount of post-processing required is therefore a measure of the detection error. There are several possible methods of post-processing, the most basic being to pre-determine the allowable velocity range and to reject vectors whose SNR falls below a certain value. However, the effectiveness of such methods is limited in highly turbulent unsteady flows and can easily result in the removal of valid data. Therefore, a more advanced technique was employed, known as a "median filter", Westerveel (1994). This algorithm assesses the likelihood of a vector being spurious by calculating the median value and standard deviation ($\pm\sigma$) of the 8 surrounding vectors. The central vector is then rejected if it falls outside a factor, c, times the standard deviation ($\pm c\sigma$) relative to the median value. The median value is used as it

is less likely to be influenced by spurious data compared to the mean value. The La Vision software also provides a "strong" removal, whereby several passes of the median filter allow for whole groups of vectors to be removed if spurious.

For both mean and RMS data it was important to replace any removed information. Initially the software checks the 2^{nd}, 3^{rd}, and 4^{th} highest correlation peaks successively and replaces the removed data if any of these correlation peaks are within $\pm c\sigma$ of the median value. If this was not successful linear interpolation was used to fill the empty spaces. Linear interpolation is not ideal and is a cure rather than the solution to the problem. However in this application where out-of-plane velocities were large some spurious data was inevitable. For the water flow experiment less than 6% of spurious data was considered acceptable, greater levels necessitated a re-optimisation of the experimental configuration.

3.4.8 Summary of PIV Operating Parameters

Table 3.2 provides a summary of the optimisation, processing and post-processing methods utilised in the water flow rig PIV experiments.

Seeding (20μm polyamide)	
Velocity slip	0
Response time	19.5μs ($<0.5\tau_n$)
Recording	
Mode	double-frame/single-exposure
Inter-frame time	20-240μs
Magnification	0.06-0.5
f-number	1.8-4.0
Processing	
Interrogation method	FFT CCF
Adaptive multi-pass grids	64×64 to 32×32 pixels
Deformed grids	yes
Correlation Based Correction	yes
Overlap	50%
Post-processing	
Predetermined limits	No
Median filter	Yes
Vector replacement	Bilinear interpolation

Table 3.5. Summary of PIV Operating Parameters

3.4.9 Conversion to Cylindrical Polar Velocity Components

From the above description of the PIV measurement technique it is clear that the calculated velocity components are Cartesian by definition; however, the most suitable velocity decomposition for the water (and airflow) rig data was cylindrical polar components due to the swirling, axi-symmetric motions of the flow. In the axial-radial plane the measured in-plane velocities represent the axial and radial components (although both positive and negative Cartesian transverse components either side of the x-axis are a positive radial component). However in the radial-circumferential plane the following transformation was required:-

$$r = \sqrt{x^2 + y^2}$$

$$\theta = \tan(y/x)$$

$$V_r = V_i \cos\theta + V_j \sin\theta$$

$$V_t = V_j \cos\theta - V_i \sin\theta$$

Where the subscripts i and j represent the in-plane Cartesian PIV measured velocity components. This transformation allowed for cylindrical polar velocity components to be displayed either in a Cartesian or cylindrical polar frames of reference. An example of raw PIV data in an r-θ plane (Cartesian velocities) and the effect of the conversion to polar velocities is shown in Figure 3.18 and Figure 3.19.

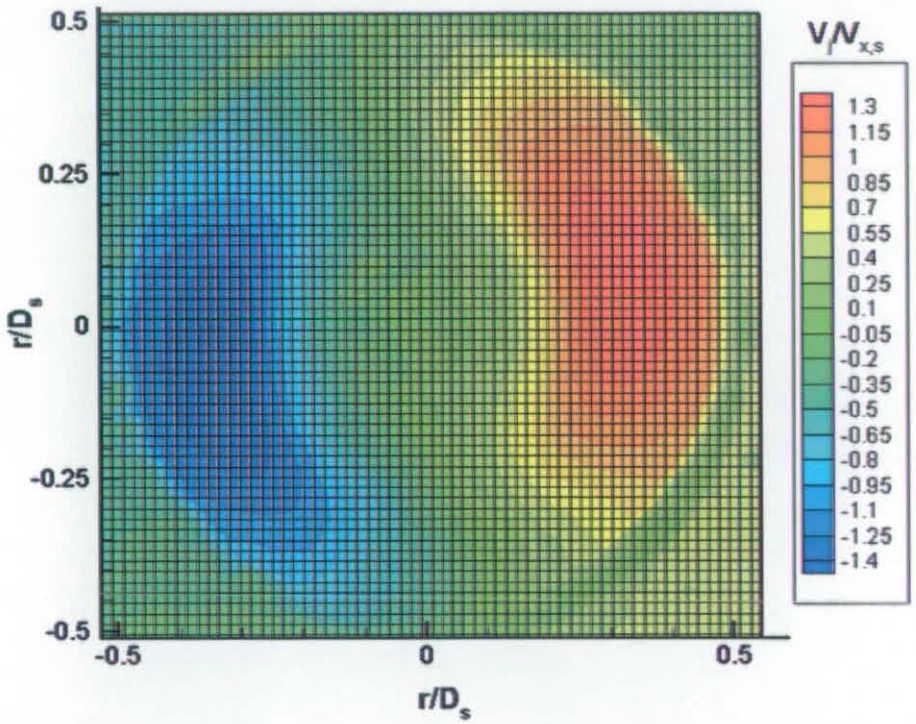

Figure 3.18. Time-Averaged j-Velocity Contours in a Cartesian Frame of Reference

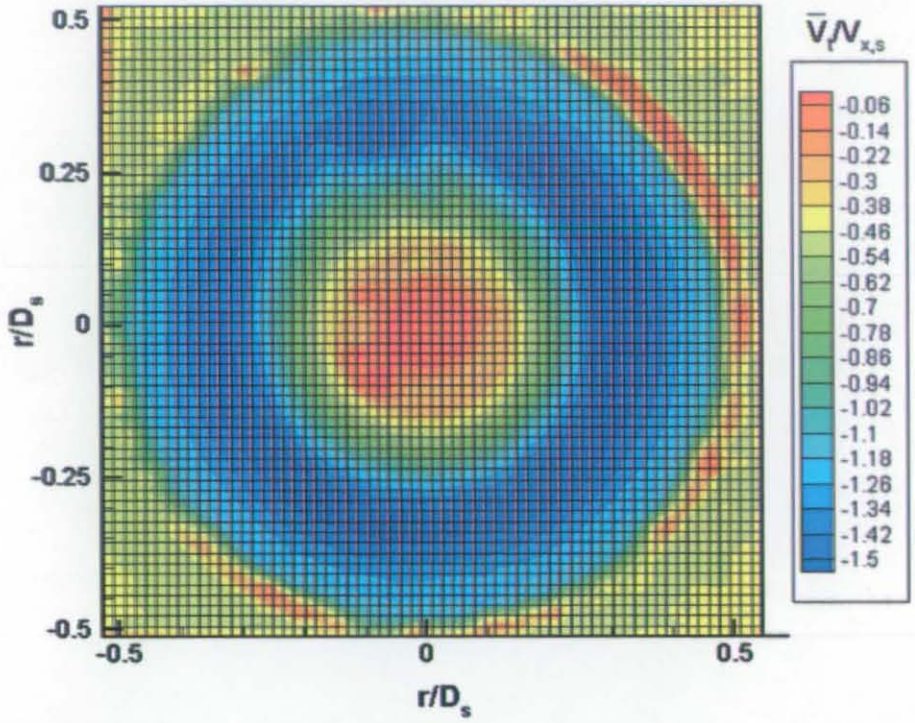

Figure 3.19. Polar Transformed Circumferential Velocity Contours in Cartesian Frame of Reference

Clearly conversion to cylindrical polar velocities has advantages in the visualisation of the velocity contours when viewed in a Cartesian frame of reference (where the negative radii is the convention undertaken in this thesis to signify theta locations 180°-360°). The further conversion to cylindrical polar velocities in a cylindrical polar frame of reference was then useful for averaging in the theta direction (circumferential averaging is discussed further in Section 3.4.13 below). Calculation of spatial velocity correlations also used radial and theta directions as these more closely matched the dominant flow directions. Spatial velocity correlations are discussed in Chapter 4.

3.4.10 Statistical Error

Whilst the optimisation procedure of the system parameters discussed above minimise the errors associated with the PIV technique, the errors in the time-averaged statistics must also be evaluated. All the time-averaged statistics reported in this thesis were calculated from LS-PIV data sets, this was because the accuracy of a time-average is dependant on the number of statistically independent samples. Statistical independence is more likely to occur if the time-step between successive sample data points is larger than the largest timescales of the flow. A measure of the largest timescales of a flow can be found by

calculation of the integral timescales. Figure 3.20 shows the integral timescale contours for the main test condition calculated from 1kHz HS-PIV data. For details on the calculation of the integral timescales from PIV data see Section 4.3.

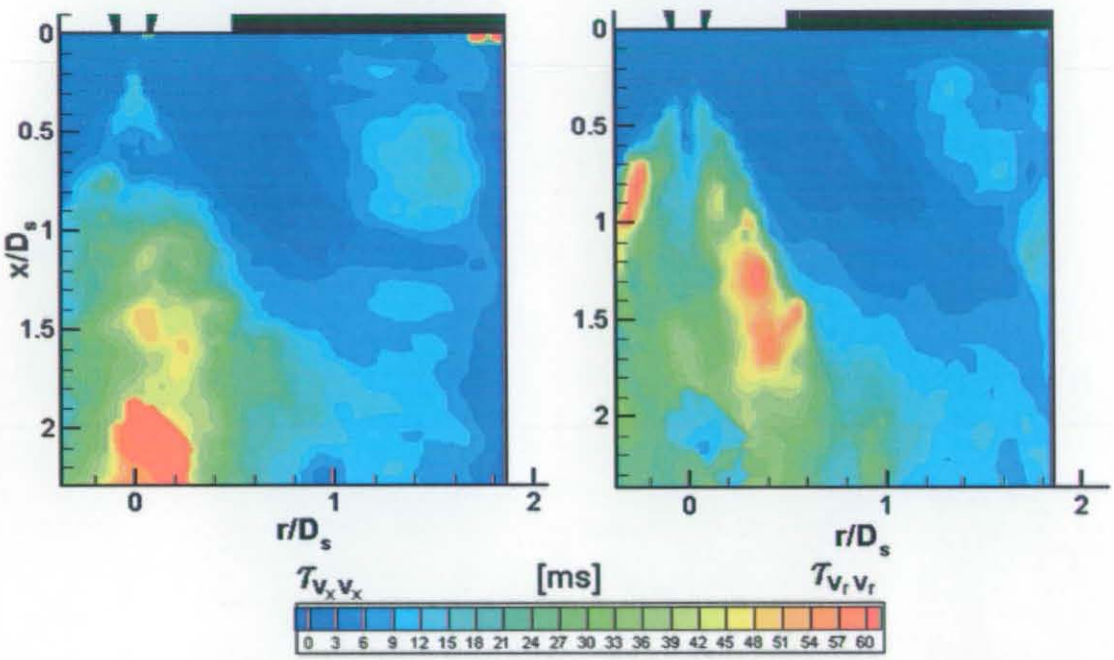

Figure 3.20. Axial [left] and Radial [right] Integral Timescales in Water Flow (Main Test Condition)

As shown in Figure 3.20, peak integral timescales were greater than 60ms by $x/D_s=2$. Therefore, data points collected using the LS-PIV system with temporal resolution of 15Hz (66.66ms time-steps) could assumed to be statistically independent, however, data points collected using the HS-PIV system with a temporal resolution of 1kHz (1ms time-steps) would not be.

3.4.10.1 Statistical Convergence

The statistical convergence of LS-PIV data sets was assessed from point velocity time-histories. Figure 3.21 and Figure 3.22 show typical examples of the percentage error of mean and RMS axial velocity (relative to the value calculated from N=650 points) for data block sizes ranging between N=5 and N=650. The convergence of the statistics collected from the various sample sizes are compared to theoretical percentage standard error estimates:-

$$\frac{\varepsilon_{\bar{V}}}{V_{x,s}} = \pm z \frac{v'}{V_{x,s}} \sqrt{\frac{1}{2N}}$$

$$\frac{\varepsilon_{v'}}{v'} = \pm \frac{z}{\sqrt{N}}$$

Where the confidence level is defined by the value chosen for z (z=2.576 corresponds to 99% confidence).

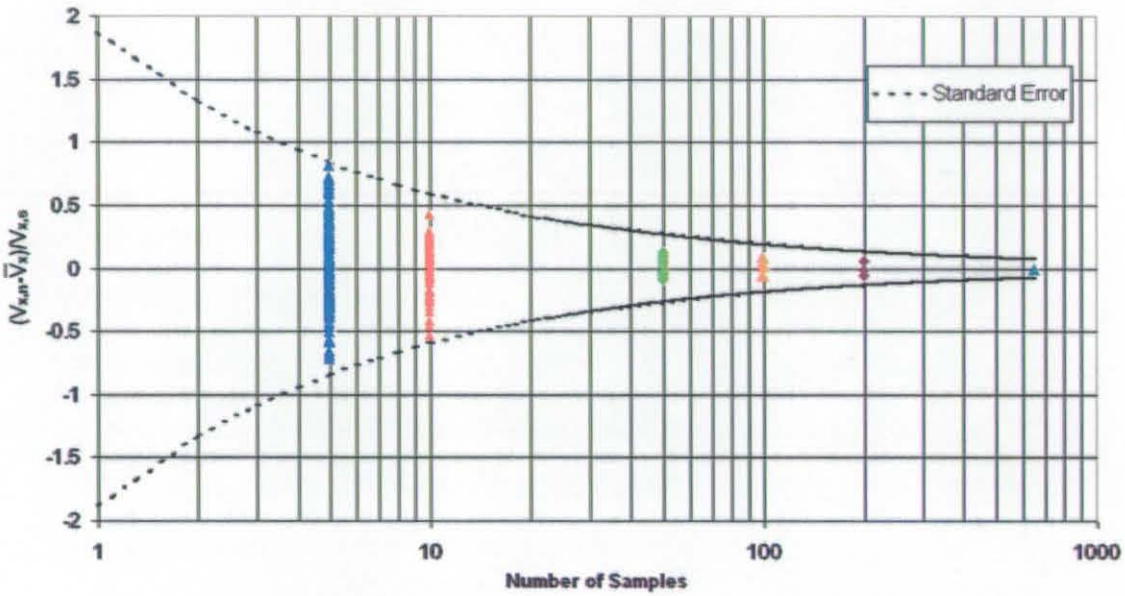

Figure 3.21. Convergence of LS-PIV Mean Axial Velocity

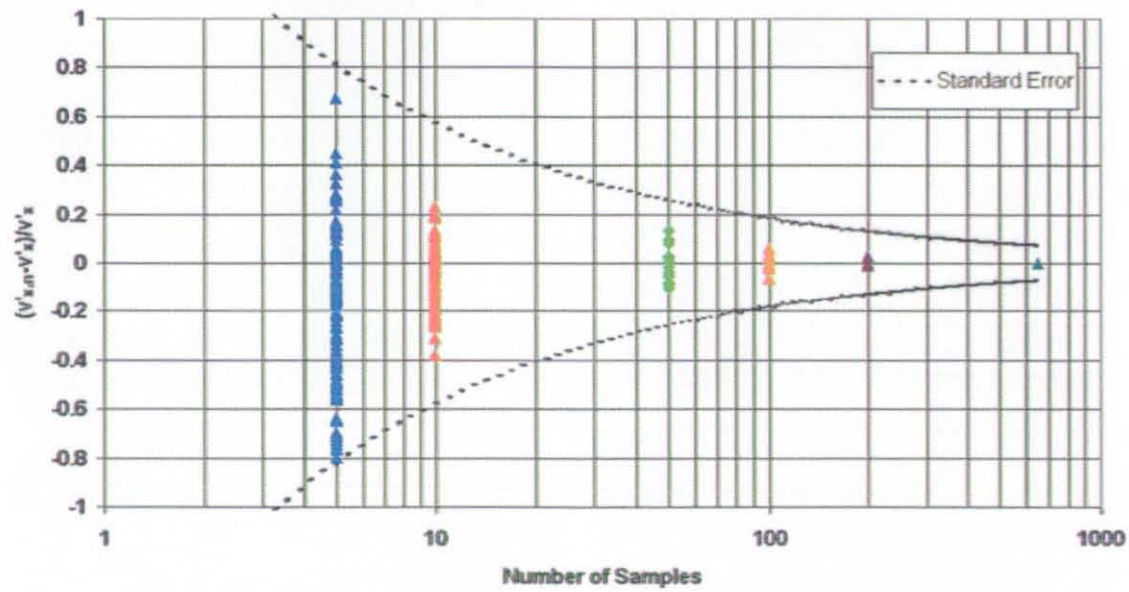

Figure 3.22. Convergence of LS-PIV RMS Axial Velocity

As can be seen, the LS-PIV data sets converge in agreement with standard error estimates; this was found to be the case at all locations tested. Hence, using standard error estimates the statistical RMS velocity error (calculated from an LS-PIV data set) is only a function of the number of samples, so for N=650, $\varepsilon_{v'}=\pm 7.2\%$. However, the mean velocity error is proportional to both the number of images taken and the turbulence intensity $\left(v'_x / V_{x,s}\right)$. In most regions of the flow this resulted in errors of $\varepsilon_v < \pm 1\%$ however in regions of the flow where turbulence intensities were high (such as the re-circulation bubble shear layer) the mean velocity statistical errors could be as high as $\pm 10\%$.

3.4.10.2 Spatial Averaging

Whilst the statistical convergence plots indicate that enough samples were taken to give a converged answer, this does not guarantee that the data set has converged to the correct or "true" value. In terms of the mean velocity data, biases can occur due to faster moving particles being convected out of the camera depth-of-field; however, mean bias is minimised by conforming to the optimisation parameters outlined in Table 3.5 and by the use of the advanced processing techniques such as adaptive deformed grids. In terms of RMS data however, one must also assess the impact of sub-grid filtering which may serve to reduce the measured RMS. Since PIV CCF algorithms return a single velocity vector (per interrogation cell) that represents the most common (modal) particle displacement, anything other than a homogenous motion of particles will result in some spatial filtering. Spatial filtering is minimised in the PIV optimisation process by controlling the in-plane displacement variation (see Section 3.4.5).

Höest-Madsen and Nielsen (1998) have examined the influence of the filtering effects of finite interrogation cell sizes on measured RMS values. They suggested a theoretical model assuming isotropic turbulence and used turbulent correlation functions to estimate the error in the measured turbulence quantity as a function of the interrogation cell size. Hollis (2004) developed this work, creating an estimate for the sub-grid filtering based on experimental measurements in highly turbulent flows. This is shown in Figure 3.23 where the sub-grid filtering (v'/v'_{true}) is expressed as a function of the ratio of interrogation cell size to the local turbulent integral length-scale (dx/L_{11}).

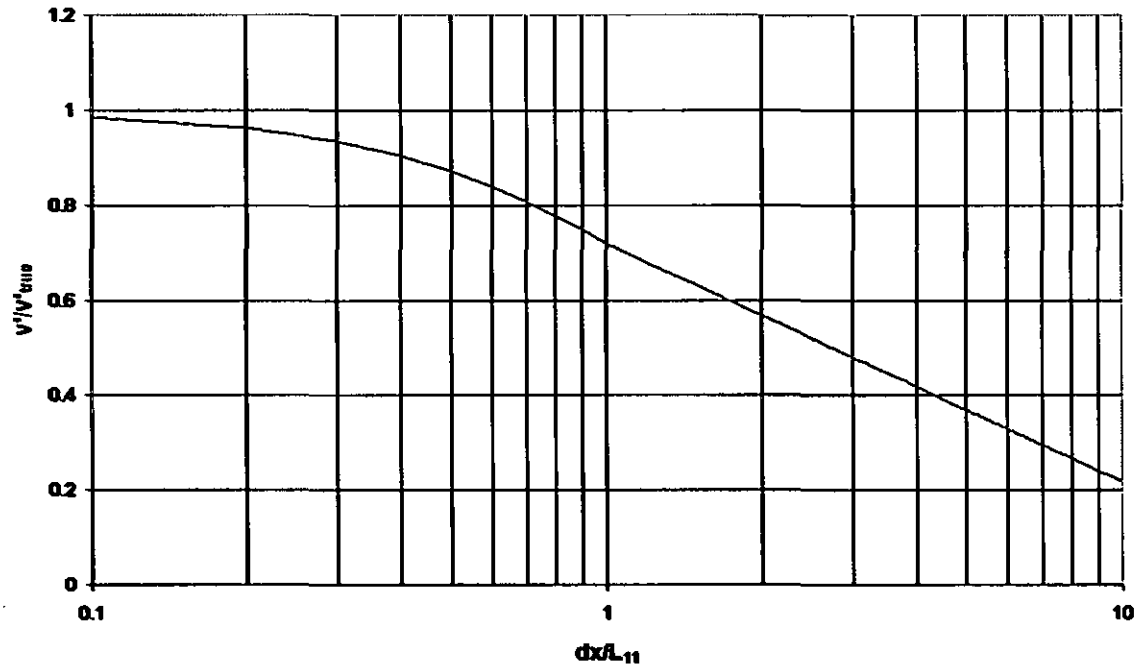

Figure 3.23. Sub-Grid Filtering Expressed as a Function of the Ratio of Interrogation Cell Size to the Local Turbulent Integral Length-Scale, Hollis (2004)

Hence the larger the interrogation cell size relative to the local integral length-scale the greater the sub-grid filtering. To capture >90% of the turbulent motions Figure 3.23 suggests the cell size has of order $0.4L_{11}$. The method for the calculation of the turbulent integral length-scales directly from PIV data sets is described in Chapter 4.

3.4.11 Data Collection

So far the optical arrangement, optimisation and statistical errors of the PIV technique have been discussed; the following section details the practical application of the PIV system to the fuel injector and modular swirler induced flowfields. From the discussion above it is clear that both the PIV system optimisation and the minimisation of spatial filtering are dependant on the image magnification, where the more adverse the flow conditions the larger the image magnification (i.e. the smaller the FoV). However, in extremely adverse flow conditions, such as those created by strongly swirling flows, where the dynamic range of velocity is high, velocity gradients are large, out-of-plane motions are of a similar order of magnitude to in-plane velocities and turbulent integral length-scales are small, this strategy often leads to FoVs' tending to the size of a point measurement control volume.

Whilst this may be essential for measuring accurate time-averaged statistics, it must also be borne in mind that the considerable advantage of PIV over point measurement techniques (such as LDA) is that it allows the capture of spatially resolved flowfields, providing evidence of the instantaneous flow structures. This attribute must be capitalised on both to provide important validation data for LES predictions and to help improving our fundamental knowledge of the flow physics typical to combustors. It is clear therefore that a compromise (or optimal methodology) is needed to guide the data collection process. For the present investigation the following methodology was applied:-

i. Use large FoVs' (small magnifications) for assessment of the instantaneous flow structures, whilst accepting that the mean velocity and RMS turbulence data gathered in these measurements may contain some errors.
ii. Select a range of smaller FoVs' (large magnifications) optimised to the local flow conditions (based on the data gathered in step (i)) to ensure accurate flowfield statistics.

The FoV sizes utilised to meet criteria (i) and (ii) in the x-r and r-θ planes are shown in Table 3.6. B_0 denotes the FoV side length as defined in Figure 3.5. The interrogation cell size was calculated from $dx=32d_r/M$ where d_r is the pixel width and 32 was the final interrogation cell size in pixels (see Section 3.4.5).

B_0 [mm]	B_0/D_s	M	dx (dy) [mm]	f#	ΔZ_0 [mm]
140	3.72	0.06	4.8	1.8	2.5
80	2.13	0.11	2.56	1.8	0.7
40	1.06	0.22	1.28	2.8	0.53
20	0.53	0.45	0.64	4	0.35

Table 3.6. Field of Views Details

The following sections describe the experimental methodology for selecting FoVs' for the inlet and exit conditions (Section 3.4.11.1) and the dump area expansion chamber x-r plane (Section 3.4.11.2) and r-θ planes (Section 3.4.11.3). The optimisation process detailed below is based on PIV data sets collected at the main test condition, with the

understanding that a similar optimisation process was carried out for the no-jet test condition that provided similar results.

3.4.11.1 Inlet and Exit Conditions

Data was captured in the central jet feed pipe and the annular gap feeding the swirl stream using 0.53^2 FoVs' which just encompassed the desired regions. These are shown in Figure 3.24 where the blue square represents the central jet feed pipe measurement region and the red square the annular swirl stream feed flow inlet region.

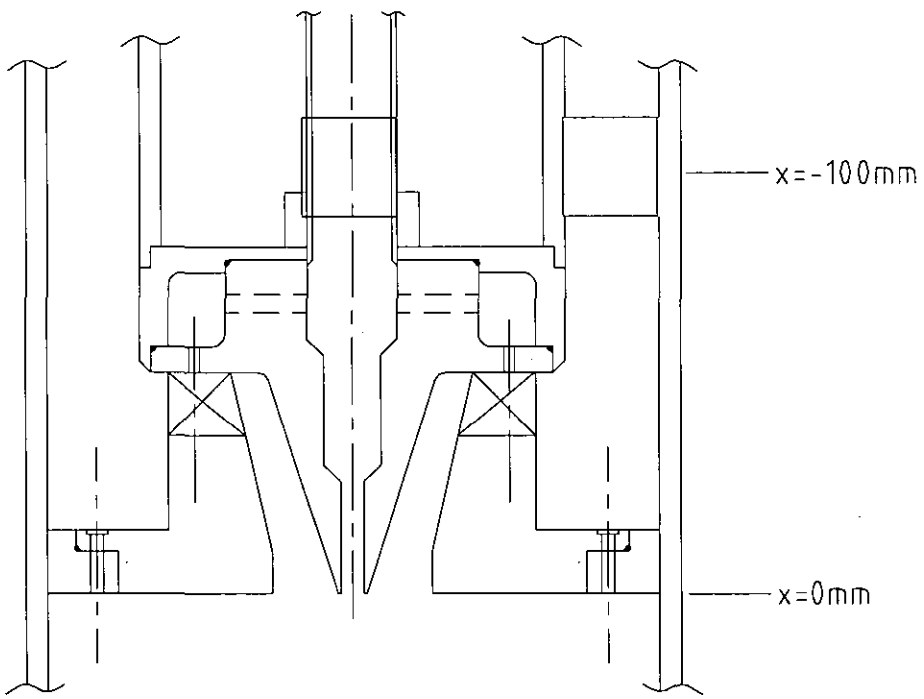

Figure 3.24. Location of PIV Measurement Regions for Inlet Conditions

The measurement regions (which included the axial location x=-100mm) were chosen because preliminary PIV data had indicated that further downstream the radially fed swirl slots started to influence the velocity profiles. This is shown in Figure 3.25, where the top of the fuel injector is at -86mm.

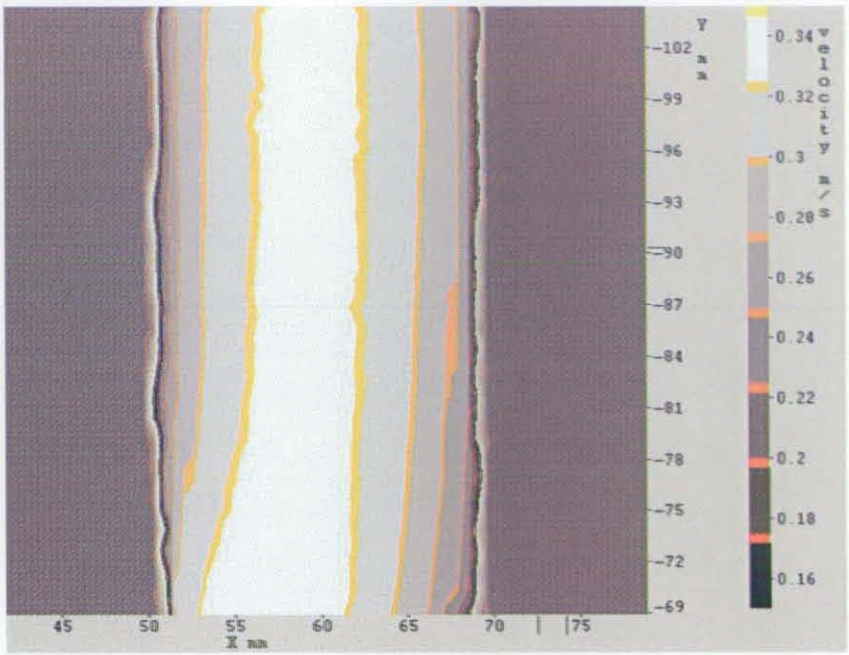

Figure 3.25. Swirl Stream Feed Flow Mean Axial Velocity

As x-r plane measurements in both the annular gap and the central jet feed pipe had little out-of-plane (circumferential) motion, the inter-frame time could be set to adhere to the quarter rule in most regions of the flow. However, in the very near wall region (<1mm) where the velocity decayed to zero (at the wall) and the velocity gradients were high it was impossible to meet the optimisation parameters. The loss of turbulence data (sub-grid filtering) was estimated by calculating the axial, $L^{x}_{v_x v_x}$ and radial, $L^{r}_{v_r v_r}$ turbulent length-scales from the LS-PIV data sets and applying the sub-grid filtering estimation curve (see Figure 3.23). As the flow within the PIV measurement region was fully developed, and far enough upstream not to be influenced by the downstream fuel injector, the length-scales should not change in the axial direction. Therefore, to provide the most representative radial inlet profiles, all of the constant axial lines (captured within the FoV measurement region) were averaged. Radial profiles of axial and radial length-scales are shown in Figure 3.26 and Figure 3.27. The indicated loss in RMS velocity due to sub-grid filtering is then shown in Figure 3.28 and Figure 3.29.

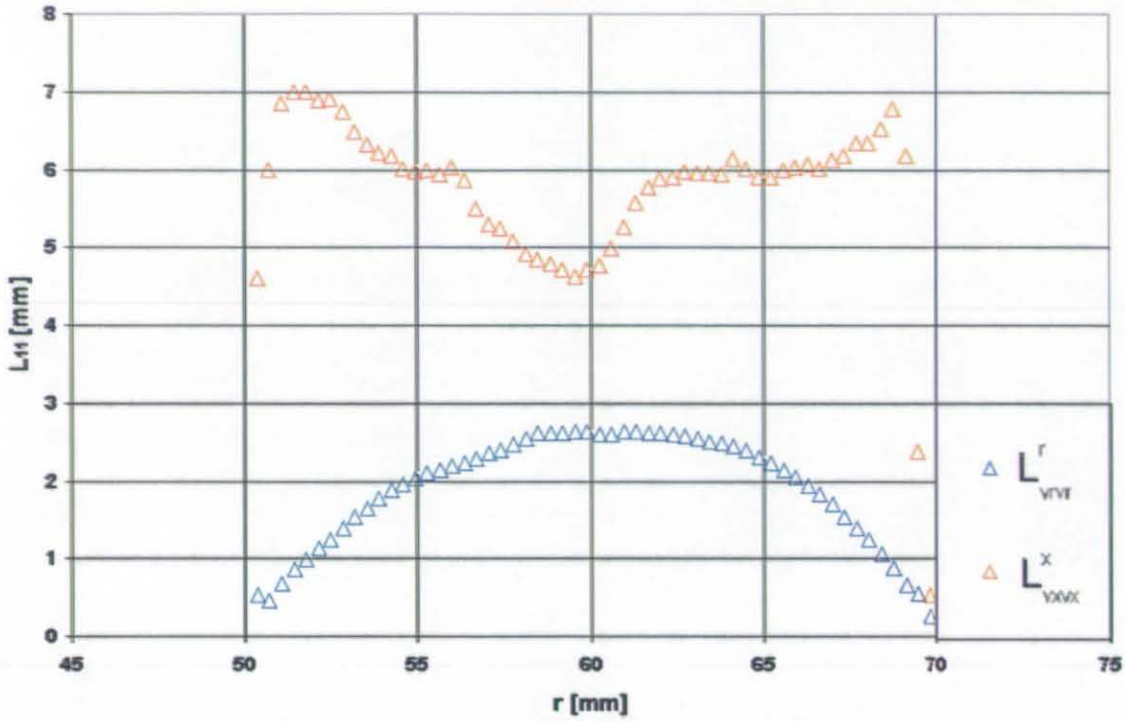

Figure 3.26. Turbulent Integral Length-Scales in Swirl Stream Feed Path

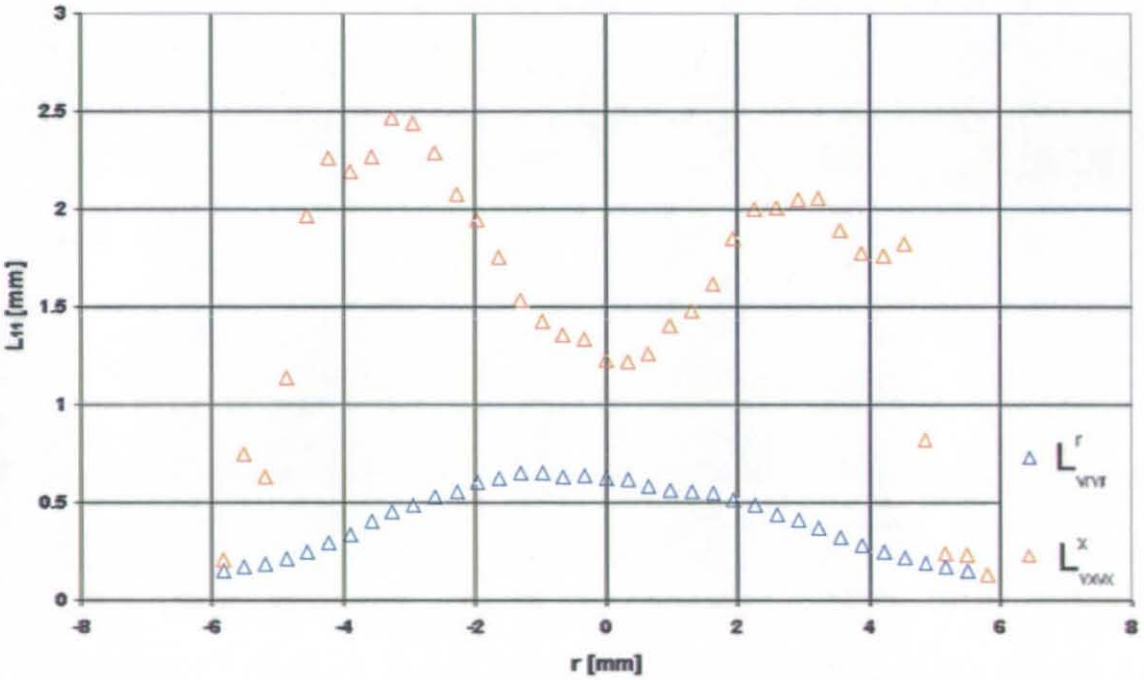

Figure 3.27. Turbulent Integral Length-Scales in Pipe Feeding Central Jet

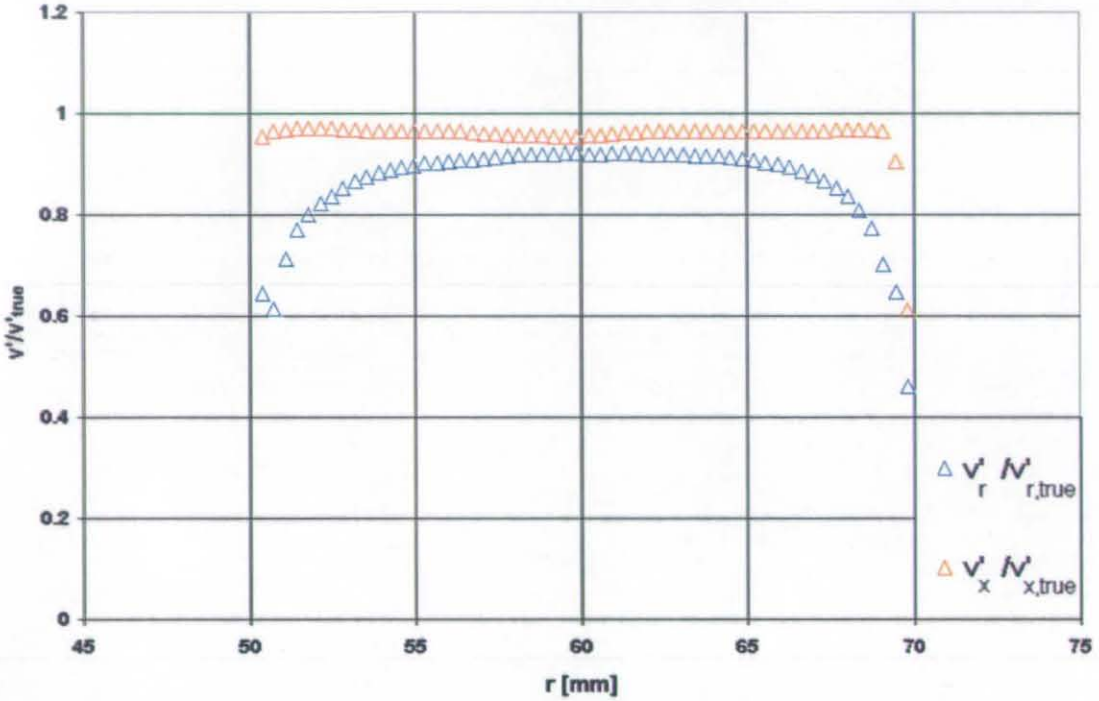

Figure 3.28. RMS Velocity Loss Estimation in Swirl Stream Flow Path

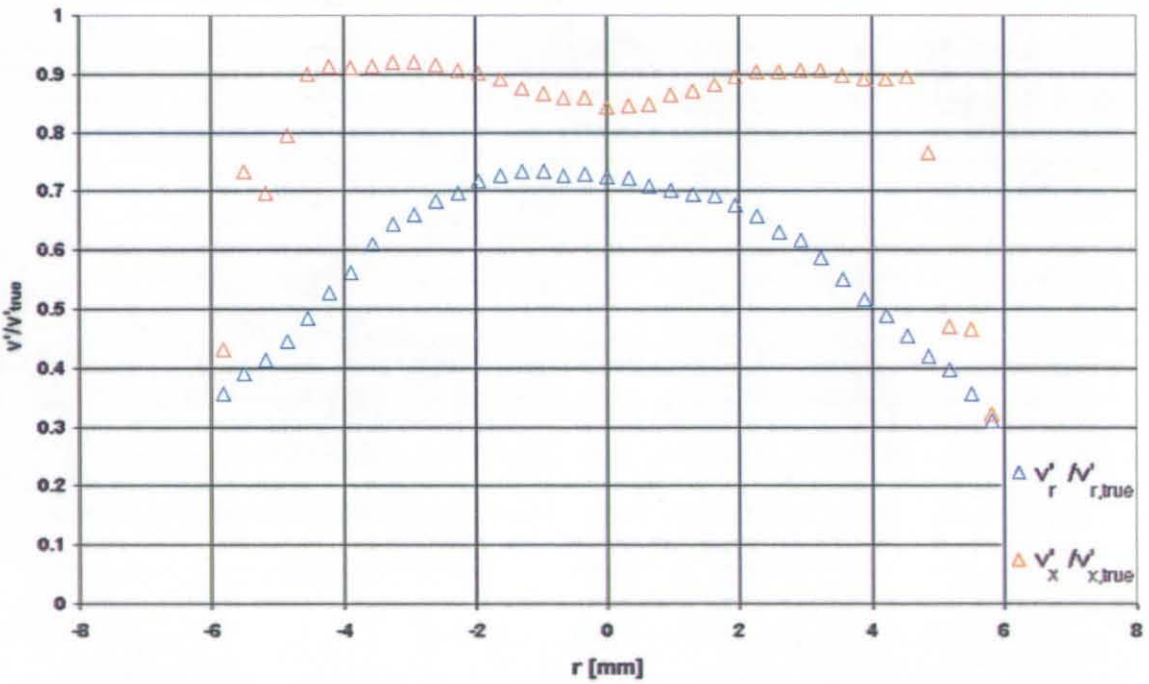

Figure 3.29. RMS Velocity Loss Estimation in Pipe Feeding Central Jet

As shown, axial length-scales are larger towards the boundaries with minima close to the centreline and radial length-scales and largest towards to centreline and reduced towards to walls. In the axial direction this resulted in an indicated capture of more than 90% in most regions of the central jet feed pipe and more than 95% in the annular swirl stream.

However, in the radial direction indicted losses became high approaching the walls. Therefore, to improve accuracy and provide the best experimental estimates of the inlet profiles the "true" RMS velocity components, v'_{true} were used, i.e. the measured RMS value, v′ divided by the indicted loss (see Chapter 5 for results).

In the annular exhaust flow gap, enclosed between the outer duct wall and the downstream blockage, a 1.06^2 FoV was used to capture data. As exit plane profiles need not be specified for CFD calculations the accuracy of this data was not deemed critical, hence a larger FoV was used as to assess any large-scale flow features that may occur and may be significant to an exit boundary condition of a CFD model, the results are reported in Chapter 5.

3.4.11.2 Axial-Radial Plane

All x-r plane data was captured with the FoVs' plane passing along the fuel injector centreline. Figure 3.30 shows the location of four 2.13^2 FoVs' (B_0=80mm, Table 3.6) used to map the entire test section (labelled A-D), overlaid on a "patched" image of the mean velocity vectors superimposed on axial velocity contours. The term "patched" here refers to the linear interpolation of several adjacent data sets onto a single structured grid. In Figure 3.30, this indicates the interpolation of the four 2.13^2 regions (A-D) onto a single common grid of a similar grid resolution to that of the original data ($dx=16d_r/M$). Also included in Figure 3.30 are the axial positions of the data captured in the radial-circumferential plane at locations within the fuel injector body (green lines) and within the dump area expansion chamber (red lines). The radial-circumferential data collection methodology is described in detail in Section 3.4.11.3.

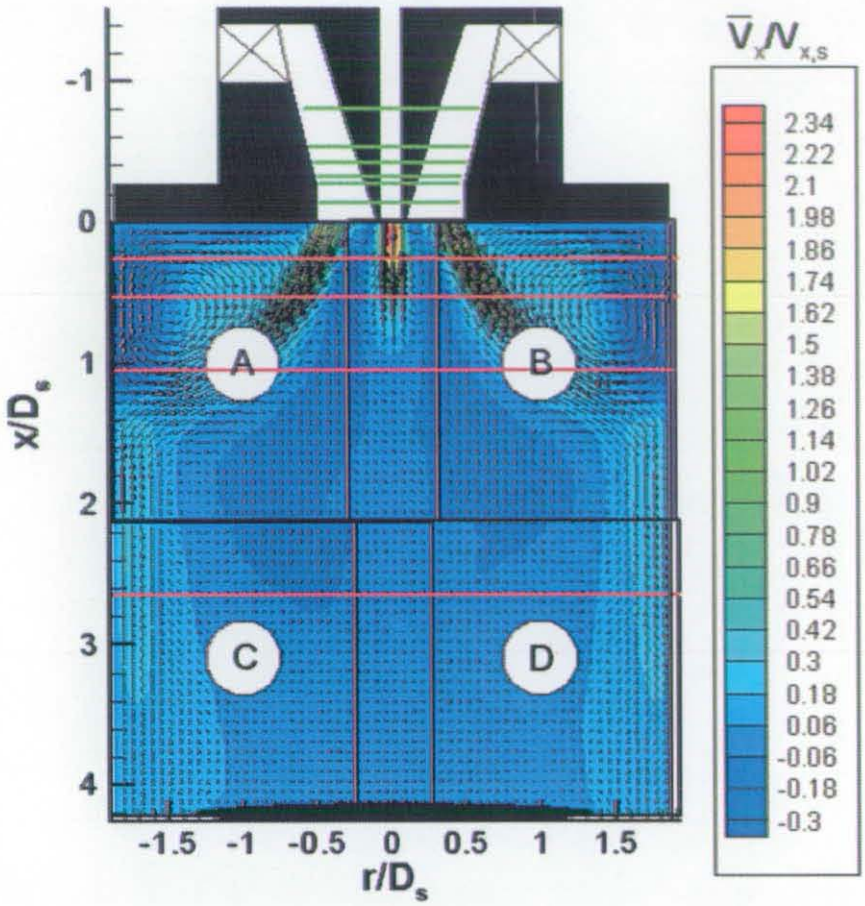

Figure 3.30. Location of 2.13^2 FoV Regions (A-D)

In locations C and D it was found that as the swirl and jet stream shear layers diminished in strength and peak velocities reduced it was possible to satisfy all the PIV optimisation guidelines. However in positions A and B large velocity variations occurred and the optimisation of the inter-frame time according to the quarter-rule was determined by the high velocities in the near field ($x/D_s<1$) resulting in particle displacements close to zero in slower moving areas such as the re-circulation bubble. Assessment of $M\Delta V_i\Delta t/MD_p$ is shown for both axial and radial in-plane displacements in Figure 3.31.

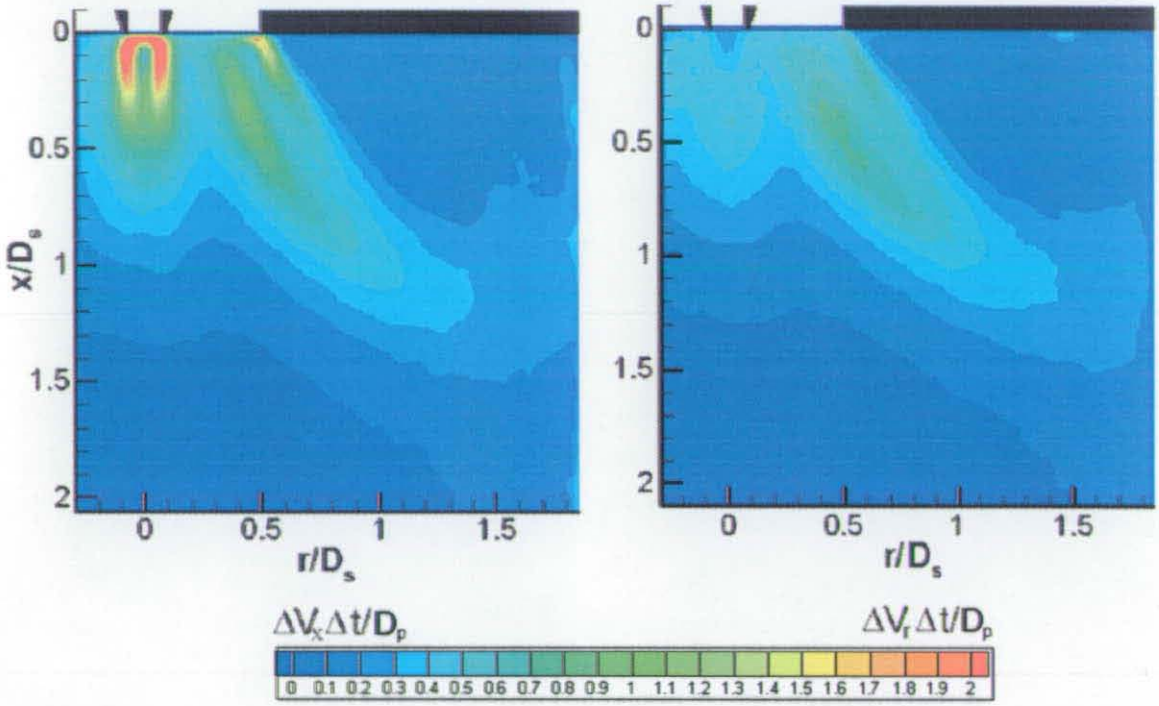

Figure 3.31. Axial [left] and Radial [right] Displacement Variation Contours for LFoV Region B

As Figure 3.31 shows, in regions of the jet and swirl stream shear layers the displacement variation across interrogation cells exceeded 1 particle image diameter. In the far-field ($x/D_s>1$) however, as velocity gradients reduced, displacement variation was insignificant. The loss of RMS data due to sub-grid filtering was again estimated by calculating the axial, $L^{x}_{v_x v_x}$ and radial, $L^{r}_{v_r v_r}$ length-scales as shown for measurement region B in Figure 3.32 and then applying the loss estimation curve (Figure 3.23) to the data, as shown in Figure 3.33.

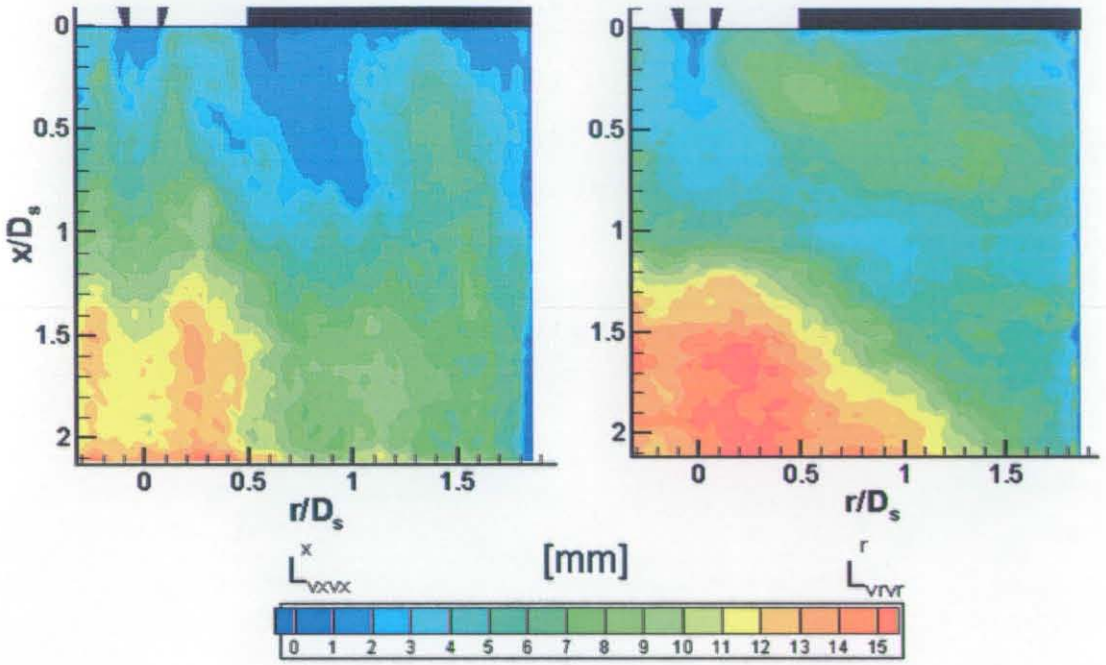

Figure 3.32. Axial [left] and Radial [right] Turbulent Integral Length-Scale Contours for Measurement Region B.

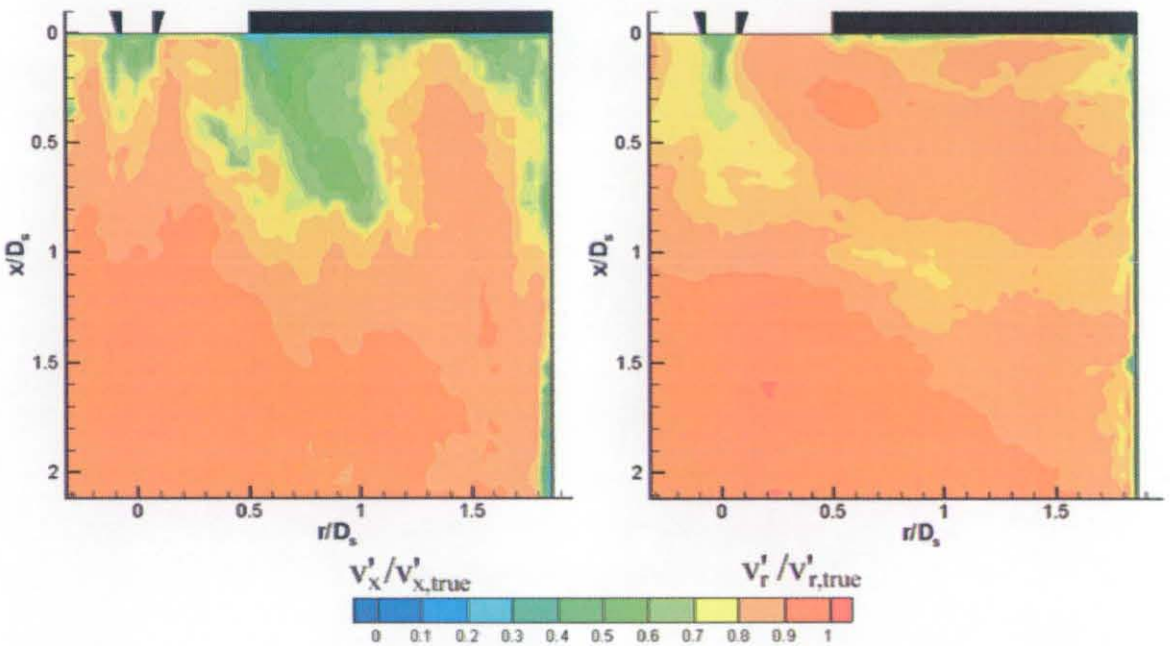

Figure 3.33 Axial [left] and Radial [right] RMS Velocity Error Estimate Contours for Measurement Region B

Figure 3.33 shows that in the near field the length-scales were small and, as indicated by the displacement variation contours, the interrogation cells were too large for accurate

assessment of RMS levels. However, it can also be seen that as the flow develops into the far-field $v_i'/v'_{i,true}>90\%$ (where the subscript i denotes either in-plane displacement).

It was therefore concluded that 2.13^2 FoVs' were suitable for accurate data capture in the far-field (measurement regions C-D) but not in measurement regions A-B where the optimisation parameters could not be met and spatial filtering was excessive. Therefore this data was only used for the assessment of instantaneous flow structures (criteria (i)). For accurate statistics an increased magnification was required. As Figure 3.30 shows good flow symmetry about the fuel injector centreline it was considered justifiable to concentrate measurements only on one side of the test section, therefore only Position B was segmented into four 1.06^2 FoVs' (B_o=40mm) which are shown in Figure 3.34 (labelled B1-B4) on a patched image (at 1.06^2 FoV resolution) with velocity vectors superimposed on axial velocity contours.

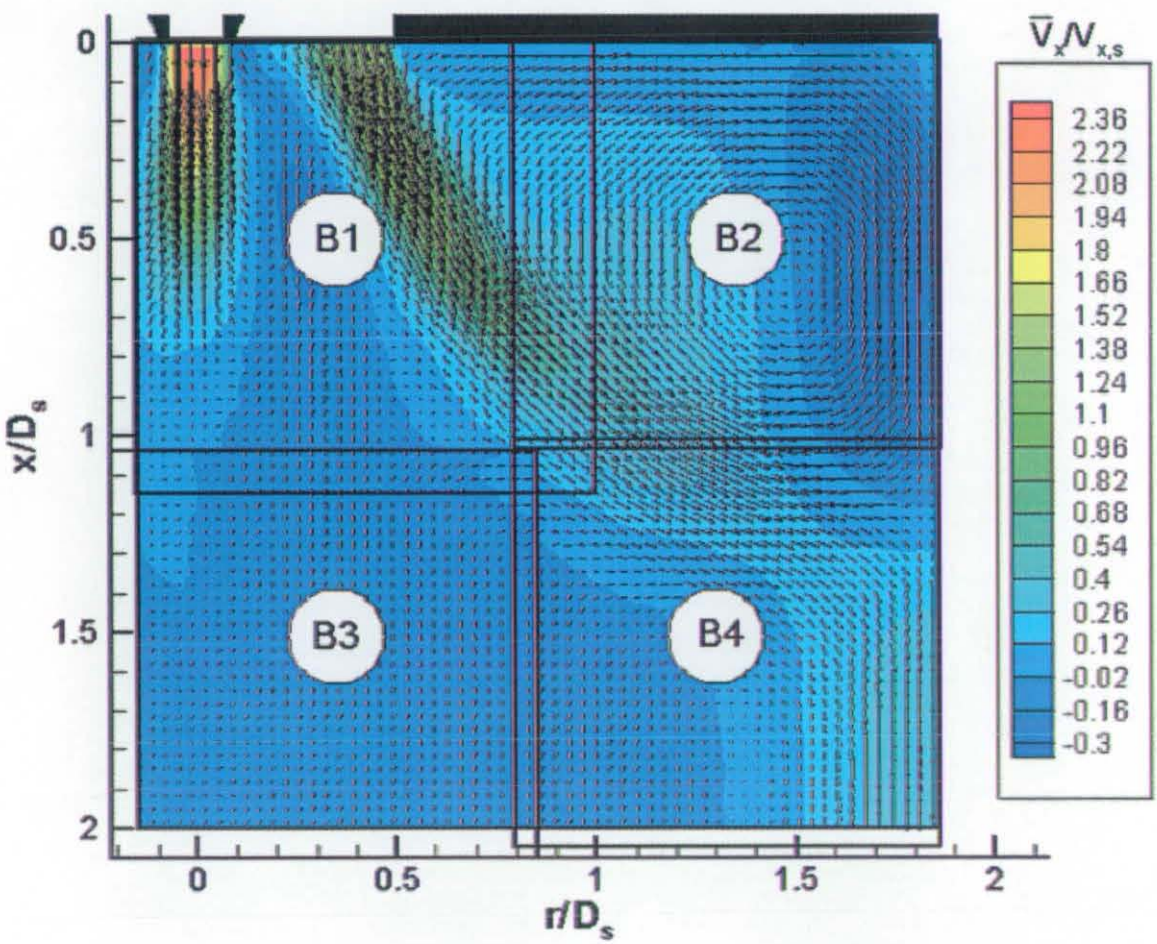

Figure 3.34 Location of 1.06^2 FoV Regions (B1-B4)

In measurement regions B2, B3 and B4 it was found that the image magnification allowed for acceptable in-plane particle displacements without excessive out-of-plane losses. However, in location B1 the inter-frame time was dominated by the peak central jet velocities and, in regions of slower moving fluid, the in-plane displacements were small. Calculation of the displacement variation across the interrogation cells showed $M\Delta V_i\Delta t/MD_p<1$ for all regions except in the very near field of the central jet (in Position B1). Sub-grid spatial filtering was also only significant in Position B1, and in all other regions $v_i'/v'_{i,true} > 90\%$ as shown on a composite image of the 1.06^2 data in Figure 3.35.

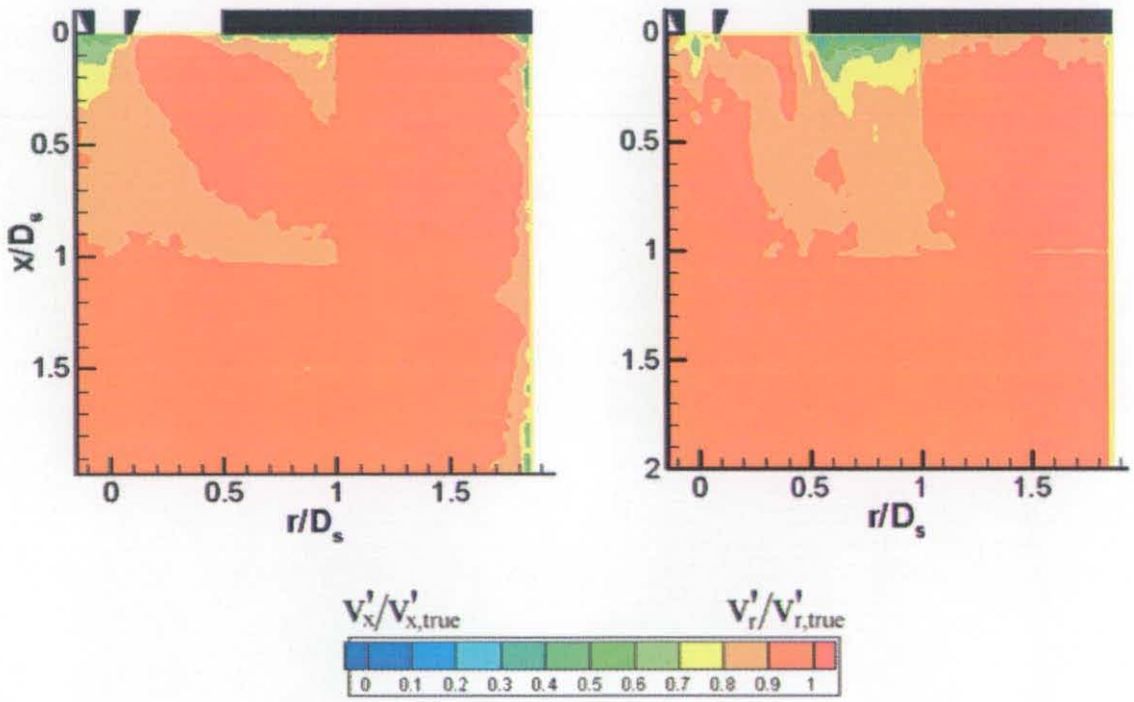

Figure 3.35. Axial [left] and Radial [right] RMS Velocity Error Estimate Contours for 1.06^2 Data

Therefore measurement region B1 was further segmented into four 0.53^2 FoVs' (B_0= 20mm). Figure 3.36 shows the location of the four regions labelled (B1i-B1iv) on a composite image (at 0.53^2 FoV resolution) with velocity vectors superimposed on axial velocity contours. For the no-jet test condition this third size FoV was not required and the 2.13^2 and 1.06^2 FoVs' allowed for the full optimisation of the system parameters in all x-r plane locations.

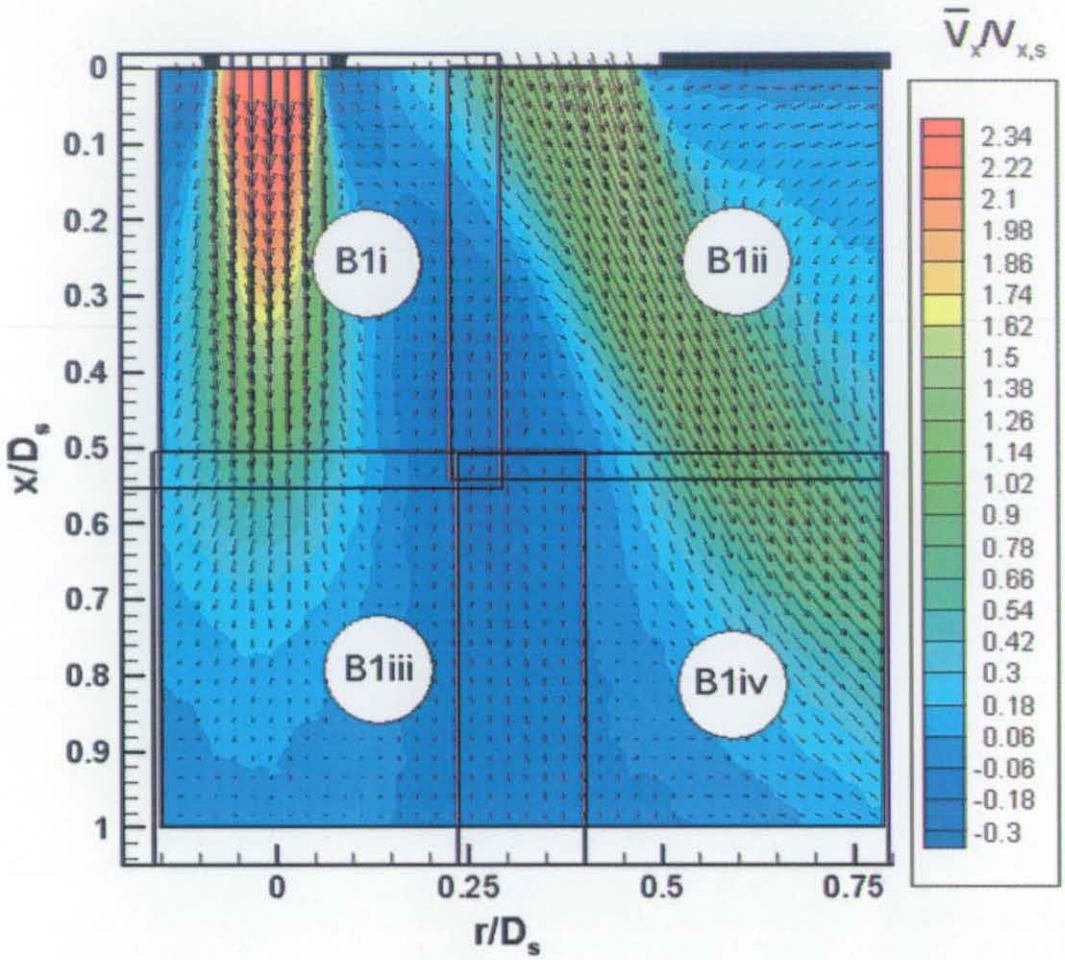

Figure 3.36. Location of 0.53^2 FoV Regions (B1i-B1iv)

The use of dx=0.63mm interrogation cells in the near field using this FoV size provided sufficient spatial resolution that the PIV system could be fully optimised whist minimising spatial filtering and $v_i'/v'_{i,true} > 90\%$ in all areas. Therefore, by use of 3 different size FoVs' the flow statistics could be accurately captured for the whole of the xr-plane for the main test condition. The affect of the FoV size on the radial profiles of mean and RMS axial velocity in the x-r plane at axial location $x/D_s=0.27$ is shown in Figure 3.37.

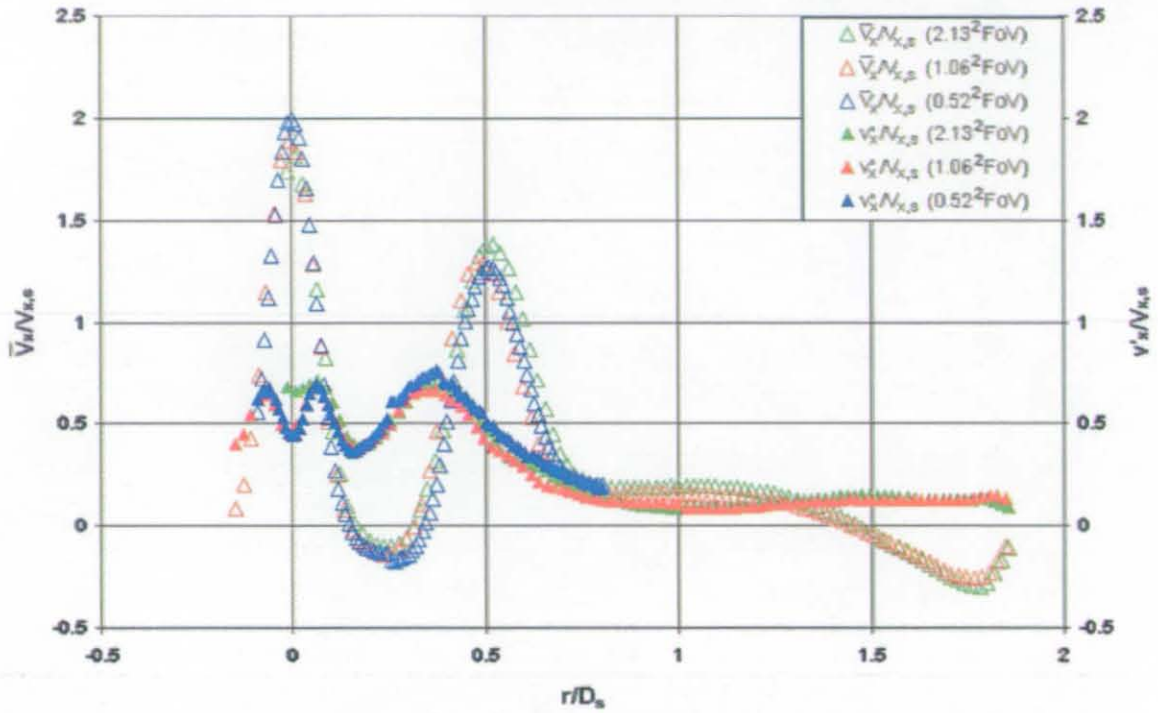

Figure 3.37. Mean and RMS Axial Velocity Profiles at x/D_s=0.27 for the Different Sized FoVs' for the Main Test Condition

As can be seen, the mean velocity profiles are broadly similar, however in terms of RMS data, as expected from spatial error estimates, the smallest FoV records the highest peak RMS levels. At the centreline the resolution of the 2.13^2 FOV is not sufficient to record the lower RMS levels towards the centre of the jet, as resolved by the smaller FoVs'.

3.4.11.3 Radial-Circumferential Plane

In the r-θ plane data was captured at several planes both within the fuel injector body at x/D_s=, -0.13, -0.27, -0.43, -0.53 and -0.80 and within the test section at x/D_s=0, 0.27, 0.53, 1.06 and 2.65. The axial locations of the measurement planes are shown in Figure 3.30. Measurements inside the fuel injector were taken using 1.06^2 FoVs', which was just sufficient to capture the entire diameter of the swirl stream. This FoV ensured good optimisation of the PIV system, Figure 3.38 shows the radial and circumferential non-dimensional displacement variation contours at x/D_s=0 (plotted in a Cartesian frame of reference). The location of the 1.06^2 FoV is shown around the radial displacement variation contours.

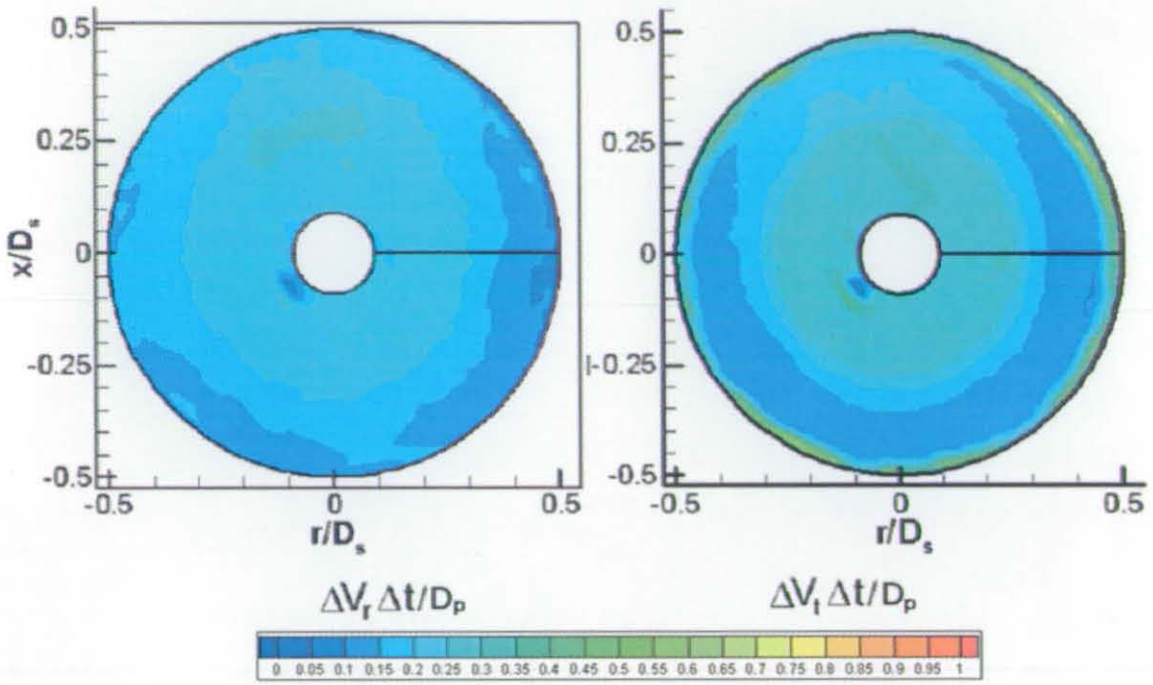

Figure 3.38 Radial [left] and Circumferential [right] Displacement Variation Contours at $x/D_s=0$ using a 1.06^2 FoV

As can be seen, the interrogation cell size is sufficiently small that the non-dimensional displacement variation is insignificant in all regions of the flow. This was found to be the case in all axial locations within the fuel injector body. Radial profiles of circumferentially averaged radial and circumferential integral length-scales calculated from a polar grid in radial and constant theta directions are shown in Figure 3.39.

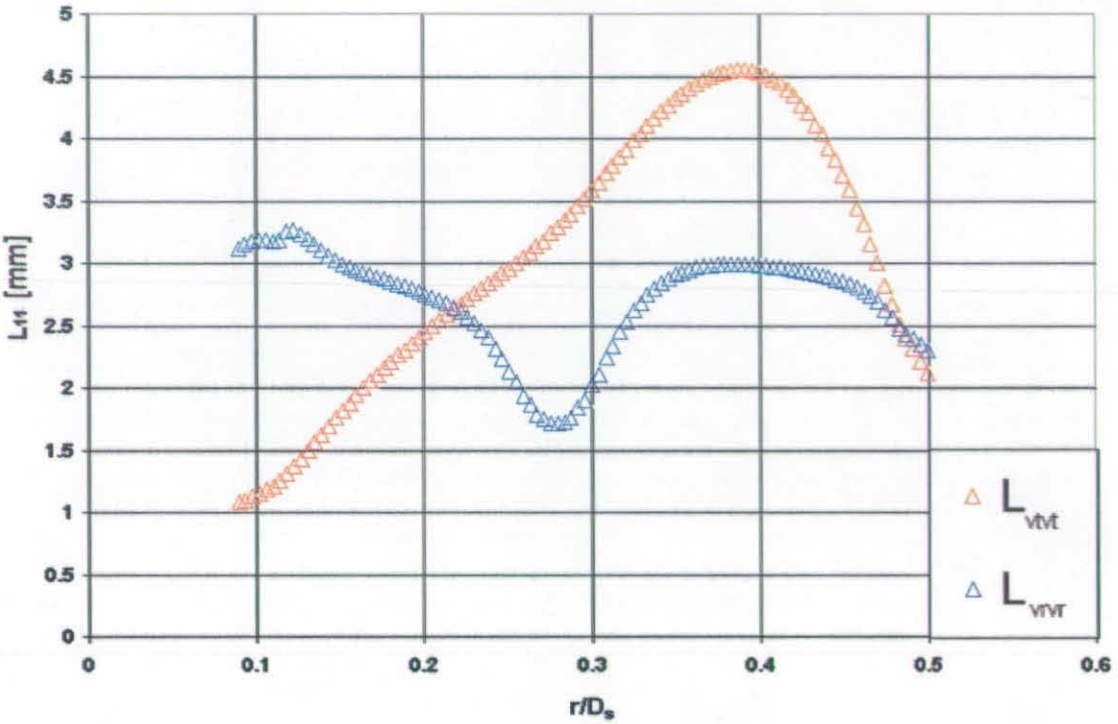

Figure 3.39. Circumferentially Averaged Turbulent Integral Length-Scales at $x/D_s=0$

In the circumferential direction at $r/D_s>0.25$ the length-scales were greater than 3mm resulting in $v'_t/v'_{t,true}>0.8$. This was also the case towards the swirl stream flow passage walls in the radial direction, however it is also apparent that radial length-scales become increasingly small to a minimum value at a radius of $r/D_s=0.26$. This was due to the presence of large-scale vortex structures rotating within in swirl stream passages; these are to be discussed in detail in Chapter 5.

In the dump area expansion chamber data was initially collected using a 3.72^2 FoV ($B_0=140$mm) to encompass the entire diameter, however using such large FoVs' several of the optimisation parameters could not be met. $MD_p/d_r<2$, ΔZ_0 was excessive at 2.5mm and with dx=4.8mm the in-plane particle displacements were of the order 0.1dx. However, due to much less severe velocity gradients in the r-θ plane the parameter $M\Delta V_i\Delta t<MD_p$ was still met, as shown at $x/D_s=0.27$ for both in-plane displacements, the location of the 3.72^2 FoV measurement region is around the radial displacement variation contours and the dashed line indicates the dump area expansion chamber outer wall.

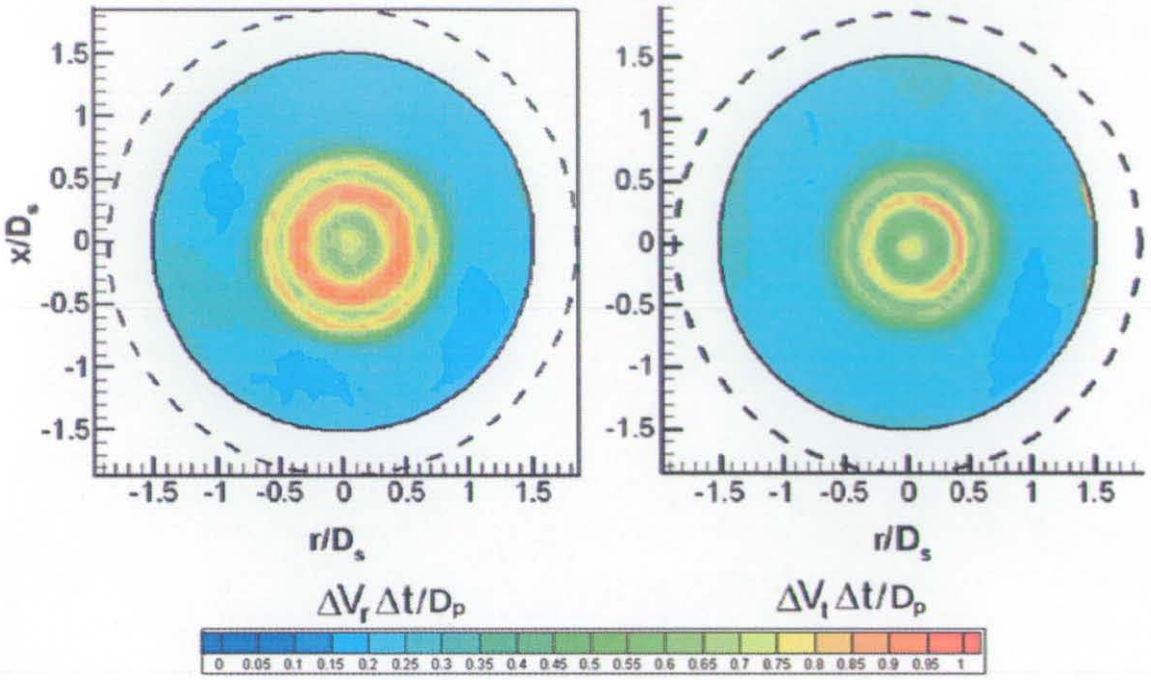

Figure 3.40. Radial [left] and Circumferential [right] Displacement Variation Contours for 3.72^2 FoV at $x/D_s=0.27$

Data could not be captured across the whole diameter due to interference with the corners of the downstream blockage, the largest radius captured was $r/D_s=1.5$ as indicated in Figure 3.40, the dashed line is the radial location of the test section wall. As the flow developed the velocity gradients diminished and displacement variation was even less significant at measurement planes with increased axial distance.

However, in order to improve the accuracy of the time-averaged statistics greater magnifications were required. As the camera was fixed in its orientation within the downstream blockage (see Figure 2.10), it was only possible to capture data symmetrically across the centreline of the test section. Therefore, Figure 3.41 shows the location of a 2.13^2 FoV inside the 3.72^2 FoV measurement region, these are superimposed on radial velocity contours of a "composite" image for the two sized FoVs'. The term composite refers to the following sequence:-

1. Generate a 3.72^2 structured mesh with a grid resolution similar to that of the data resolution of the 2.13^2 FoV (16dr/M=1.28mm).
2. Interpolate the 3.72^2 time-averaged statistics onto the mesh generated in (1) using a linear interpolation.

3. Interpolate the 2.13^2 FoV time-averaged statistics (using linear interpolation) onto the mesh (over-writing the 3.72^2 FoV data within the 2.13^2 region).

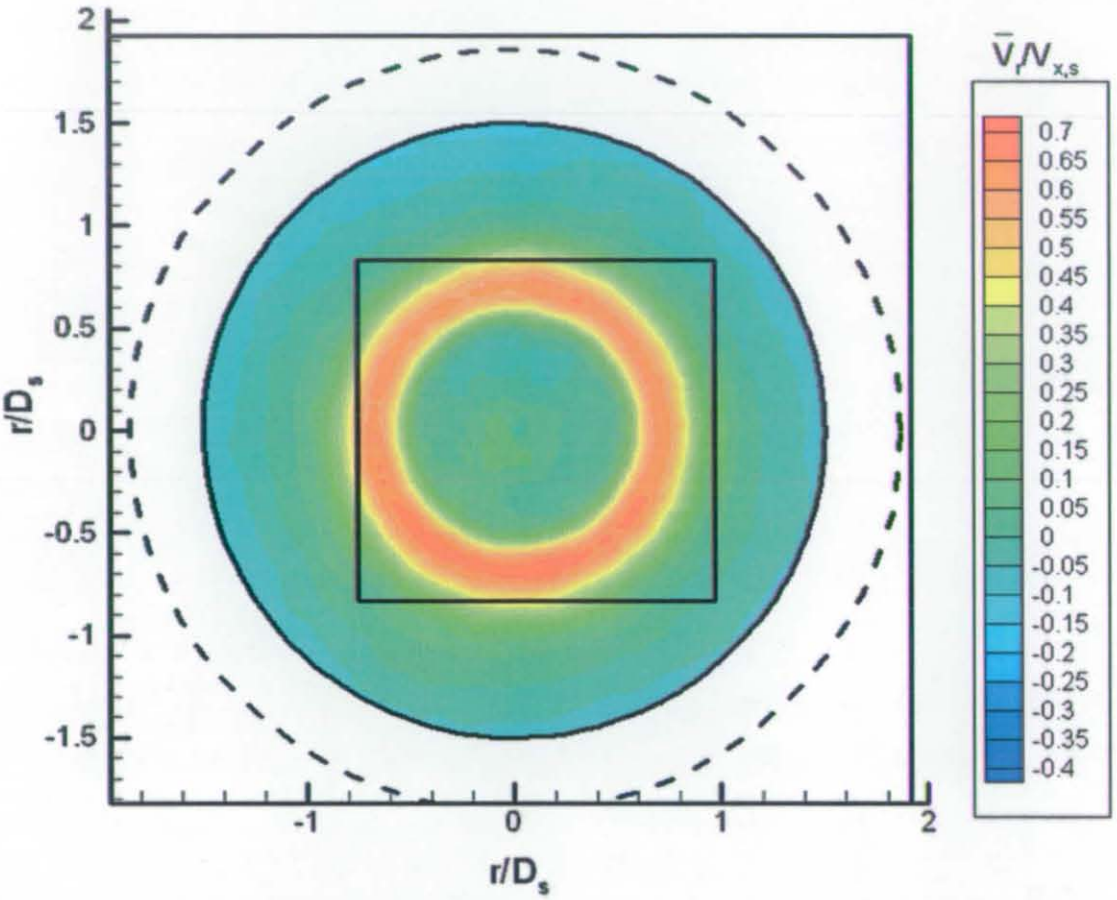

Figure 3.41. Positions of Measurement Regions in Dump Area Expansion Chamber in r–θ Plane Superimposed on Radial Velocity Contours at x/D_s=0.52

In these 2.13^2 measurement regions displacement variations were significantly less (in all constant axial planes measured) than shown in Figure 3.40 due to interrogation cells being approximately half the size. The parameters MD_p/d_r= 2, and $MV_i\Delta t$=0.25Mdx could also be adhered to, allowing for the full optimisation of the PIV system. Figure 3.42 shows circumferentially averaged radial and circumferential longitudinal turbulent integral length-scales at axial measurement location x/D_s=0.27.

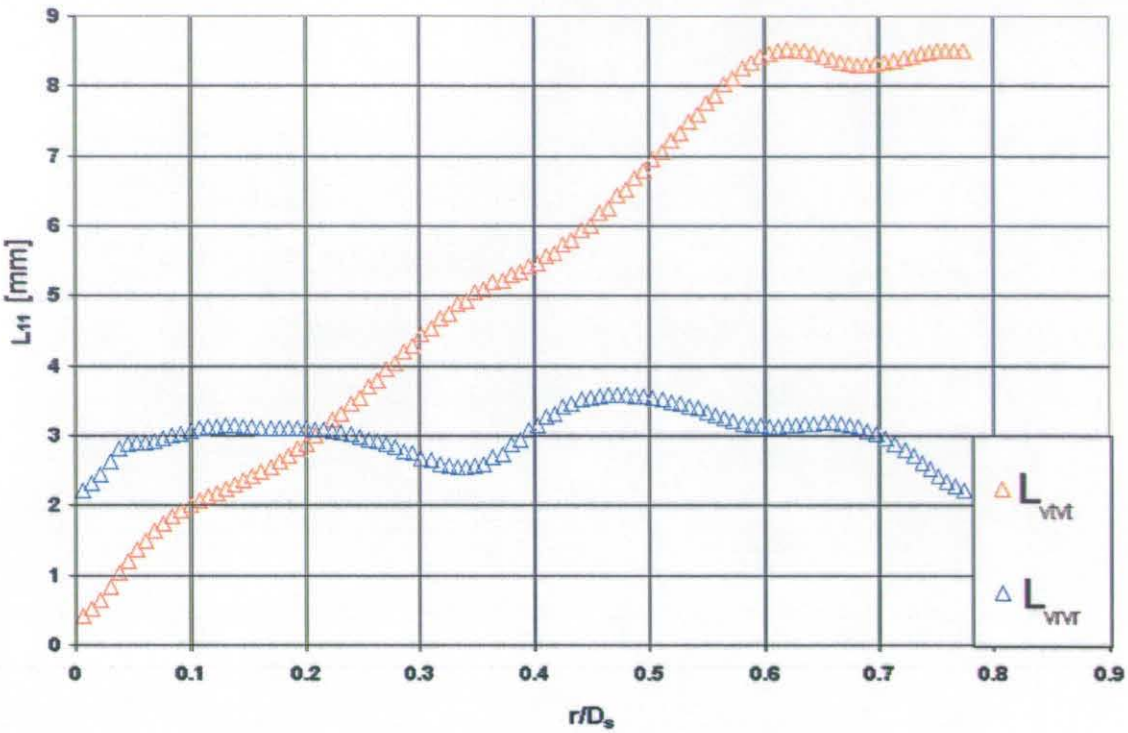

Figure 3.42. Turbulent Integral Length-Scales at x/D_s=0.27.

In the radial direction length-scales are close to 3mm resulting in $v'_r/v'_{r,true}$=0.80, however in the circumferential direction length-scales reduced to close to zero across the centreline, however this could not be avoided, at r/D_s>0.2, $v'_t/v'_{t,true}$>0.80. At increased axial distance the radial length-scales significantly increased, resulting in lower spatial averaging.

3.4.12 Summary of PIV Data Collection

The previous two sections have outlined a method for capturing the large-scale motions of the flow (with accepted errors) and for best possible optimisation of the system such that accurate time-averaged statistics could be measured despite the extremely adverse flow conditions and the constraints imposed by the limited location of the camera. Figure 3.43 below shows a summary of the PIV data captured for the datum fuel injector for both the main and no-jet test conditions. In this chart, information in red refers to LS-PIV and in blue to HS-PIV. The data captured using the modular swirler utilised similar sized FoVs' and hence similar optimisation procedures, however, the data collected depended on the modular configuration and is detailed as required.

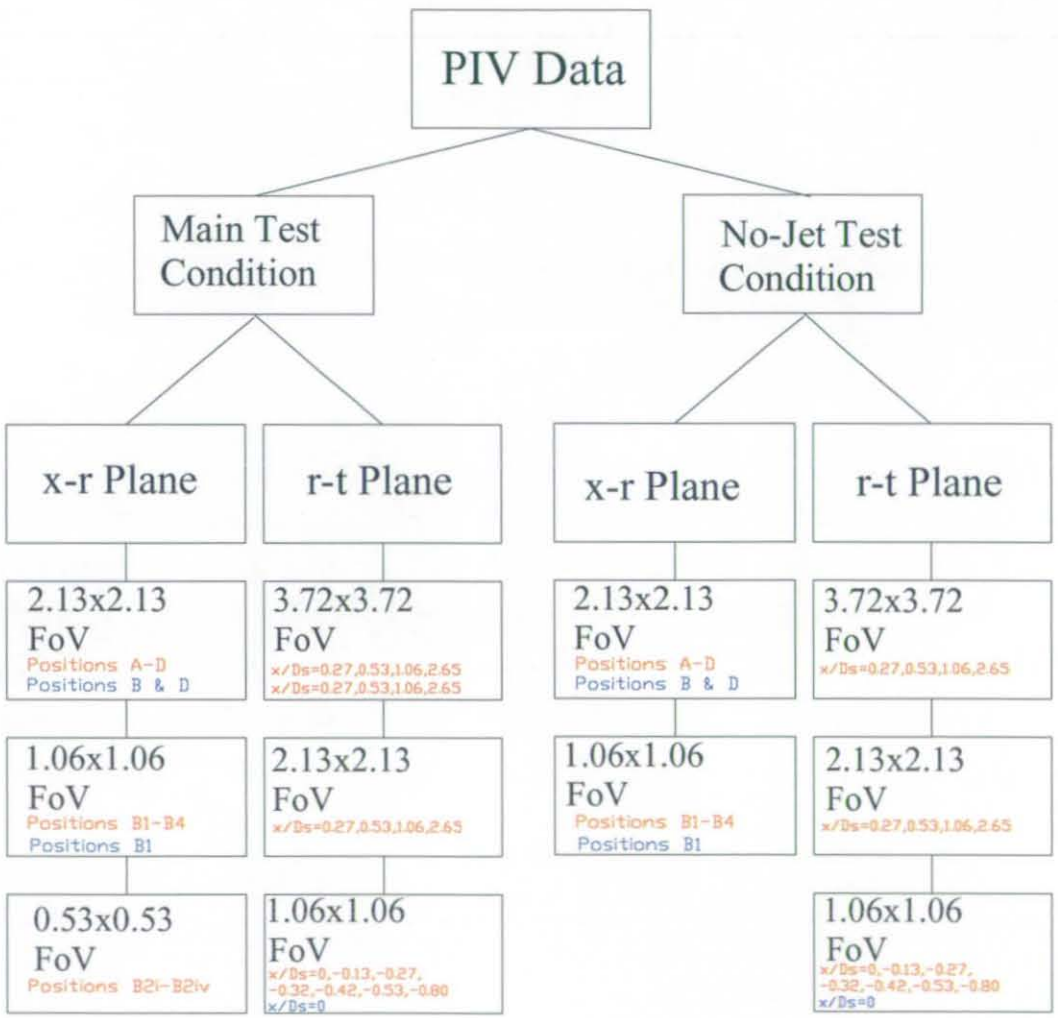

Figure 3.43. Data Collection Summary for Datum Fuel Injector

3.4.13 Creation of Single 3D Time-Averaged Data Sets

In order to make the optimised data sets more manageable a single composite data set that included all three velocity components was created for both the main and no-jet test conditions. In order to do this, initially a single x-r plane data set was created as follows:-

1. Create a grid of non-dimensional size 1.86×4.25 (dump expansion chamber dimensions) and set resolution similar to that of the smallest x-r plane FoV used.
2. Interpolate (via linear interpolation) the largest FoV data onto this grid.
3. Interpolate progressively smaller FoV data onto the grid overwriting the previous interpolated data within the area enclosed by the smaller FoVs.

Figure 3.44 shows time-averaged axial velocity contours in an x-r plane for the full dump area expansion chamber which now contains only optimised data. The boundaries of the FoVs' used to create the full x-r plane data set are superimposed in black.

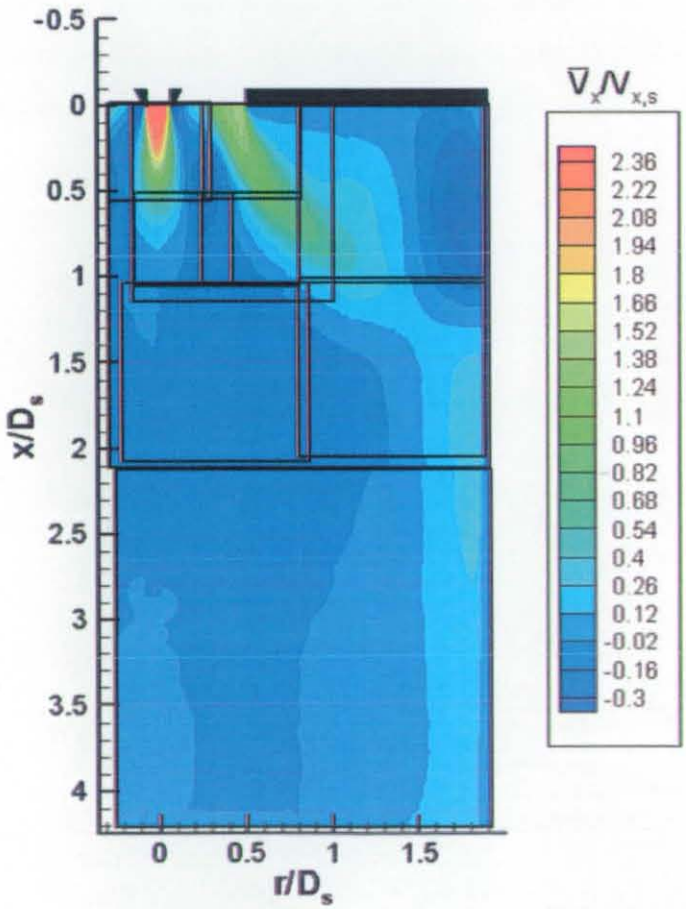

Figure 3.44. FoV Boundaries Superimposed on Mean Axial Velocity Contours for the Optimised x-r Plane Data (Main Test Condition)

In order to include the time-averaged r-θ plane data, firstly the data was transformed into cylindrical polar velocities in a cylindrical polar frame of reference (as described in Section 3.4.9). All constant theta lines were then averaged to create circumferentially averaged radial profiles of radial and tangential velocity for each axial measurement location. The circumferentially averaged radial profiles of circumferential velocity were then interpolated on to the full x-r plane data set (at the correct x/D_s measurement location). In order to provide a best estimate to the tangential velocity in regions between the axial measurement locations a kriging algorithm, available using Tecplot v8 (1998) software was used to interpolate onto the surrounding grid points. From this optimised time-averaged data set of all three velocity components a 3D representation was created by rotating the data in the theta direction.

3.4.14 Data Validation

In order to validate the PIV data, measured velocity profiles were compared to LDA measured velocity profiles. As the LDA technique measures the motions of individual particles there are no spatial averaging effects, so it could be assumed that the RMS would be representative of the true value. A comparison of radial profiles of mean and RMS axial and tangential velocity at $x/D_s=0.27$ are shown in Figure 3.45 and Figure 3.46 respectively.

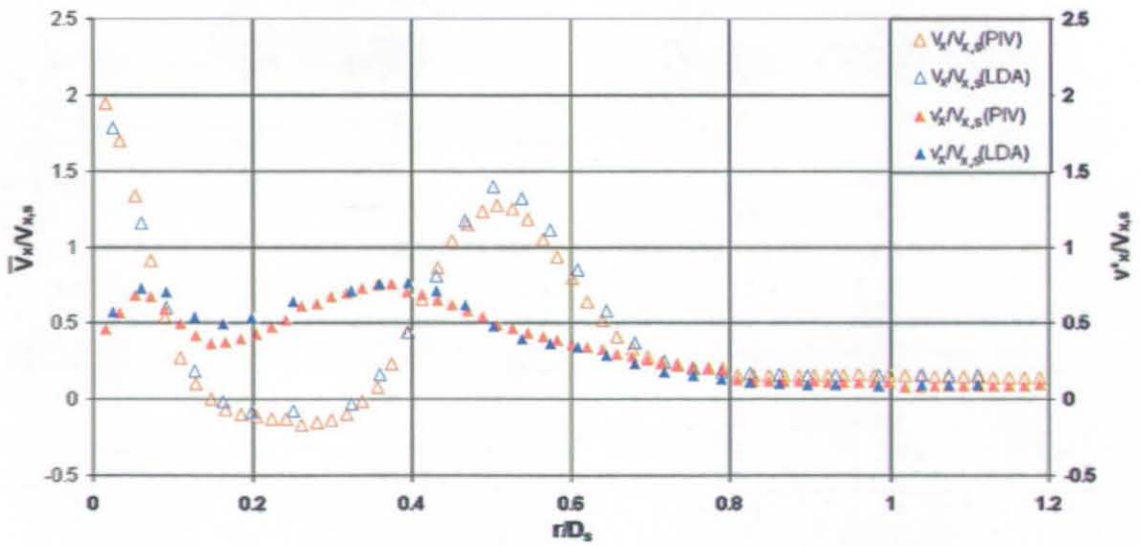

Figure 3.45. Mean and RMS Axial Velocity Profiles Measured at $x/D_s=0.27$

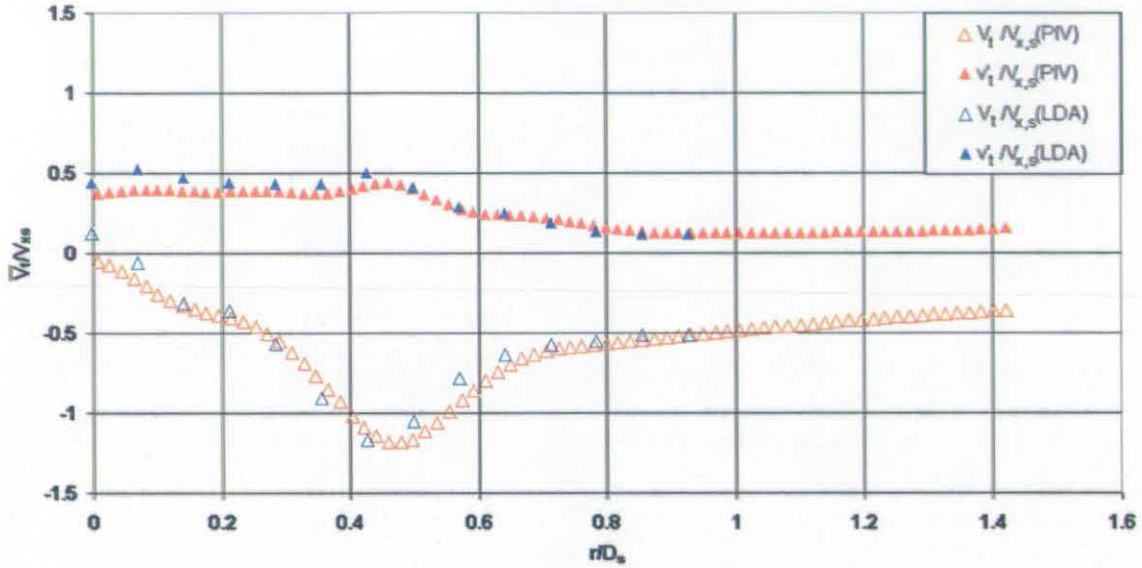

Figure 3.46. Mean and RMS Circumferential Velocity Profiles Measured at $x/D_s=0.27$

As can be seen, there is good agreement between the two measurement techniques in both velocity components for both mean and RMS velocity profiles. This was found to be the case at all axial measurement locations, thus validating the optimised full 3D PIV data set and indicating that spatial averaging effects were not significant.

3.5 Planar Laser Induced Fluorescence.

Planar Laser Induced Fluorescence (PLIF) utilises an LSI system to provide spatially resolved instantaneous concentration by measuring the fluorescent emission of a molecular seed introduced into the flow. By careful calibration (see Section 3.5.3) this emission is directly proportional to the local species concentration. Fluorescence is the transition of an electron from an excited energy state back to its ground energy state by spontaneous light emission. The initial excitation of the electron is caused by absorption of photons from the incident light sheet and the fluorescence always occurs at a longer wavelength than the incident light due to energy loss in the excited state. A comprehensive description of fluorescence is provided by Pringsheim (1949).

CW lasers such as argon-ion can be used as the incident light source in combination with tracers such as Fluorescien, Walker, (1987) or Rhodamine B, Behrouzi and McGuirk (1996). However, pulsed lasers have been shown to be much more effective for PLIF measurements due to the much greater available power densities, significantly improving

the SNR (where SNR for PLIF is defined as the ratio of the fluorescent response to the background noise level). Short pulse lengths are also more suitable for the capture of structures with small timescales. PLIF has been successfully used with pulsed lasers to measure concentration fields by Guilard *et al* (1998), Criminaldi and Koseff (2001), Westerveel *et al* (2002) and Webster *et al* (2003) and to measure temperature by Sakakibara and Adrian (1997), Lemonine *et al* (1999) and Coolen *et al* (1999).

3.5.1 Molecular Flow Seeding

The molecular flow seeding chosen for the PLIF measurements was Rhodamine B (chemical equation $C_{28}H_{31}ClN_2O_3$) which is a solid with a molar mass of 479. Rhodamine B is a particularly suitable tracer for the measurement of instantaneous concentration fields in aqueous solution due to its high solubility and stability in water, Arcoumanis *et al* (1990). Its low molecular diffusivity results in a high Schmidt number of approximately 2740 as measured by Reid *et al* (1986) where the Schmidt number is defined as the ratio of the diffusion of momentum to the molecular diffusion of the tracer:-

$$Sc = \frac{\nu}{d_f}$$

A high Schmidt number implies suitability for the measurement of passive scalar concentrations, i.e. the tracer will follow the turbulence field.

Rhodamine B has a peak fluorescent emission wavelength of 580nm (orange) which is suitably separated from the initial excitation wavelength of the incident light sheet of 532nm (green). In order to separate the incident light from the fluorescent signal a Corion 550±10nm "cut-on" filter was fixed in front of the camera lens. The absorption / fluorescence spectra of Rhodamine B are shown in Figure 3.47.

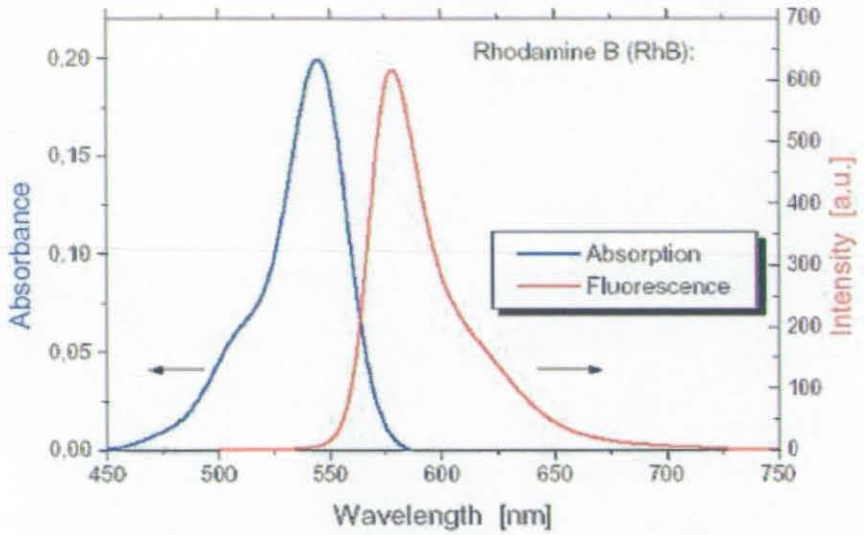

Figure 3.47 Absorption/Emission Frequency Spectra for Rhodamine B, Melton and Lipp (2003)

A 550±10nm filtered photograph of the main test condition with a Rhodamine B seeded central jet flow under excitation from the 532nm incident light is shown in Figure 3.48.

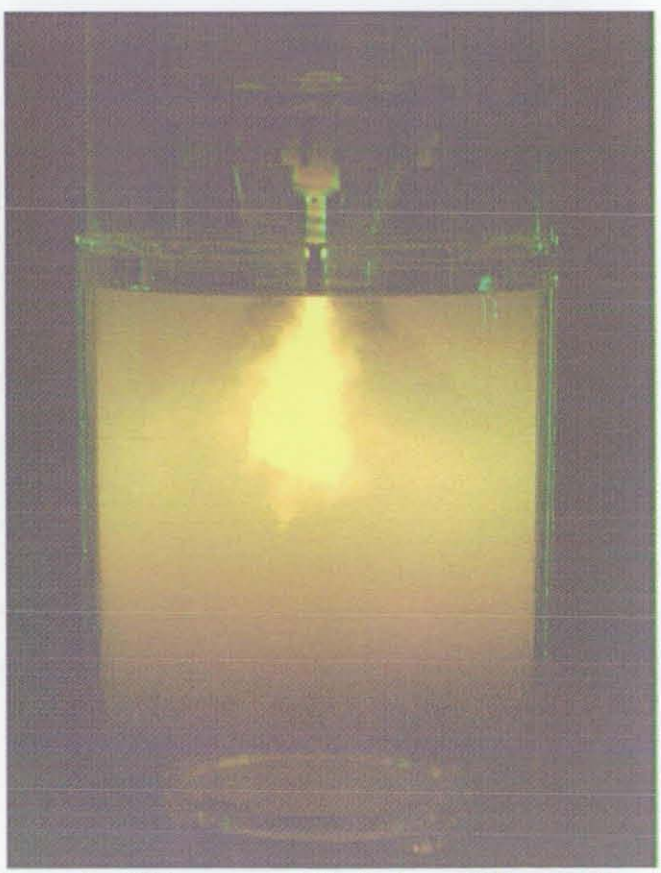

Figure 3.48. Photograph of Fluorescent Emission of Rhodamine B under Excitation of 532nm Light using a 550nm Filter

3.5.2 Experimental Set-up

For the PLIF experiments the LS-LSI system was utilised to calculate the time-averaged statistics, where both 50mJ Nd:YAG lasers were fired in tandem to provide pulses of 532nm wavelength light with a pulse length of 9ns. As the unfocused beam diameter was 3.5mm the power density was calculated to be $115.54 \times 10^{10} W/m^2$. The light sheet was created using a cylindrical lens of focal length -20mm (equating to a divergence angle of 10°) positioned 265mm from the test section centreline with a focused beam waist thickness of approximately 1mm. The divergence angle was chosen such that the light sheet only just illuminated the whole of a 1.6^2 FoV. The size of the FoV was limited to a maximum area of 1.6^2 in order to avoid the requirement of larger beam divergences which would reduce the light sheet power density across the measurement region. By maintaining a high power density the maximum tracer concentration could be reduced, this ensured that the system was close to "optically thin", a property that was essential for accurate PLIF measurements (as described in detail in Section 3.5.3). The f-number of the camera was set at a minimum value of 1.8 in order to allow the maximum possible amount of light into the camera (to maximise the SNR) which in conjunction with the image magnification used of M=0.15 provided an acceptable camera depth-of-field of 0.4mm.

The LS-LSI system Kodak ES1.0 camera was used to capture the images with 8-bit resolution allowing the light intensity to be measured on a scale of 0-256 "counts". With a pixel width of 9μm, a 1.6^2 FoV provided a spatial resolution of 60μm per pixel (dr/M=9μm/0.15). A measure of the smallest scales of turbulence is provided by calculation of the Kolmogorov length-scales, hence to resolve the concentration field fully a spatial resolution less than the Kolmogorov length-scale is required ($dr/M < L_\eta$). Figure 3.49 shows the Kolmogorov length-scale contours, L_η calculated from LS-PIV measurement region B. The methodology for the calculation of the Kolmogorov length-scales for a PIV data set is described in Chapter 4.

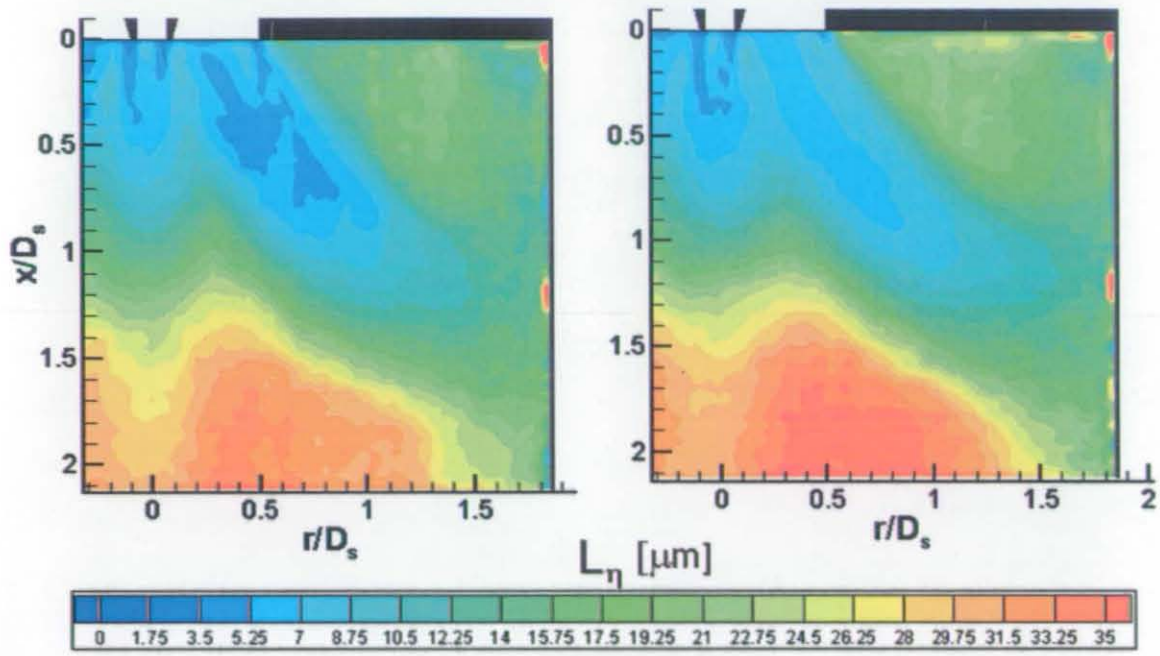

Figure 3.49. Axial [left] and Radial [right] Kolmogorov Length-Scale Contours for the Main Test Condition

Thus, in the fuel injector near field a spatial resolution of approximately 2μm would be required resulting in an image magnification of 4.5. This was out of the range of image magnifications possible with the available lenses (Figure 3.6) and would result in an unfeasibly small FoV of 0.5mm^2 (approximately the size of an LDA measurement volume). Whilst this non-resolution of the Kolmogorov length-scales would lead to a smearing of the smallest scales on the image plane, the turbulent transport phenomena are governed by the large-scale motions, so analysis of the turbulent transport of scalar concentration should not be affected.

3.5.3 Image Calibration

The equation that is commonly stated in PLIF literature to quantify the relationship between the measured fluorescence signal, S and local species concentration, C is that of Paul *et al* (1990):-

$$S = IA\Phi C$$

Where I is the intensity of the excitation beam at the point in question, Φ is the quantum efficiency (defined as the ratio between the emitted and the absorbed energy) and A is a

pixel-by-pixel efficiency parameter for the conversion of photon energy into signal output on the CCD chip. Whilst using CW lasers (where power densities are a lot lower than pulsed lasers) this linear relationship is easily obtained, with pulsed lasers such a large fraction of the fluorescent molecules may be raised to the upper excited energy state and the fluorescence signal may no longer remain linear with incident power, as found by Melton and Lipp (2003) and Shan *et al* (2004). Therefore careful calibration is required to ensure that the system operates within the linear range. The above equation can be rewritten for a pixel location (p_i,p_j) corresponding to an in-plane location (i,j) where the i-direction is the beam propagation direction and the j-direction is perpendicular to i:-

$$S(p_i, p_j, t) = I(i, j, C, t).A(p_i, p_j).\Phi.C(i, j, t) + I_{back}(p_i, p_j, t) + bI(p_i, p_j, t)$$

The additional terms I_{back} and bI account for the contribution of the background noise level and the portion of the incident light that "bleeds through" the cut-on filter. When applied to a uniformly mixed concentration field, C_{ref} this equation becomes:-

$$S_{ref}(p_i, p_j, t) = I(i, j, C_{ref}, t).A(p_i, p_j).\Phi.C_{ref} + I_{back}(p_i, p_j, t) + bI(p_i, p_j, t)$$

The reference measured signal, S_{ref} is a function of time due to possible pulse to pulse variations in the light sheet intensity and temporal variations the background noise level. Therefore a time-average is taken to remove this dependence to produce $\overline{S_{ref}}(p_i, p_j)$. If images are captured in a solution containing no tracer, i.e. C_{ref}=0, the total contribution of I_{back} and bI can be assessed, denoted I_{dark}:-

$$I_{dark}(p_i, p_j, t) = bI(p_i, p_j, t) + I_{back}(p_i, p_j, t)$$

Again I_{dark} is only a function of time due to possible pulse-to-pulse variations in the light sheet and background, again this is eliminated by time-averaging to produce, $\overline{I_{dark}}(p_i, p_j)$. The non-dimensional instantaneous concentration field can then be found from:-

$$\frac{C(i,j,t)}{\overline{C_{ref}}} = \frac{S(p_i,p_j,t) - \overline{I_{dark}}(p_i,p_j)}{\overline{S_{ref}}(p_i,p_j) - \overline{I_{dark}}(p_i,p_j)}$$

As Φ and $A(p_y,p_z)$ are independent of species concentration and time they have cancelled from the equation, however $C/\overline{C_{ref}}$ is only accurate if the instantaneous incident light sheet matches the time-averaged incident light sheet using a uniform concentration, $I(i,j,C,t) = \bar{I}(i,j,C_{ref})$. Clearly due to pulse to pulse variations in the incident light sheet intensity the time-averaged and instantaneous quantities will never exactly match however, this assumption is reasonable as the standard deviation of the light sheet variation was calculated at less than ±5%.

In both i and j directions, laser intensity variations will occur due to the Gaussian intensity profile of the light sheet, lens aberrations, interference of the light sheet by imperfection in the test section walls and increases in the beam cross-sectional area as the light sheet diverges, but these effects are independent of species concentration and will be the same for instantaneous and reference concentration fields. However in the beam propagation direction (the i-direction) light sheet absorption will occur according to the Beer-Lambert law:-

$$I(i) = I(i=0).\exp\left[-\int_0^i \varepsilon C(i)di\right]$$

Where ε is known as the extinction coefficient of the tracer. To ensure a weak absorption the argument of the exponent needs to be as small as possible, i.e. minimise the species concentration; however, reducing the species concentrations reduces the SNR. Therefore, to assess the optimum maximum species concentration (that provided an adequate SNR without resulting in significant light sheet absorption in the beam propagation direction) a calibration box was created directly above the test section (but still within the region enclosed by the water jacket) by sealing a plate onto the spigotted flange used to hold the fuel injector in position. For details of the location of the flange in the water rig see Figure 2.11. The calibration box is shown in Figure 3.50. The 1.6^2 FoV used is marked

by the red square, the light sheet divergence (created by the -20mm focal length cylindrical lens) is shown, which is just sufficient to illuminate the measurement region.

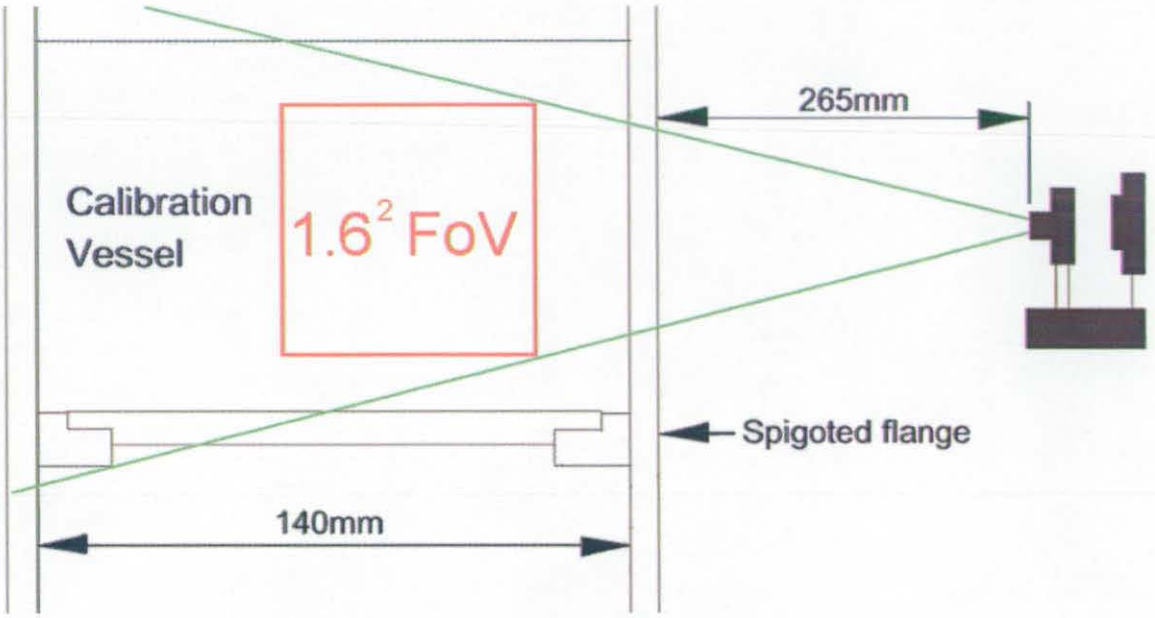

Figure 3.50. PLIF Calibration Vessel

The calibration box was initially filled with 2 litres of un-dyed water and 200 images of this zero tracer concentration (C_{ref}=0) were captured and time-averaged to provide a value for $\overline{I_{dark}}$. In order to increase incrementally the Rhodamine B concentration in the calibration box, a stock solution was created. This was achieved by dissolving 2.0g of Rhodamine B into 1 litre of water, thus creating a 4.18×10^{-3} mols/l concentration, to reduce the concentration further, 1.0ml of this solution was added to 1.0 litre of water, creating a stock solution of 4.18×10^{-6}mols/l (2.0mg/l). Therefore, the reference concentration in the calibration box could be increased in steps of 1.04×10^{-8} mols/l (5µg/litre) with the addition of 5.0ml of the stock solution. 200 images were then captured and time-averaged, for species concentrations ranging from 1.04×10^{-8}–1.04×10^{-7} mols/l. The dark-field image was then subtracted from all of the time-averaged fluorescent intensity images and all of the j-rows (0-975) were averaged to create one single intensity profile for each concentration as a function of beam propagation distance (i) as shown in Figure 3.51.

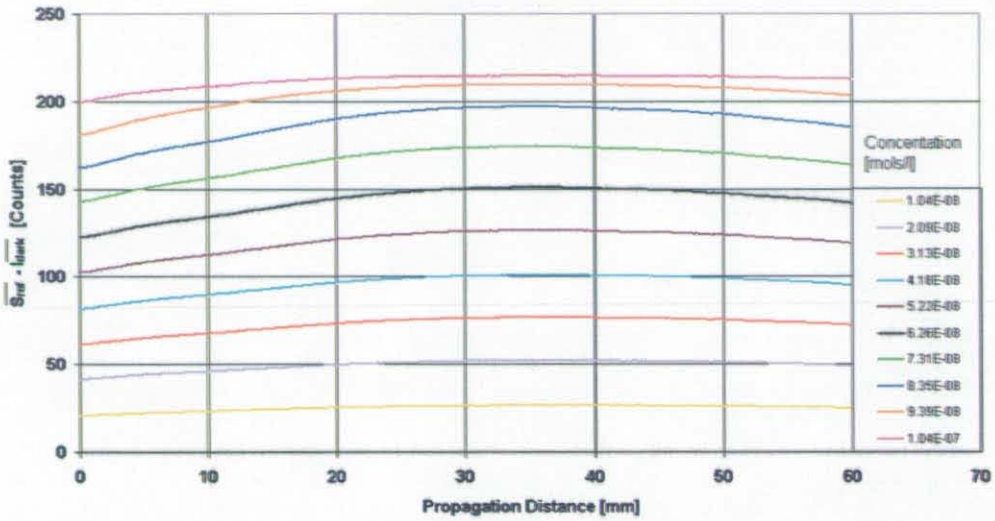

Figure 3.51 Measured Fluorescence Intensity as a Function of Beam Propagation Distance

This figure clearly indicates that the CCD chip becomes saturated, i.e. $\overline{S_{ref}}$ approaches 256 at species concentrations greater than 8.53×10^{-8}mols/l. It may be noticed that there is an initial increase in the measured fluorescence intensity, this is a direct contradiction of the Beer-Lambert law. This phenomenon has been previously identified by Karasso and Mungal (1997) and is currently unexplainable. However, it is not significant to the accuracy of the concentration calculations here as the profiles appear to be similar irrespective of the reference concentration. The similarity of the profiles at species concentrations less than 8.53×10^{-8}mols/l is proven by dividing each profile by the profile where $C_{ref}=8.35\times10^{-8}$mols/l, as shown in Figure 3.52.

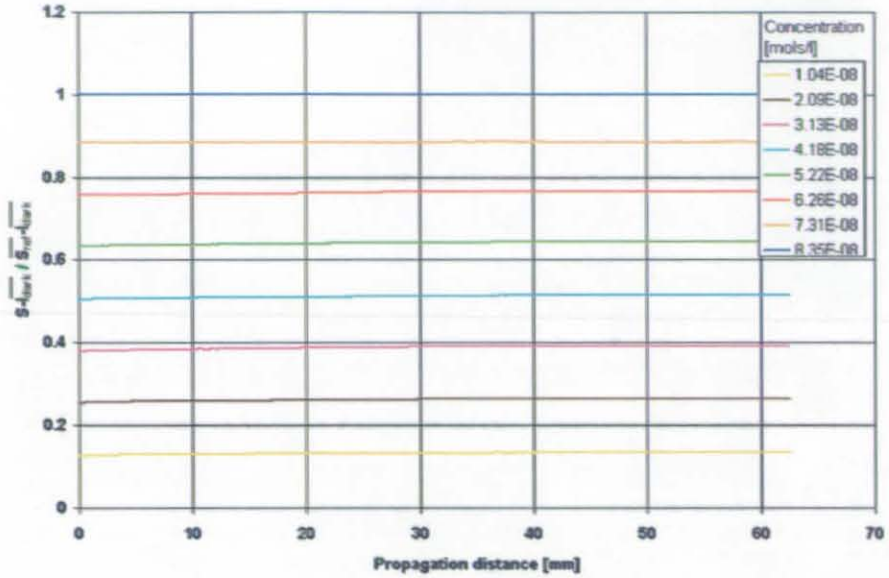

Figure 3.52 Non-Dimensional Measured Fluorescent Intensity as a Function of Beam Propagation Distance.

The profiles now become flat, thus proving that with species concentration less than 8.35×10^{-8}mols/l the absorption of the incident light sheet is negligible. A graph of non-dimensional measured fluorescent intensity against non-dimensional species concentration is shown in Figure 3.53.

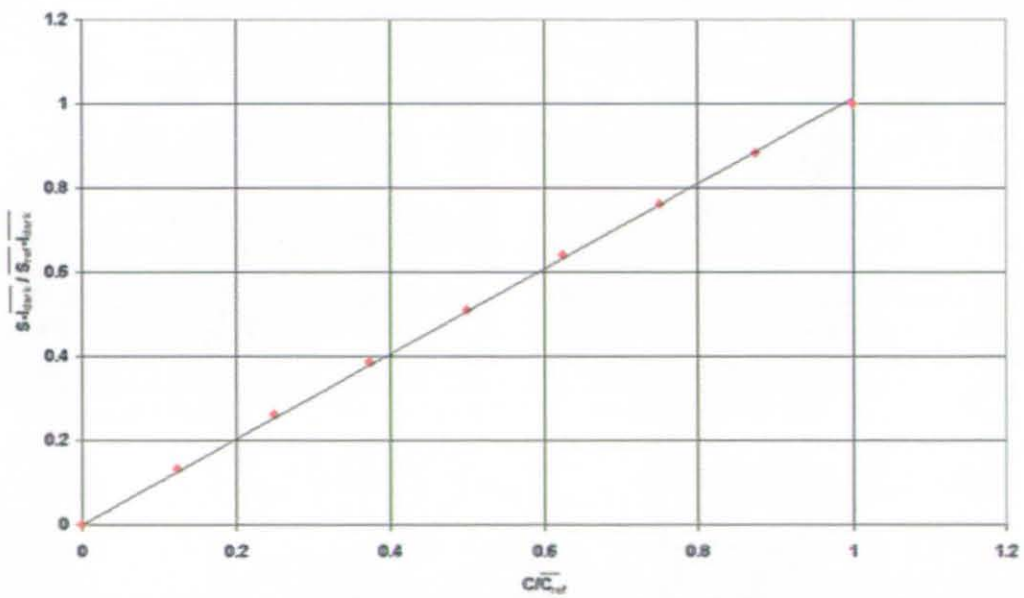

Figure 3.53. Non-Dimensional Measured Fluorescence Intensity as a Function of Non-Dimensional Species Concentration.

As required, there is a linear relationship with a gradient of 1 thus validating the methodology and allowing for the accurate calculation of $\frac{C}{C_{ref}}$ from the measurement of $\frac{S(p_i,p_j,t)-\overline{I_{dark}}(p_i,p_j)}{\overline{S_{ref}}(p_i,p_j)-\overline{I_{dark}}(p_i,p_j)}$.

By using a concentration of 8.35×10^{-8}mols/l the maximum measured intensity would be approximately 200 counts resulting in a measurement resolution of $4.18\text{x}10^{-10}$ (mols/l)/count or incidental steps in concentration of 0.5%. This was the operating condition that was used for all the PLIF test results reported in Chapter 5.

3.6 Closure

In this chapter the LDA and HWA systems that were used have been described, followed by a general description of LSI systems. It has been argued that PIV is susceptible to several forms of inaccuracy, which in general may be alleviated with increased image magnifications, however, the larger the image magnification the smaller the measurement region and the less effective the measurements are at assessing the large-scale flow structures. Therefore a methodology has been described that used initially large measurement regions to assess the large-scale flow features, then, in regions of the flowfield where the large measurement regions could not be fully optimised, smaller FoVs', based on the local flow conditions, were used to measure accurate statistics. This allowed for the whole of the x-r plane (including the centreline) and several r-θ planes to be accurately assessed. This data was then amalgamated onto one common grid and rotated to create a representative 3D data set of the optimised time-averaged statistics for both the main and no-jet test conditions.

For PLIF measurements Rhodamine B was shown to be a suitable molecular tracer for scalar concentration measurements. In order to calculate the whole-field concentration measurements accurately, careful optimisation was required to ensure a linear relationship existed between the measured signal and the species concentration and that the system was close to optically thin (whilst maintaining an acceptable SNR). This was achieved by maximising the laser power density in the measurement region and optimisation of the maximum species concentration. It was also shown that to resolve the smallest scales of mixing would require a pixel resolution smaller than the local

Kolmogorov length-scale, which in the fuel injector near field would have resulted in measurement region of order $0.5mm^2$ which was clearly impractical. However the turbulent transport phenomena would be governed by the large-scale motions, therefore a measurement region was chosen that was large enough to assess these large-scale motions, but which did not require an excessive beam divergence was chosen.

4 DATA REDUCTION

From the velocity and scalar field data collected several methods have been employed to deduce quantitative statistical information about the flowfield. The capture of single-point time-histories has been possible for many years via experimental techniques such as HWA and LDA. Hence point time-history data processing practices form the bases of the vast majority of data presented in the published literature with regard to turbulent flows and form the corner stone for RANS CFD methods validation. Single-point statistics are described first in Section 4.1. However, single-point statistics provide only limited insight into the turbulent flow structure. Using the spatially and temporally resolved LSI technique, Section 4.2 describes methods of quantifying aspects of the largest scale turbulence motions including the calculation of spatial velocity correlations and turbulent integral length-scales. Section 4.3 then describes methods for the identification and visualisation of the largest instantaneous turbulent flow structures using a swirling strength algorithm and a Singular Value Decomposition (SVD) approach. In order to create a time-averaged representation of the large-scale turbulence structure, conditional averaging and rotational averaging have been used. Proper Orthogonal Decomposition (POD) was then applied to ascertain information on the most energetic flow structures contributing to the flowfield.

4.1 Single-Point Statistics

A fundamental property of a turbulent flow is that the velocity field varies in both space and time, i.e. it is a stochastic value. Several methods are used to characterise its nature based on single-point statistics.

4.1.1 Reynolds Decomposition

Any parameter that is a function of time and is captured over a sufficiently long time-history (and whose behaviour corresponds to a statistically stationary process) can be separated into a time-independent mean component and a time-dependent fluctuating component; this is known as Reynolds decomposition:-

$$V(\mathbf{x},t) = \bar{V}(\mathbf{x}) + v(\mathbf{x},t)$$

Where

$$\overline{V}(\mathbf{x}) = \lim_{T\to\infty} \frac{1}{T} \int_{t}^{t+T} V(\mathbf{x}, t)dt$$

The overbar denotes a time-average. For experimental measurements where a number of sample data points (N) are collected at discrete time instants (t_k) the time-average is calculated by a summation over the number of samples:-

$$\bar{V}(\mathbf{x}) = \frac{1}{N} \sum_{k=1}^{N} V(\mathbf{x}, t_k)$$

Clearly it will be necessary to establish how long the sample size (N) needs to be to contain a sufficiently long number of statistically independent samples. The number of samples required for data taken in the water flow rig is discussed in Section 3.4.10 and from here it is assumed that a long enough sample is used. From the fluctuating component the variance and root mean square (RMS) $v'(\mathbf{x})$, can be calculated as follows:-

$$\overline{v^2}(\mathbf{x}) = \frac{1}{N} \sum_{k=1}^{N} \left(V(\mathbf{x}, t_k) - \overline{V}(\mathbf{x})\right)^2 \qquad v'(\mathbf{x}) = \sqrt{\overline{v^2(\mathbf{x})}}$$

The Reynolds stresses are then defined as:-

$$\overline{v_i(\mathbf{x})v_j(\mathbf{x})} = \frac{1}{N} \sum_{k=1}^{N} v_i(\mathbf{x}, t_k)v_j(\mathbf{x}, t_k)$$

For PIV measurements the subscripts i and j are the in-plane velocity components for a particular light sheet orientation. If the velocity components are taken as the same (i=j) the equation denotes a Reynolds normal stress (equal to the variance) which is always positive, however if they are different ($i \neq j$) the value is identified as a Reynolds shear stress. Turbulent kinetic energy, k may be calculated from the normal stresses:-

$$k = \frac{1}{2}\left(\overline{v_i^2} + \overline{v_j^2} + \overline{v_k^2}\right)$$

For the full 3D PIV data sets, where all three velocity components were interpolated onto a single structured grid (described in Section 3.4.13) this equation could be applied. However, for data within the fuel injector body where only radial and circumferential velocity components could be measured the turbulent kinetic energy was estimated by assuming that the out-of-plane normal stress was equal to one of the in-plane normal stresses:-

$$k = \frac{1}{2}\left(2\overline{v_i^2} + \overline{v_j^2}\right)$$

In this case, the axial normal stress was assumed to be similar to the radial normal stress. This was because axial and radial normal stresses were observed to be most similar inside the fuel injector, as shown in Chapter 5.

4.1.2 Probability Density Function

Whilst by definition, a stochastic signal does not have a unique value, the PDF provides a method for calculating the probability that the signal will take on a given value. The probability, P, that a random signal has a value within a small range, V to V+δV, is the fraction of the total time that the signal is within that range. Clearly P is a function of δV, however as δV→0, P tends to a constant value dependant only on V. This principle is known as the Probability Density Function (PDF) value of V. As the signal will always be a finite value, integration of the PDF between the range V=-∞ to V=∞ must always yield a probability of 1.

Experimentally, where the time-history is not continuous but sampled at a series of discrete time intervals, the data is plotted as a histogram consisting of several sub-ranges of time or "bins". As the bin widths are reduced the shape the histogram approaches the PDF shape, but the smaller the bin widths, the larger the number of samples required to ensure accuracy. For spatially resolved data a PDF(**x**) may by calculated whereby the

probability of an event occurring at a spatial location (x) may be calculated from using spatial bin widths.

4.1.3 Timescales and Frequency Spectra

Various time-domain properties and frequency domain characteristic of a time-history (e.g. spectra) can be evaluated from the auto-correlation function (ACF). The ACF is the normalised version of the auto-covariance, defined as the time-averaged product of the signal and a time-shifted version of itself:-

$$\overline{ACF_{ij}(s)} = \frac{\overline{v_i(t).v_j(t+s)}}{v_i' v_j'}$$

Where s is the time-separation, and it is noted that the velocity fluctuations about the mean are now used. By definition the integral timescale is the integral of the ACF from s=0 (where $\overline{ACF_{ij}(s)} = 1$) to s=∞. However a good approximation to the integral timescale is provided by integrating to the first point at which there is no correlation between v(t) and its time shifted self, v(t+s), i.e. the first point at which $\overline{ACF_{ij}(s)} = 0$, this is denoted as the first zero crossing point (FZC). This time-separation is dependent on the largest timescales of the flow.

$$\tau_{ij} = \int_0^{FZC} \overline{ACF_{ij}(s)}.ds$$

The frequency spectrum of the time-history can then be evaluated by Fourier transform of the ACF. Since the ACF can be shown to be an even function, the Fourier transform can be written as, Lynn (1975):-

$$E_{ij}(\omega) = \frac{2}{\pi} \int_0^{\infty} \overline{ACF_{ij}(s)} \cos n(\omega s) ds$$

By plotting $E_{ij}(\omega)$ against frequency (ω) the energy spectrum of the time-history is attained. If (i=j) then this function is known as the power spectral density (PSD), if (i≠j)

then a coherence spectrum is calculated. If significant spikes can be identified in either the PSD or the coherence spectrum then the frequency at which these spikes occur will correspond to a dominant frequency embedded within the time-history.

4.2 Turbulence Length-Scales

In high Reynolds number flows there is a separation of the flow scales and turbulent motions or "eddies" of many different sizes can exist. An "eddy" is defined by Pope (2000) as *"a turbulent motion, localised within a region that is at least moderately coherent over this region"*. Kinetic energy usually enters the turbulence field at the largest scale eddies via the production mechanisms (usually vortex structures), these large-scale eddies are strongly influenced by the geometry of the flow and have characteristic length and velocity scales similar to the characteristic length and velocity scales of the global flowfield. The energy is then transferred by invicid processes to smaller and smaller scales, until at the smallest scales, the length and velocity scales become low enough that the Reynolds number becomes close to 1, and the energy is dissipated by molecular viscosity. This process is known as the energy cascade, as first conceived by Richardson (1922).

Information with regard to the size of turbulent structures can be obtained from evaluation of the time-averaged non-dimensional two-point correlation function, $\overline{R_{ij}(\mathbf{x},\mathbf{r},s)}$:-

$$\overline{R_{ij}(\mathbf{x},\mathbf{r},s)} = \frac{\overline{v_i(\mathbf{x},t).v_j(\mathbf{x}+\mathbf{r},t+s)}}{v_i'(\mathbf{x}).v_j'(\mathbf{x}+\mathbf{r})}$$

Where **r** is a separation vector (when **r**=0 the correlation function reduces to the ACF). When the time-step, s=0, the two-point correlation function is denotes a spatial velocity correlation; when s≠0 the two-point correlation function describes a spatial velocity cross-correlation. From a spatial velocity correlation (s=0) a turbulent integral length-scale can be calculated by integration from the zero shift (**r**=0) and $\overline{R_{ij}(\mathbf{x},\mathbf{r})} = 1$ until the FZC where there is no spatial correlation $\overline{R_{ij}(\mathbf{x},\mathbf{r})} = 0$:-

$$L_{ij}(x) = \int_0^{FZC} \overline{R_{ij}}(x,r)dr$$

For PIV data the separation vector may be taken in any in-plane direction, however for simplicity only the length-scales defined below have been calculated in the thesis:-

$$L^{i}_{ii}(x) = \int_0^{FZC} \overline{R_{ii}}(x,r)dr$$

$$L^{j}_{jj}(x) = \int_0^{FZC} \overline{R_{jj}}(x,r)dr$$

Where the superscript denotes the direction that the spatial correlation function was calculated and the subscripts the velocity components, Pope (2000) states that the integral length-scales provide a useful measure of the turbulence scales that are *'characteristic of the larger eddies'*.

As the energy passes down from these largest scales in the energy cascade the influences of the flowfield geometry are lost and the smallest scales are locally isotropic and universal to all turbulent flows. These small scale eddies can be characterised by the kinematic viscosity and the dissipation rate of the turbulent kinetic energy as defined by Kolmogorov (1941). The Kolmogorov micro time and length scales are defined as:-

$$\tau_\eta = \left(\frac{\upsilon}{\varepsilon}\right)^{1/2}$$

$$L_\eta = \left(\frac{\upsilon^3}{\varepsilon}\right)^{1/4}$$

The rate of dissipation of turbulent kinetic energy is a function of the Reynolds number, where the higher the Reynolds number the greater the dissipation rate, thus the smaller the smallest flow scales. Both integral length-scales and Kolmogorov microscales were calculated directly from PIV data using the methodology outlined by Hollis (2004).

4.3 Methods for Identifying Coherent Structures

Locally coherent motions (eddies) are usually associated with local vortical motions but preclude precise definition. However, a description of a vortex that is generally accepted is that of Kline and Robertson (1989) who state that: *"A vortex exists when instantaneous streamlines mapped onto a plane normal to the core exhibit a roughly circular or spiral pattern"*.

Whilst vortex structures can be identified via calculation of vorticity ($\omega=\nabla\times\mathbf{V}$), this can be noisy as vorticity not only identifies vortices but also any shearing motions present in the flow. Therefore a method of identifying vortex information using a critical-point analysis of the local velocity gradient tensor (with its determinant, Δ) is usually employed. If Δ is positive the velocity gradient tensor has one real eigenvalue (λ) and a pair of conjugate complex eigenvalues ($\lambda\pm\lambda_{ci}$). Zhou *et al* (1999) show that the strength of any swirling motion is quantified by λ_{ci}. Since the period of the spiralling motion will be at its shortest near to the "eye" of a vortex, λ_{ci} will be maximal here. Therefore, plotting contours of swirling strength reveals peak values close to the eye of a vortex with contours of reducing strength at increased radii within the vortex structure. In pure shear the particle orbits are infinitely long ellipses, thus $\lambda_{ci}=0$ and regions of significant vorticity but no swirling motion are not identified by this method. Adrian *et al* (2000) compared the effectiveness of vorticity and the swirling strength parameter in identification of vortices in a pipe flow and found that *"the shortcomings of vorticity make swirling strength a more useful means of identifying eddies"*.

Whilst swirling motions may be identifiable from raw instantaneous PIV data, improved visualisation of the structures is achieved by a Reynolds decomposition of the instantaneous velocity field, allowing for just the fluctuating velocity components to be assessed. This can often reveal structures that otherwise may be hidden or distorted within the raw velocity vectors. As large-scale motions tend to move with convection velocities close to the local mean velocity, Reynolds decompositions often reveals the vortex centres more clearly. Therefore the calculation of swirling strength contours from a Reynolds decomposed fluctuating velocity field often improves the identification of centres of coherent vortex structures.

4.3.4 Singular Value Decomposition

To improve further the identification of the largest scales of turbulence structure, Singular Value Decomposition (SVD) may be used. Mathematically the singular value decomposition (SVD) is a technique that allows for the decomposition of an m×n matrix, **A**, into the product of an m×n orthogonal matrix, **U**, an n×n matrix, **Σ**, with positive or zero elements, σ (the singular values), and the transpose of an n×n matrix, **V**. The proof of this can be found in Golub and Van Loan (1989), but the end result is sufficient for the present purposes:-

$$\mathbf{A} = \mathbf{U}\Sigma\mathbf{V}^T$$

Or in terms of the matrix shapes:-

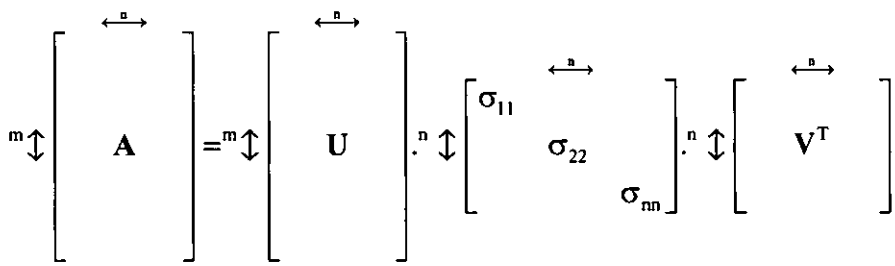

The matrix operations necessary for this decomposition are as follows:-

1. Calculate the rank, r of **A**
2. Calculate the eigenvalues, λ of **A**. The eigenvalues (and the corresponding eigenvectors) are calculated through the diagonalisation of **A** as described by Stroud (1997).
3. Arrange the eigenvalues in descending order $\lambda_{i=1}>\lambda_{i=2}>\ldots>\lambda_{i=n}$ (where by definition $\lambda_i=0$ for i>r).
4. Form a diagonal matrix, **Σ** placing on the leading diagonal the square roots of the ordered eigenvalues, $\sigma_{ii} = \sqrt{\lambda_i}$ ($\sigma_{ii}=0$ for i>r)
5. Arrange eigenvectors (of matrix **A**) in the same order as the corresonding eigenvalues in Σ to form the **V** matrix.

6. Calculate the **U** matrix via the vector operation on the i^{th} column $u_i = \sigma_{ii}^{-1} A v_i$ ($u_i = 0$ for $i>r$)

An approximation to **A** can then be found for by choosing a value or "rank" for k where ($k<r$) and setting $\sigma_{ii}=0$ for all $i>k$.

$$\mathbf{A}_k = \mathbf{A}\Sigma_k \mathbf{V}^T$$

Hence, if k=r matrix **A** will be fully reconstructed. Berkooz *et al* (1993) show that the eigenvalues are representative of the energy contribution, hence the proportion of energy projected onto $\mathbf{A}_k$ is:-

$$E = \frac{\sum_{i=1}^{k} \lambda_i}{\sum_{i=1}^{r} \lambda_i}$$

Therefore, by ordering the eigenvalues in descending order each rank will then be an optimal (in an energy sense) projection to the original matrix **A**, i.e. each $\mathbf{A}_k$ will minimise the least squares error on **A**. Pope (2000) estimates that 80% of the total turbulence energy is contained within turbulence motions of length-scales 1/6L-6L, therefore treating any instantaneous PIV velocity field as a 63×61 (m×n) matrix the SVD can be applied to both in-plane velocity component directions. By selecting a low rank approximation the largest-scale motions are likely to be projected onto the reconstructed matrix and smaller energy containing motions, i.e. the higher frequency incoherent turbulent fluctuations will be eliminated. The SVD was calculated using a Fortran 77 algorithm as described by Press *et al* (1992).

4.3.5 Conditional Averaging

In order to obtain an ensemble averaged picture of the turbulence structures identified through Reynolds decomposed or SVD flowfields, conditional averaging may be used, as described by Hollis (2004). Conditional averaging calculates the ensemble average of all instantaneous planar data that contain velocity fluctuations a factor (K) greater than the

standard deviation of the time history at a predetermined point (x_0,y_0) i.e. only fluctuations that occur in either "tail" of the PDF of the time-history are used, as shown in Figure 4.1.

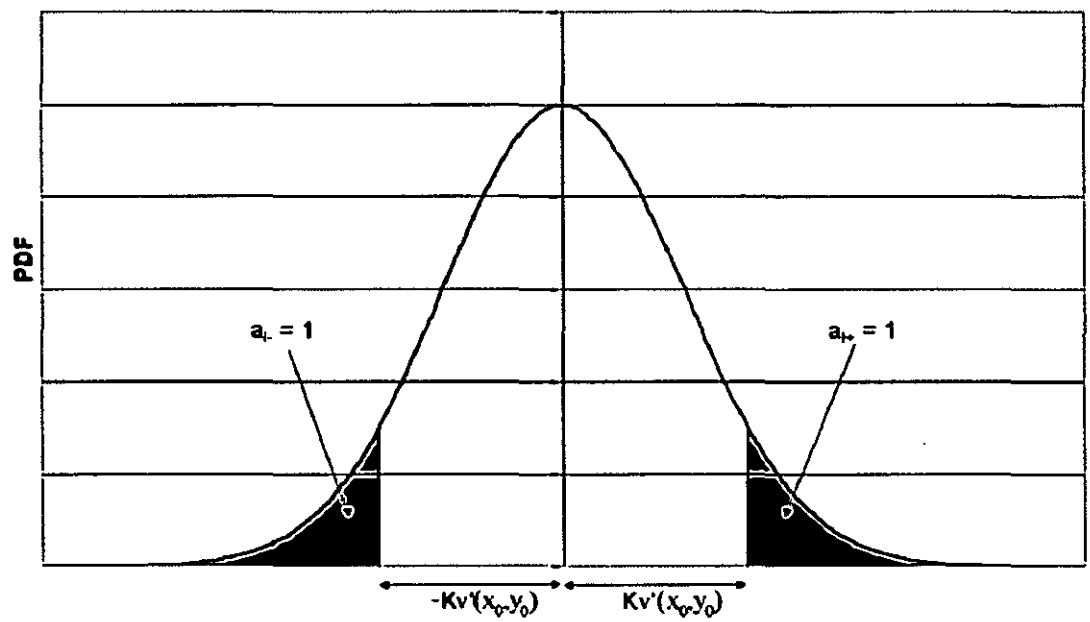

Figure 4.1. Conditional Averaging Based on the "Tail Ends" of a PDF

Conditional averaging can be described mathematically as:-

$$\langle v_{ca-}(x,y)\rangle = \frac{1}{N_{ca-}}\sum_{i=1}^{N} a_{i-}v_i(x,y,t_i) \qquad a_{i-} = \begin{cases} 0 & v(x_0,y_0) > Kv'(x_0,y_0,t) \\ 1 & v(x_0,y_0) < Kv'(x_0,y_0,t) \end{cases} \qquad N_{ca-} = \sum_{i=1}^{N} a_{i-}$$

$$\langle v_{ca+}(x,y)\rangle = \frac{1}{N_{ca+}}\sum_{i=1}^{N} a_{i+}v_i(x,y,t_i) \qquad a_{i+} = \begin{cases} 0 & v(x_0,y_0) < Kv'(x_0,y_0,t) \\ 1 & v(x_0,y_0) > Kv'(x_0,y_0,t) \end{cases} \qquad N_{ca+} = \sum_{i=1}^{N} a_{i+}$$

Where K is a coefficient chosen such that the number of samples selected is high enough to ensure that the ensemble average becomes reliable. A value that worked effectively in the present work was K=±1.5, which, if the PDF showed a normal distribution, would equate to the most extreme ±10% values of the time-history.

Conditional averaging effectively phase-locks the flow field to a high energy turbulence containing event passing a chosen point, the ensemble average then not only improves the visualisation of this high energy structure but will also identify regions in the domain that

are strongly correlated to this event. Hence the conditional average can provide an improved insight into spatial velocity correlation plots. The choice of location of (x_0,y_0) and the velocity component investigated determines the part of the structure that the ensemble average is locked to.

4.3.6 Rotating Frame of Reference

As the flow is swirling, any coherent turbulent events will also rotate with a characteristic angular velocity. Therefore, if each individual velocity field is rotated (in an r-θ plane) by an angle corresponding to the rotation of these turbulent events then a time-average of the velocity field following the trajectory of the coherent event can be calculated. If the Reynolds decomposed velocity vectors are rotated then a time-averaged representation of the turbulent structure may be found, or, using the SVD a rotational average of the largest energy containing flow structures. Rotational averaging, like conditional averaging will provide a clearer picture of the turbulence structure by eliminating incoherent motions. Again all structures in the domain that are correlated with these rotating events will also be identified, providing insight into spatial velocity correlation functions.

4.3.7 Proper Orthogonal Decomposition

Proper Orthogonal Decomposition (POD) also known as Principle Component Analysis or Karhunen-Loéve Decomposition as described by Lumley (1967) allows for time-averaged representations of the most energetic mode shapes pertaining to a *set* of fluctuating velocity data. A velocity field can be expanded into a series of spatial basis functions $\varphi_k(\mathbf{x})$ (or POD modes) and uncorrelated temporal coefficients $a_k(t)$ such that the reconstruction is given by:-

$$\mathbf{v}(\mathbf{x},t_j)=\sum_{k=1}^{N}a_k(t_j)\varphi_k(\mathbf{x}) \qquad j=1,\ldots,N$$

Where k denotes the mode number and $\mathbf{v}(\mathbf{x},t_j)$are the column vectors $[v(\mathbf{x}_1t_j,\ldots,v(\mathbf{x}_m,t_j]^T$ at an instant in time, t_j. The fluctuating velocity data set created by the column vectors at N instants in time is shown below:-

$$\begin{bmatrix} v_{i,j} & \cdots & v_{i,N} \\ \vdots & \ddots & \vdots \\ v_{m,j} & \cdots & v_{m,N} \end{bmatrix}$$

For PIV data m=3743 which corresponds to all (63×61) velocity vectors at one instant in time (t_j) arranged in a single column. The exact order is not important as long as it is replicated for all N instants in time. The POD decomposition of this data matrix is optimal in the sense that it is the most efficient way of extracting the most energetic components of the velocity field, hence it minimises the average least-squares truncation error for all k<N, Cizmas *et al* (2003):-

$$\varepsilon_n = \left\langle \left\| v(\mathbf{x}, t_j) - \sum_{k=1}^{N} a_k(t_j)\varphi_k(\mathbf{x}) \right\|^2 \right\rangle$$

This is equivalent to finding the spatial functions that maximise the averaged normalised projection of v onto φ:-

$$\frac{\left\langle (v,\varphi)^2 \right\rangle}{\left\langle (v,v)^2 \right\rangle}$$

Where the notation (.,.) refers to an inner product. Maximising the inner product leads to the solution of the following eigenvalue problem, Berkooz *et al* (1993):-

$$\int_D R(\mathbf{x},\mathbf{x}')\varphi(\mathbf{x}')d\mathbf{x}' = \lambda\varphi(\mathbf{x})$$

Over a spatial domain, D, where R(**x**,**x**') is the ensemble averaged spatial correlation function $R(\mathbf{x},\mathbf{x}') = \langle v(\mathbf{x})v(\mathbf{x}') \rangle$. In the discrete case R(**x**,**x**') is replaced by the tensor matrix product:-

$$R_{ij} = \frac{1}{N}\sum_{i=1}^{N} v_i v_i^T$$

Therefore the eigenvectors of R_{ij} are the POD modes $\varphi_k(\mathbf{x})$ and the temporal modes can be calculated by projecting the data set onto the eigenfunctions:-

$$a_k(t_j) = (v(\mathbf{x}, t_j), \varphi(\mathbf{x}))$$

Unfortunately the R_{ij} matrix is of size m×m, which in this case would contain 14.76×10^6 points (per velocity component). Therefore, calculating all m POD modes would be very computationally expensive. Therefore the "snap-shot" method has been used, as proposed by Sirovich (1987) where the first N eigenvectors can be calculated by converting the problem from an m×m matrix to that of an N×N matrix, which contains only 0.42×10^{-6} sample points (per velocity component). Sirovich (1987) shows that the POD modes can be written as a linear combination of the data vectors and coefficients κ:-

$$\varphi_k = \sum_{i=1}^{N} \kappa_i^k v_i$$

Therefore substitution into the original eigenvalue problem yields:-

$$\frac{1}{N}\sum_{i=1}^{N}\sum_{i=1}^{N} \kappa_i^k v_i v_i^T v_i = \lambda \sum_{i=1}^{N} \kappa_i^k v_i$$

If the inner product of the fluctuating velocity data set is denoted by **C**:-

$$\mathbf{C} = \frac{1}{N}\sum_{i=1}^{N} v_i^T v_i$$

therefore

$$\frac{1}{N}\sum_{i=1}^{N}\sum_{i=1}^{N} v_i\left(\mathbf{C}\kappa_i^k - \lambda\kappa_i^k\right) = 0$$

and

$$\mathbf{C}\kappa_i^k = \lambda\kappa_i^k$$

Hence, calculation of the eigenvalues (λ) and eigenvectors (κ) of the **C** matrix allows for the calculation of the first N POD through linear combination of κ^k_i with v_i. The eigenvalues (λ) and eigenvectors (κ) were calculated through diagonalisation of the **C** matrix using the SVD algorithm (described in 4.3.4 above). Again, the eigenvalues represent the energy contribution of each POD mode, hence the arrangement of the eigenvalues in descending order by the SVD algorithm resulted in each POD mode representing the optimal energy projection onto the data set.

4.4 Closure

In this chapter various methods of data reduction have been described that allow for time-averaged statistics to be calculated. For spatially resolved measurements quantitative information pertaining to the turbulent velocity field can be found through velocity correlations and turbulent integral length-scales. In order to improve identification of instantaneous large-scale turbulent eddies the SVD method and calculation of the swirling strength have been described, as have methods of creating time-averaged representations of the turbulent structure, namely conditional and rotational averaging. POD has then been described as a method of calculating the most energetic most shapes corresponding to an ensemble of data. All these data reduction/analysis methods are now available for application to the data collected, and this is the topic of the next chapter.

5 RESULTS

The results to be presented in this chapter are split into the following sections. Section 5.1 describes the inlet and exit conditions, Section 5.2 investigates the velocity and scalar fields of datum fuel injector at the main test condition and in Section 5.3, the no-jet condition test condition velocity field is described. Finally, Section 5.4 describes the flowfields created by the various modular swirler configurations.

5.1 Inlet and Exit Conditions

As discussed in Chapter 2, the inlet flow path definition was carefully designed and the mass flow rates set such that the inlet velocity profiles were fully developed. This was important for both repeatable experiments and CFD model inlet boundary conditions. Figure 5.1 and Figure 5.2 show radial profiles of the time-averaged mean and "true" RMS axial velocity calculated from PIV data (in water) at a location 100mm upstream of the fuel injector exit plane (x/D_s=-2.65) in the central jet feed pipe ($Re=11.69\times10^3$) and in the annular gap that feeds the swirl stream ($Re=5.68\times10^3$). The term "true" refers to RMS velocities corrected to account for sub-grid filtering, as discussed in Section 3.4.10. In both figures a $1/7^{th}$ power law, proposed by Prandtl (1921) to predict the shape of a boundary layer is overlaid of the form:-

$$\frac{\overline{V_x}}{V_{x,s}} = c\left(\frac{r}{D_s}\right)^{1/7}$$

Where c is a constant dependent on the flow. The good agreement between the $1/7^{th}$ power law and the mean axial velocity profiles confirms the fully developed nature of both inlet flow streams at the test condition mass flow rates. In the airflow experiments, since both inlet feed flows had Re>4000 it was safely assumed that these profiles would also be fully developed by x/D_s=-2.65. As good non-dimensional agreement between mean and RMS velocities in air and water has previously been shown (see Section 2.5.3) the non-dimensional inlet profiles in air may be assumed to be the same as those shown in Figure 5.1 and Figure 5.2. As would be expected in the near wall regions mean velocity gradients were high as the mean velocity decayed to zero at the wall. As a result RMS velocity profiles peaked near the walls, with minima close to the centreline.

Turbulent integral length-scales at these two locations and have been shown previously for the swirl stream feed and central jet feed pipes in Figures 3.26 and 3.27 respectively. The axial length-scale showed minima close to the centreline and peak values towards the duct walls. In the swirl stream flow path the minimum value was 23% of the annular gap height and the peak value close to 35%, in the central fed pipe the minima was 10% of the central feed pipe diameter and the peak close to 20%. In terms of the radial length-scales, peak values occurred close to the centreline (approximately 13% of the annular gap height and 5% of the central feed pipe diameter) and decayed gradually towards the wall.

Mean velocity vectors superimposed on axial RMS velocity contours are shown in exhaust flow annular gap (between the downstream blockage and test section wall) in Figure 5.3. The mean velocity vectors indicate a smooth channel flow. By x/D_s=5.25 the axial RMS contours indicate a close to constant level across the radius, however, further upstream peak turbulence levels occur close to the downstream blockage. Instantaneous PIV measurements reveal that this peak turbulence intensity is due to a flow separation off the top of the blockage, as shown in Figure 5.4, where the axial velocity contours clearly indicate a reverse flow. The first two POD modes calculated from N=650 LS-PIV data indicate two forms of coherent vortex structure most probably associated with this flow separation, shown in Figure 5.5 and Figure 5.6 and accounting for 26% and 11% of the total turbulent kinetic energy respectively. These vortices seem to influence the flow up to x/D_s=5.25, therefore it is recommended that CFD boundary condition should be set below this location. These inlet and exit (boundary) conditions are applicable to both main and no-jet test configurations, which are discussed in the following two sections.

5.2 Main Test Condition

The results at the main test condition are split into the following sections, the time-averaged velocity field is detailed Section 5.2.1 and measurements relating to unsteady flow features are described in Section 5.2.2. The scalar field is described in Section 5.2.3.

5.2.1 Time-Averaged Velocity Field

Figure 5.7 shows the mean velocity vectors in the dump area expansion chamber on a constant theta plane of the full 3D data set (described in Section 3.4.13). As can be seen, the central jet has a time mean penetration close to x/D_s=0.75 where a free stagnation point is found. A swirl stream "cone" isolates a corner re-circulation region where the swirl flow cone impinges on the cylindrical duct wall at around x/D_s=1.2. The attached swirl cone then forms a strong wall jet that exits the duct through the annular gap around the concentrically mounted downstream blockage; in the region enclosed by the attached wall jet a region of close to stagnant fluid exists. Examination of the velocity vectors close to the fuel injector exit plane indicate a backflow near the inner wall of the swirl passage, confined between the strong forward flows of the central jet and the swirl cone, this is more clearly illustrated in Figure 5.8.

Radial profiles of mean axial velocity for five axial locations within the dump area expansion chamber (x/D_s=0, 0.27, 0.53, 1.05 and 2.65) are shown in Figure 5.9, corresponding to the axial locations where r-θ plane measurements were made (as indicated in Figure 3.32). Integration of these axial velocity profiles indicate mass flow rates within ±10% of the orifice plate calculated mass flow rates at all axial measurement planes. As can be seen, at the fuel injector exit plane (x/D_s=0) at radial locations corresponding to the swirl stream flow path (r/D_s=0.09-0.5) a strong bias exists with a peak velocity of $\overline{V_x}/V_{x,s} = 1.5$ at r/D_s=0.47. Close to the inner wall of the swirl passage the previously mentioned backflow is identified with a peak negative velocity of $\overline{V_x}/V_{x,s} = -0.3$. As the flow develops downstream the peak swirl stream axial velocity decays rapidly whilst following the mean flow path of the swirl stream cone as it moves towards the mean wall attachment point. The central jet peak velocity rapidly decays as it approaches the mean free stagnation point. The swirl stream cone and central jet can be more easily visualised by plotting iso-surfaces of $\overline{V_x}/V_{x,s} = 0.4$ for the full 3D data set, as shown in Figure 5.10. The previously identified region of weakly negative backflow is shown to occur by measurement location x/D_s=1.06 which increases in area until it extends from the centreline to r/D_s=1.2 (by the final measurement location, x/D_s=2.65). Integral timescales and integral length-scales as previously presented in Figures 3.22 and 3.34 respectively indicate that in this stagnant region timescales evolve (from less than

2ms in the near-field) up to values close to 60ms. The length-scales also increase from less than $0.19D_s$ at the fuel injector exit plane to a peak value of over $0.4D_s$.

Radial profiles of the mean radial velocity are shown in Figure 5.11, again at x/D_s=0, 0.27, 0.53, 1.05 and 2.65. At the fuel injector exit plane the peak radial velocity of $\overline{V_r}/V_{x,s} = 0.4$ is seen towards the outer wall of the fuel injector which then rapidly decay to close to zero. At x/D_s=0.27 and 0.53 the negative radial velocities at large radii indicate the mean motion of the corner re-circulation zone.

Circumferentially averaged radial profiles of mean circumferential velocity are shown in Figure 5.12. At the fuel injector exit plane these exhibit a roughly Rankine vortex shape with a peak velocity of $\overline{V_t}/V_{x,s} = -1.5$ at r/D_s=0.3 separating a region of strong solid body rotation from a less well defined potential vortex (the negative sign identifies an anti-clockwise mean flow rotation using the right hand cylindrical polar definition). As the flow develops the peak circumferential velocity follows the swirl stream cone outwards towards the wall whilst steadily diminishing in strength until a large region of weak solid body rotation (across the area previously identified as close to stagnant) exists. From the mean axial and circumferential velocity profiles the swirl number was calculated at the exit plane to be Sn=0.78.

Figure 5.13 Figure 5.14 and Figure 5.15 show radial profiles of axial, radial, and circumferentially averaged circumferential RMS velocity within the dump area expansion chamber. In the fuel injector near-field ($x/D_s<1$) the axial RMS velocity indicates two distinct peaks, whilst the radial and circumferential RMS velocity profiles exhibit one peak (of a similar magnitude), however, the circumferential RMS peak velocity decays rapidly to approximately half that of the peak axial and radial RMS velocities. This anisotropic turbulence flow state exists throughout the fuel injector near-field. In the far-field ($x/D_s>1$) the RMS values all decay to a close to isotropic background level of approximately 10% of the bulk average swirl stream exit velocity. Inspection of the axial-radial shear stress Figure 5.16 and the radial-circumferential shear stress Figure 5.17 indicate that, as would be expected, a strong velocity coupling exists in regions corresponding to the peak turbulence production, which in the axial-radial plane

correspond to the shear layers of the jet stream (positive shear) and the inner shear layer of the swirl stream (negative shear).

The turbulent kinetic energy in the axial-radial plane is shown in Figure 5.18. What is most notable is that, despite the positive and negative shear stresses within the jet shear layer and inner swirl stream shear layer respectively having similar magnitudes, the levels of turbulent kinetic energy in the inner shear layer of the swirl stream are almost double those in the jet shear layer. This high turbulence energy is therefore unexpected and it cannot simply be due to turbulence production alone. This result points to the presence of significant localised turbulence events within the inner shear layer of the swirl stream. The apparent jumps in the contour levels of Figure 5.18 are due to the boundaries of the various size FoV's used to create the 3D data set, where the small jumps reflect the reducing effects of spatial averaging (See Section 3.4.10) with the increasingly small interrogation cells.

Inside the datum fuel injector swirl passage ($x/D_s<0$) radial profiles of circumferentially averaged mean and RMS radial velocity are shown in Figure 5.19 and Figure 5.20 respectively at axial measurement locations x/D_s=-0.13, -0.27, -0.43, -0.53. Unsurprisingly the mean radial profiles show negative (inward) velocities close to the exit of the radial flow slots, however, by x/D_s=-0.27 the mean radial velocities are positive with a peak close to the inner body of $\overline{V_r}/V_{x,s} = 0.2$, which by x/D_s=-0.13 had moved outboard to a radial location of r/D_s=0.3 with an increased peak value of $\overline{V_r}/V_{x,s} = 0.3$. By the fuel injector exit plane this peak velocity is close to the swirl stream outer wall, as previously discussed. These observations indicate a flow separation off the inner body, between axial measurement locations x/D_s=-0.43 and -0.27. As would be expected in a flow separation region the peak radial RMS values rapidly increase near the inner body from approximately $v'_r/V_{x,s}$=0.15 (at x/D_s=-0.53) to $v'_r/V_{x,s}$=0.6 (at x/D_s=-0.13). Circumferentially averaged radial profiles of mean and RMS circumferential velocities at the same locations inside the fuel injector are shown in Figure 5.21 and Figure 5.22. The mean profiles clearly exhibit a Rankine vortex shape which develops through the swirl stream passage. Again, peak RMS levels occur close to the inner body by x/D_s=-0.43 and increase towards the exit plane.

Whilst the most appropriate method of presenting the radial and circumferential velocity data captured within the fuel injector was circumferentially averaged radial profiles as described in Section 3.4.13, it is worth noting that close to the swirl slot exit plane the flow exhibited a strong steady-state three dimensionality. This was because regions of high and low inward radial velocity were caused by the blockage effect of the discrete swirl slots, as shown in Figure 5.23. In this figure the dashed line indicates the outer wall of the swirl stream, but measurements could not be taken in the outer extremities due to excessive glare of the fuel injector body at the image plane. The regions of shear between these maxima and minima of radial velocity resulted in a similar three dimensionality in the second order statistics, as shown in Figure 5.24. Evidence of this three dimensionality had mixed out by axial measurement location x/D_s=-0.43.

The time-averaged results discussed above utilised similar data reduction techniques and data presentation methods as employed in previous RANS methods validation data sets, as discussed in Section 1.7. As shown this profile based approach of analysing the time mean and RMS velocity data provides a valuable insight into the flow physics and reveals some of the fundamental aspects of a strongly swirling flow, i.e. a swirl cone flowing radially outwards to move past a large region of slow moving or reverse flow which acts as an aerodynamic blockage. However, the data reported so far does not reveal much information with regards to the instantaneous flow structure. This is both useful for LES validation purposes and may also help us to understand the, as yet unexplained, peak turbulent kinetic energy in the swirl stream inner shear layer (see Figure 5.18). The instantaneous flow field is described below.

5.2.2 Measurements Relating to Flow Unsteadiness

Figure 5.25 shows an example of an instantaneous x-r velocity field, from this image alone it is clear that the instantaneous flowfield is significantly different to the time-averaged representation. The central jet can be observed to be "flapping" slightly and along the centreline the instantaneous free stagnation point is at approximately x/D_s=0.5 (compared to a mean location of x/D_s=0.75). The corner re-circulation zone also seems much less well defined. However, the most apparent difference is the occurrence of

large-scale coherent vortex structures in the swirl stream, these vortices have clearly been identified by the swirling strength algorithm, as described in Chapter 4.

A Reynolds decomposition shown in Figure 5.26 for the same time-instant improves the identification of the vortices by providing a clearer representation of the vortex centres. These are seen on both sides of the swirl cone in the shear layers but the vortices occurring in the inner shear layer display higher fluctuating velocity components. The inner shear layer vortices will therefore contribute significantly to the measured turbulent intensity. An SVD of this image is then shown in Figure 5.27 using the first five singular values (rank 5), which account for 79% of the instantaneous turbulent kinetic energy. The SVD further improves the large-scale structure visualisation by eliminating a significant proportion of the low-energy incoherent motions observed in the Reynolds decomposition.

A sequential set of instantaneous velocity fields reveal that the location of the forward stagnation point of the central jet penetration and the swirl cone attachment location on the test section outer wall are both time-dependent. From a set of N=3072 instantaneous velocity fields (captured using HS-PIV in measurement region B) the spatial PDF of the location of the free stagnation point and the corner attachment point are shown in Figure 5.28 and Figure 5.29 respectively. As shown, the unsteady variation of the free stagnation point is large, ranging from x/D_s=0.1-2.4 (an overall variation of $2.3D_s$). The mean central jet penetration was noted from the mean velocity components in Figure 5.7 to be about x/D_s=0.75, however, the PDF indicates that the most probable location of the free stagnation point is within the range (bin-width) 0.8-0.88; the longer PDF "tail" on the high penetration side accounts for this difference. For the swirl cone attachment point the mean value of x/D_s=1.2 closely matches the most probable position indicated by the PDF as 1.27, the good agreement is due to a close to normal distribution with a variation of only $\pm 0.5D_s$.

PSDs' calculated from HWA in airflow at a sample rate of 10kHz and HS-PIV in water flow at 1kHz taken at reference point (x/D_s=0.27,r/D_s=0.27,θ=0) within the swirl stream inner shear layer are shown in Figure 5.30. As can be seen the two spectra agree extremely well-showing that strong periodic events are occurring at frequencies well,

within the energy containing range of the turbulence. The strongest peak is at St=1.15 with a second, weaker, peak at St=2.30 (where the Strouhal number is based on the bulk average axial swirl stream exit velocity ($V_{x,s}$=1.99ms^{-1}) and the hydraulic diameter of the swirl stream exit, D_h=30.87mm). The non-dimensional peak frequency contours (calculated from HS-PIV measurements in region B) are shown in Figure 5.31. As can be seen this dominant periodicity of St=1.15 exists throughout the near-field region of the swirl stream (in both axial and radial velocity component directions) indicating that these strongly periodic events are linked to the energetic vortices identified in the swirl stream.

The link between the large-scale vortices observed in the swirl stream shear layer and the strongly periodic events observed in the spectra is clarified by spatial velocity correlations. Time-averaged radial velocity correlation contours (calculated from LS-PIV data in measurement region B) are shown in Figure 5.32, the white dot indicates the origin of the correlation. As shown, within the swirl stream flow path there are sequential regions of strong positive and negative correlation indicating highly coherent and periodic turbulence events in this region. The periodicity of these events can be calculated from the distance between the origin and the first positive correlation maximum denoted as "d" in Figure 5.32, which has a dimensionless length d/D_s=0.6. Assuming a convection velocity of the periodic events to be close to the mean axial velocity at a point of d/2 (which is shown in Figure 5.9 is approximately $\overline{V_x}/V_{x,s} = 0.84$ the Strouhal number is St=1.15 which matches the dominant spike in the temporal domain. Where the Strouhal number (using non-dimensional parameters) reduces to:-

$$St = \frac{\left(\overline{V_x}/V_{x,s}\right)}{d/D_s} \cdot \frac{D_h}{D_s}$$

The second peak in the PSD can now be identified as corresponding to the correlation between positive and negative maxima in the swirl stream, with a wavelength of 0.5d. This result intrinsically links the unsteady turbulent events occurring in the swirl stream to the dominant frequencies identified in the spectra. This can be more easily visualised by evaluation of a conditional average (of the N=3072 HS-PIV instantaneous snap-shots for measurement region B). To identify only the high energy turbulent events a sub-set of data was created by only selecting instantaneous velocity fields that exhibited axial

fluctuating velocities greater than 1.5 times the standard deviation at a point (used as the origin of the radial velocity correlation in Figure 5.32). This created a sub-set of N=259 instantaneous images which were then ensemble-averaged. The ensemble-averaged fluctuating velocity field is shown overlaid on the radial velocity spatial correlation contours in Figure 5.33. As can be seen, this conditional average shows clearly a sequence of counter-rotating vortices convecting along the mean flow path of the swirl stream inner shear layer, a turbulent structure that is predicted by the time-averaged radial velocity correlation contours. Calculation of the axial RMS velocity from this sub-set of data, shown in Figure 5.34 indicates that it is co-rotating vortices (separated by the distance d) that are highly energetic and thus contribute significantly to the high values of measured k in the inner shear layer of the long time average (Figure 5.18).

Figure 5.35 and Figure 5.36 show the first two POD mode shapes (deduced from N=650 LS-PIV images for measurement region B), which clearly identify the turbulent flow structure implied by the conditional average and the spatial velocity correlation. The two mode shapes represent the two distinct possibilities in the flow structure, i.e. from the fuel injector exit plane the pattern could be a clockwise-rotating vortex followed by counter-clockwise rotating vortex or visa-versa. As the vortices decay in strength with increased axial distance though the dump expansion chamber and the POD modes represents a whole field energy contribution, it would be misleading to assign the energy of the first two POD modes to the large-scale energy contribution of the vortices.

PIV measurements in the r-θ plane at the fuel injector exit ($x/D_s=0$) reveal further information about these unsteady vortex structures. Figure 5.37 shows an instantaneous velocity field superimposed on swirling strength contours; the swirling strength contours identify the occurrence of two swirling structures close to the inner body of the fuel injector. Reynolds decomposition, as shown in Figure 5.38 again more clearly identifies these structures as co-rotating vortices and also reveals evidence of a secondary pair of weaker counter-rotating vortices embedded within the instantaneous structure. A rank 5 SVD (Figure 5.39) of the Reynolds decomposed velocity vectors (containing 77% of the total energy) then allowed for the swirling strength contour maxima to identify more accurately the centres of the two strong co-rotating vortex pair. A characteristic that was important for the rotational averaging methodology to be described further below.

A PSD of the circumferential velocity component deduced from 1kHz HS-PIV measurements at location (x/D_s=0, r/D_s=0.25, θ=0) is shown in Figure 5.40. The spectrum shows a dominant spike at St=1.18 and a second less intense spike at St=2.36, which is very similar to the axial velocity PSD shown in Figure 5.30. A plot of the peak frequency contours (calculated from HS-PIV axial measurement at location x/D_s=0) is shown in Figure 5.41; it can be seen that the dominant frequency of St=1.18 prevails for all radial locations and all values of theta within the swirl stream exit plane.

The radial location of the vortex eyes in Figure 5.39 are estimated to be at a time-averaged radial location of r/D_s=0.26 or r=9.8mm at the fuel injector exit plane, hence the circumferential distance for one full rotation is 61.6mm. If a vortex travelled this distance with a velocity of $\overline{V_t}/V_{x,s} = 2.36$, a Strouhal number of St=1.18 would be observed. However, Figure 5.12 shows that at r/D_s=0.26 the mean circumferential velocity is close to $\overline{V_t}/V_{x,s} = 1.2$, assuming the vortices move with an angular velocity dependent on the circumferential velocity, this is half that required. This implies therefore that in the r-θ plane the peak frequency at St=1.18 is in fact a frequency characteristic of the two strong vortex pair moving past a fixed point and the weaker spike at St=2.36 (Figure 5.40) is the frequency of the two-strong two-weak counter-rotating vortex pairs moving past a fixed point.

The above analysis indicates that these turbulent events are being convected with a path defined by the local mean velocity. By plotting stream-traces issuing from four points at a radial location of r/D_s=0.26 at theta locations 0°, 90°, 180° and 270° from the full 3D data set these flow paths can be visualised, as shown in Figure 5.42. The helical flow path observed for the stronger co-rotating vortex pair is analogous to the classical right-handed double helix structure of a DNA strand as proposed by Watson and Crick (1953), the two-weaker vortices must then form a secondary double helix occupying the spaces between the two-strong vortices.

To provide a time-averaged representation of the fuel injector exit plane vortex pattern a rotating frame of reference was applied to the LS-PIV data, where each instantaneous

rank 5 SVD velocity field was rotated relative to the average angular location of the one of the vortex structures. To achieve this, the angular location of the maximum swirling strength on the first instantaneous SVD velocity field was identified; this corresponded to the eye of one of the strong vortex pair and was denoted as vortex A. The second highest swirling strength maximum was then identified which corresponded to the location of the second strong vortex, this was denoted vortex B. In subsequent images vortex A was identified by assuming initially a frequency of St=0.59 (half the peak frequency identified by the spectral analysis) and the swirling strength maximum which corresponded most closely to the predicted location was denoted vortex A, the other peak was then assumed to be vortex B. Once vortex A and B were identified, the average rotation angle for each for instantaneous SVD velocity field was calculated. With this information, all N=650 images could be rotated by the appropriate average rotational angle and then time-averaged as shown in Figure 5.43. Analysis of the angular locations of vortex A and B also revealed that the phase difference between vortex A and B was 180°±15°.

The rotationally averaged turbulent kinetic energy contours are shown in Figure 5.44 overlaid by the rotationally averaged velocity vectors. As can be seen the effect of the rotational averaging process is to create two regions of turbulence maxima of approximately k=0.64 close to the eyes of the stronger vortex pair compared to a turbulence level of approximately k=0.08 in the region of the weaker vortices (at r=0.26). The long time-averaged turbulent kinetic energy calculated from the same LS-PIV data set is shown in Figure 5.45 which shows a turbulent kinetic energy in the radial location of the vortices to be almost constant for all θ locations. At r=0.26 the circumferentially averaged k=0.44. It seems therefore that the energy contribution of the two-strong vortices at the exit plane is close to 82% ((0.44-0.08)/0.44).

The first two POD modes (calculated from the same N=650 LS-PIV instantaneous fluctuating velocity fields) are shown in Figure 5.46 and Figure 5.47 respectively. Both POD modes capture the two pairs of counter-rotating vortices, and again represent two distinct possibilities in the flow structure. In the r-θ plane, as the vortices do not decay in strength and are present across the majority of the measurement region, partitioning of the total turbulent kinetic energy into large-scale coherent motion and small scale incoherent turbulence based on the percentage energy contributions of the POD modes

will be much more representative than attempting the same in the x-r plane where the vortices do decay in strength with increased axial distance (as discussed previously). Each of the two POD modes account for 23%, so this analysis indicates that 46% of the measured turbulent kinetic energy is due to large-scale coherent contribution. This estimate is more conservative than the rotational average estimation but still indicates a very large contribution of the vortex structures to the total measured turbulent kinetic energy.

Spatial velocity correlations of the radial velocity in the radial direction and circumferential velocity in the theta direction (using polar grids) were calculated (from LS-PIV measurement location $x/D_s=0$) and are shown in a Cartesian frame of reference in Figure 5.48 and Figure 5.49 respectively, where the white dot indicates the reference point of the correlation. The velocity correlations clearly predict the presence of 4 coherent structures, where each of the 3 vortices (away from the origin) are correlated at close to ±70%. This extremely strong spatial correlation of the vortex pairs helps to explain why the dominant frequency in the PSD relates to the motion of the vortex pairs and not to single vortex motions. The circumferential velocity correlation contours in particular indicate the presence of the two counter-rotating vortex pairs. This is shown by overlaying the rotationally averaged fluctuating vectors onto the circumferential velocity correlation contours as shown in Figure 5.50. Regions of positive correlation match almost exactly with the regions of turbulence structure with a positive circumferential orientation.

The vortices can also be shown to be highly correlated in time by a velocity cross-correlation. Figure 5.51 shows a cross-correlation of the circumferential velocity over a time-step of 330ms, where the integral timescales at the fuel injector exit plane were approximately 2ms, i.e. the correlation is taken over a duration of 165 times the integral timescale (the axial and radial integral timescales are shown for the main test condition in Figure 3.20). As can be seen the vortex pairs are still highly correlated (approximately 50%). This extremely strong correlation in time helps to explain why the strong spikes in the spectra occur at distinct frequencies and are not broadband.

Measurements in the r-θ plane inside the fuel injector swirl stream ($x/D_s<0$) reveal that the counter-rotating vortex pair is still visible at $x/D_s=-0.13$ and -0.27, as shown in Figure 5.52 and Figure 5.53 respectively, where rotationally averaged velocity vectors are overlaid on the time-averaged circumferential velocity correlations. Although the spatial velocity correlation remains strong, at $x/D_s=-0.27$ the structures have moved very close to the inner body of the fuel injector and, according to the definition *"a vortex exists when instantaneous streamlines mapped onto a plane normal to the core exhibit a roughly circular or spiral pattern"* Kline and Robertson (1989), they are no longer strictly speaking vortices, however the four distinct structures certainly correspond to the more clearly developed vortex structures further downstream. Velocity cross-correlation again reveals these structures to be highly coherent in time, and POD analysis at $x/D_s=-0.13$ and -0.27 revealed coherent structure in the first two modes however the energy contribution dropped to 44% by $x/D_s=-0.27$ and 32% by $x/D_s=-0.13$.

Further upstream into the fuel injector ($x/D_s<-0.27$) no coherent structure was identifiable, as indicated by the spatial velocity correlations of circumferential velocity at $x/D_s=-0.43$ and -0.53, shown in Figure 5.54 and Figure 5.55. As can be seen, there is only a weak correlation between the vortex pairs (less than 20%) at $x/D_s=-0.43$ which reduces to background noise by $x/D_s=-0.53$. Velocity cross-correlations at both axial measurement locations decay to a background noise level within 66ms indicating a significantly reduced temporal coherence. Therefore it seem that the origin to the vortex structures is related to an event inside the fuel injector close to the inner wall and at $x/D_s>-0.27$, however, it remains unclear as to whether this is due to either the flow separation of the swill flow off the inner wall or the internal corner of the swirl stream flow path.

These unsteady and highly energetic large-scale motions identified in the fuel injector flowfield will inevitably influence the scalar transport mechanisms and mixing properties of the flowfield. This is investigated in the following section.

5.2.3 Scalar Field

Figure 5.56 shows the non-dimensional mean scalar field (where C_{max} is the tracer concentration in the central jet feed flow pipe). At the fuel injector exit plane across the

swirl stream radius, as would be expected, a close to zero concentration occurs. However, the penetration into the dump area expansion chamber increases with increasing radius up to the outer wall (r/D_s=0.5), this is due to the strong outer wall bias of the swirl stream axial velocity. It can also be seen (from Figure 5.56) that the mean scalar field is almost fully mixed by the final axial measurement location of x/D_s=1.5 to a level close to $\overline{C}/C_{ref} = 0.05$. This value is expected, as the mass flow split between the central jet and the swirl stream is $\dot{m}_j/\dot{m}_s = 5.14\times10^{-2}$ as discussed in Chapter 2. Figure 5.57 shows the mean scalar field measured in the r-θ plane at x/D_s=0.27, which shows good rotational symmetry. The scalar RMS field is shown in Figure 5.58, as would be expected peak RMS levels occur in the central jet shear layer where the scalar concentration gradient is highest. This is worth noting that the scalar RMS is not much higher than the background level in the region of the inner shear layer of the swirl stream, where the high energy large-scale vortices were observed to exist. However, the vortices do have a significant impact on the scalar mixing and transport phenomena of the fuel injector flowfield, this is clearly shown from instantaneous measurements as discussed below.

Instantaneous scalar fields reveal that, not surprisingly the central jet penetration is highly time-dependent; examples of high and low penetration are shown at two instants in time in Figure 5.59 and Figure 5.60 respectively. The penetration of the concentration field is most likely linked to the time-dependent motion of the central jet and the free stagnation point. In the region downstream of the free stagnation point, previously identified as close to stagnant, HS-PLIF measurements at 2kHz revealed that packets of high concentration fluid remained coherent for long periods of time relative to rapid changes further upstream. This is due to the much longer integral timescales (Figure 3.20) and turbulent integral length-scales (Figure 3.32) in this region (up to 30 times longer than in the near-field) as previously discussed in the velocity field measurements.

Whilst it has been noted that the high levels of turbulent kinetic energy in the swirl steam do not correspond to high levels of scalar variance, occasionally tracer containing fluid was entrained into the vortex structures as is evident in Figure 5.60. This entrainment is more clearly seen by conditional averaging of the x-r plane velocity and scalar fields. Sub-sets of data were created by selecting instantaneous velocity vector fields with radial

velocity fluctuations greater than 1.5 times the radial RMS and instantaneous scalar fields that exhibited scalar fluctuations greater than 1.5 times the scalar RMS, as shown in Figure 5.61 (the point used to create these conditional sub-sets is indicated by a white dot). This figure indicates that there is a tendency for the stronger vortices to entrain tracer containing fluid from the region of the central jet which result in localised "bursts" of dyed / non-dyed fluid mixing. In a combusting test case, if these localised regions of fuel/air are close to stoichiometric then they may result in themo-acoustic instability. Therefore the vortices that are responsible for the strong combustor oscillations observed by Lartigue *et al* (2004) whilst using the original Turbomeca geometry (see Figure 2.1).

In the r-θ plane at x/D_s=0.27 the entrainment of the passive scalar into two vortex structures (presumably the strong vortex pair) can clearly be seen; an example of this is shown in Figure 5.62, where the dashed line indicates the location of the outer wall of the fuel injector swirl flow path. Again, a conditional average of the velocity and scalar fields (at a point indicated by the white dot) at x/D_s=0.27 provides evidence that this is the case, as shown in Figure 5.63, where the rotational symmetry exhibited by the long time-average (Figure 5.57) has been clearly distorted due to the vortices entraining dyed fluid.

In the above section the velocity and scalar fields of the main test condition have been discussed, and several important fluid mechanic properties of the flowfield have been identified, most notably the high energy periodic vortices issuing from the swirl stream which may be the cause of previously observed combustor oscillations. The impact of the central jet on these observed flow phenomena is assessed by comparison of the main test condition data to results of the no-jet test condition (where there is no addition of a central jet). The no-jet test conditions results are discussed in the following section.

5.3 No-Jet Test Condition

For the no-jet test condition the results are split into the following sections, the time-averaged velocity field is described in Section 5.3.1 and the measurements relating to flow unsteadiness are described in Section 5.3.2.

5.3.1 Time-Averaged Velocity Field

Figure 5.64 shows the mean velocity vectors in the x-r plane for the no-jet condition taken from the full 3D data set of the LS-PIV data. In this case, the backflow region in central region of the dump area expansion chamber induced by the swirl extends right up to the fuel injector exit plane (indicating a maximum radial pressure gradient in the fuel injector near-field) that seems to penetrate into the fuel injector swirl stream passage. Compared to the main test condition the corner re-circulation is less well defined and the swirl cone attachment point is further downstream with a mean location of x/D_S=1.5 (compared to x/D_S=1.2 in the main test condition). Since there is backflow right up to the fuel injector exit plane there is no free stagnation point.

Radial profiles of mean axial velocity within the dump area expansion chamber (at similar axial measurement locations used for the main test condition) are shown in Figure 5.65. Neglecting the obvious differences due to the central jet, the profiles exhibit similar trends. Iso-surfaces of $\overline{V_x}/V_{x,s} = 0.4$ are plotted in Figure 5.66, where the swirl stream cone shape can easily be seen; comparison to the iso-surfaces for the main condition (Figure 5.10) indicates that there is less flaring of the cone without the presence of a central jet at a location close to x/D_S=1, this is therefore why the mean attachment occurs further downstream.

Radial profiles of mean radial velocity within the dump area expansion chamber are shown in Figure 5.67, which also exhibit broad similarities with those observed for the main test condition. Circumferentially averaged radial profiles of mean circumferential velocity are shown in Figure 5.68. The circumferential velocity profiles are also broadly similar in shape to those at the main test condition for measurement locations x/D_S=0, 0.27 and 0.53. At axial locations beyond x/D_S=0.53 the similarity ends. Whilst in the main test condition the solid body rotation from the centreline continues to grow in size and diminish in strength (as the peak velocity reduces to $\overline{V_t}/V_{x,s} = -0.35$), in the no-jet test condition by x/D_S=2.65 the peak circumferential velocity has moved inboard to r/D_S=0.3 and has a peak velocity of $\overline{V_t}/V_{x,s} = -0.7$ resulting in the region of strong solid body rotation across the centreline with a well defined potential vortex further outboard. From the mean axial and circumferential velocity profiles the swirl number at the fuel

injector exit plane was calculated as Sn=0.80 (compared to Sn=0.78 for the main test condition).

Radial profiles of axial, radial and circumferentially averaged circumferential RMS velocity are shown in Figure 5.69, Figure 5.70 and Figure 5.71 respectively. In the fuel injector near-field ($x/D_s<1$) the turbulence field is again highly anisotropic and, neglecting the influence of the absent central jet, is broadly similar to that of the main test condition. However, in the fuel injector far-field, where in the main test condition the turbulence decayed to an isotropic background level, in the no-jet test condition the turbulence field remained anisotropic with a region of peak turbulence intensity persisting close to the centreline in radial and circumferential velocity component directions. Axial-radial and radial-circumferential shear stresses are shown in Figure 5.72 and Figure 5.73 where significant magnitudes of turbulence producing shear are not observed within the region of the far-field solid body rotation. Hence, the peak radial and circumferential turbulence levels are unexpected and must be attributable to some form of large-scale motion. It will be shown below that this large-scale motion is a Precessing Vortex Core (PVC). Inside the swirl stream passage, radial profiles of radial and circumferential velocity remained very similar to the main test condition, again indicting a flow separation between x/D_s=-0.43 and -0.27.

Figure 5.74 shows the turbulent kinetic energy in the x-r plane for one constant theta plane of the full 3D data set, again, in common with the main test condition, peak values occur in the inner edge of the swirl stream shear layer; however, the peak value is lower at k=0.6 compared to k=0.75 in the main test case. The region of high turbulence energy along the fuel injector centreline in the far-field is also shown. It is worth remembering that these peak values should not be considered as "true" turbulence energy as they contain large contributions from high-energy periodic events.

Turbulent integral timescales (calculated from HS-PIV measurement region B) are shown in Figure 5.75; the timescales derived from the axial velocity develop from less than 2ms in the near-field to over 60ms in the region identified as close to stagnant in common with the timescales calculated for the main test condition (Figure 3.20). However in the radial direction the timescales remained much lower (close to 30ms) relative to the main

test condition (where peak timescales approached 60ms). This difference is most likely due to the effect of the PVC. Turbulent integral length-scales are shown in Figure 5.76 (calculated from LS-PIV measurement region B), in the radial direction length-scales develop from $0.2D_s$ in the near-field to over $0.4D_s$ in the far-field in common with the main test condition (Figure 3.34), indicating that the PVC has little effect on turbulent length-scales. However, as would be expected, axial length-scales differ significantly between the test conditions; in the no-jet condition much longer length-scales are observed near the centreline in the fuel injector near-field, indicating a strongly correlated backflow region, this difference is clearly due to the influence of the absent central jet.

The data presented above has indicated that one significant difference between the two test conditions is the presence of a Precessing Vortex Core (PVC), clearly instantaneous measurements will provide a much more comprehensive analysis of this unsteady phenomenon. Measurements relating to the unsteady fluid mechanical behaviour of the flowfield in the no-jet test condition are discussed in the following section.

5.3.2 Measurements Relating to Flow Unsteadiness

A spatial PDF of the wall attachment point is shown in Figure 5.77 indicating a location of $x/D_s=1.5\pm1.0$ (as opposed to $x/D_s=1.2\pm0.5$ at the main test condition). The greater variance in this result indicates a larger "flapping" of the swirl stream cone without the presence of a central jet. It is also clear from Figure 5.77 that the mean attachment point does not represent the most probable reattachment point which occurs within the bin width $x/D_s=1.7$-1.8, the reason for this disparity is that a longer tail exists on the weaker penetration side relative to the higher penetration side.

PSD's deduced from axial velocity components at location ($x/D_s=0.27$, $r/D_s=0.27$, $\theta=0$) within the swirl stream inner shear layer are shown in Figure 5.78 as calculated from HWA in airflow (10kHz) and HS-PIV measurement region B in water flow (1kHz). As shown the two spectra agree very well, and again show strong periodic events occurring at frequencies well within the energy containing range of the turbulence. These peaks however occur over a broader range of frequencies than in the main test condition and have frequencies approximately half those identified in the main test condition (leading to Strouhal number of $St=0.6$ and $St=1.2$). The energy intensity is also close to an order of

magnitude less, this corresponds to the lower measured turbulent kinetic energy in the swirl stream shear layer. Contours of the peak frequency (calculated from HS-PIV measurement region B) are shown in Figure 5.79; this plot exhibits a similar pattern to that observed in the main test condition but at half the peak frequency.

A conditional average (calculated from HS-PIV in measurement region B) where the velocity fields were selected that exhibited fluctuating velocities 1.5 times the standard deviation at the point marked by a white dot, as shown in Figure 5.80. This conditionally averaged fluctuating velocity field is shown overlaid on the time-averaged radial velocity correlation contours in which again confirm the highly energetic periodic events are linked to coherent vortex structures observed in the swirl stream. However, the coherence between the positive maxima is significantly lower at 30% relative to the value in the main test condition of 50% and the distance between the positive maxima has increased to d=1.0 (d=0.6 in the main test condition). Again the Strouhal number corresponding to the dominant spike in the spectra can be linked to the length-scale d and the mean velocity. Due to the lower spatial coherence of the vortices, calculation of the RMS of the conditional sub-set of data did not reveal distinct localised peaks in turbulence energy (as found in the main test condition), this reduction in the spatial coherence also resulted in much noisier POD modes. Whilst the first two POD modes did identify some coherent turbulent structure it was a much less clear representation relative to the main test condition.

In the r-θ plane, Figure 5.81 shows a rank 5 SVD analysis (containing 78% of the total energy) of a Reynolds decomposed instantaneous velocity field at $x/D_s=0$. Whilst the two-strong co-rotating vortices are again clearly visible the weaker counter-rotating vortex pair that may be expected is not distinguishable. A PSD sampled at 1kHz taken at location ($x/D_s=0$, $r/D_s=0.25$, $\theta=0$) deduced from the circumferential velocity component (of HS-PIV axial measurement location $x/D_s=0$) is shown in Figure 5.82. The spectral pattern exhibits a similar shape to the axial and radial velocity PSDs' shown in Figure 5.78 with a dominant spike at St=0.6 and a second much less intense spike at St=1.2. Peak frequency contours are shown in Figure 5.83, where it can be seen that again, the dominant frequency of St=0.6 is prevalent at all radial locations and at all θ values within the swirl stream flow path at the fuel injector exit plane. For a Strouhal number of 0.6 the

circumferential velocity must be $\overline{V_t}/V_{x,s}=1.2$. This value is close to the mean circumferential velocity measured at $r/D_s=0.26$ (shown in Figure 5.68). Therefore the dominant spike in the spectrum corresponds to the motion of a *single* strong vortex passing a fixed point and thus the second (much weaker) peak is due to the frequency of rotation of the two strong co-rotating vortex pair past a fixed point. This differs from the main test condition in that the dominant frequency corresponded to the motion of the strong vortex *pair* and the second highest peak corresponded to the motion of the two-strong two-weak vortex pattern.

A time-averaged representation of these exit plane vortices was created using a rotating frame of reference as shown in Figure 5.84, where each rank 5 SVD instantaneous velocity field was rotated relative to the average angular velocity of the vortex structures using the methodology outlined in Section 5.2.2. The rotational average reveals the two-strong vortices and the previously unidentifiable two-weak vortex pair. The identification of the angular locations of the two strong vortex pair revealed that one strong vortex rotated 180°±25° (compared to 180°±14° in the main test condition). Calculation of the turbulent kinetic energy of the rotated data set is shown in Figure 5.85 where peak values occur in the region of the two-strong vortex pair at close to k=0.56 with values in the region of the weak vortices of approximately k=0.3. These regions of k are much more diffuse than in the main test condition, so partitioning the total turbulent kinetic energy into large and small scale contributions is difficult, however, for comparison the long time-averaged turbulent kinetic energy is shown in Figure 5.86 and at r=0.26 circumferentially averaged k=0.41. The first two POD modes (calculated from N=650 LS-PIV measurement location $x/D_s=0$ data) are shown in Figure 5.87 and Figure 5.88 respectively and show the two pairs of counter-rotating vortices, the POD analysis indicates that 31% of the total turbulent kinetic energy at the exit plane is as a result of large-scale coherent motion. POD analysis therefore highlights a tend of reducing energy contribution of the vortices without the central jet. This agrees with the spectral analysis.

Stream-traces issuing from $x/D_s=0$ at θ=0°, 90°, 180°, 270° in the full 3D data set are shown in Figure 5.89, which again exhibit helical flow paths. In comparison to the main test condition it can be seen that there are slight differences, especially in the fuel injector near-field where in the main test condition the stream-traces followed a tighter helical

path. This agrees with the differences observed in wavelength, d in the x-r plane spatial velocity correlation.

Figure 5.90 shows the time-averaged radial velocity correlation contours (calculated from LS-PIV measurement location) at $x/D_s=0$, the spatial correlation between the vortices can be seen to be close to 30% (70% in the main test condition, Figure 5.48). This again is as a result of the increased standard deviation in the out-of-phase vortex rotation, and helps to explain why the dominant frequency corresponds to the rotation of a single strong vortex past a fixed point and not a vortex pair. A cross-correlation of the circumferential velocity over one time-step (66ms) is shown in Figure 5.91 and reveals that the vortices are also much less coherent in time (25%) relative to the main test condition (50% over 330ms, see Figure 5.51). The reduction in spatial and temporal coherence explains the broader band spectral peaks and the lower peak energy intensities, which will have the net affect of reducing the energy contribution of the vortices, as also identified by the rotational average and first two POD modes.

Measurements inside the fuel injector swirl stream again reveal that the counter-rotating vortex pairs are visible up to $x/D_s=-0.27$; however, by this point the spatial correlation is very weak and a rotational average reveals that the weakly coherent structures appears very close to the inner body. Velocity cross-correlation also reduces to background noise over one 66ms. At $x/D_s=-0.13$ the first two POD modes identify the turbulent structure, however, the energy contribution of the vortices is only 16% and by $x/D_s=-0.27$ no clear coherent structure could be identified. Further upstream into the fuel injector spatial velocity correlations decay to background noise as shown for $x/D_s=-0.43$ in Figure 5.93 and POD identifies no coherent structures in the first few modes.

From the above discussion it seems that whilst the swirl stream inner shear layer vortices are still present without the addition of a central jet, they are much less coherent in space and time and therefore contain much less energy. This reduction in energy of the vortices must then be linked to the motion of a PVC (which is damped with the addition of a central jet). The PVC is discussed in the following section.

5.3.2.1 Precessing Vortex Core

As previously mentioned, a significant difference between the main and no-jet test conditions was observed in the radial profiles of radial and circumferential velocity the fuel injector far-field. In the main test condition an area of weak solid body rotation was observed, this weak rotation meant that no clear aerodynamic swirl centre could be observed. However, in the no-jet test condition a strong solid body rotation existed near the centreline and (in r-θ plane PIV measurements) the aerodynamic swirl centre was clearly observed. The aerodynamic centre of this strong solid body rotation then precessed significantly with time about the geometric centre of the dump area expansion chamber. This is shown for two time instants in Figure 5.94 and Figure 5.95; the geometric centre is indicated by the red dot. Reynolds decomposition at the same instants in time are shown in Figure 5.96 and Figure 5.97 and reveal that the turbulence field forms two counter-rotating vortices as previously identified by Graftieux *et al* (2001) where the large fluctuating velocity components in the centreline region will contribute significantly to the high centreline turbulence intensities. The first POD mode shape clearly identifies these counter-rotating vortices as shown in Figure 5.98.

A PSD in air using HWA at a sampling rate of 1kHz at x/D_s=2.65 and r/D_s =0.19 (within the region of the solid body rotation) reveals a broadband frequency spike between St=0.66 and 0.78 as shown in Figure 5.99. The Strouhal number is now based on the dump area expansion chamber diameter, D_{ex}=140mm and the corresponding bulk average velocity. This is consistent with the measurements of Syred *et al* (1994) who predicted that for a swirl number of 0.75, the Strouhal number, $St_Q = 0.72$, see Figure 1.7 (noting that St_Q is a factor of $\pi/4$ greater than the Strouhal number defined in this thesis).

Using the swirling strength algorithm to identify the aerodynamic centre of the instantaneous solid body rotation, its angular location could be plotted against time, as shown in Figure 5.100. The saw tooth pattern indicates a coherent rotational motion of the PVC about the geometric centre. A spatial PDF of the location of the PVC is then shown in Figure 5.101 (calculated from LS-PIV axial measurement location x/D_s=2.65), the most probable location of the aerodynamic centre of the PVC is close to the geometric centre of the duct with the outer bounds of the vortex centre precession being close to

r/D_s=0.4. Streamlines from a rotational average (calculated from N=650 LS-PIV data) at x/D_s=2.65 using the previously calculated angular locations of the aerodynamic swirl centres as the reference rotation angle are shown in Figure 5.102. As can be seen there is a mean displacement of the aerodynamic centre of r/D_s=0.12 relative to the geometric centre (yellow dot), or in terms of the dump area expansion chamber diameter r/D_{ex}=0.03 (3.2%); this closely matches the findings of Froud *et al* (1995) who estimated the mean displacement (in a circumferential entry swirl burner) to be 3.5%. Figure 5.103 shows the rotationally averaged turbulent kinetic energy, where at r/D_s=0.12, close to the centre of the mean displacement, k=0.24, whereas at r/D_s=0.12 in the location 180° out-of-phase with the centre of the mean displacement k=0.035. The long time-averaged turbulent kinetic energy (calculated from the same LS-PIV axial measurement location x/D_s=2.65 data) is shown in Figure 5.104 and where at r/D_s=0.12, k=0.2. This indicates that the large-scale contribution of the PVC to the measured turbulence is approximately 82.5% ((0.2-0.035)/0.2), this agrees closely with the estimations of Grosjean *et al* (1997) and Graftieux *et al* (2001).

The above discussions of the main and no-jet test conditions indicate the presence of high energy vortices in the swirl stream inner shear layer that both influence the scalar transport and mixing processes and seem to be destabilised by a PVC. However, at this point, what causes them is not known. What is known is that they originate inside the fuel injector at a point (perhaps coincidentally) near to the internal corner of the swirl stream passage; a point that radial profiles of radial and circumferential velocity have indicated as a region of flow separation off the inner body. In order to improve our understanding of the vortex production mechanisms the modular swirler was used. The modular swirler results are discussed in the following section.

5.4 Modular Swirler

The modular swirler was used to allow for the effects of varying the swirl flow path geometrical definition and the radial flow slot angle to be investigated, in particular the multiple helical vortices originating inside the swirl stream passage. Initially the modular swirler was configured in a "base" case configuration which had similar axial and circumferential velocity ratios (between inlet and exit planes of the swirler) to the datum fuel injector, but without the discontinuous wall gradient (corner) at x/D_s=-0.27, see

Figures 2.6 and 2.7. The base case configuration with a slot angle of α_1=30° provided the most similar configuration to the datum fuel injector (in the no-jet test condition). Therefore, unless stated otherwise, all comparisons between the base case modular swirler results and the datum fuel injector results, are based on comparison to the no-jet test condition results.

Figure 5.105 Figure 5.106 and Figure 5.107 show radial profiles of mean axial, radial and circumferentially averaged circumferential velocity at the swirler exit plane (x/D_s=0). As expected, the base case configuration with α_1=30° provides broadly similar profiles to those measured for the datum fuel injector (see Figure 5.65 to Figure 5.68). Clearly the slot angle has a significant impact on the exit plane radial profiles; as the slot angle is increased from the no swirl condition (α_1=0°) the mean axial velocity profiles change from a close to constant plug flow to a heavily outer wall bias. The increase in peak radial velocity signifies a greater outboard motion and mean circumferential velocity profiles change from a well developed Rankine vortex shape to a clearly defined inner region of solid body rotation and a less well defined potential vortex at large radii. The changes in mean axial and circumferential velocity profiles result in an increase in swirl number with increasing slot angles as shown below:-

Sn=0.72	(α_1=30°)
Sn=0.57	(α_1=20°)
Sn=0.47	(α_1=10°)
Sn=0	(α_1=0°)

Where, the base case swirl number of Sn=0.72 (with a slot angle α_1=30°) compares well to the datum fuel injector swirl number (in the no-jet test condition) of Sn=0.8.

PSDs' deduced from HWA radial traverses at x/D_s=0.27 in the airflow rig (at a 25kHz sampling rate) are shown for the base case flow path configuration with a swirl slot angle of 30° (Sn=0.72) in Figure 5.108. As can be seen, two spikes are observed at St= 0.54 and St=1.08; these are similar to those observed for the datum fuel injector, where dominant spikes occurred at St=0.6 and St=1.2 (see Section 5.3.2). From the previous analysis, these dominant frequencies must correspond to the motion of one strong vortex

and a pair of co-rotating vortices past a fixed point. This result shows conclusively that the internal corner of the datum fuel injector is *not* the cause of the instabilities in the swirl stream. The fact that the spikes occur at the same frequency at all radial traverse locations is not surprising as frequency contours for the datum fuel injector indicated that the dominant frequency was constant throughout the near-field within the region swirl stream flow path. The difference in the intensity of the spectral spikes at different locations in the radial traverse is due to the variation of turbulent kinetic energy across the swirl stream as shown in Figure 5.109 where the black line indicates the location of the HWA radial traverse. Comparison of the turbulent kinetic energy with that measured for the datum fuel injector (Figure 5.74) again shows a good commonality between the flowfields, further justifying the conclusion that the internal corner is not a primary cause of the unsteady flow features. As the modular swirler flowfield is comparable to the no-jet condition, it is not surprising to observe far-field peak levels of turbulent kinetic energy close to the centreline, which correspond to the motion of a PVC. However, peak levels of k are slightly lower for the modular swirler geometry at k=0.15 than for the datum fuel injector at k=0.2. It seems therefore, that the internal geometry of the swirler passage does exert a small influence on the downstream flow and has an effect on the motion of the PVC.

By reducing the swirl slot angle (an hence the swirl number) in the base case configuration, the change in the spectral characteristic is shown in Figure 5.110. In this figure each PSD was selected (from a radial traverse set) so that it represented the maximum turbulent kinetic energy location, as calculated from integration of the PSD. It can be seen that the intensity of the two dominant spikes in the spectra diminishes with reducing slot angle until by α_l=10°, no dominant spikes are observed. The effect on the turbulent kinetic energy of this reduction in the dominant spikes (measured by integration of the spectra) is shown in Figure 5.111 which shows a linear trend of increasing k with increasing slot angle (swirl number). It may also be seen from the spectra presented in Figure 5.110 that the dominant frequency increases with increasing slot angle (or swirl number), this is shown more clearly in Figure 5.112.

Whilst the above analysis shows the dominant frequency of the flow instabilities is influenced by the swirl number, in order to assess the impact of the swirl stream flow

path geometry, the modular swirler was configured with various swirl stream geometries. By carefully selecting inner and outer wall definitions (see Section 2.2), the effects of varying the bulk average axial velocity ratio between the swirler inlet and exit planes ($V_{x,s}/V_{x,r}$) relative to the base case, or varying the bulk average circumferential velocity ratio ($V_{t,s}/V_{t,r}$) relative to the base case could be assessed. The results showed that in all cases similar spectral characteristics (to the base case) were observed, whereby two dominant spikes occurred, which reduced in intensity with reducing slot angle until $\alpha_1<10°$ where no visible spikes were observed. The dominant frequencies, however, shifted depending on the flow path definition. The effect of the axial and circumferential velocity ratio variation (over the swirl stream passage) on the dominant frequency is shown in Figure 5.113 and Figure 5.114 respectively. As can be seen the peak Strouhal number reduces with increased axial acceleration and increases with increased circumferential velocity ratio for a given slot angle. The reason for this is simply that by increasing the flow streamwise acceleration (for a constant circumferential velocity ratio) the swirl number will reduce, however, by increasing the swirl velocity spool up (for a constant axial acceleration) the exit plane swirl number will increase. This result provides further evidence of the swirl stream flow instabilities dependence on the swirl number.

Some of the frequency domain observations (for the base case flow path definition) were confirmed in the spatial domain using PIV measurements. Measurements of the turbulent kinetic energy confirm the reduction in peak values with decreasing swirl number, as shown by comparison of Figure 5.109, Figure 5.115 are Figure 5.116 for slot angles of $\alpha_1=30°$, $\alpha_1=20°$ and $\alpha_1=10°$. The reduction in the intensity of the second highest spike in the spectra is indicated by radial velocity spatial correlations in the r-θ plane at $x/D_s=0$ for $\alpha_1=30°$, $\alpha_1=20°$ and $\alpha_1=10°$, which are shown in Figure 5.117, Figure 5.118 and Figure 5.119. The correlation between the vortices reduces from approximately 60% for $\alpha_1=30°$ to 10% for $\alpha_1=20°$, and by $\alpha 1=10°$ there is no discernable correlation. The reduction in the intensity of the primary spike with reducing swirl number is indicated by cross-correlation of the radial velocity over a time-step of 66ms, as shown for $\alpha_1=30°$ and $\alpha_1=20°$ in Figure 5.120 and Figure 5.121. At $\alpha_1=30°$, it can be seen that there is a 35% cross-correlation, however, by $\alpha_1=20°$, the cross-correlation has reduced to a level close to background noise. An interesting feature of the base case configuration with $\alpha_1=30°$ is

that the coherence between the two strong vortices is much greater at 60%, than for similar measurements using the datum fuel injector (in the no-jet test condition) where the coherence was 30% (see Figure 5.90). Velocity cross-correlations also reveal a greater coherence with time, where for the base case configuration the coherence over 66ms was 35% however for the datum fuel injector this value was only 25% (see Figure 5.91). It seems therefore that the removal of the internal corner has a stabilising affect on the coherent turbulent event issuing from the fuel injector. This increased stabilisation must therefore be linked to the reduction in strength of the PVC, indicating that, as hypothesised, the PVC is responsible for destabilising the vortices in the no-jet test condition.

Measurements using the datum fuel injector (discussed previously) showed that these periodic vortices not only occurred in the dump area expansion chamber, but also inside the swirl stream passage up to x/D_s=-0.27 (in both the main and no-jet test cases). This axial location (perhaps coincidentally) corresponded to the point of the internal corner and also the point of a possible flow separation off the inner body of the fuel injector. However, this last point could not be confirmed for the datum geometry, due to significant distortion in the x-r plane through the flange. Utilising the modular swirler base case definition with α_1=30° a clear optical path into the swirl stream (in an x-r plane) was provided by placing the movable flange (see Figure 2.5) close to the swirl slot exit plane. The flow separation can now be seen clearly, as shown in Figure 5.122, where the mean separation point is at x/D_s=-0.25. This result proves conclusively that the internal corner is *not* the primary trigger for the flow separation off the inner body of the fuel injector. The mean point of flow separation moves further downstream to x/D_s=-0.1 for α_1=20° (Figure 5.123) and by α1=10° there is no flow separation, as shown in Figure 5.124. When the slot angle is large enough to induce a flow separation of the inner body, spatial velocity correlations confirm that the flow separation is intrinsically linked to the coherent turbulent events in the dump area expansion chamber. Using α_1=30° and the base case geometry, Figure 5.125 shows a radial velocity spatial correlation map with its reference point (signified by the white dot) in the region of the flow separation. As seen the correlation map indicates a strong coherence with a repeating pattern in the swirl stream which is known to be linked to the helical vortices. However, a correlation map created using a reference point upstream of the mean flow separation point shows no

significant coherence with events in the dump area expansion chamber, see Figure 5.126. This is strong evidence that the vortices are linked to the flow separation and not other processes such as shedding off the radial entry slots.

For the base case configuration with α_l=30° the first two POD modes, accounting for 47% of the total turbulent energy, are shown in Figure 5.127 and Figure 5.128. Both these POD modes show (as indicated previously by the spatial correlation maps) the vortices to originate in the region of the flow separation inside the swirler body. For the base case geometry with α_l=20° the first two POD modes are shown in Figure 5.129 and Figure 5.130. The most energetic spatial projection now contains 40% of the total turbulent kinetic energy but shows no indication of coherent turbulent structure, however, the second and third POD modes indicates the presence of the vortex structures which contribute 21% of the total energy, the second POD mode is shown in Figure 5.130. POD analysis for the base case geometry with α_l=10° reveals no coherent structure. The POD analysis indicates that the vortices become less energetic with reducing slot angle until by α_l=10° they are not detectable. This result agrees with the spectral analysis, where periodicity due to the strong co-rotating vortices was not observed with slot angles of α_l<10° (see Figure 5.110) and a reducing peak turbulent kinetic energy was measured in the swirl stream shear layer with reducing slot angle (see Figure 5.111).

What is not clear up to this point is whether the vortices are formed due to the direct effect of increased slot angle (swirl number) in the swirl passage or due to some interaction in the flow separation, i.e. are the vortices formed if the swirl number is high but the internal geometry is such that there is no separation of the inner wall? This question is to a large part answered by analysis of measurements taken using the modular swirler with parallel walls (where $V_{x,e}/V_{x,r}$=1 and $V_{t,e}/V_{t,r}$=1). By selecting a slot angle of 30° (resulting in a swirl number of 0.95) the mean velocity vectors overlaid on turbulent kinetic energy contours are shown in Figure 5.131. There is now no mean flow separation observed off the inner body and even though the swirl number is higher than in all of previous test cases the peak levels of k=0.35 are half that of the base case. Radial velocity spatial correlation contours at the fuel injector exit plane then indicate no coherent turbulent structure issuing from within the swirl passage (Figure 5.132). Thus without a flow separation vortices are not formed inside the fuel injector. However,

spectra deduced from radial traverses of 25kHz sampling rate HWA, taken at x/D_s=0.27 with a slot angle varying from 0°-30° show a distinct spectral spike at $\alpha 1$>20°, as shown in Figure 5.133. Whilst, instantaneous x-r plane velocity field measurements provided no strong evidence of periodic coherent turbulence structure in the inner shear layer region of the swirl stream (which would create a spike in the spectra) the first POD mode does indicate the formation of a vortex structure close to the swirler exit, shown in Figure 5.134.

From the above analysis it is therefore postulated that the vortices are formed due to an interaction of the forward flow of the swirl stream with the backflow (reverse flow) occurring in the main dump expansion chamber. Therefore if the swirl number is high enough to create a vortex breakdown they an inevitable consequence. However, as the swirl number increases the reverse flow gets stronger and is able to penetrate further upstream, thus this interaction also moves upstream, eventually entering the fuel injector itself. If the vortices form inside the swirl stream flow path they are much more coherent and energetic than if they form in the dump area expansion chamber.

5.5 Closure

In this chapter the datum fuel injector flowfield was described for two test conditions, the main test condition (with the presence of a central jet) and the no-jet test condition (without a central jet). This enabled several important fluid mechanical characteristics of the flowfield to be identified. Measurements using the modular swirler then helped to improve our understanding of the observed unsteady turbulent phenomena. In the main test condition, unexpectedly high time-averaged turbulent kinetic energy levels in the inner shear layer of the swirl stream were shown to be significantly influenced by the periodic appearance of high-energy time-dependent vortices. These vortices formed a two-strong two-weak rotating vortex pattern that was convected in a helical flowpath. It is unclear as to why two strong vortices exist, although it may be hypothesised that this flow pattern must form the most energy efficient structure, with the two-weak vortices necessarily counter-rotating relative to the two-strong vortices to satisfy continuity. The strong vortex pair was shown to entrain bursts of dyed fluid towards the vortex centres with a mixture fraction that would be close to stoichiometric in a combusting test case.

Hence, these vortices will cause bursts of high heat release and will be responsible for undesirable combustor oscillations.

By comparison, in the no-jet condition the helical vortex pattern was much less coherent in space and time resulting in a lower energy contribution and hence, lower turbulent kinetic energy levels in the region of the swirl stream inner shear layer. This trend was confirmed by POD analysis where the energy contribution of the first two modes reduced from 46% (main test condition) to 31% (no-jet test condition). The reduction in coherence and energy of the shear layer vortices was due to the appearance of a PVC motion, which was only observable in tests without the presence of the central jet. The PVC is a periodic rotation of the aerodynamic centre of a strong solid body rotation about the geometrical centre. This large-scale and highly energetic motion destabilised the swirl stream cone, which was indicated by the increased variation in the cone attachment point on the outer wall from $1.2D_s \pm 0.5$ (with the central jet) to $1.5D_s \pm 1.0$ (without the central jet). The reduction in coherence of the inner shear layer vortices in tests without a central jet also resulted in a dominant frequency in the fuel injector near-field being related to the motion of a single shear layer vortex. However, when the PVC was damped out (on addition of a central jet) the dominant frequency was related to the motion of the strong shear layer vortex pair, hence the dominant frequency was doubled.

Measurements using the modular swirler showed that the corner in the internal geometry of the fuel injector swirl stream passage did not cause the observed flow separation off the inner wall which had been identified as linked to the origin of the helical shear layer vortices. The link between the internal flow separation and the periodic helical shear layer vortices was established by spatial velocity correlations, which showed that turbulent events inside the flow separation were correlated to the vortices further downstream. However, it was also found that vortex formation still occurred even when the fuel injector geometry was changed so that the internal flow separation was not present, if the Swirl number was high enough. Therefore, it is postulated that the shear layer vortex formation is a function of the Swirl number and the interaction between the forward flow of the swirl stream with the backflow (reverse flow) occurring in the main dump expansion chamber. It is believed that this occurrence was a "secondary" vortex breakdown mechanism (the primary occurrence being the reverse flow in the main dump

expansion chamber) and is similar to the helical mode flow instability observed by Sarpkaya (1971). As the Swirl number increases, the reverse flow gets stronger and is therefore able to penetrate further upstream. Hence, the interaction also moves upstream, possibly entering the fuel injector itself if the Swirl number is high enough. If the vortices are formed inside the fuel injector then they appear much more coherent in space and time and hence are higher energy. Perhaps this is because they are stabilised by the confining nature of the swirl passage geometry.

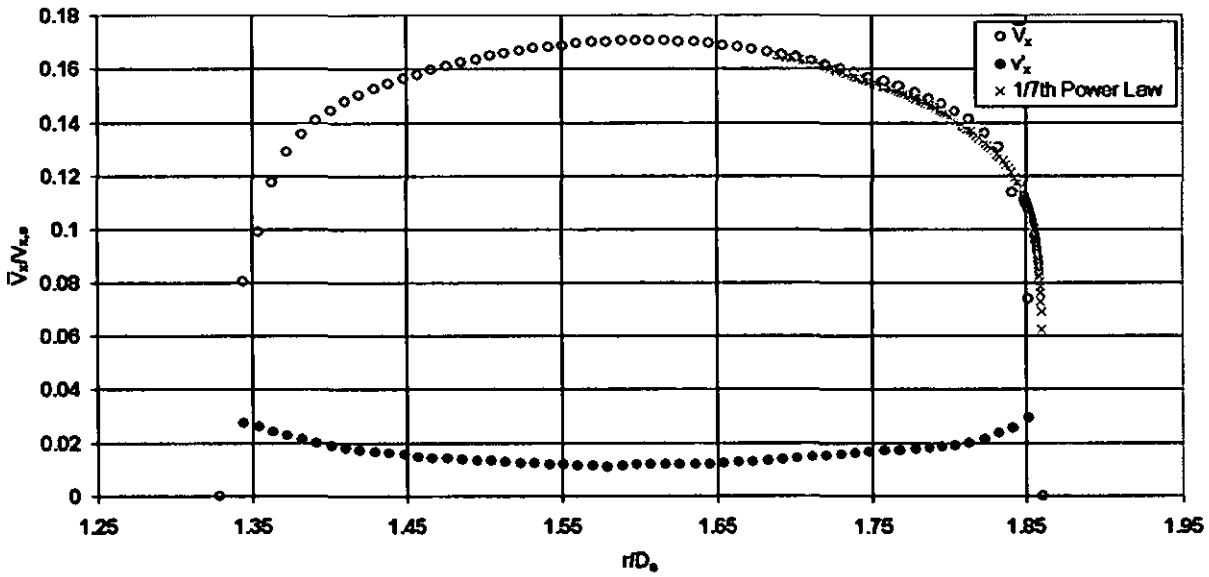

Figure 5.1. Mean and RMS Axial Velocity Profiles and 1/7th Power Law Approximation at x/D_s=-2.65 in the Swirl Stream Feed Path ($Re=5.68\times10^3$)

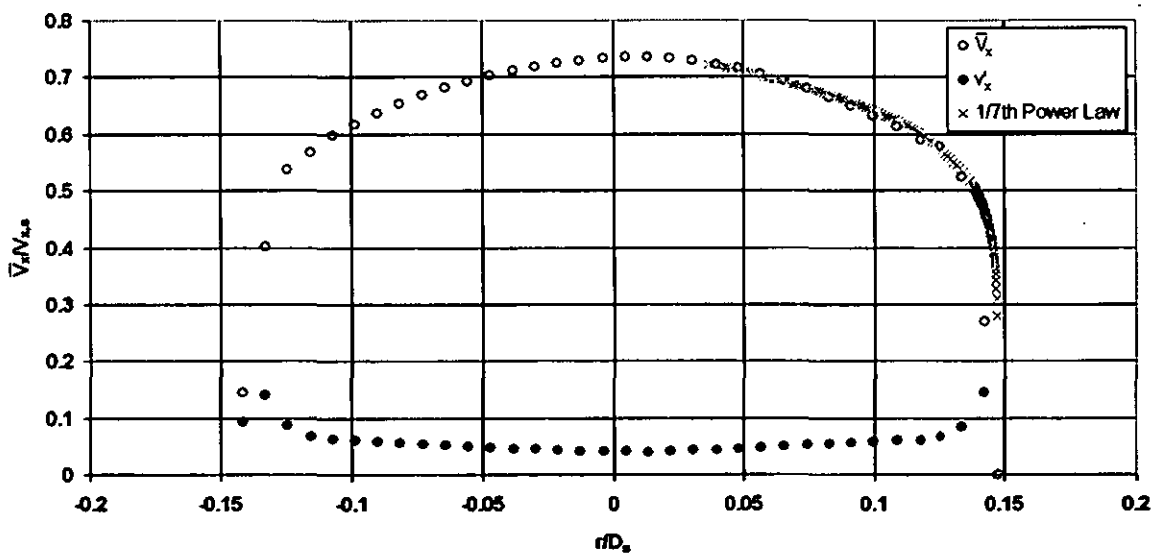

Figure 5.2. Mean and RMS Axial Velocity Profiles and 1/7th Power Law Approximation at x/D_s=-2.65 in the Central Jet Feed Pipe ($Re=11.69\times10^3$)

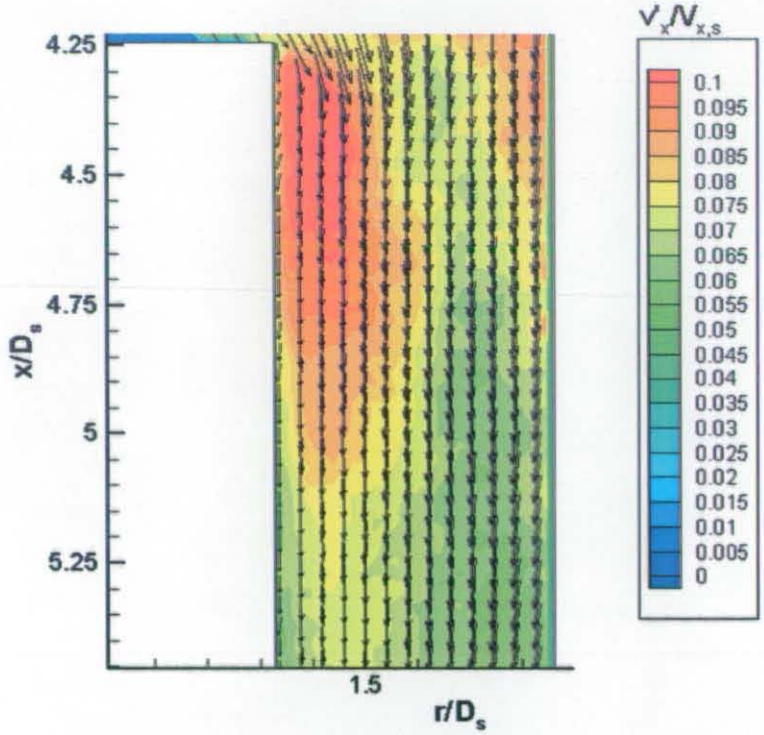

Figure 5.3. Mean Velocity Vectors Superimposed on Axial RMS Velocity Contours in Annular Exit Gap

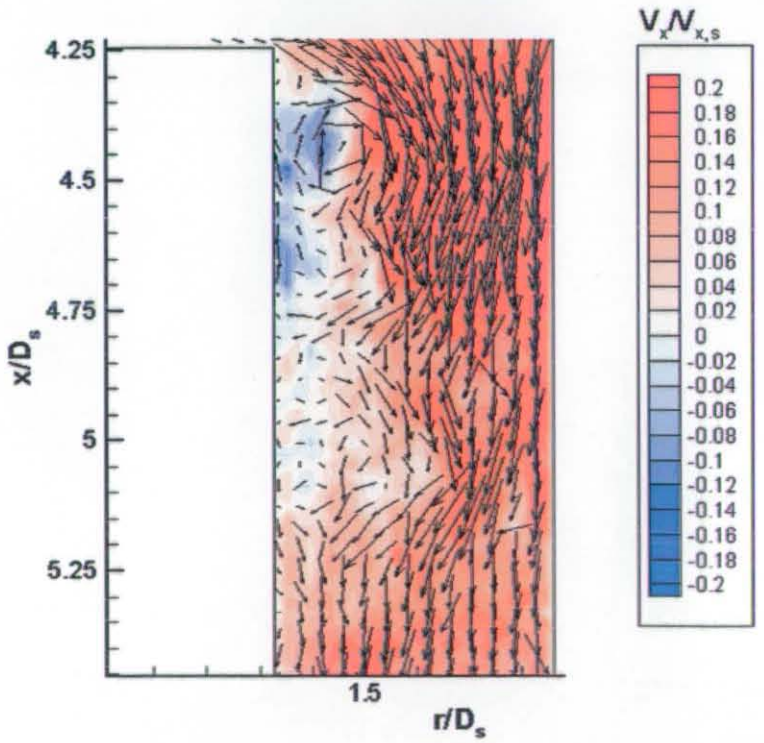

Figure 5.4. Instantaneous Velocity Vectors Superimposed on Instantaneous Axial RMS Contours in Annular Exit Gap

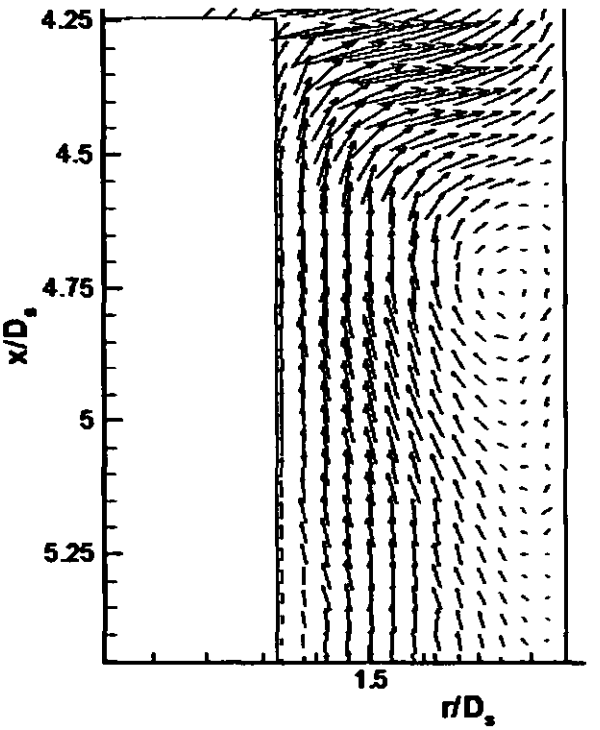

Figure 5.5. Fist POD Mode in Annular Exit Gap

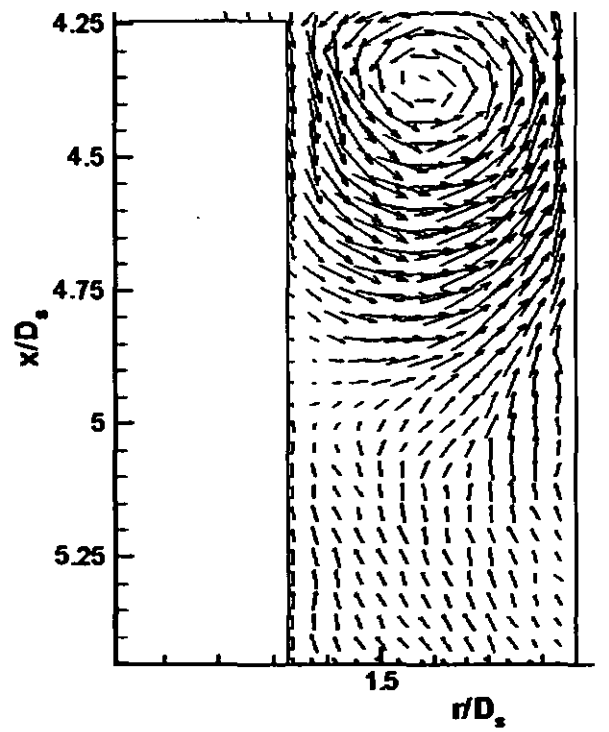

Figure 5.6. Second POD Mode in Annular Exit Gap

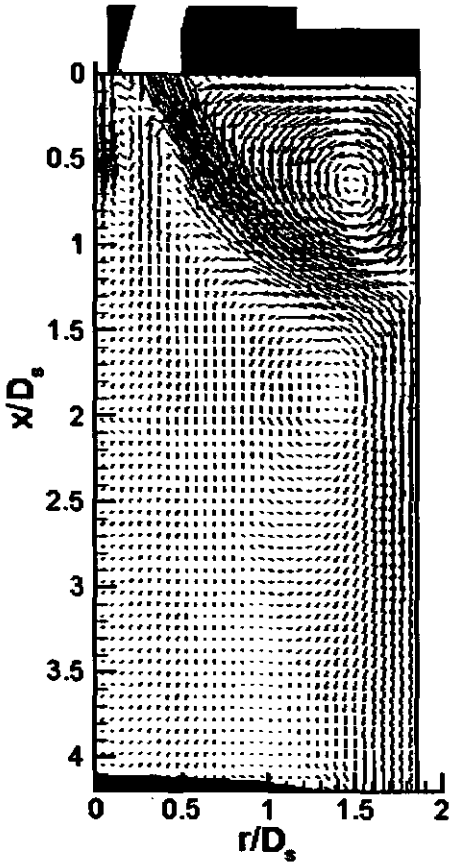

Figure 5.7. Mean Velocity Vectors in Dump Area Expansion Chamber (Main Test Condition)

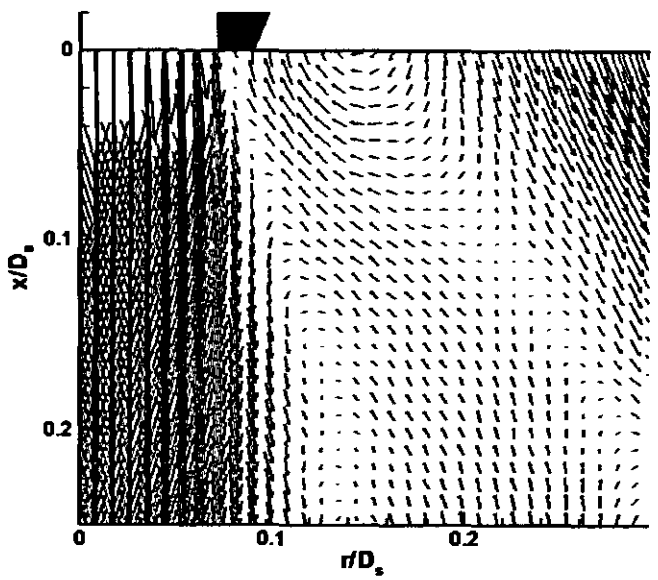

Figure 5.8. Mean Velocity Vectors Close to the Fuel Injector Exit (Main Test Condition)

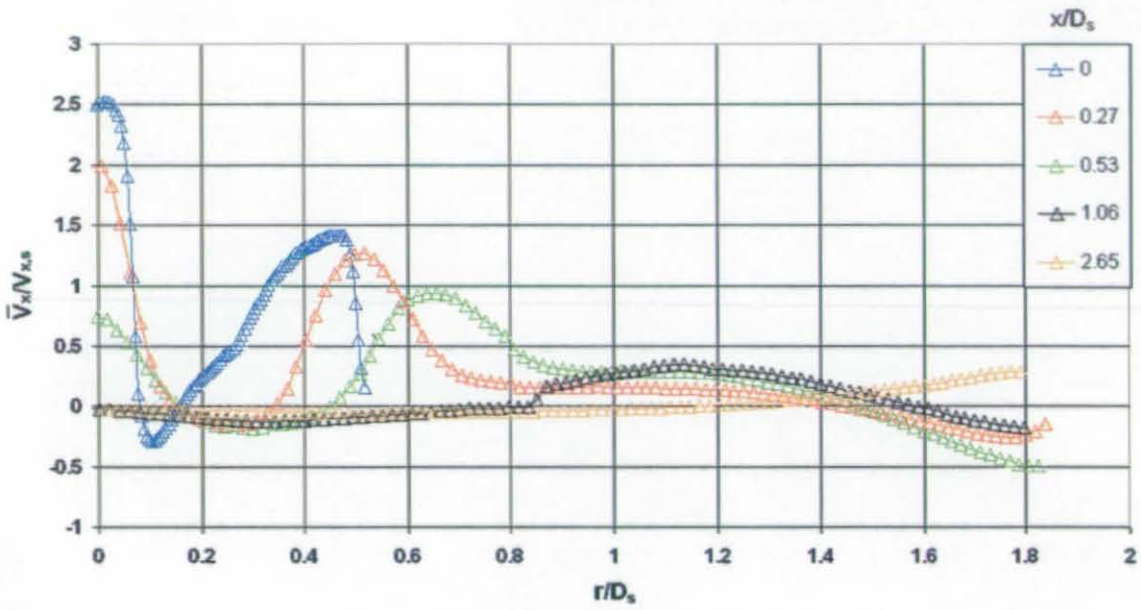

Figure 5.9. Mean Axial Velocity Profiles in Dump Area Expansion Chamber (Main Test Condition)

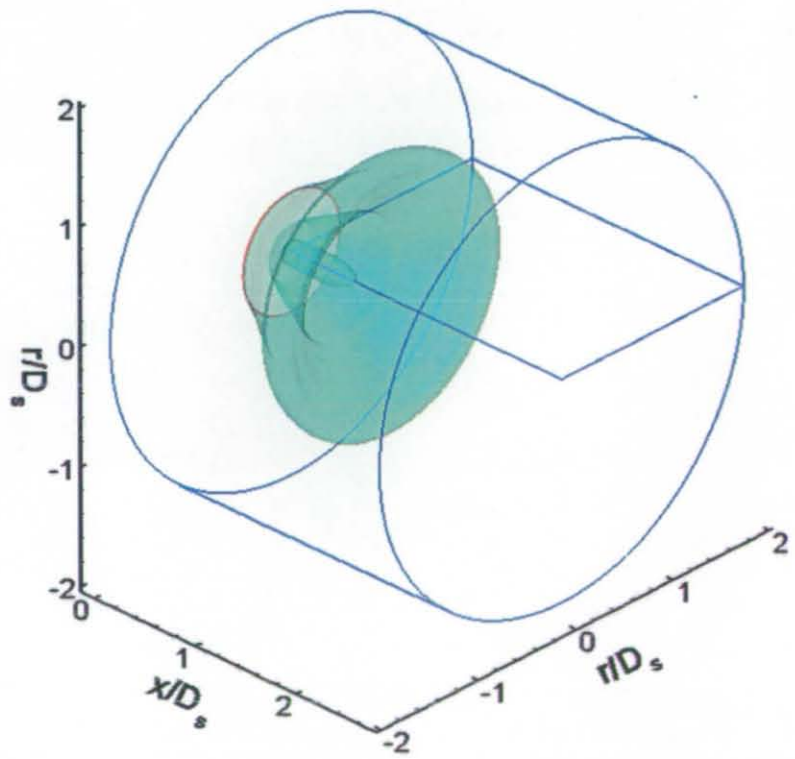

Figure 5.10. Iso-Surfaces of $\overline{V_x} / V_{x,s} = 0.4$ (Main Test Condition)

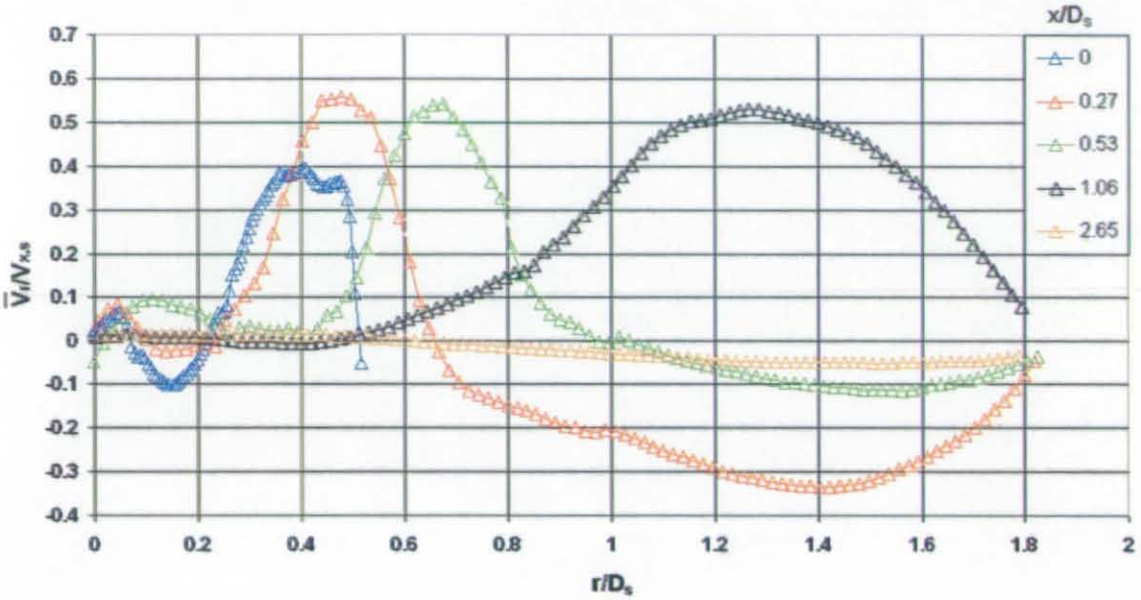

Figure 5.11. Mean Radial Velocity Profiles in Dump Area Expansion Chamber (Main Test Condition)

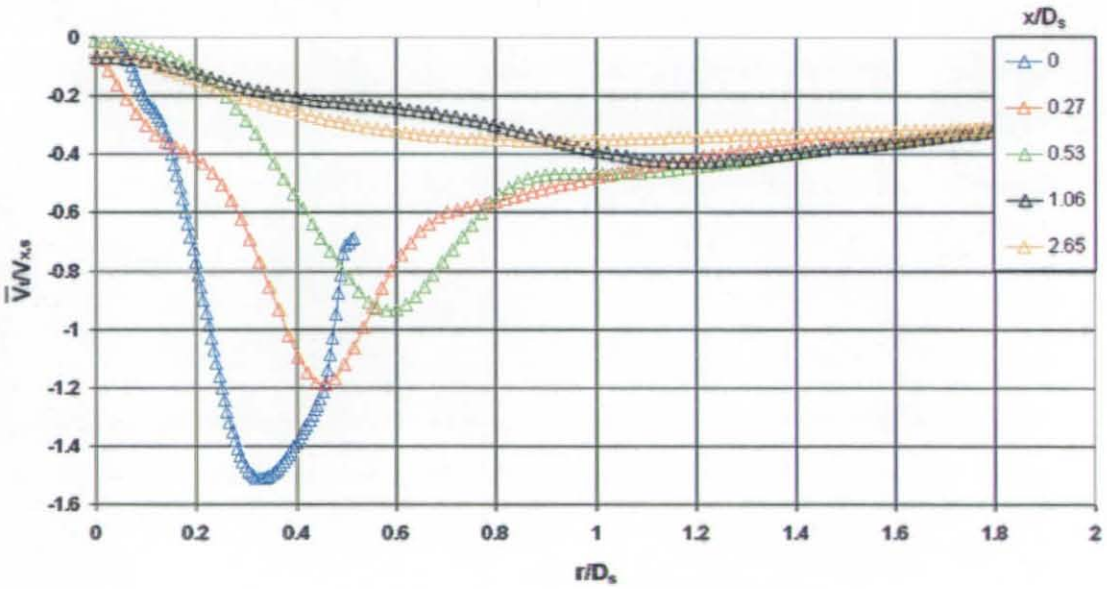

Figure 5.12. Mean Circumferential Velocity Profiles in Dump Area Expansion Chamber (Main Test Condition)

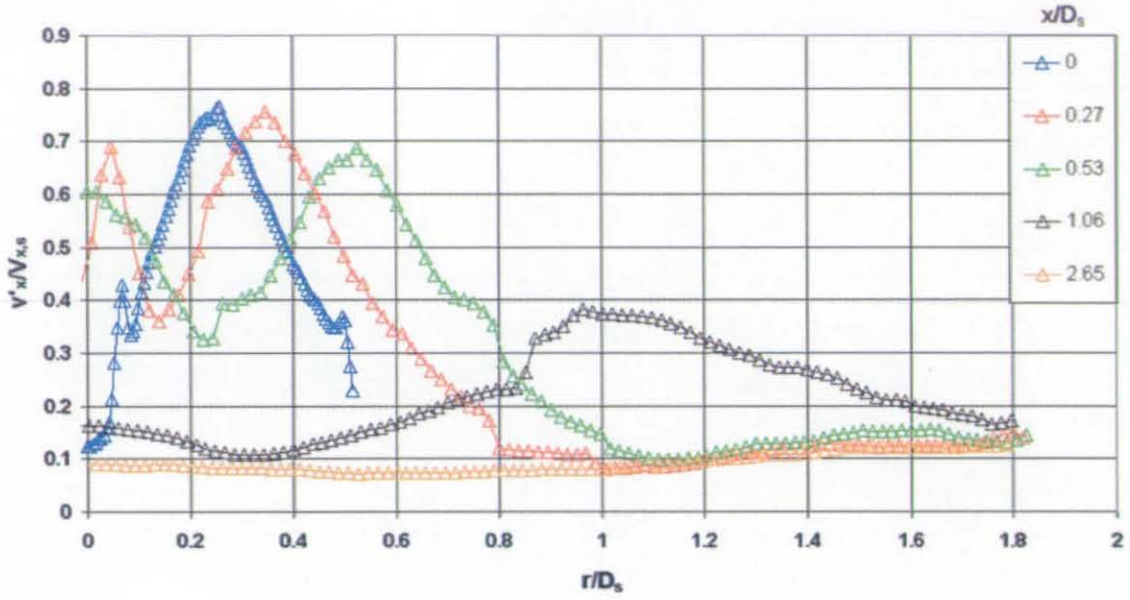

Figure 5.13. Axial RMS Velocity Profiles in Dump Area Expansion Chamber (Main Test Condition)

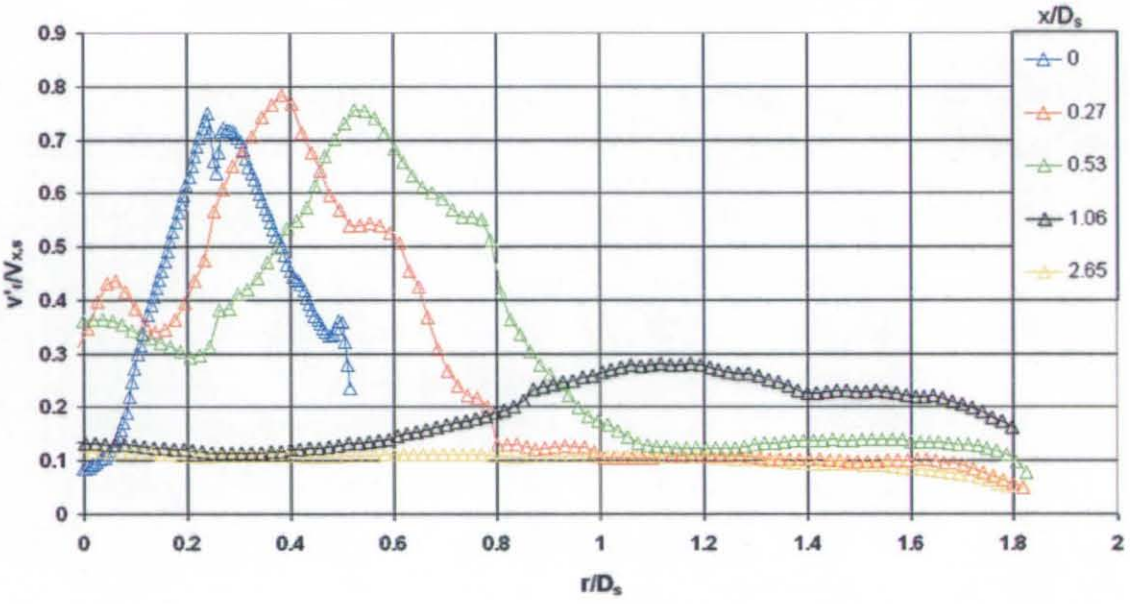

Figure 5.14. Radial RMS Velocity Profiles in Dump Area Expansion Chamber (Main Test Condition)

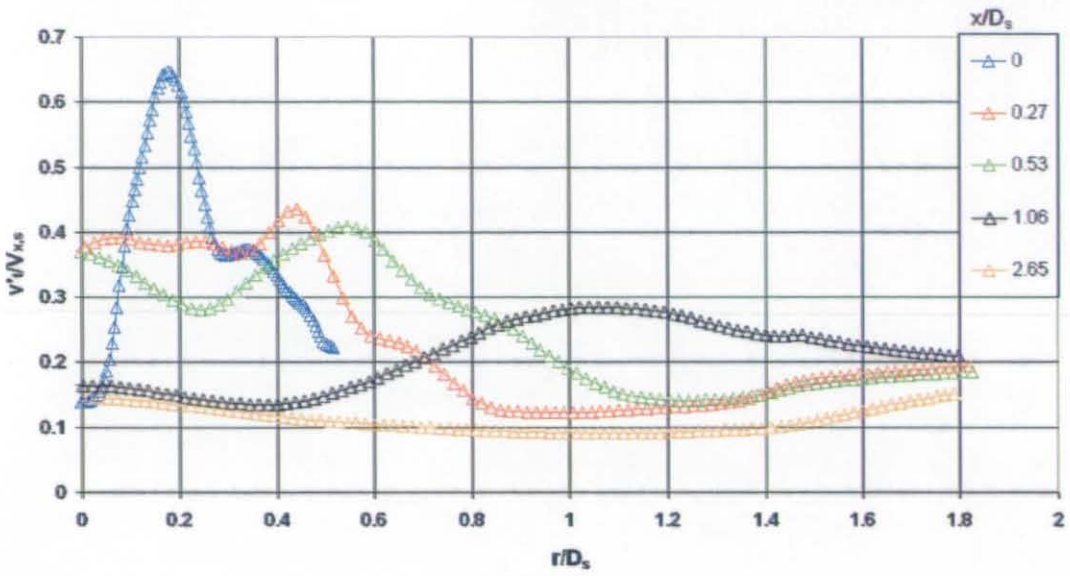

Figure 5.15. Circumferential RMS Velocity Profiles in Dump Area Expansion Chamber (Main Test Condition)

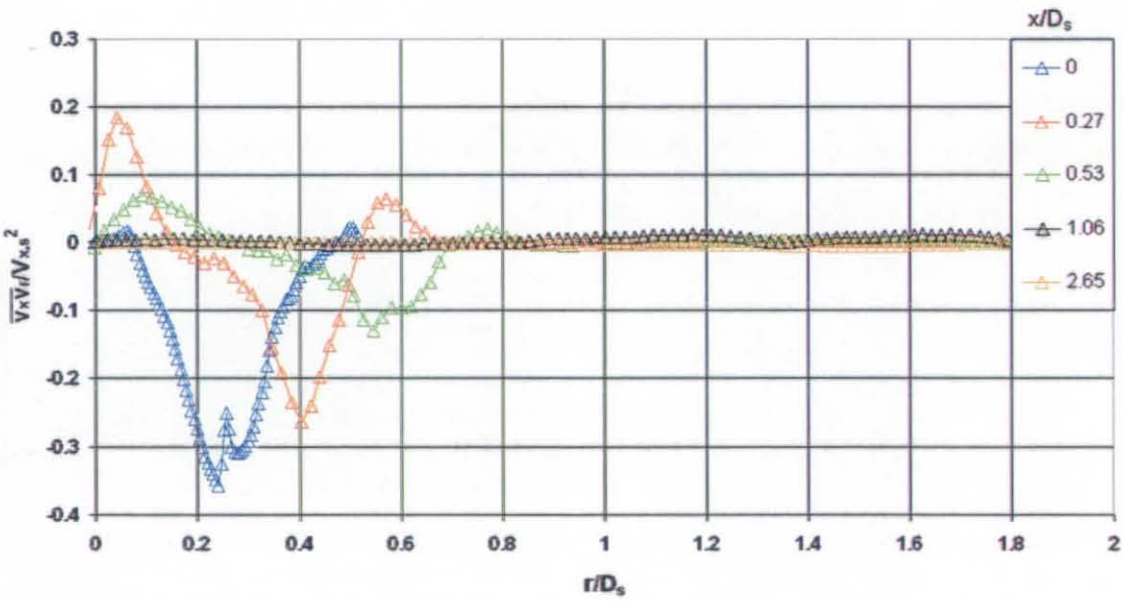

Figure 5.16. Axial-Radial Shear Stress Profiles in Dump Area Expansion Chamber (Main Test Condition)

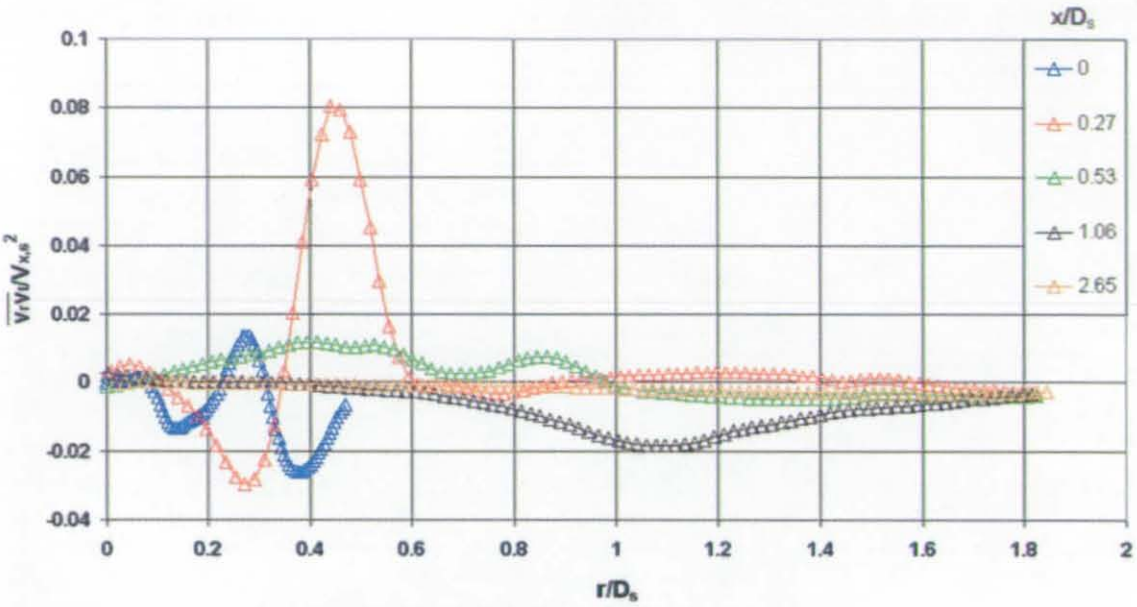

Figure 5.17. Radial- Circumferential Shear Stress Profiles in Dump Area Expansion Chamber (Main Test Condition)

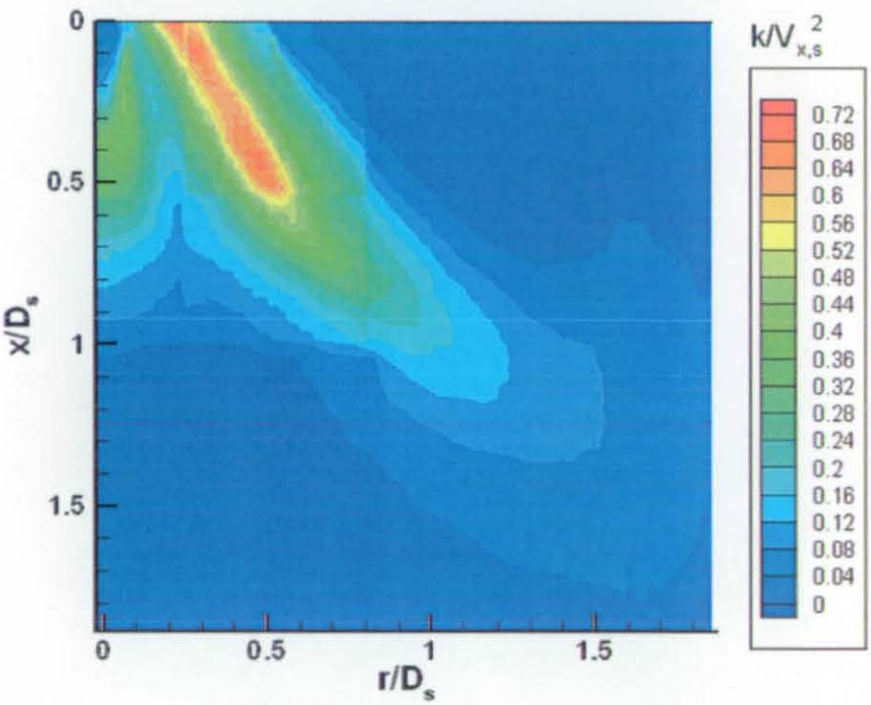

Figure 5.18. Turbulent Kinetic Energy Contours (Main Test Condition)

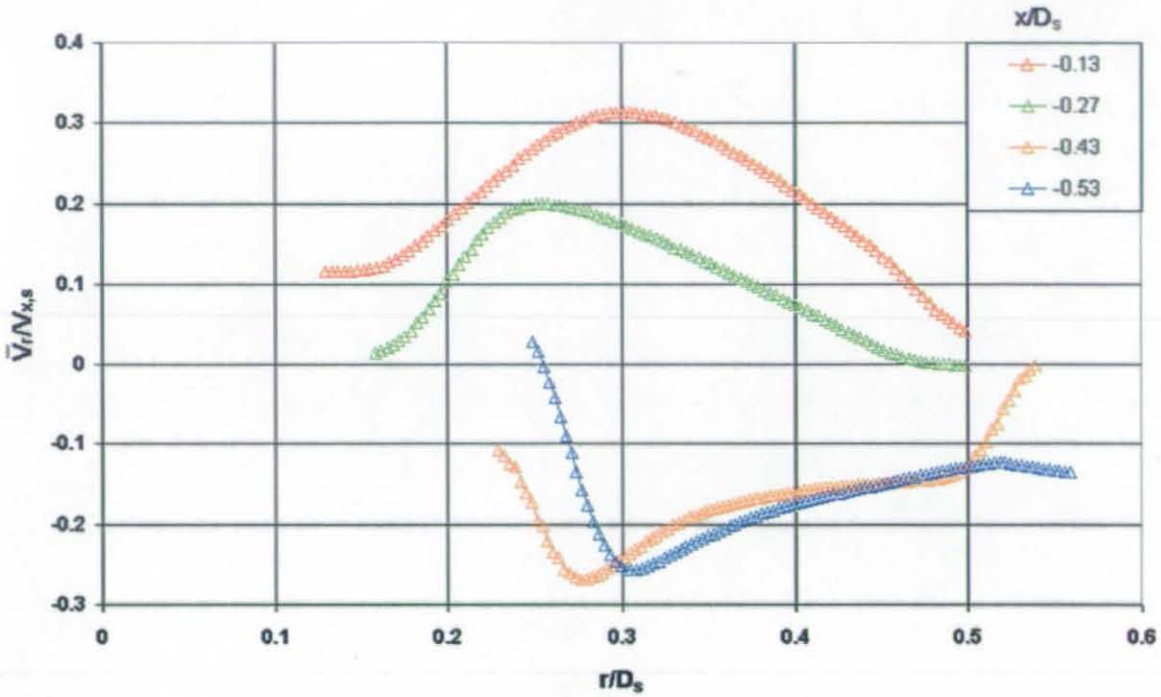

Figure 5.19. Mean Radial Velocity Profiles Inside Fuel Injector (Main Test Condition)

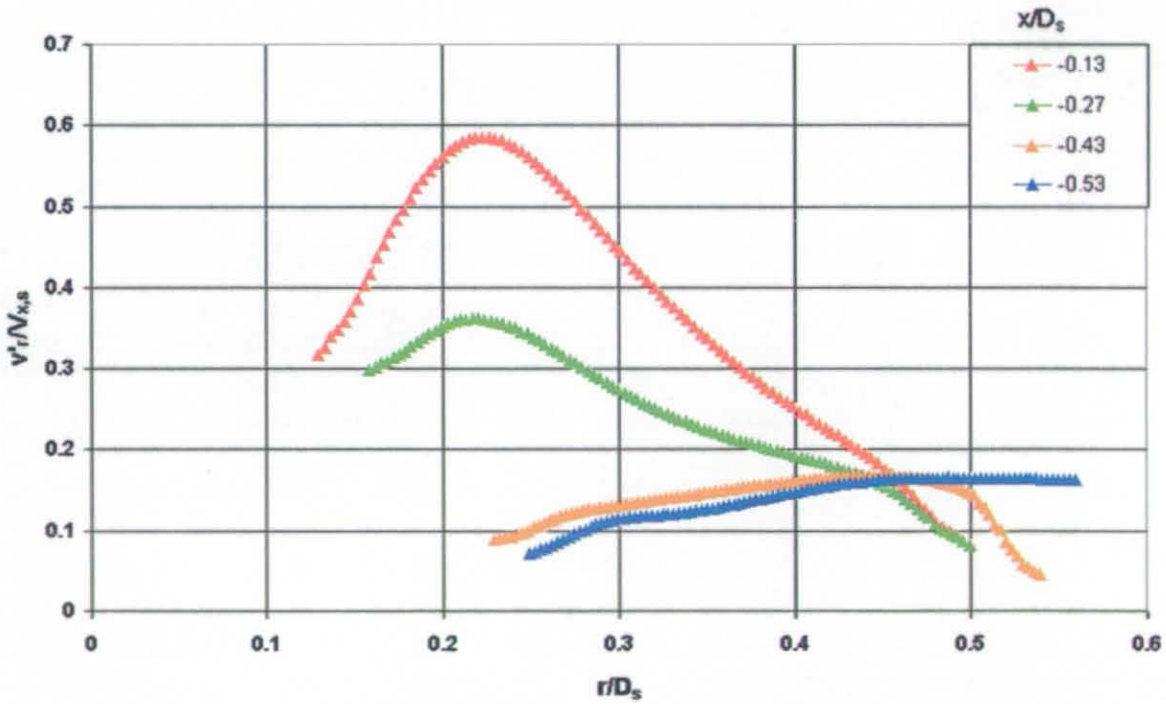

Figure 5.20. Radial RMS Velocity Profiles Inside Fuel Injector (Main Test Condition)

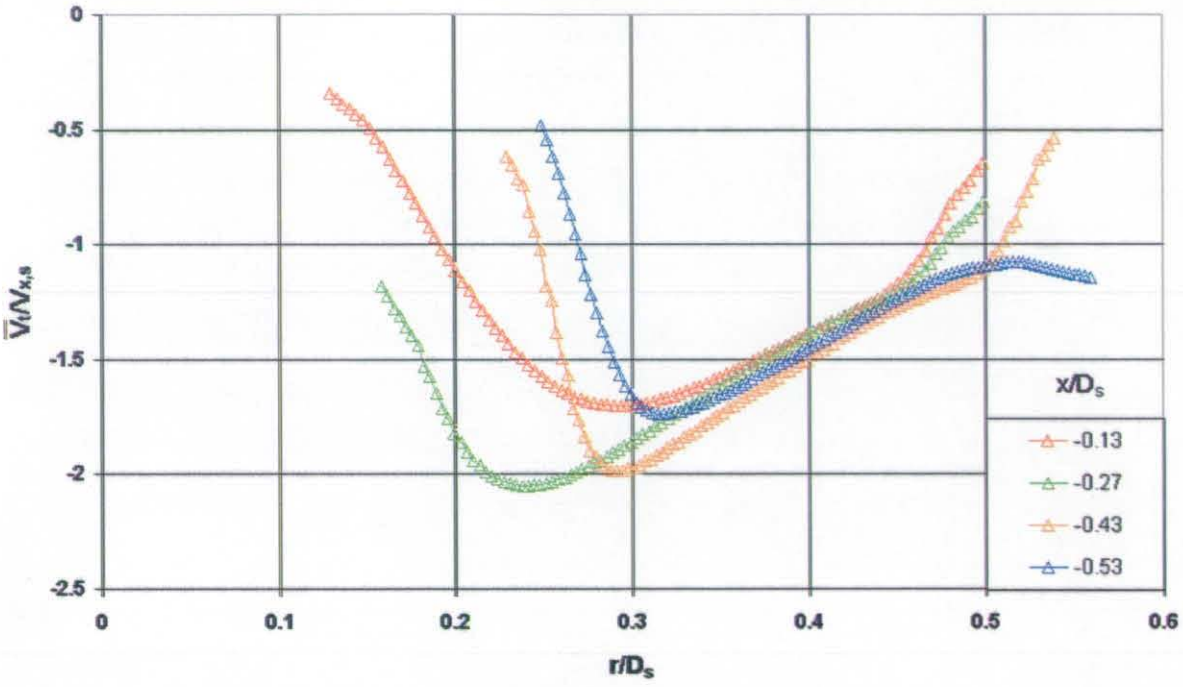

Figure 5.21. Mean Circumferential Velocity Profiles Inside Fuel Injector (Main Test Condition)

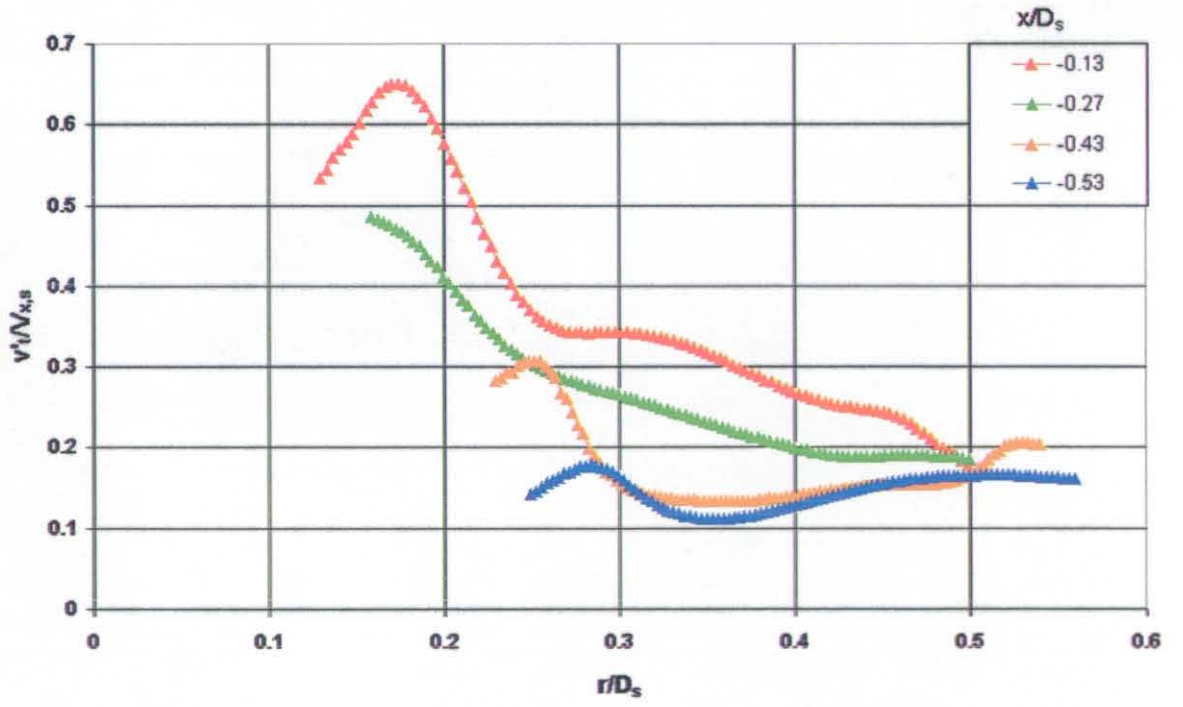

Figure 5.22. Circumferential RMS Velocity Profiles Inside Fuel Injector (Main Test Condition)

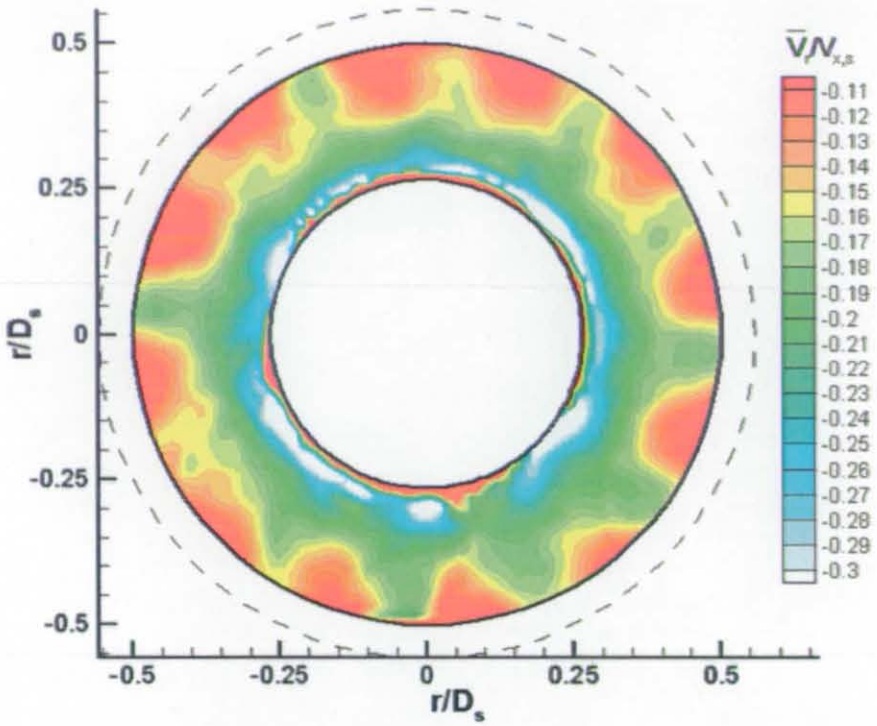

Figure 5.23. Mean Radial Velocity Contours at x/D_s=-0.53 (Main Test Condition)

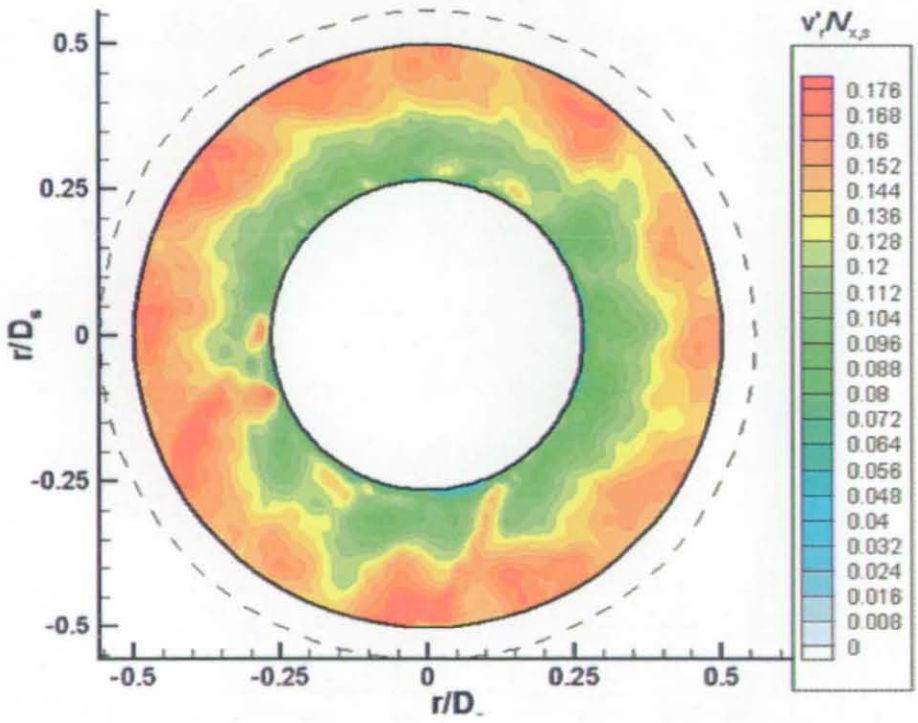

Figure 5.24. Radial RMS Velocity Contours at x/D_s=-0.53 (Main Test Condition)

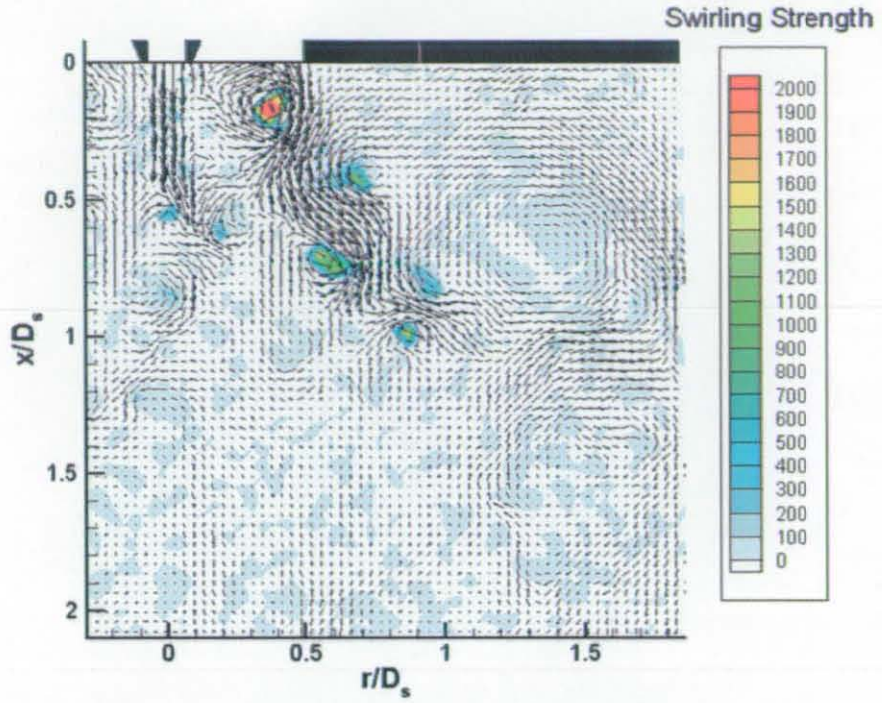

Figure 5.25. Instantaneous Velocity Vectors Superimposed on Swirling Strength Contours (Main Test Condition)

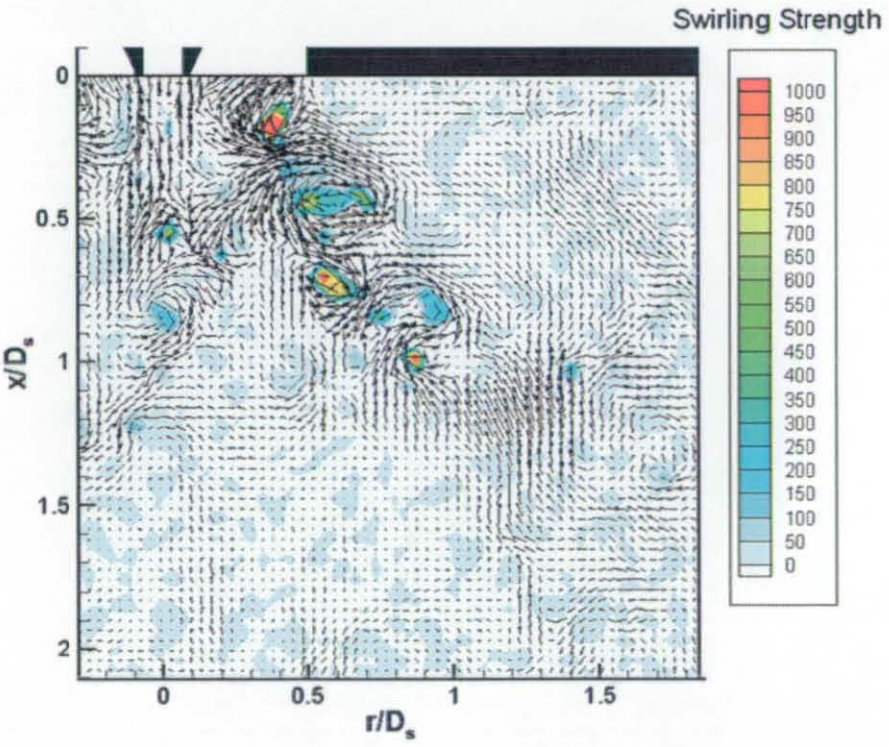

Figure 5.26. Reynolds Decomposed Velocity Vectors Superimposed on Swirling Strength Contours (Main Test Condition)

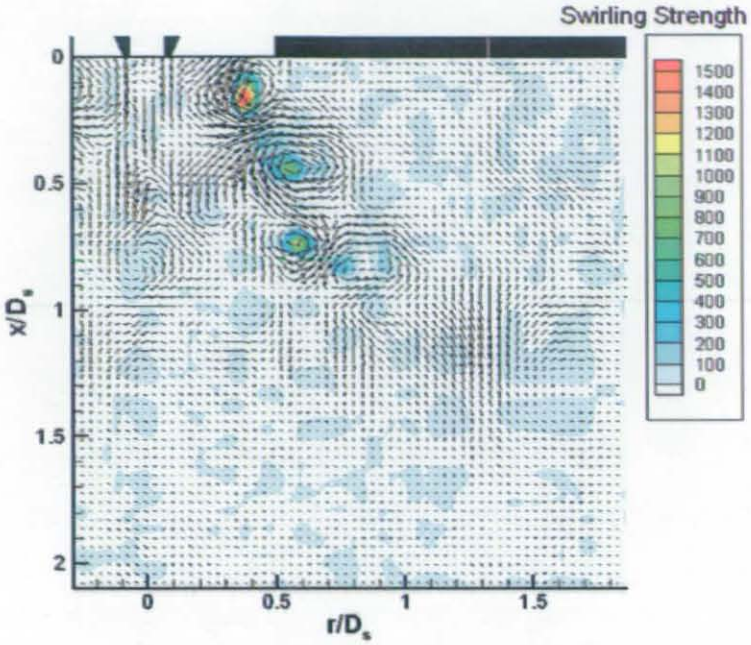

Figure 5.27. SVD (rank 5) Velocity Vectors Superimposed on Swirling Strength Contours (Main Test Condition)

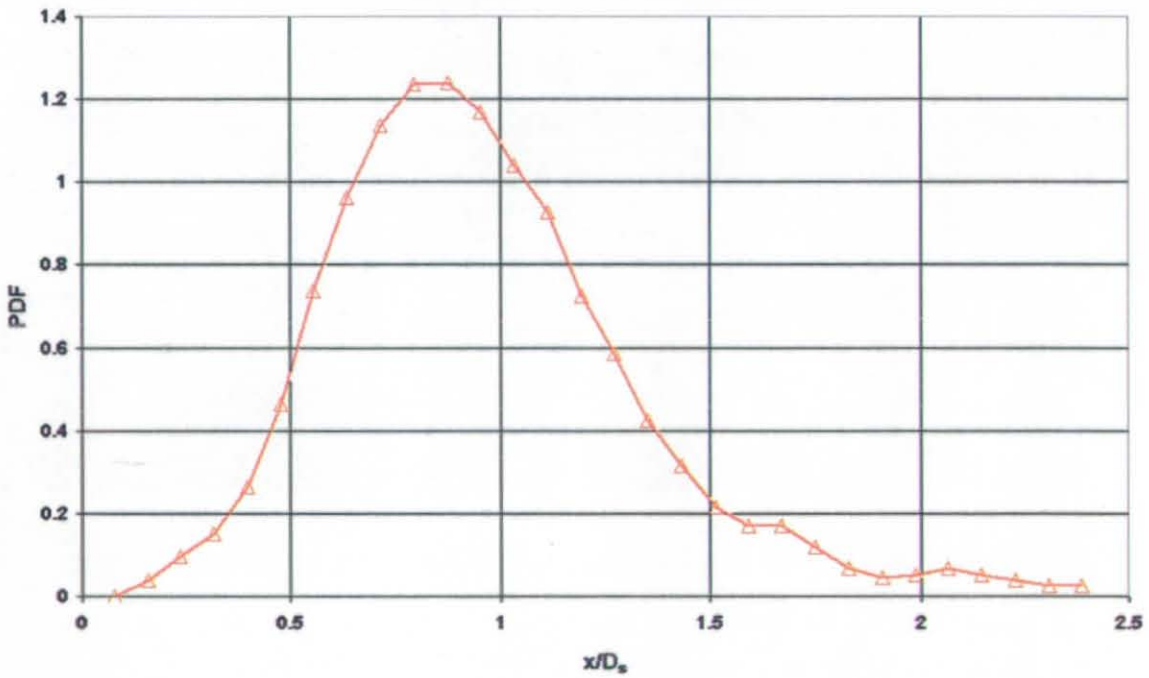

Figure 5.28. Spatial PDF of Free Stagnation Point (Main Test Condition)

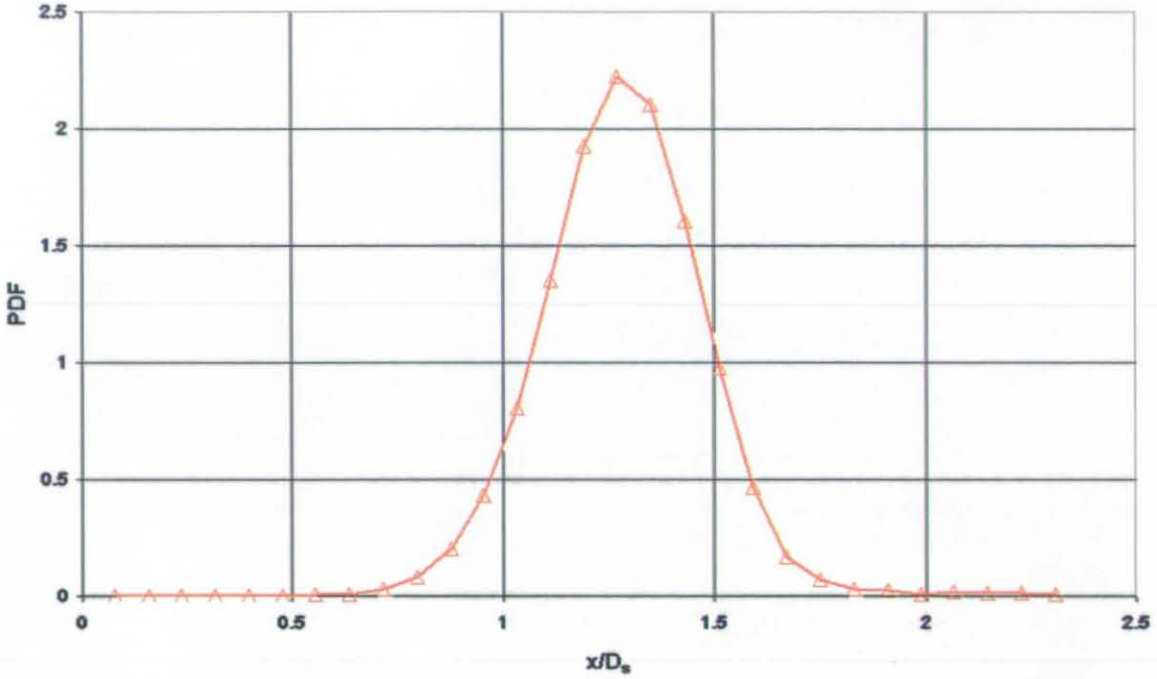

Figure 5.29. Spatial PDF of Swirl Cone Attachment Point (Main Test Condition)

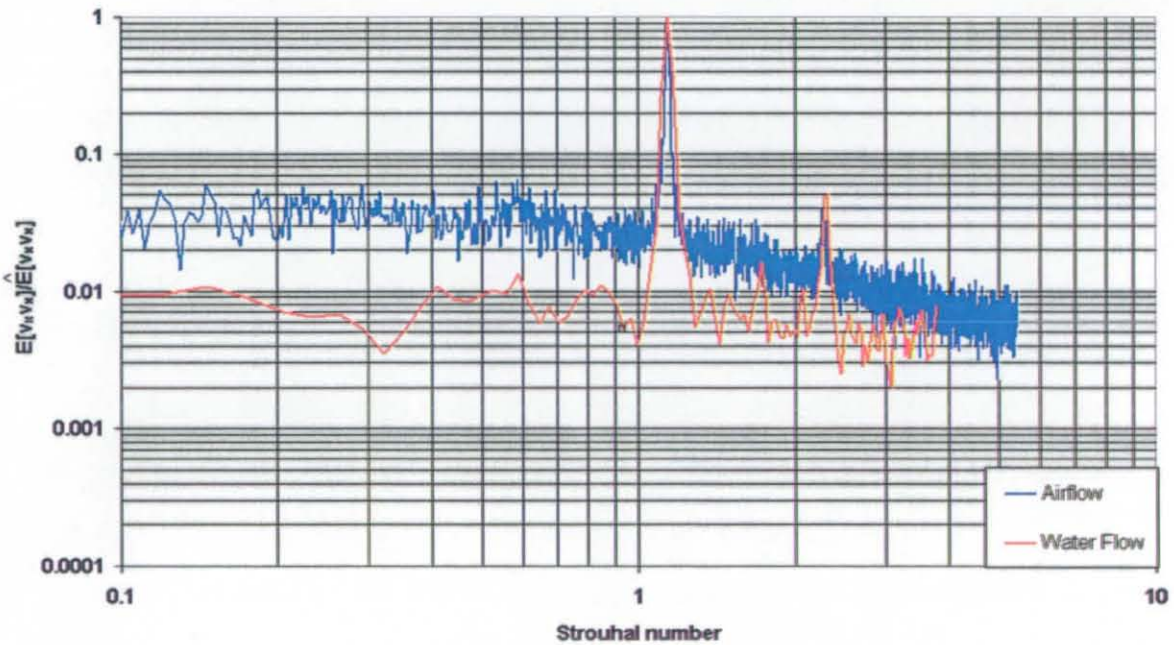

Figure 5.30. PSD Deduced from Axial Velocity at Location (x=0.27,r=0.27,θ=0) (Main Test Condition)

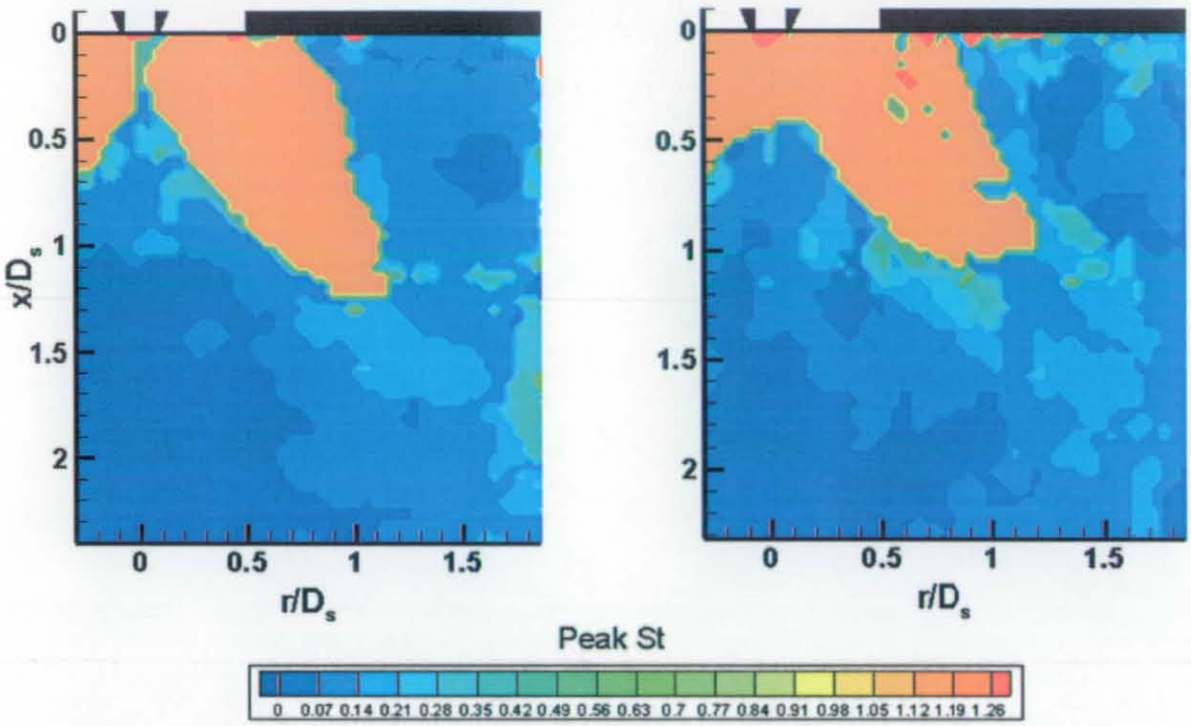

Figure 5.31. Peak Frequency Contours Deduced from Axial Velocity [left] and Radial Velocity [right] (Main Test Condition)

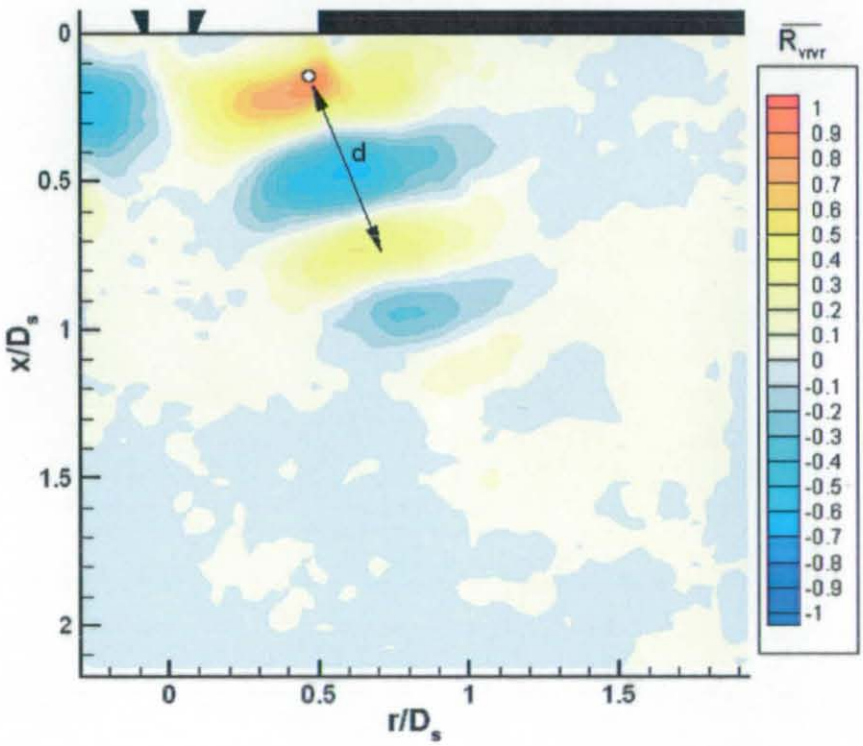

Figure 5.32. Radial Velocity Spatial Correlation Contours (Main Test Condition)

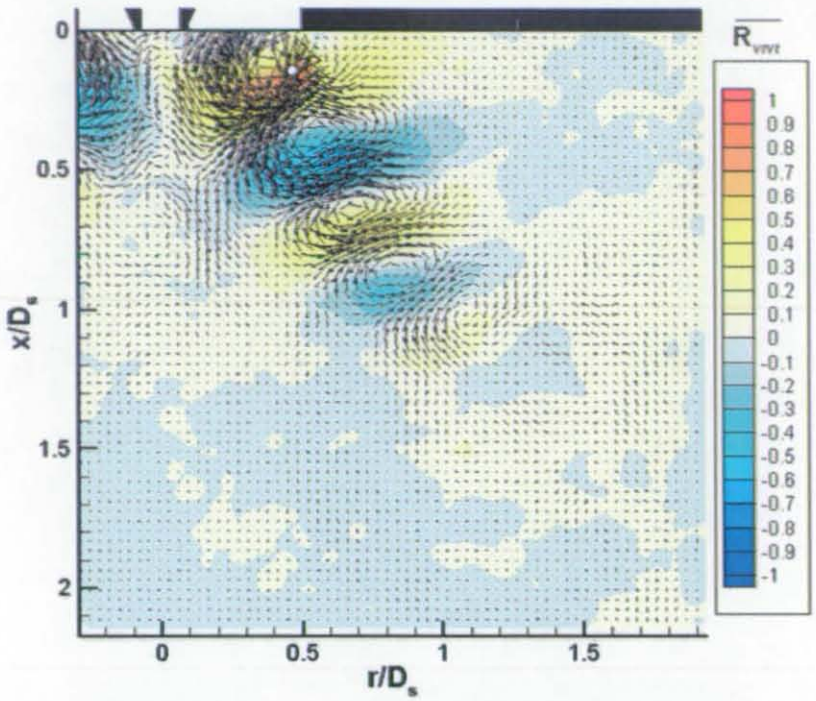

Figure 5.33. Conditionally Averaged Fluctuating Velocity Vectors Superimposed on Radial Velocity Spatial Correlation Contours (Main Test Condition)

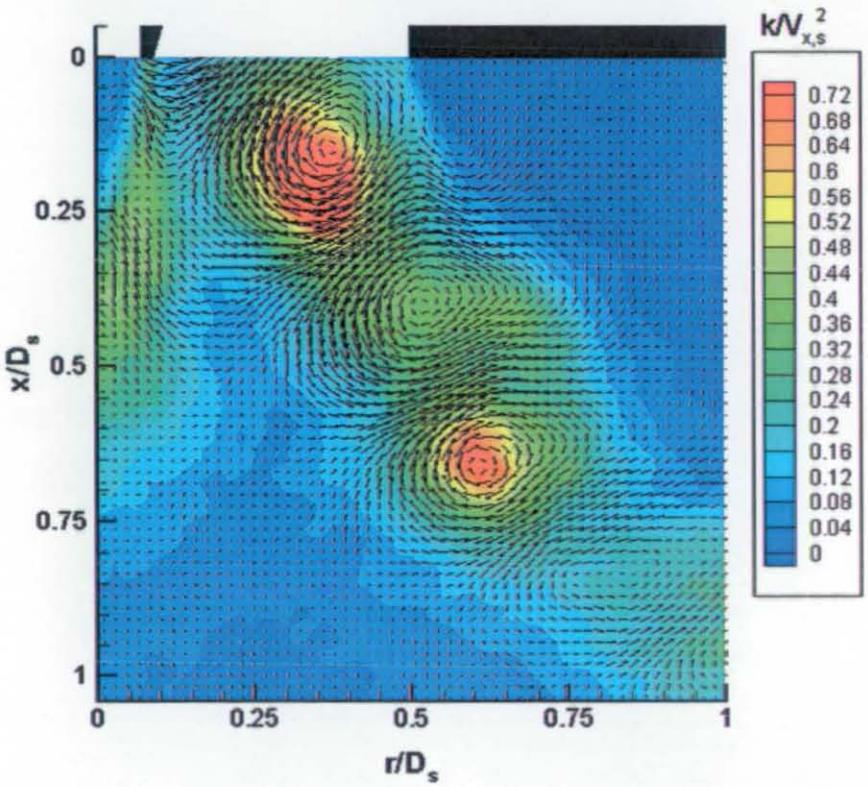

Figure 5.34. Conditionally Averaged Fluctuating Velocity Vectors Superimposed on Conditionally Averaged Turbulent Kinetic Energy Contours (Main Test Condition)

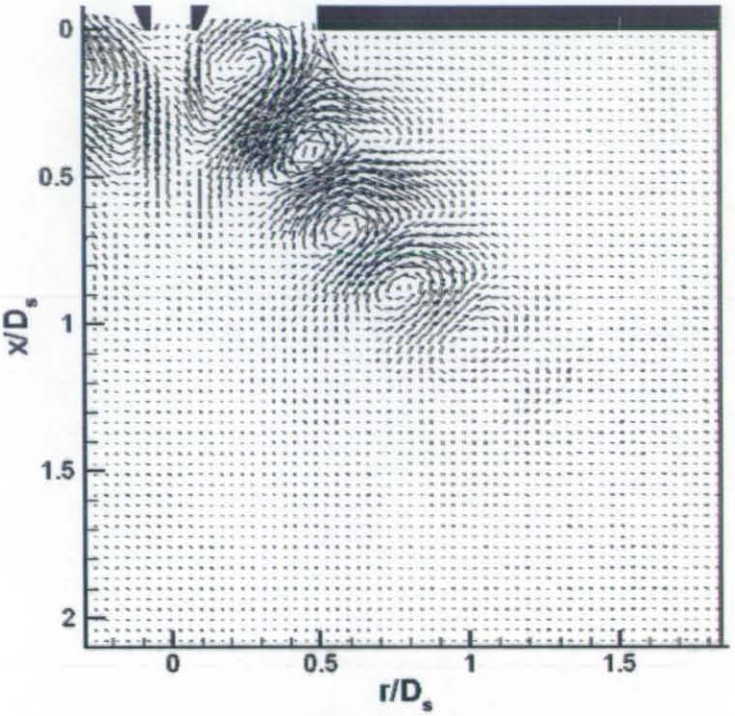

Figure 5.35. First POD Mode (Main Test Condition)

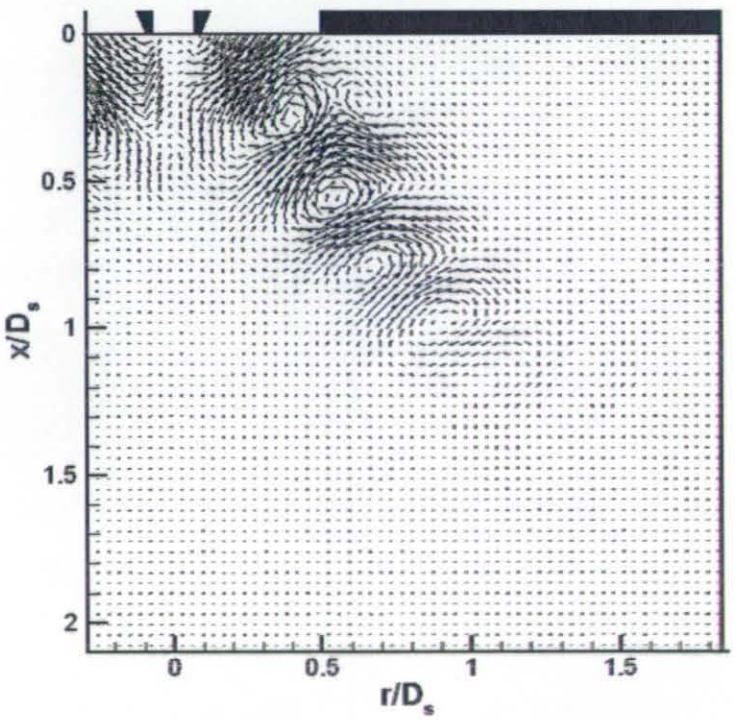

Figure 5.36. Second POD Mode (Main Test Condition)

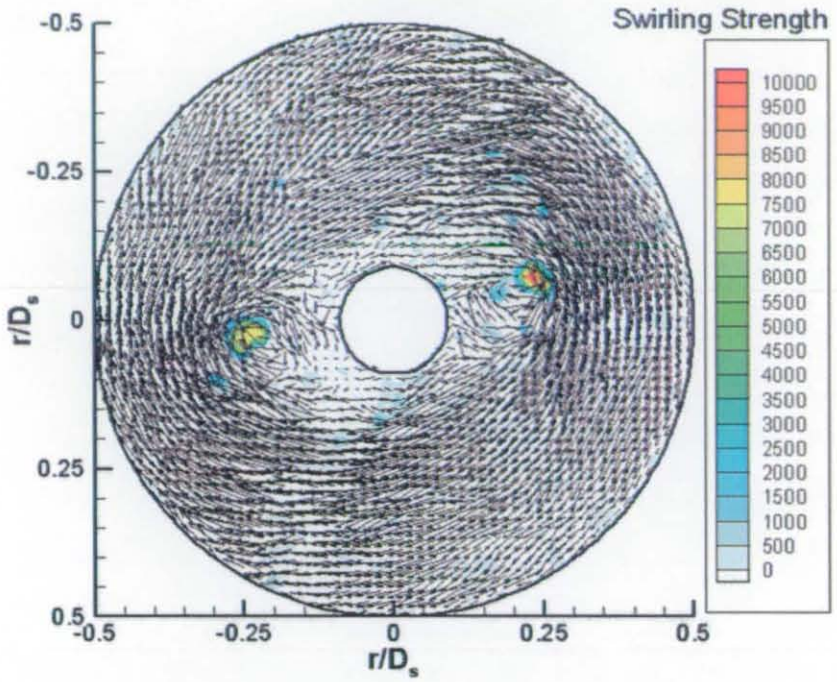

Figure 5.37. Instantaneous Velocity Vectors Superimposed on Swirling Strength Contours at $x/D_s=0$ (Main Test Condition)

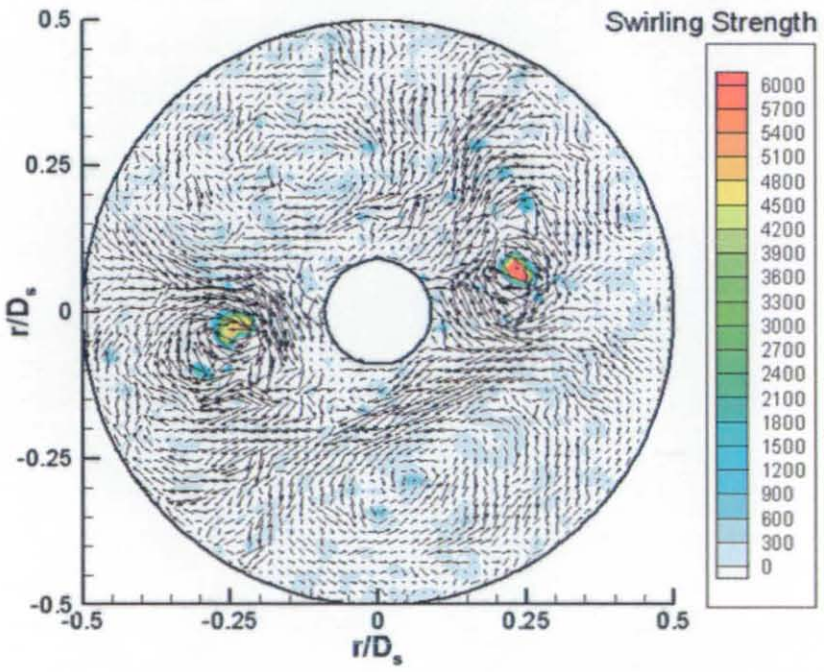

Figure 5.38. Reynolds Decomposed Velocity Vectors Superimposed on Swirling Strength Contours at $x/D_s=0$ (Main Test Condition)

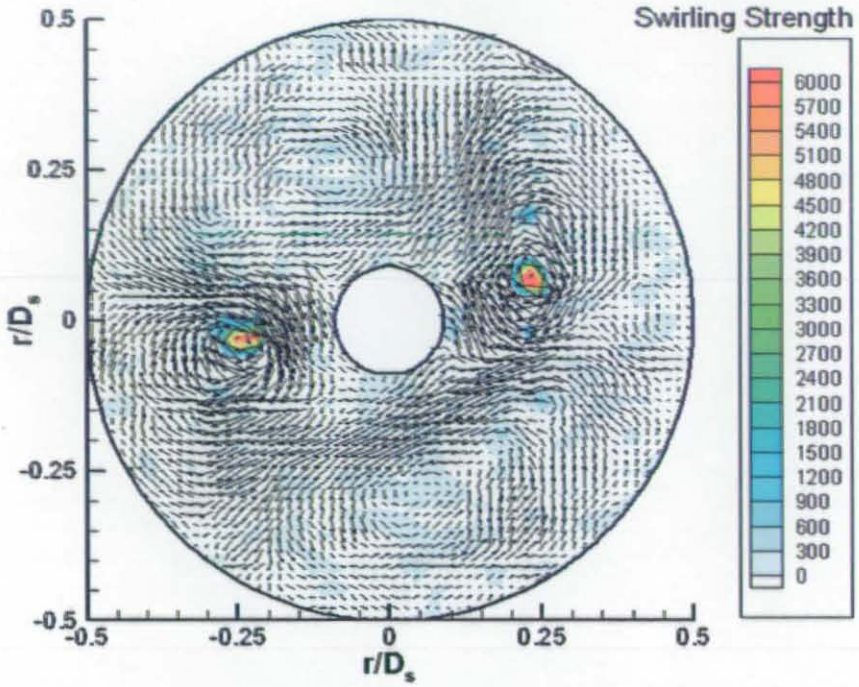

Figure 5.39. SVD (rank 5) Velocity Vectors Superimposed on Swirling Strength Contours at $x/D_s=0$ (Main Test Condition)

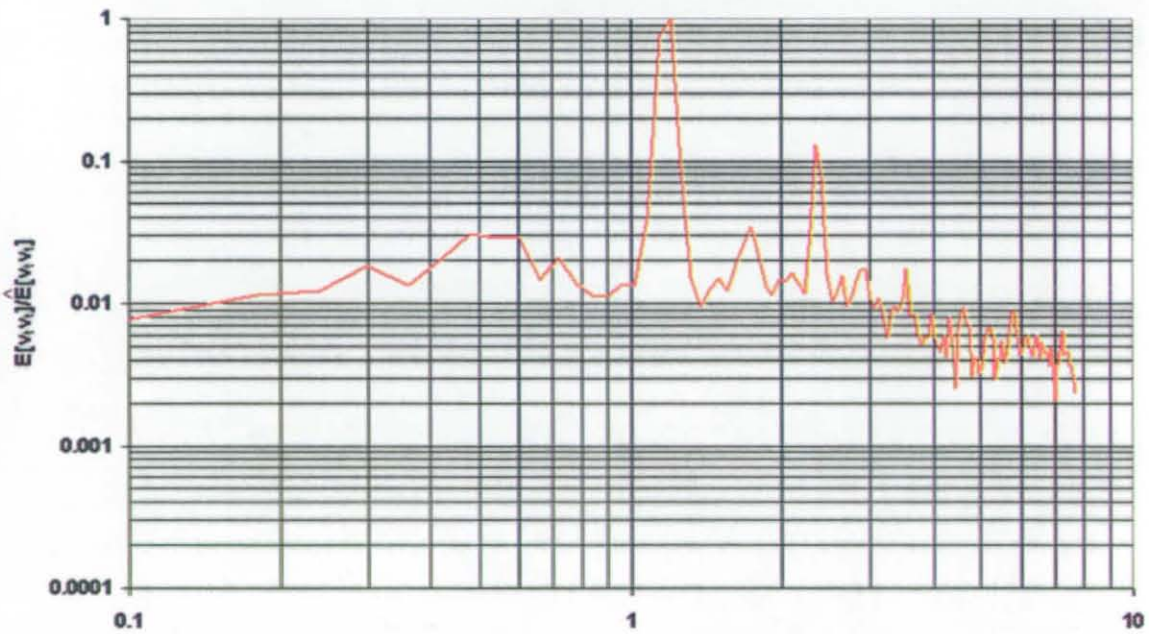

Figure 5.40. PSD Deduced from Circumferential Velocity at Location (x=0,r=0.25,θ=0) (Main Test Condition)

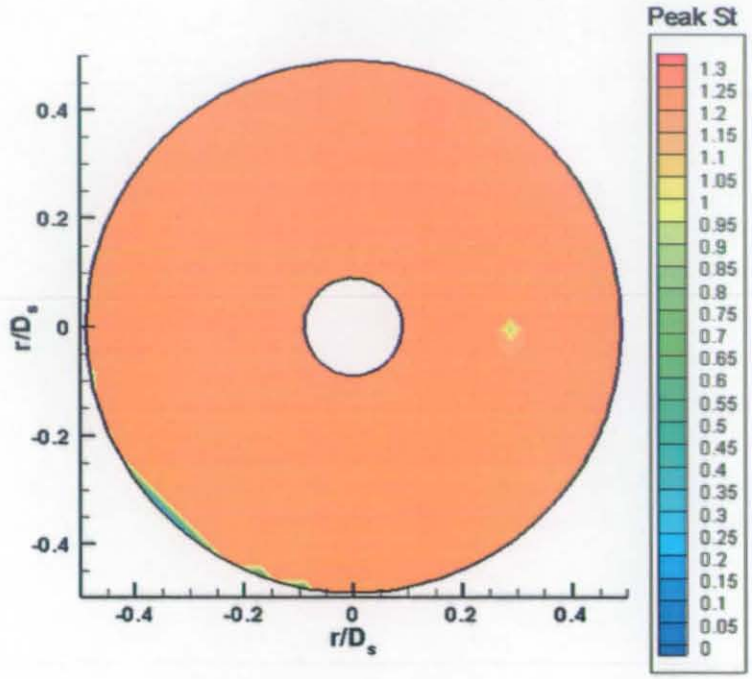

Figure 5.41. Peak Frequency Contours Deduced from Circumferential Velocity at $x/D_s=0$ (Main Test Condition)

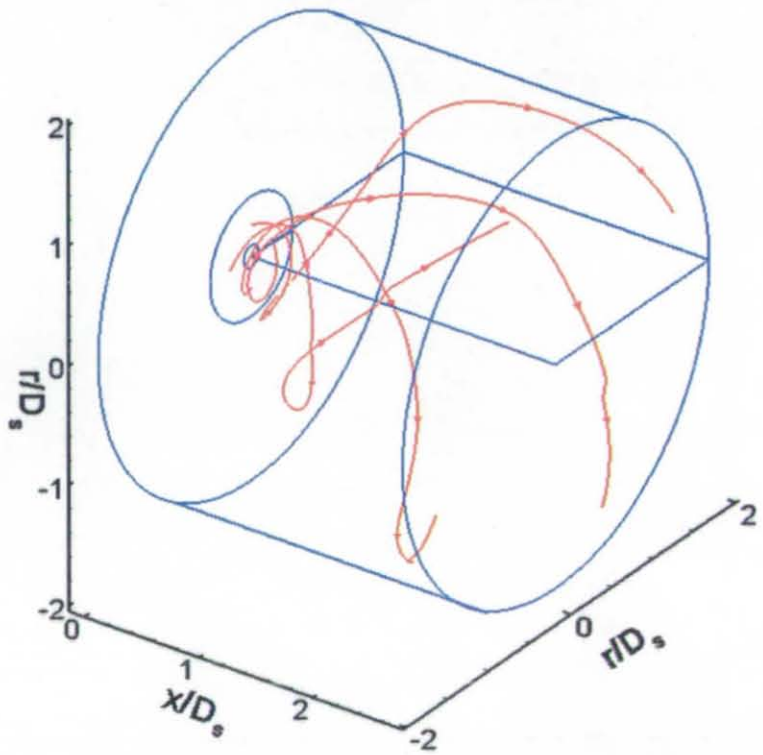

Figure 5.42. Stream-Traces Representing Mean Flow Paths of the Two-Strong and Two-Weak Counter-Rotating Vortex Pairs (Main Test Condition)

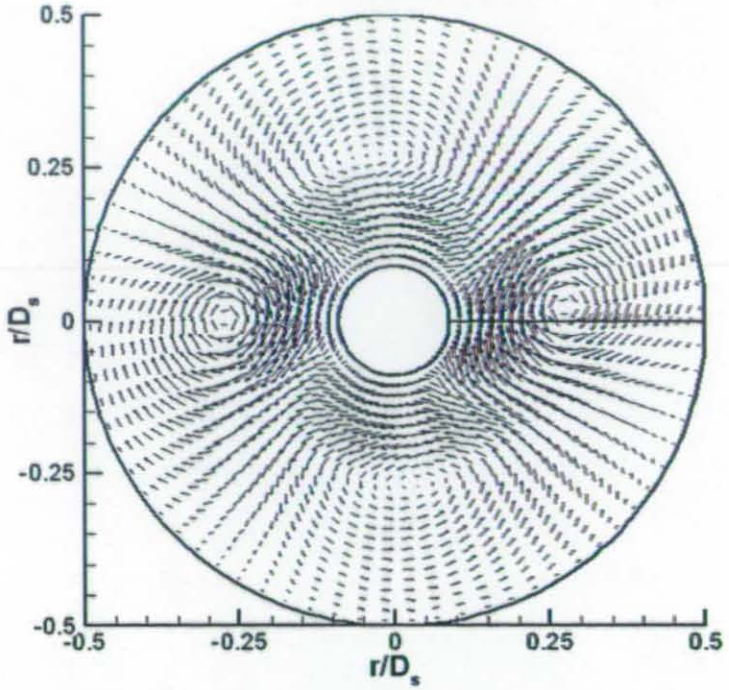

Figure 5.43. Rotationally Averaged SVD (rank 5) Velocity at x/D_s=0.0 (Main Test Condition)

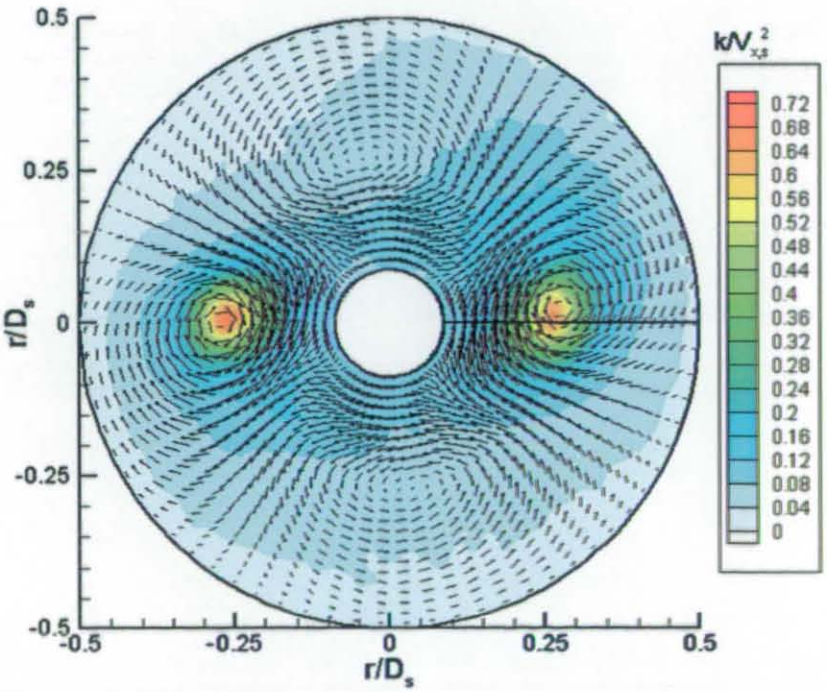

Figure 5.44. Rotationally Averaged SVD (rank 5) Velocity Vectors Superimposed on Rotationally Averaged Turbulent Kinetic Energy Contours (Main Test Condition)

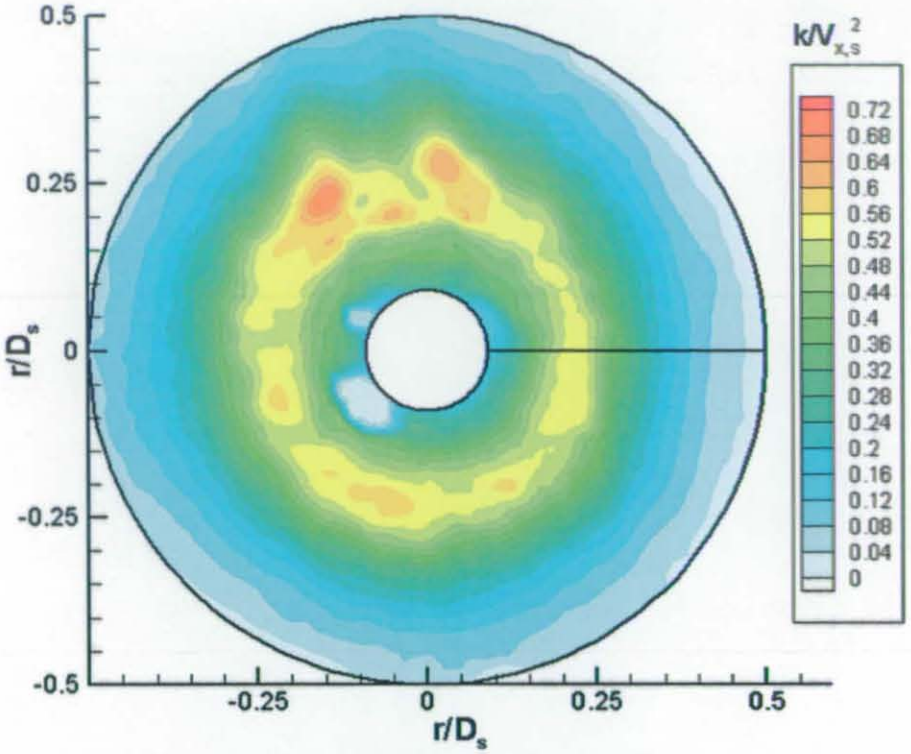

Figure 5.45. Turbulent Kinetic Energy Contours at $x/D_s=0$ (Main Test Condition)

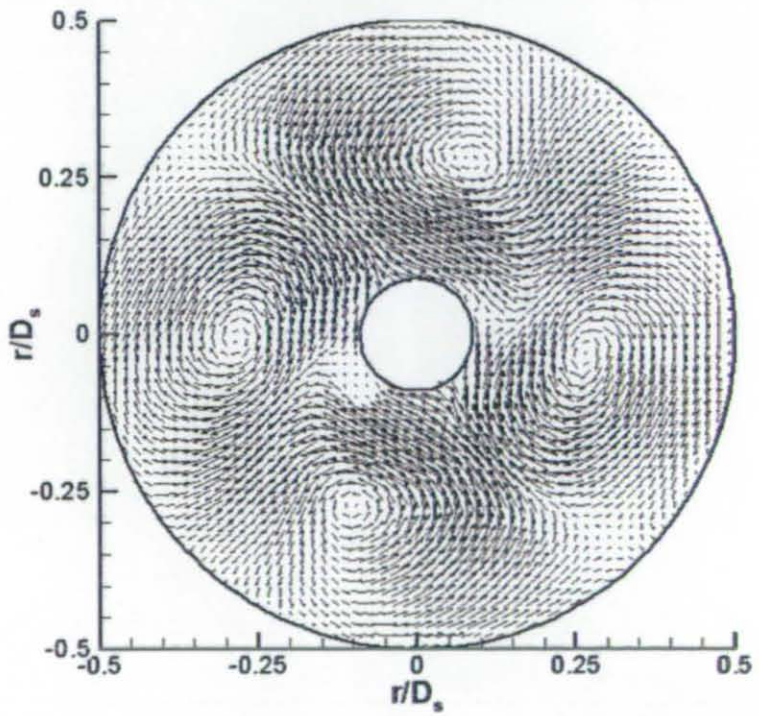

Figure 5.46. First POD Mode at $x/D_s=0$ (Main Test Condition)

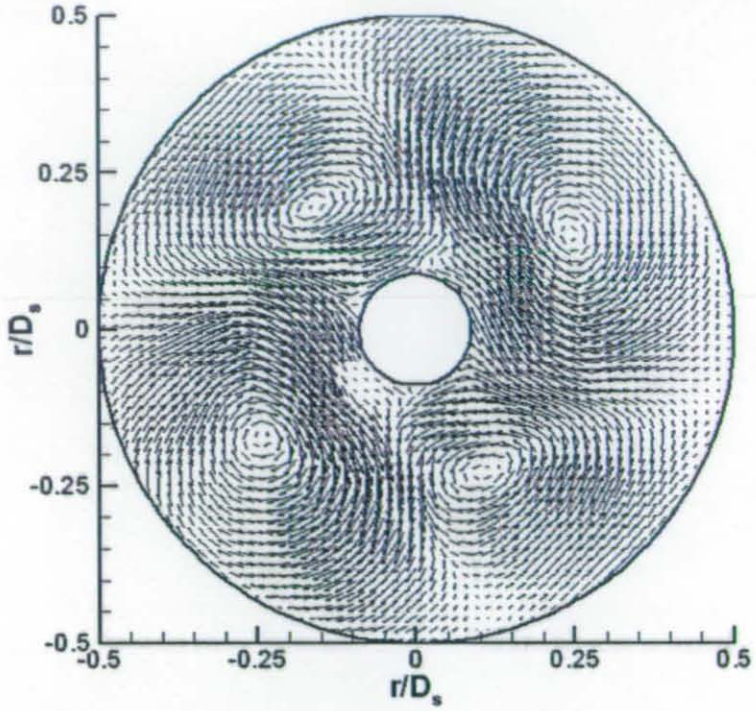

Figure 5.47. Second POD Mode at $x/D_s=0$ (Main Test Condition)

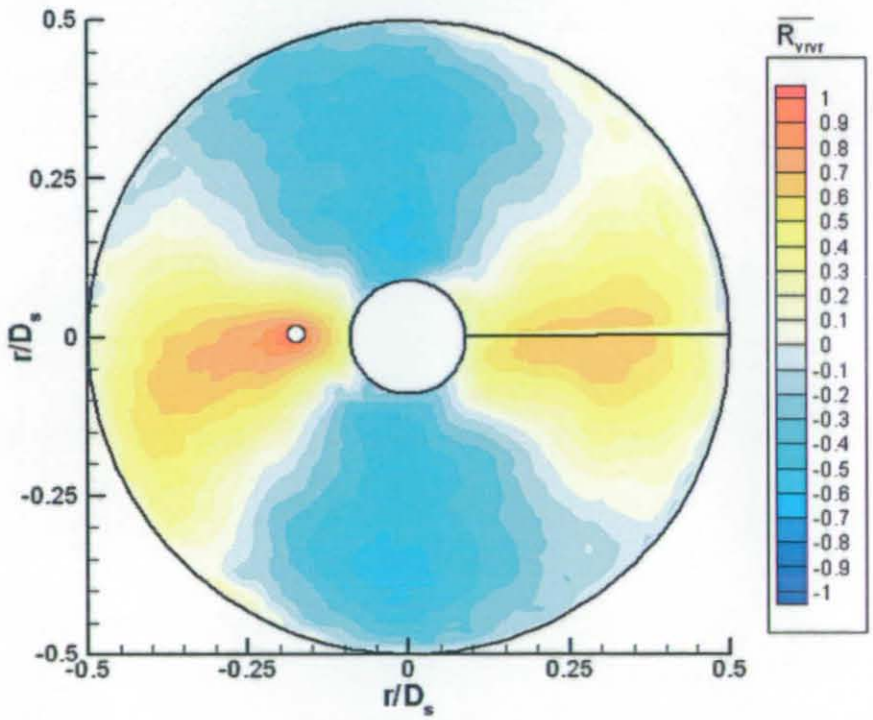

Figure 5.48. Radial Velocity Spatial Correlation Contours at $x/D_s=0$ (Main Test Condition)

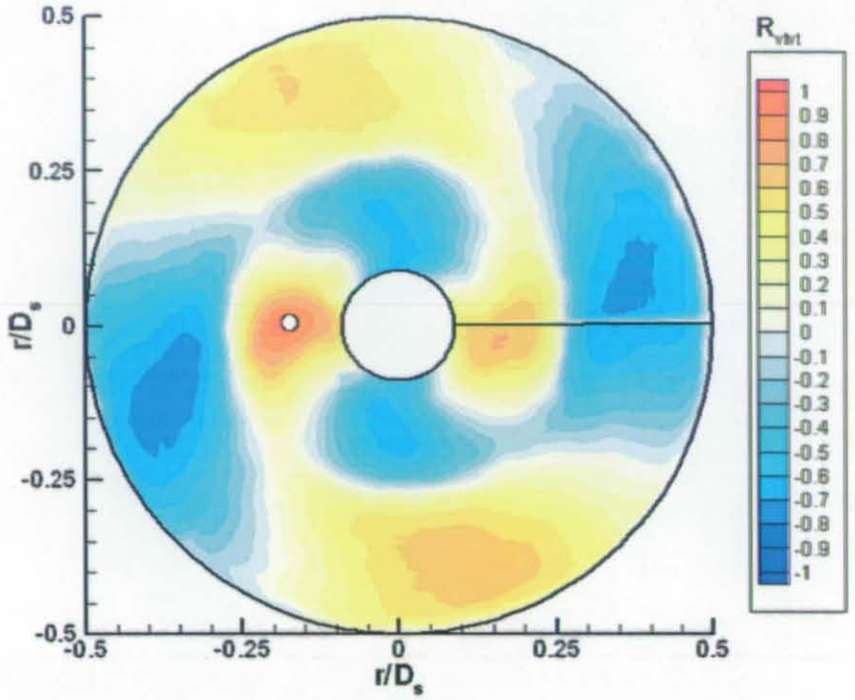

Figure 5.49. Circumferential Velocity Spatial Correlation Contours at $x/D_s=0$ (Main Test Condition)

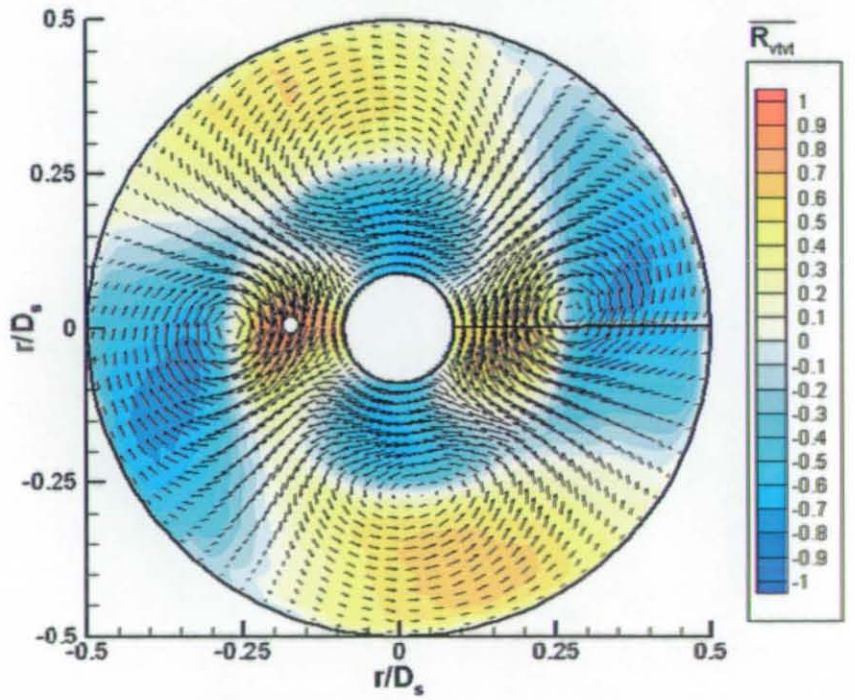

Figure 5.50. Rotationally Averaged Fluctuating Velocity Vectors Superimposed on Circumferential Velocity Spatial Correlation Contours at $x/D_s=0$ (Main Test Condition)

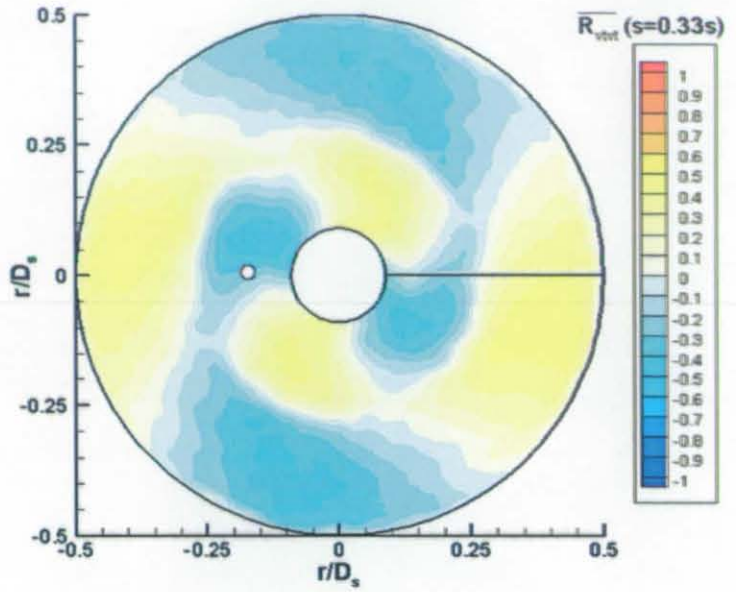

Figure 5.51. Circumferential Velocity Cross-Correlation Contours (s=0.33s) at x/D_s=0 (Main Test Condition)

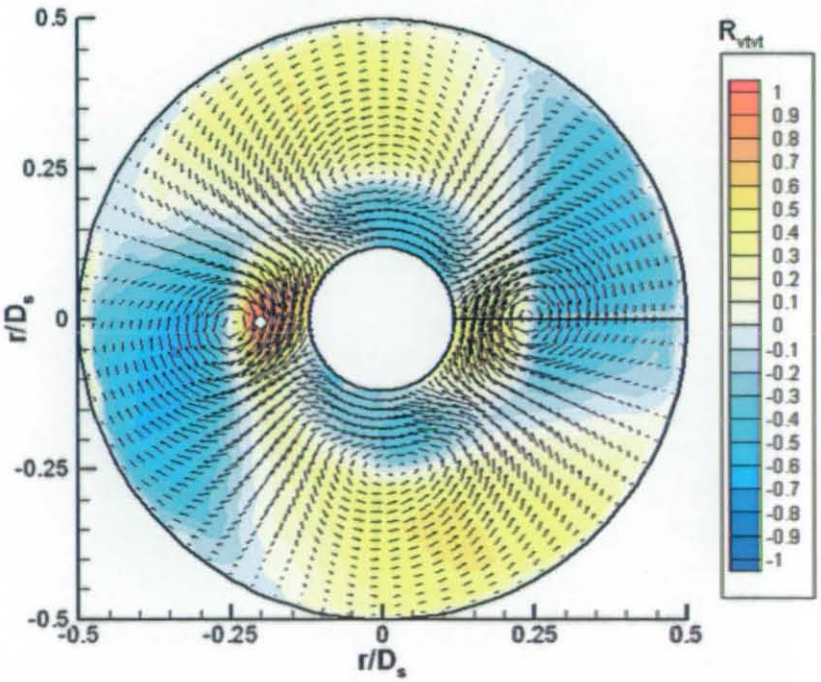

Figure 5.52. Rotationally Averaged Fluctuating Velocity Vectors Superimposed on Circumferential Velocity Spatial Correlation Contours at x/D_s=-0.13 (Main Test Condition)

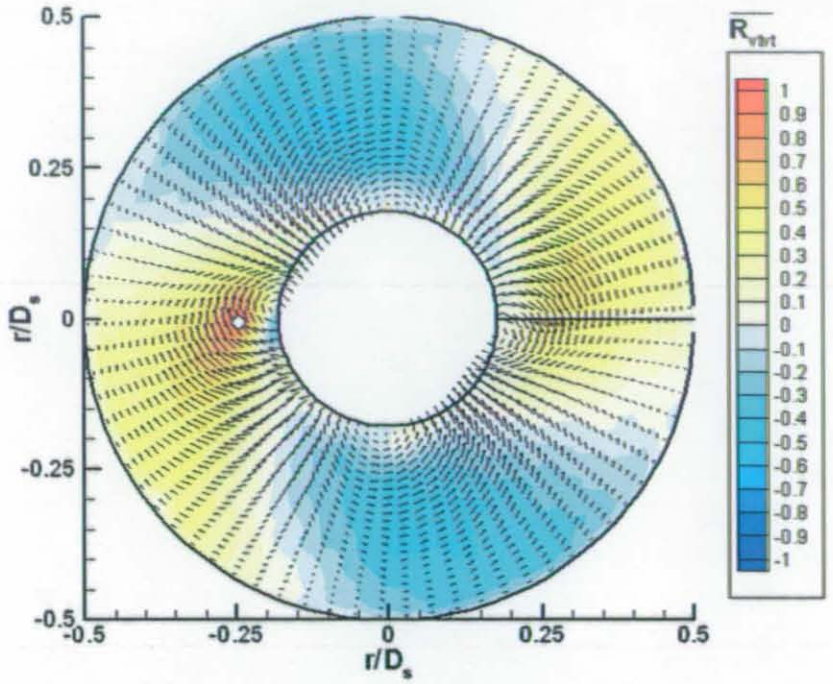

Figure 5.53 Rotationally Averaged Fluctuating Velocity Vectors Superimposed on Circumferential Velocity Spatial Correlation Contours at x/D_s=-0.27 (Main Test Condition)

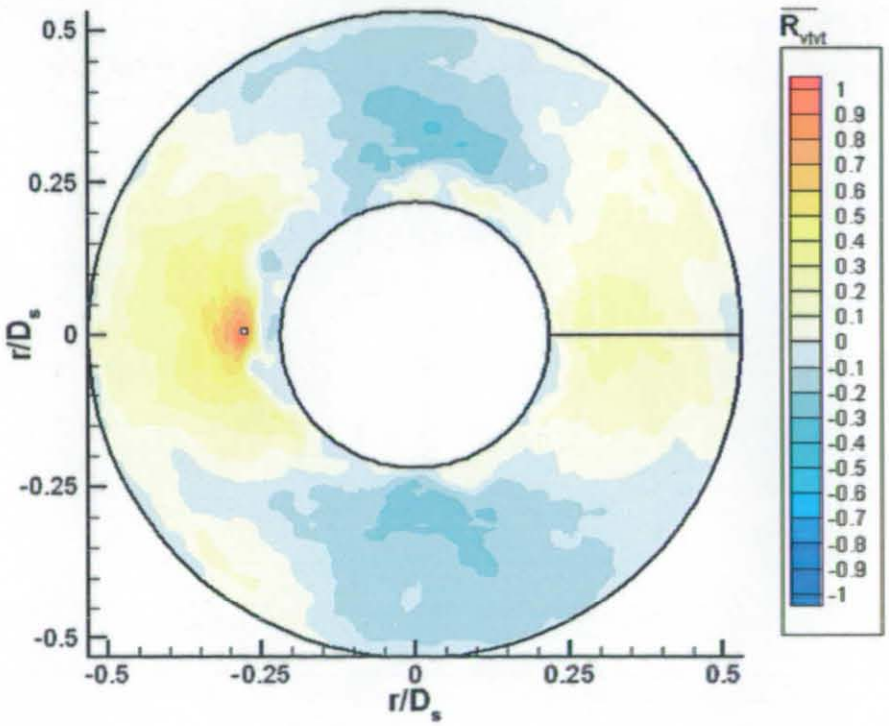

Figure 5.54. Circumferential Velocity Spatial Correlation Contours at x/D_s=-0.43 (Main Test Condition)

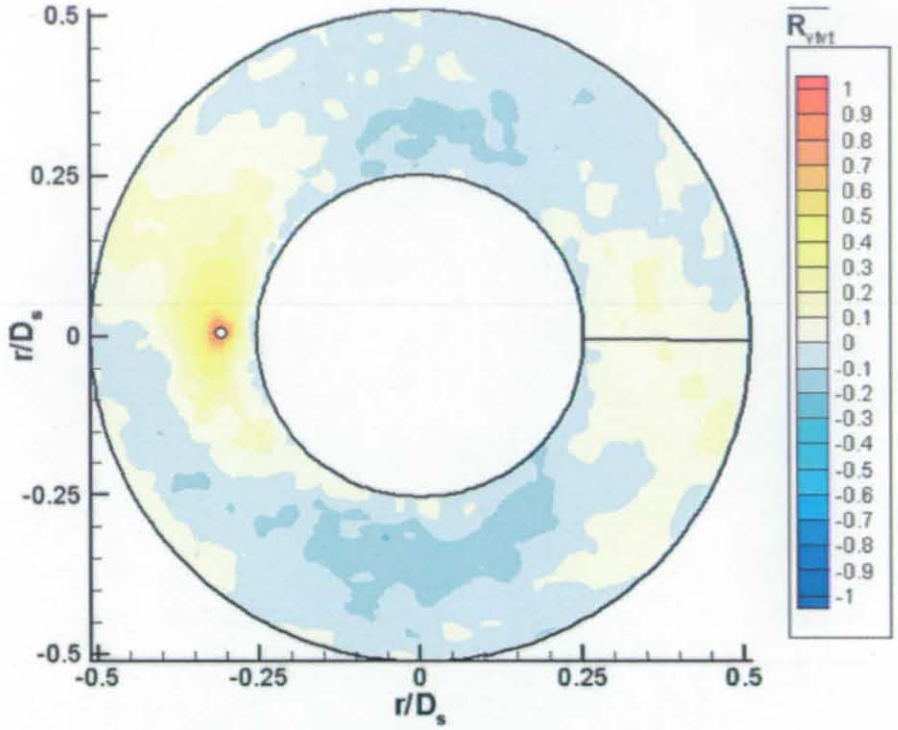

Figure 5.55. Circumferential Velocity Spatial Correlation Contours at x/D_s=-0.53 (Main Test Condition)

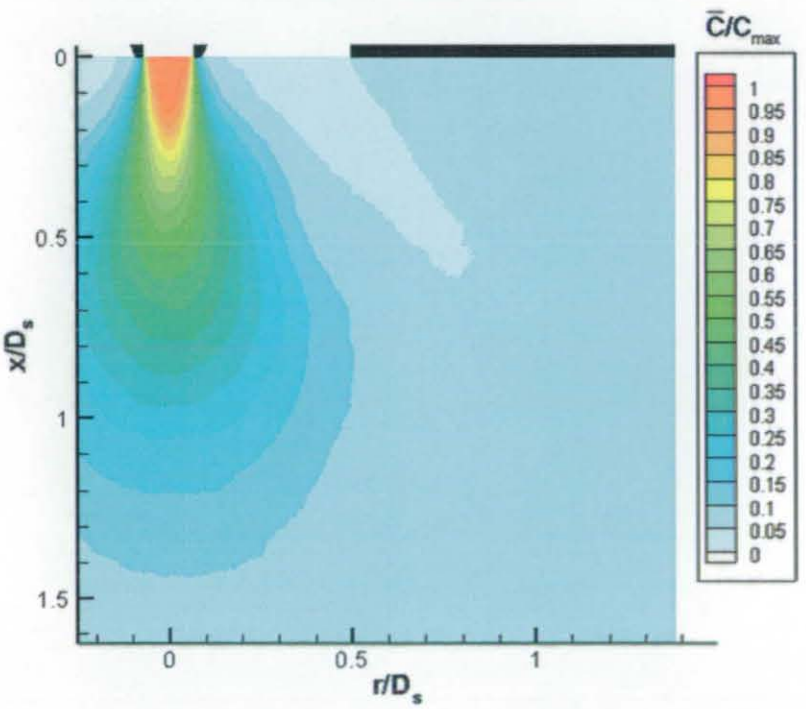

Figure 5.56. Mean Scalar Contours (Main Test Condition)

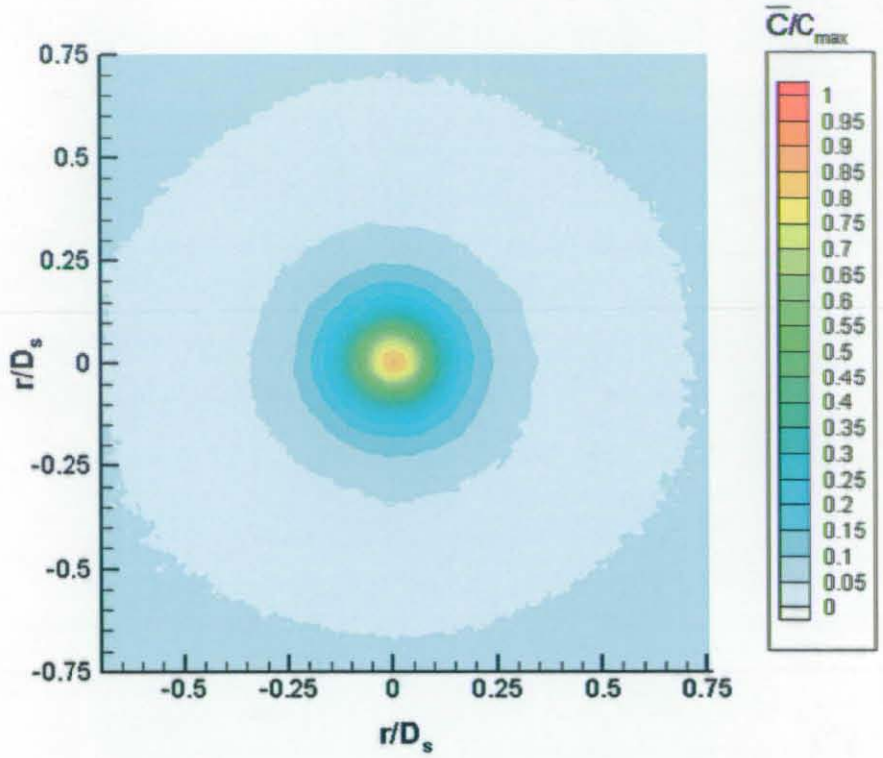

Figure 5.57. Mean Scalar Contours in r-θ Plane at x/D_s=0.27 (Main Test Condition)

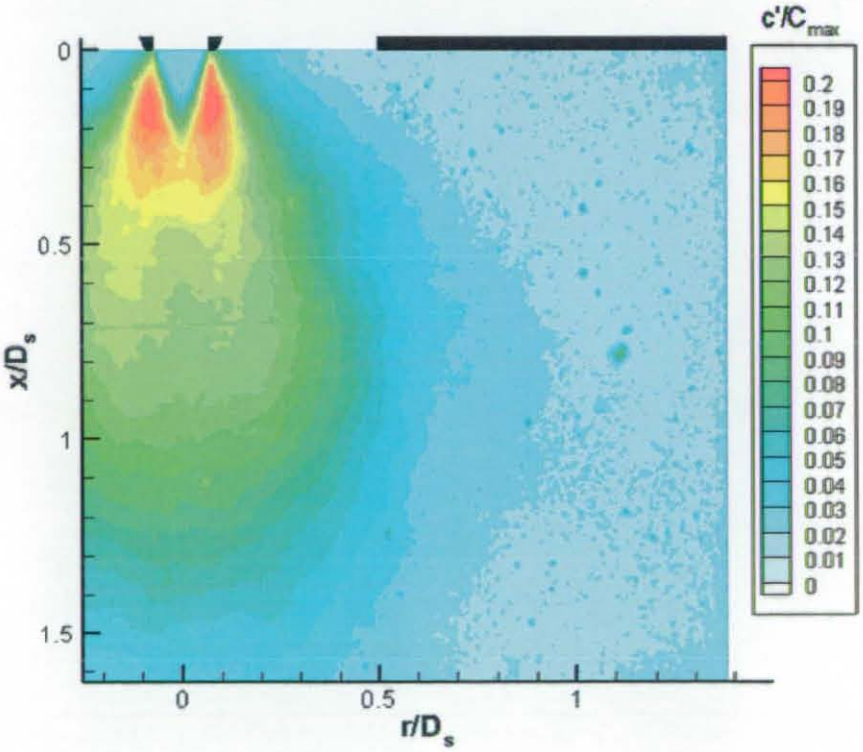

Figure 5.58. Scalar RMS Contours (Main Test Condition)

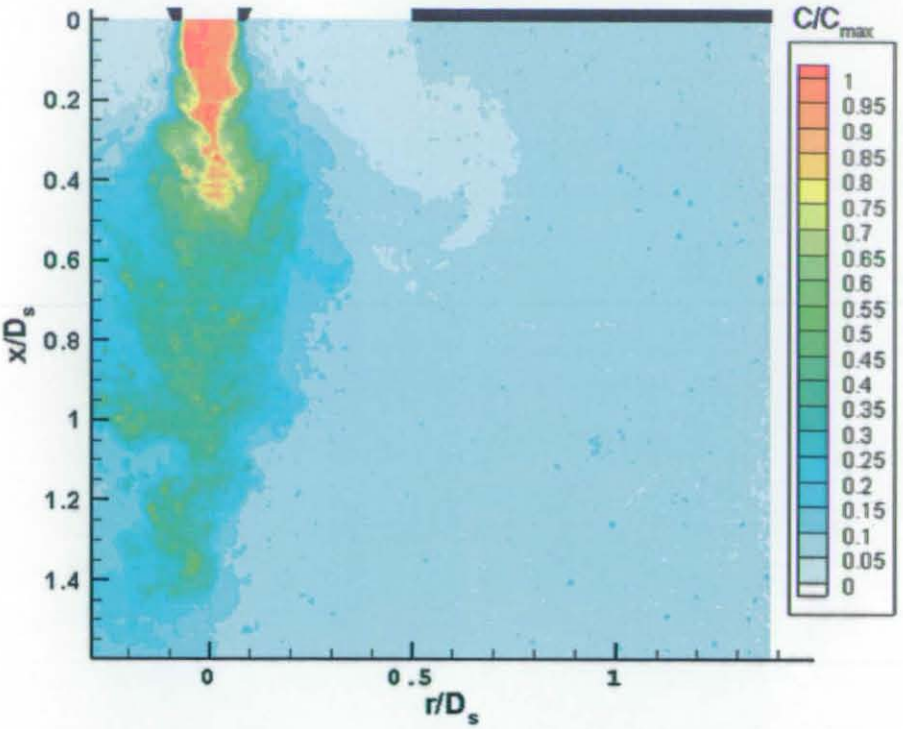

Figure 5.59. Instantaneous Scalar Contours (Main Test Condition)

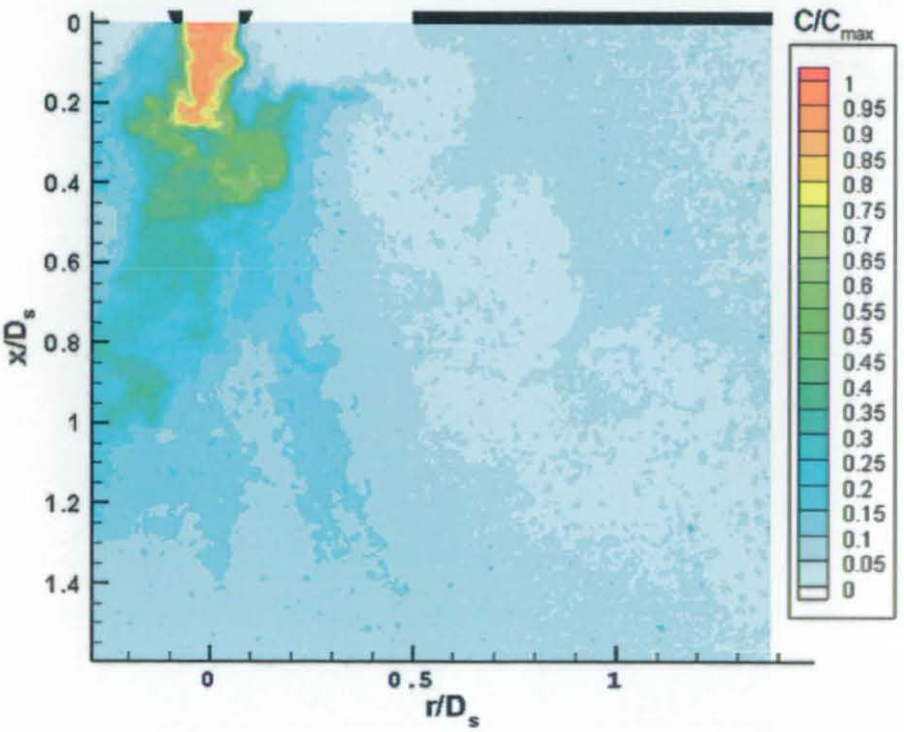

Figure 5.60. Instantaneous Scalar Contours (Main Test Condition)

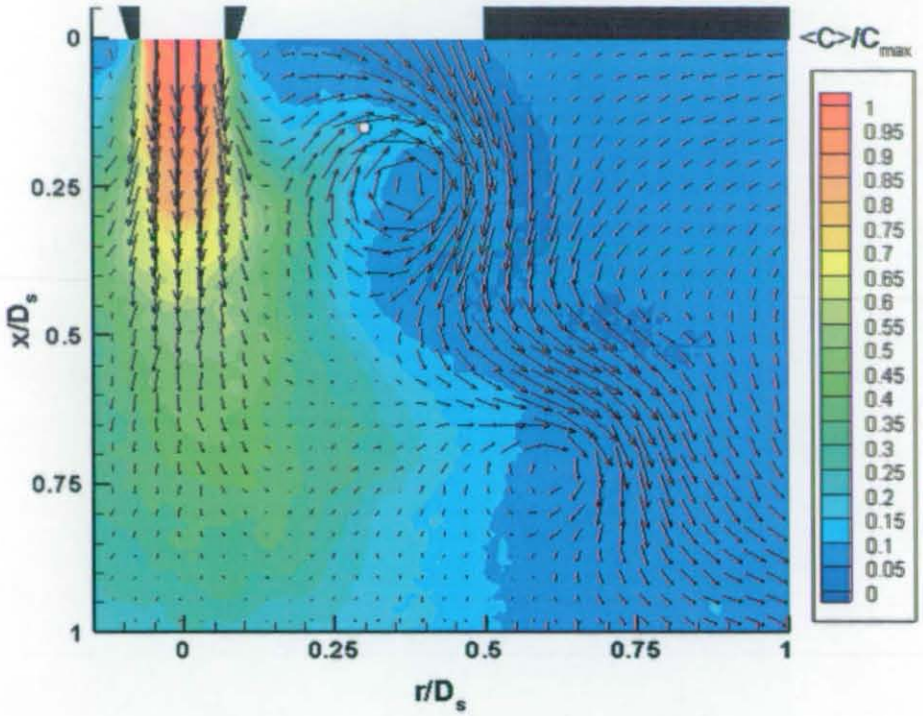

Figure 5.61. Conditionally Averaged Velocity Vectors Superimposed on Conditionally Averaged Scalar Contours (Main Test Condition)

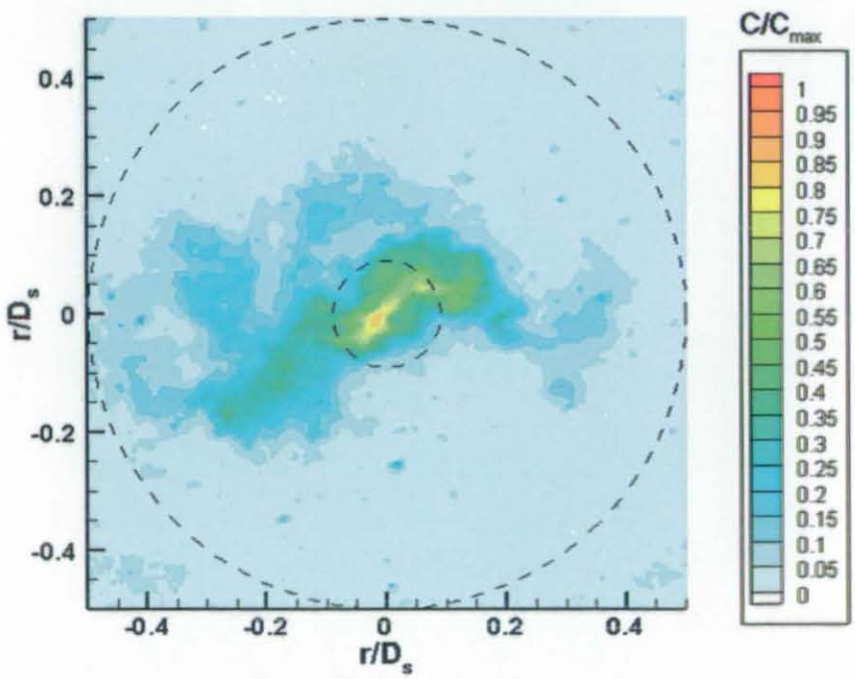

Figure 5.62. Instantaneous Scalar Contours in r-θ Plane (Main Test Condition)

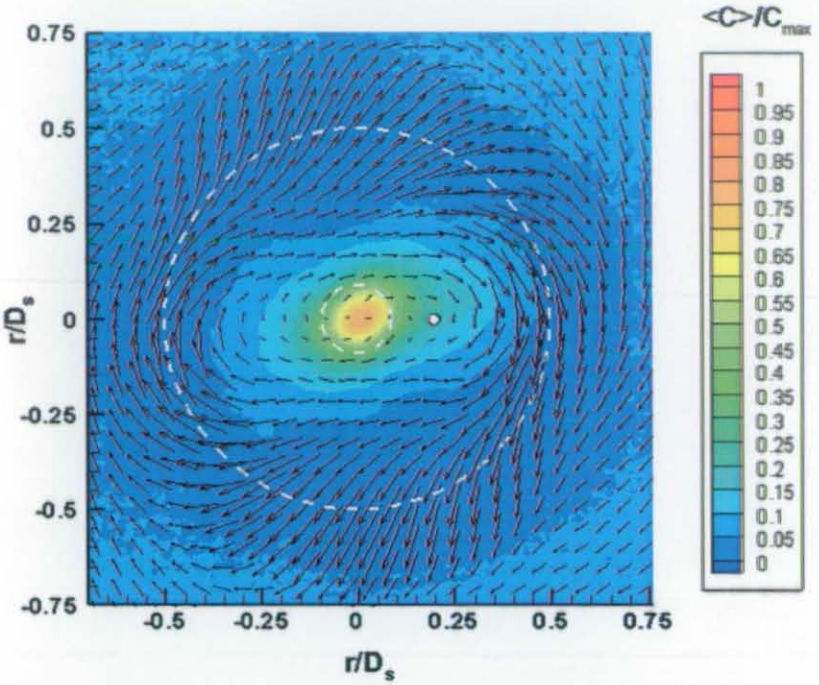

Figure 5.63. Conditionally Averaged Velocity Vectors Superimposed on Conditionally Averaged Scalar Contours in r-θ Plane at x/D_s=0.27 (Main Test Condition)

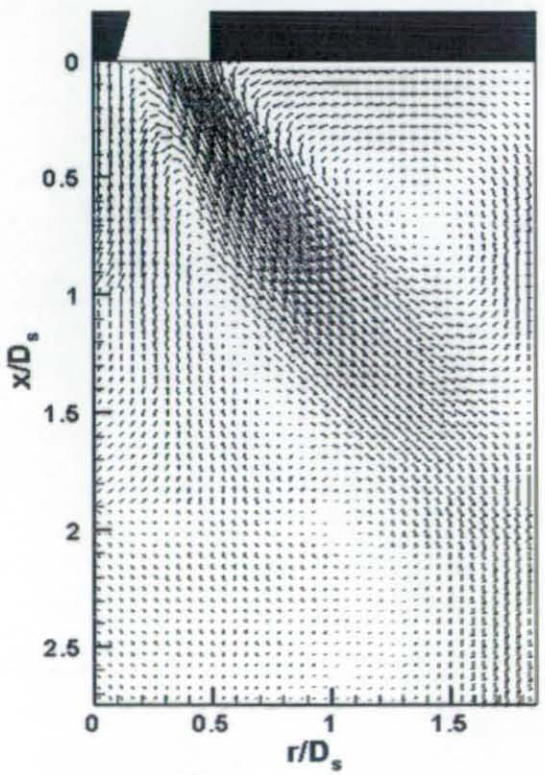

Figure 5.64. Mean Velocity Vectors for the No-Jet Test Condition

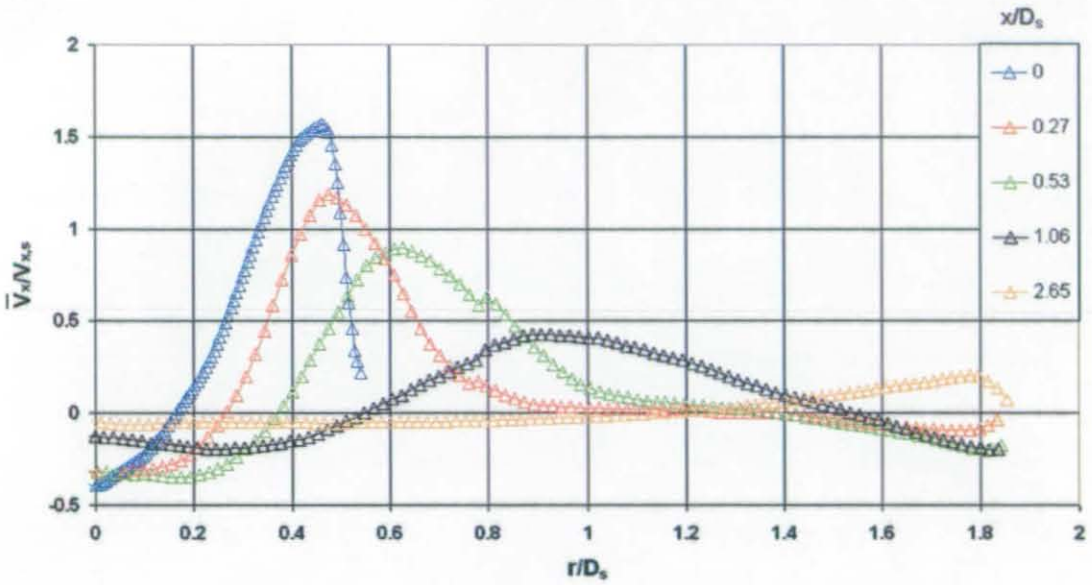

Figure 5.65. Mean Axial Velocity Profiles in Dump Area Expansion Chamber (No-Jet Test Condition)

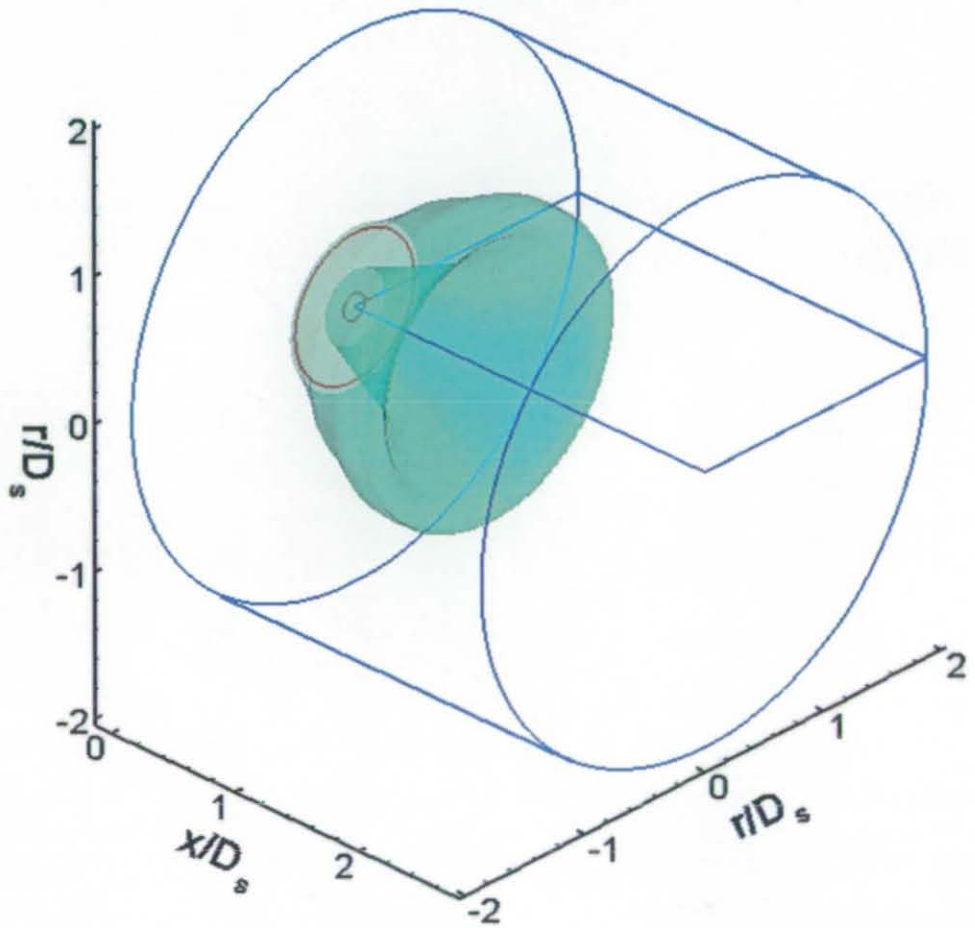

Figure 5.66. Iso-Surfaces of $\overline{V_x}/V_{x,s} = 0.4$ (No-Jet Test Condition)

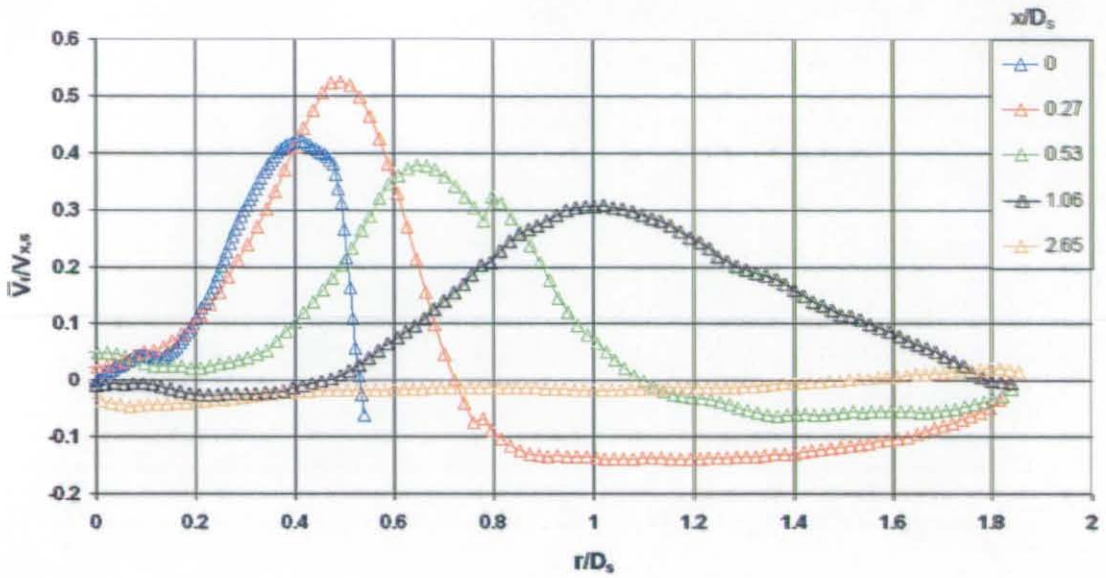

Figure 5.67. Mean Radial Velocity Profiles in Dump Area Expansion Chamber (No-Jet Test Condition)

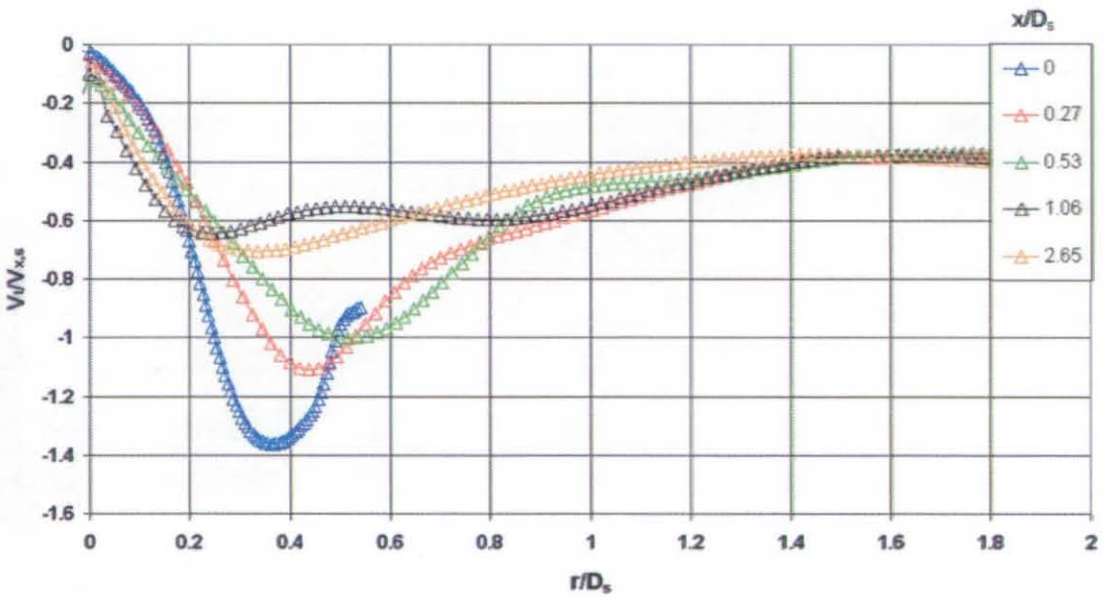

Figure 5.68. Mean Circumferential Velocity Profiles in Dump Area Expansion Chamber (No-Jet Test Condition)

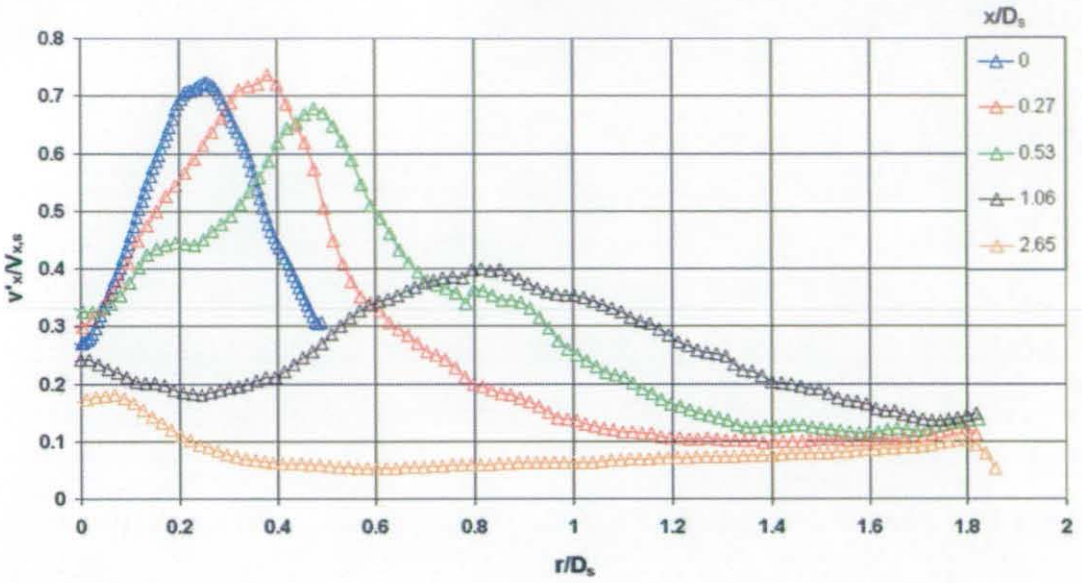

Figure 5.69. Axial RMS Velocity Profiles in Dump Area Expansion Chamber (No-Jet Test Condition)

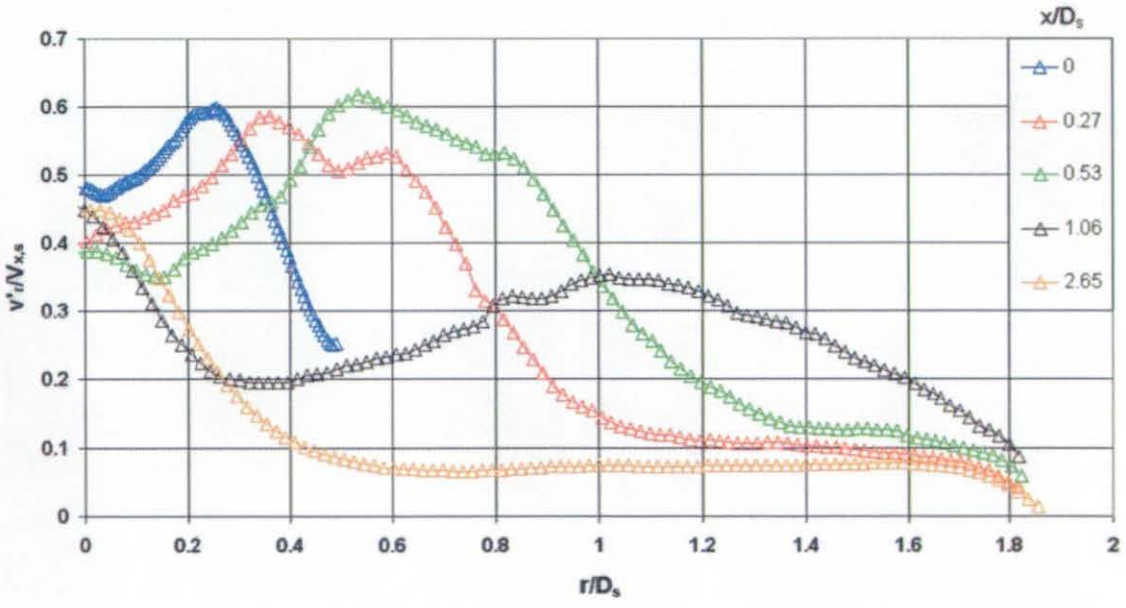

Figure 5.70. Radial RMS Velocity Profiles in Dump Area Expansion Chamber (No-Jet Test Condition)

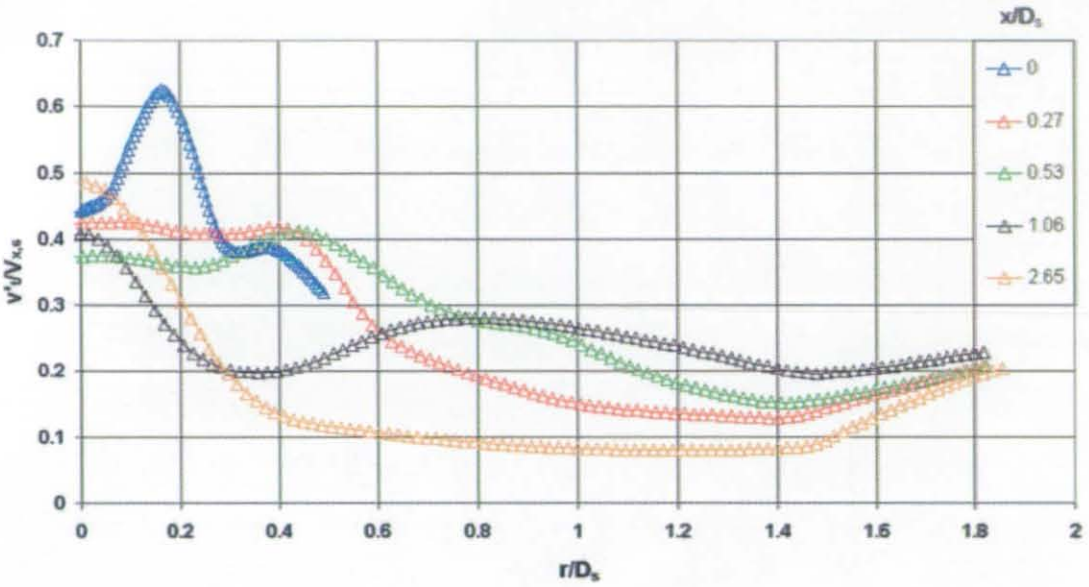

Figure 5.71. Circumferential RMS Velocity Profiles in Dump Area Expansion Chamber (No-Jet Test Condition)

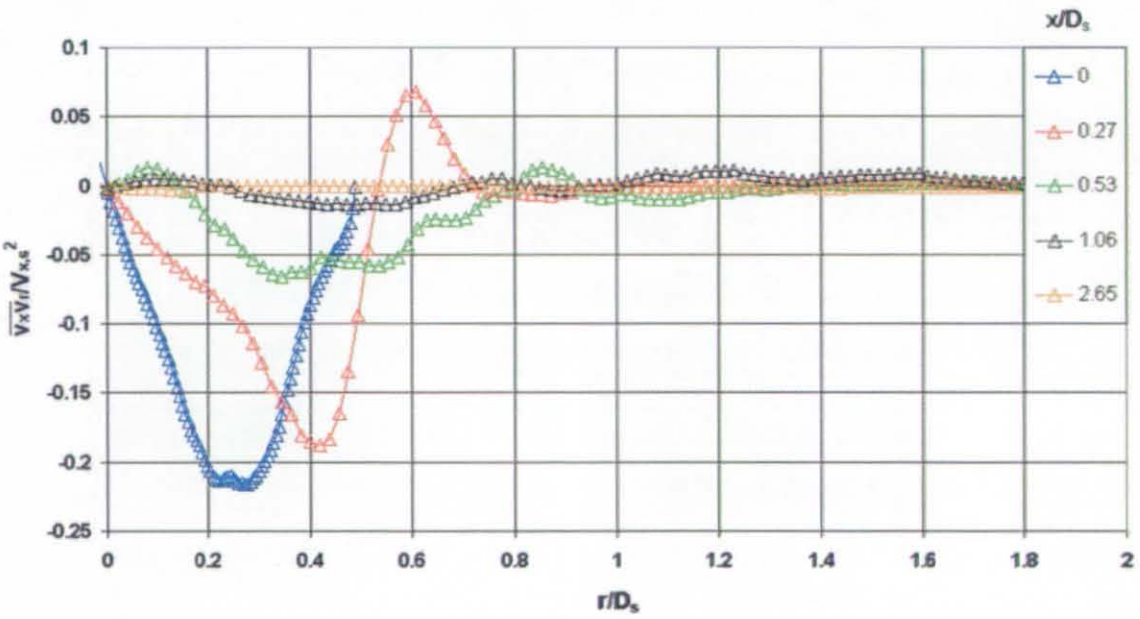

Figure 5.72. Axial-Radial Shear Stress Profiles in Dump Area Expansion Chamber (No-Jet Test Condition)

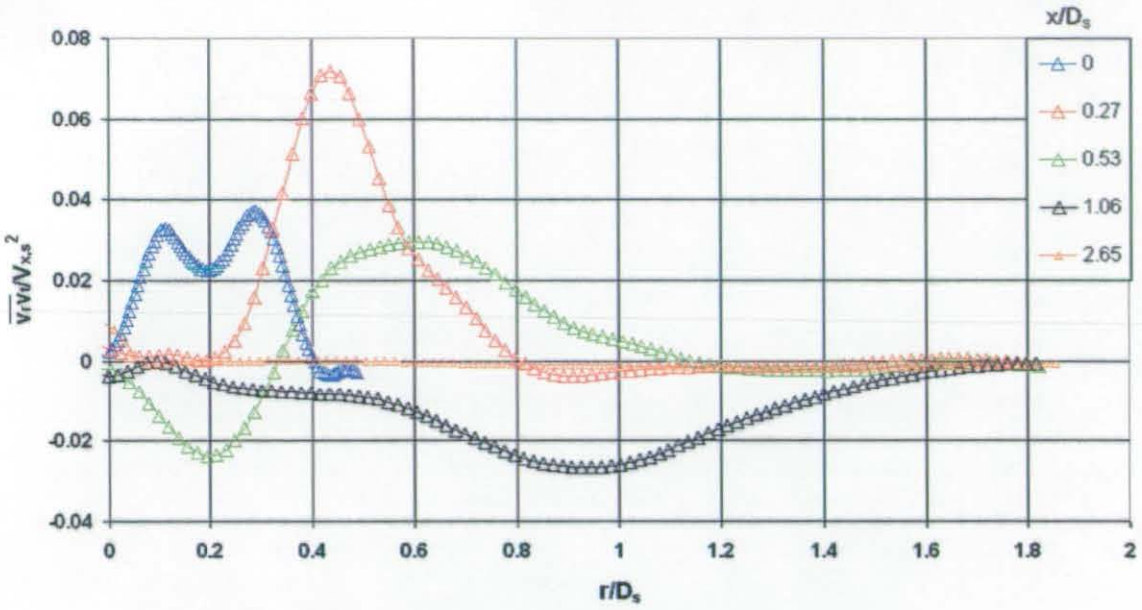

Figure 5.73. Radial- Circumferential Shear Stress Profiles in Dump Area Expansion Chamber (No-Jet Test Condition)

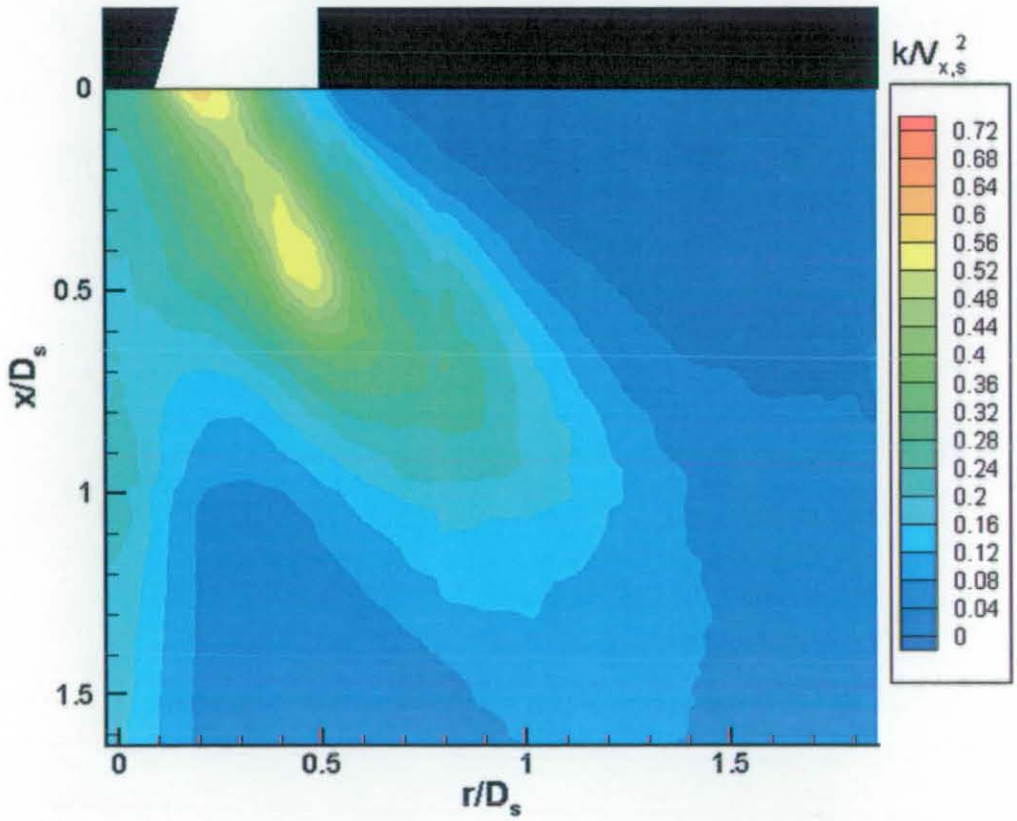

Figure 5.74. Turbulent Kinetic Energy Contours (No-Jet Test Condition)

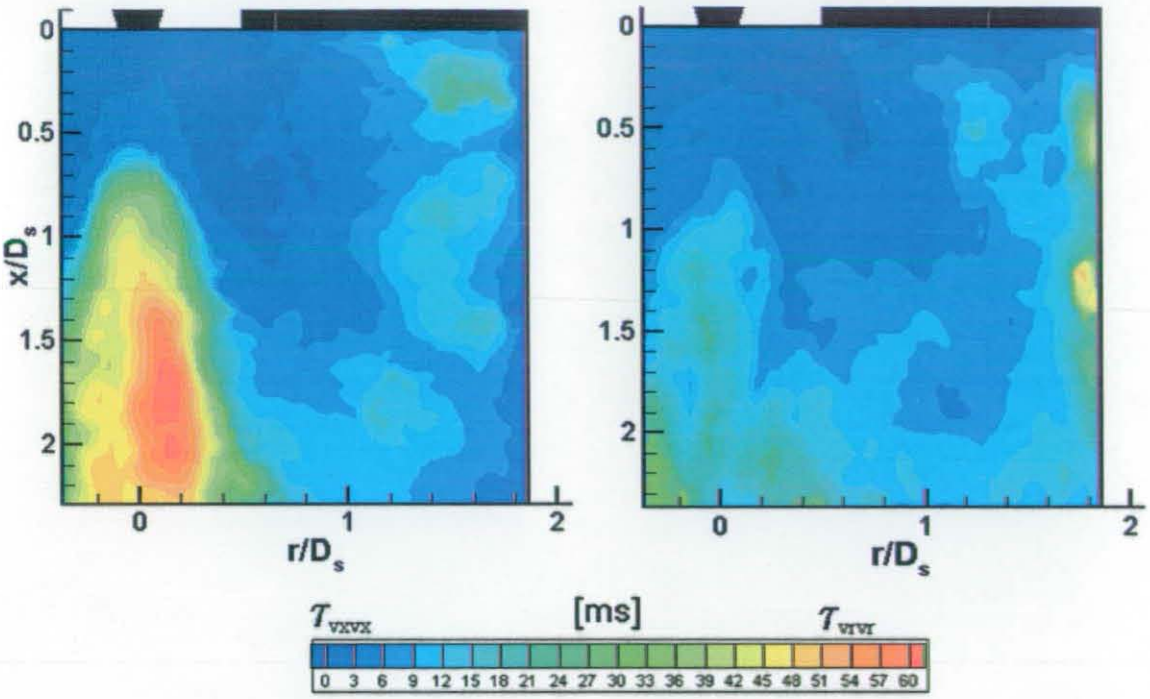

Figure 5.75. Axial [left] and Radial [right] Integral Timescale Contours (No-Jet Test Condition)

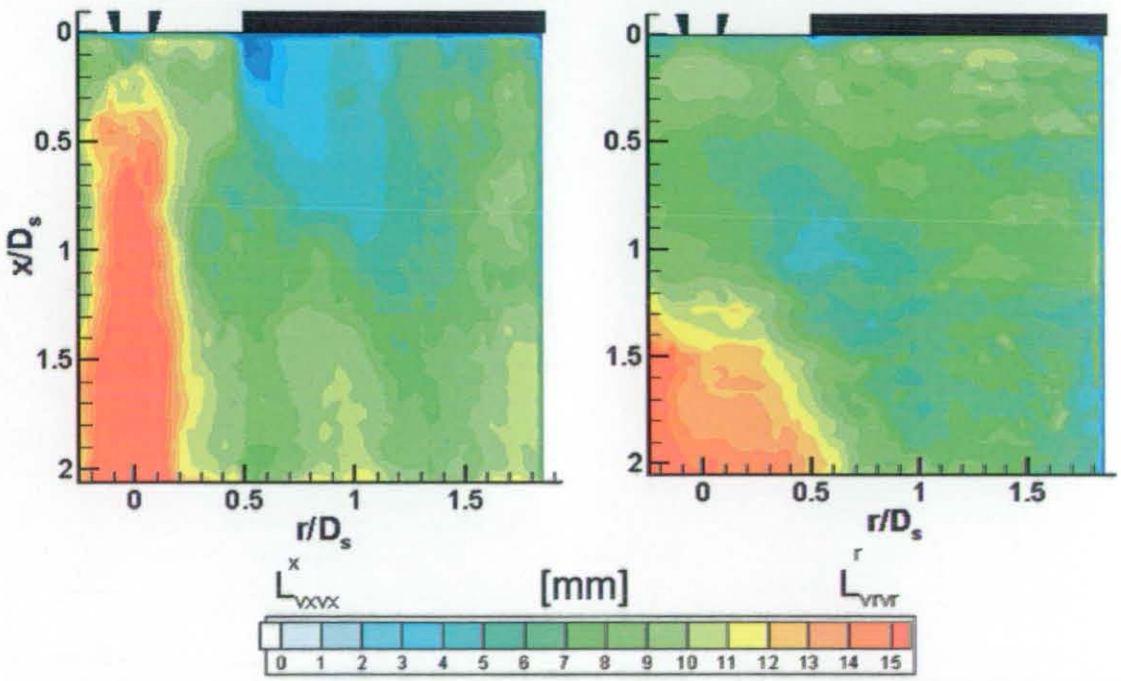

Figure 5.76. Axial [left] and Radial [right] Turbulent Integral Length-Scale Contours (No-Jet Test Condition)

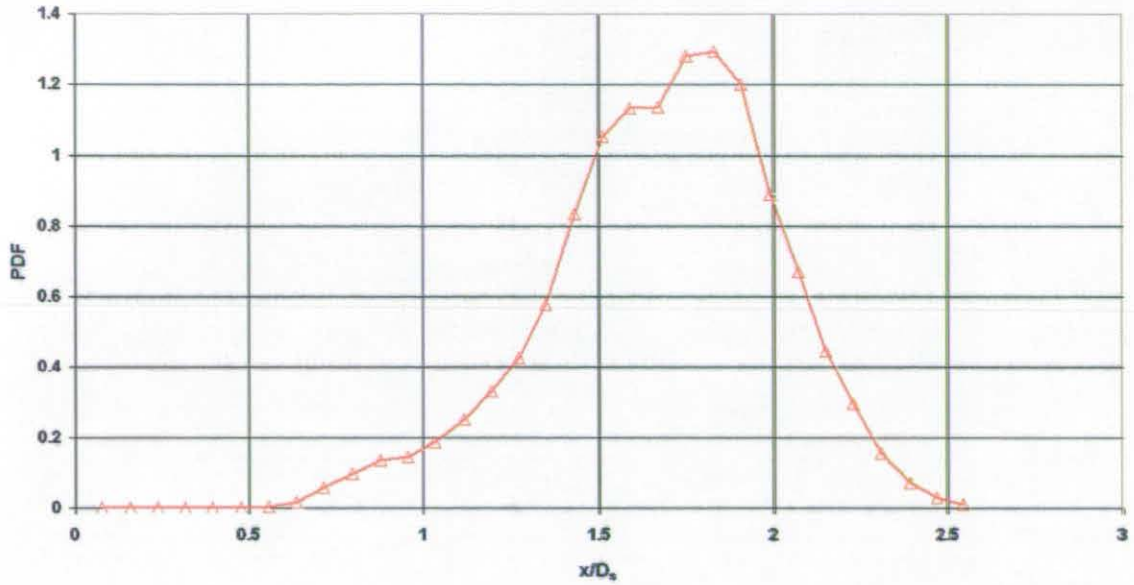

Figure 5.77. Spatial PDF of Swirl Cone Attachment Point (No-Jet Test Condition)

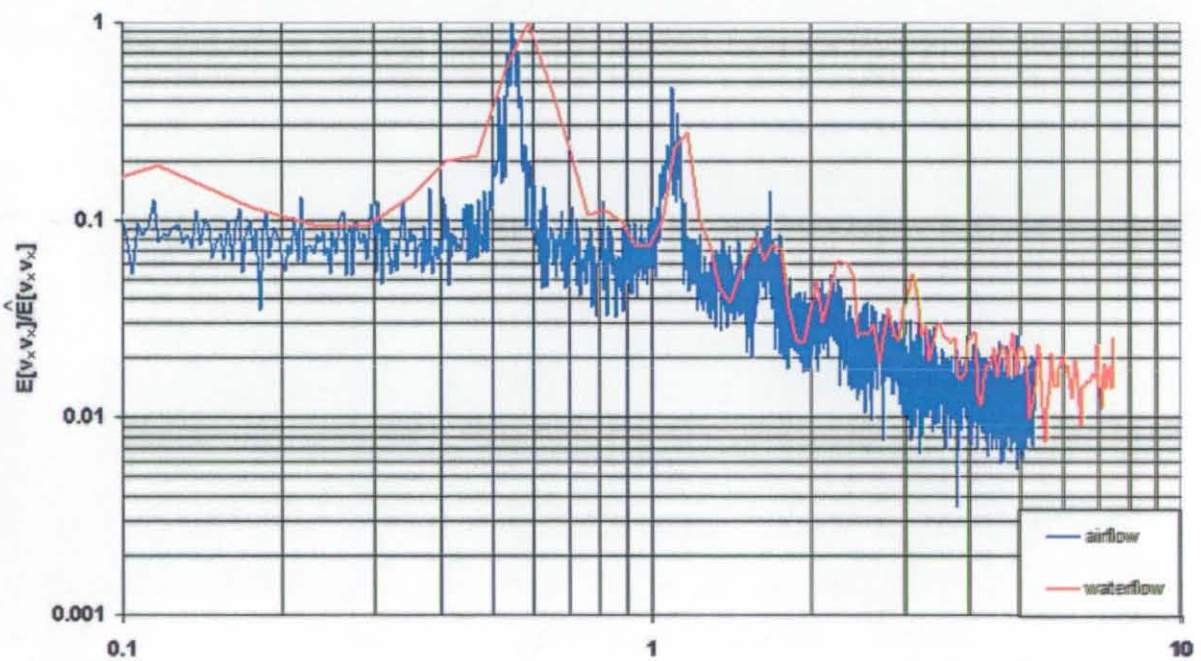

Figure 5.78. PSD Deduced from Axial Velocity at (x=0.27,r=0.27,θ=0) (No-Jet Test Condition)

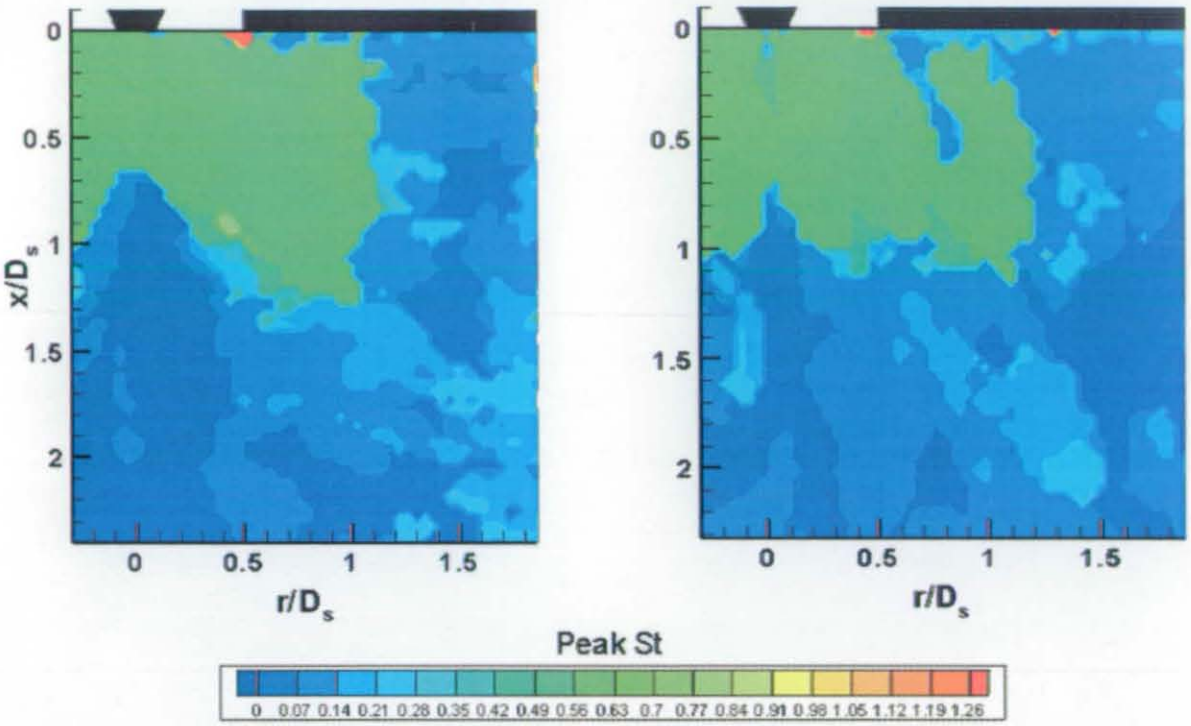

Figure 5.79. Peak Frequency Contours for Axial Velocity [left] and Radial Velocity [right] (No-Jet Test Condition)

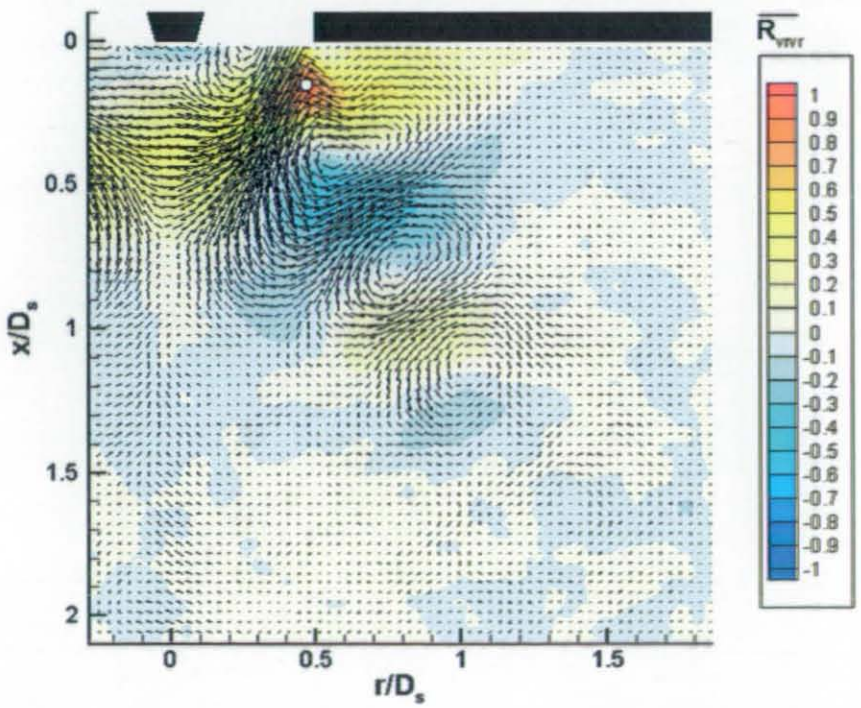

Figure 5.80. Conditionally Averaged Fluctuating Velocity Vectors Superimposed on Radial Velocity Spatial Correlation Contours (No-Jet Test Condition)

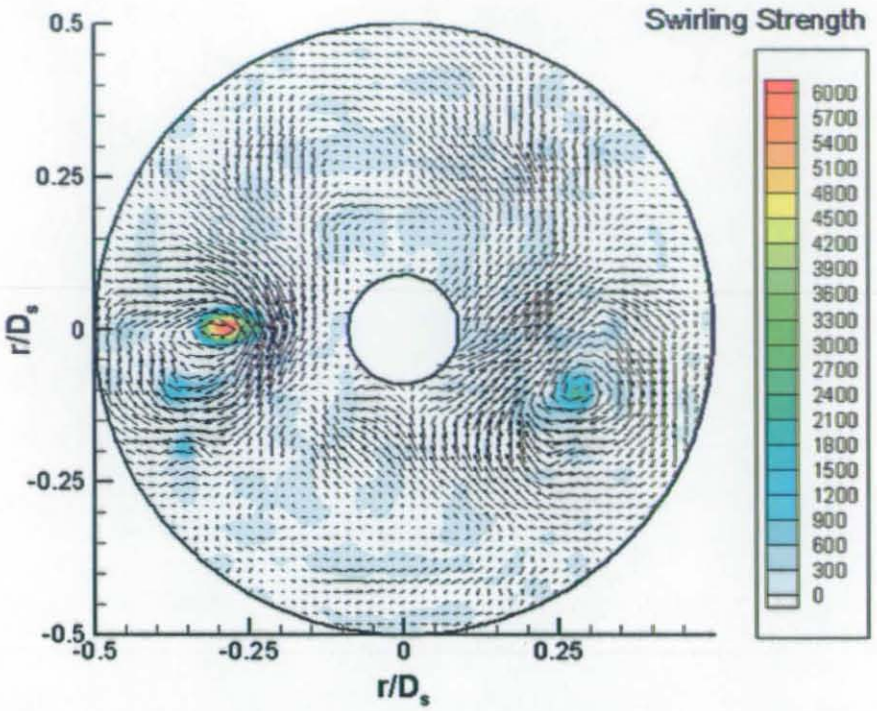

Figure 5.81. SVD (rank 5) Vectors Superimposed on Swirling Strength Contours at $x/D_s=0$ (No-Jet Test Condition)

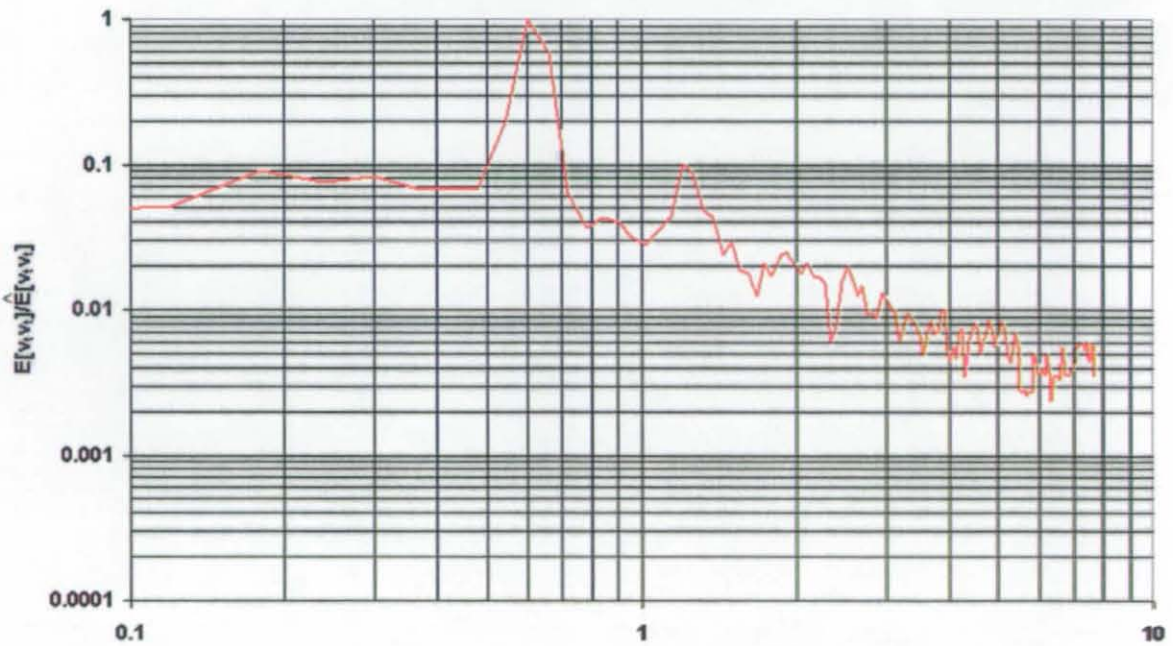

Figure 5.82. PSD Deduced From Circumferential Velocity at ($x=0, r=0.25, \theta=0$) (No-Jet Test Condition)

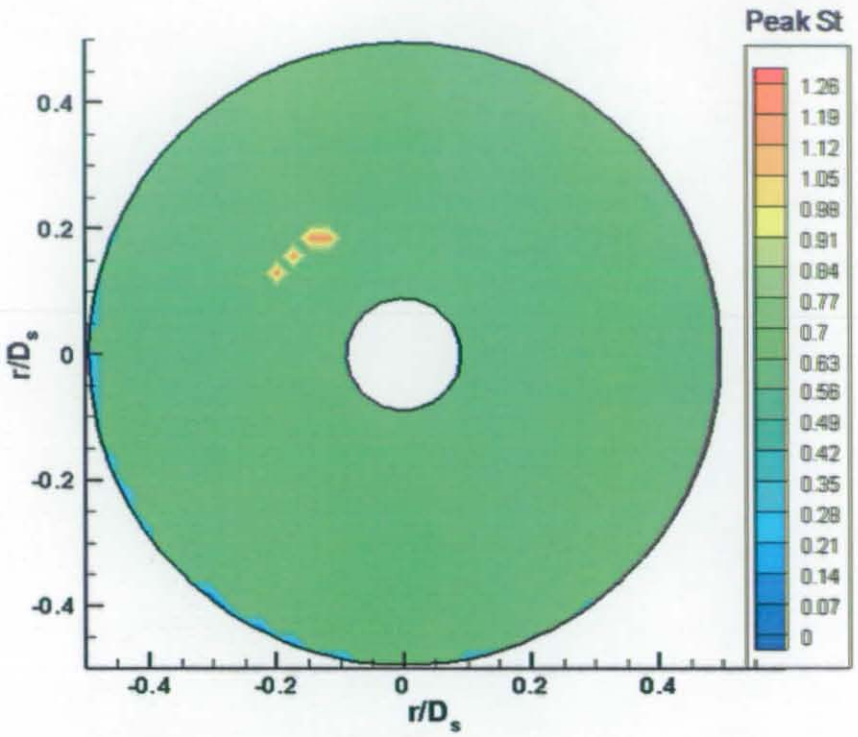

Figure 5.83. Peak Frequency Contours Deduced From Circumferential Velocity at x/D_s=0.0 (No-Jet Test Condition)

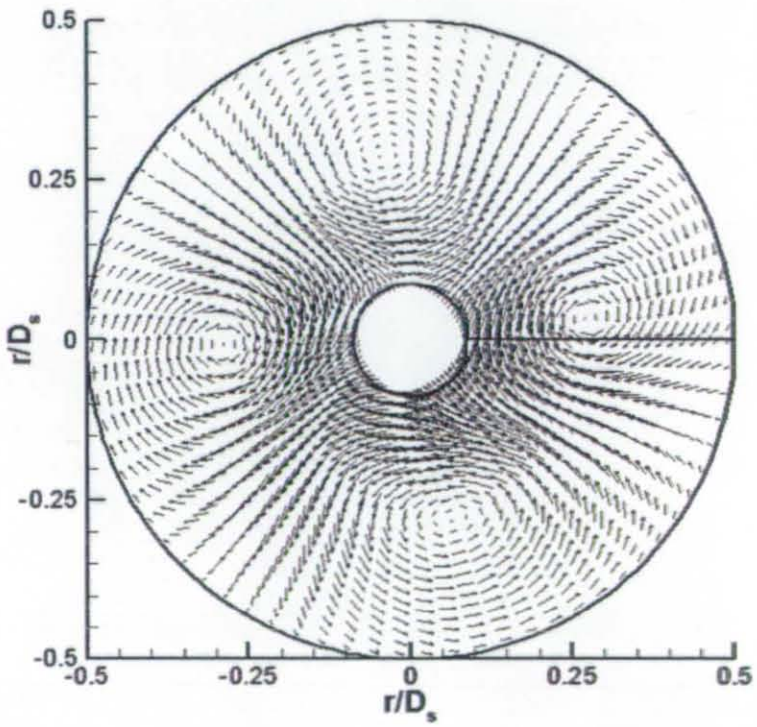

Figure 5.84. Rotational Average of SVD (rank 5) Velocity Vectors at x/D_s=0.0 (No-Jet Test Condition)

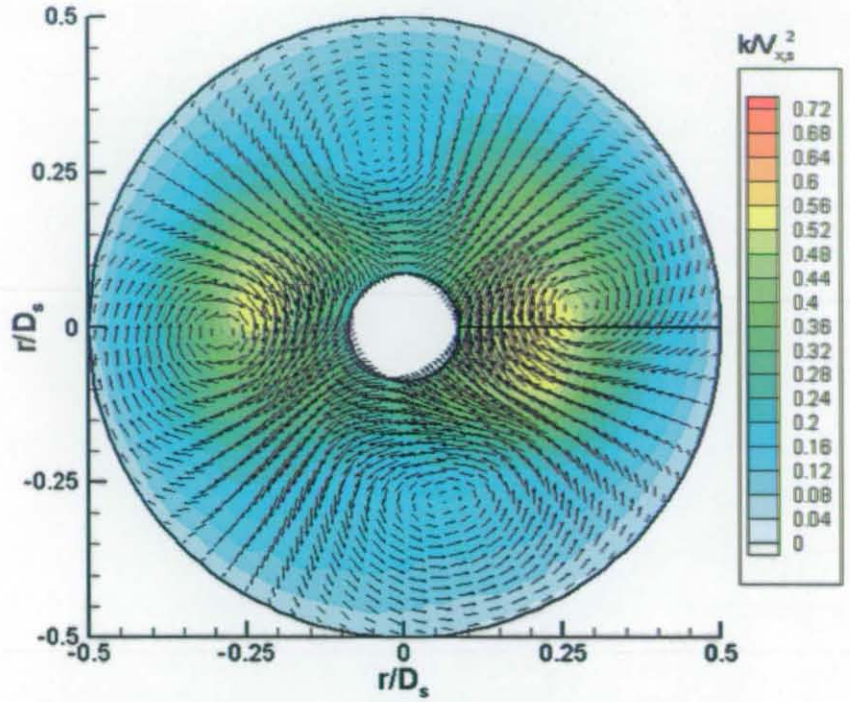

Figure 5.85. Rotationally Averaged Fluctuating Velocity Superimposed on Rotationally Averaged Turbulent Kinetic Energy Contours at x/D_s=0.0 (No-Jet Condition)

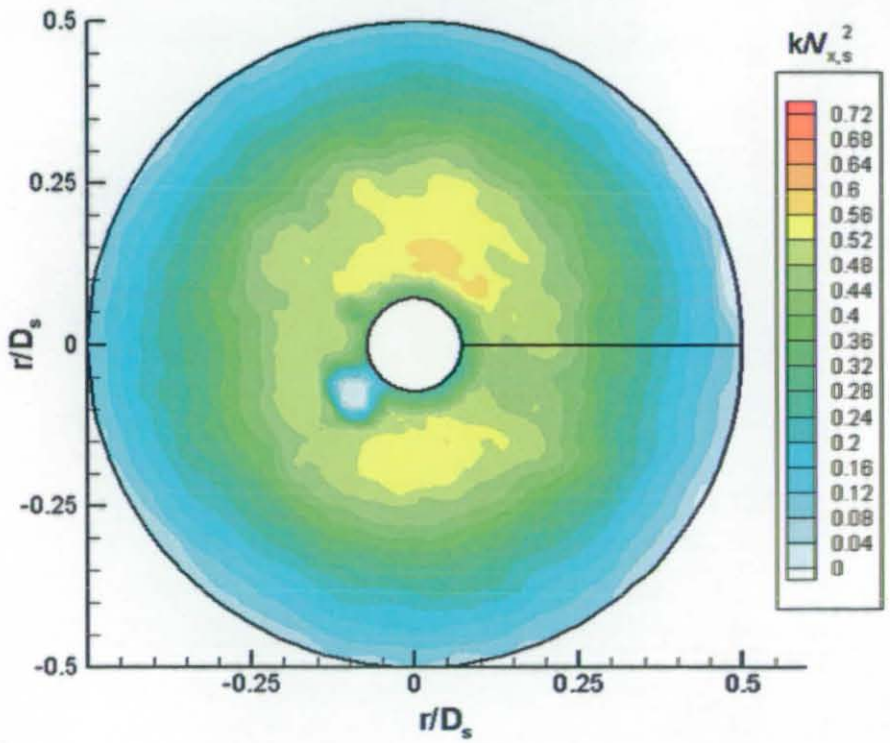

Figure 5.86. Turbulent Kinetic Energy Contours at x/D_s=0 (No-Jet Test Condition)

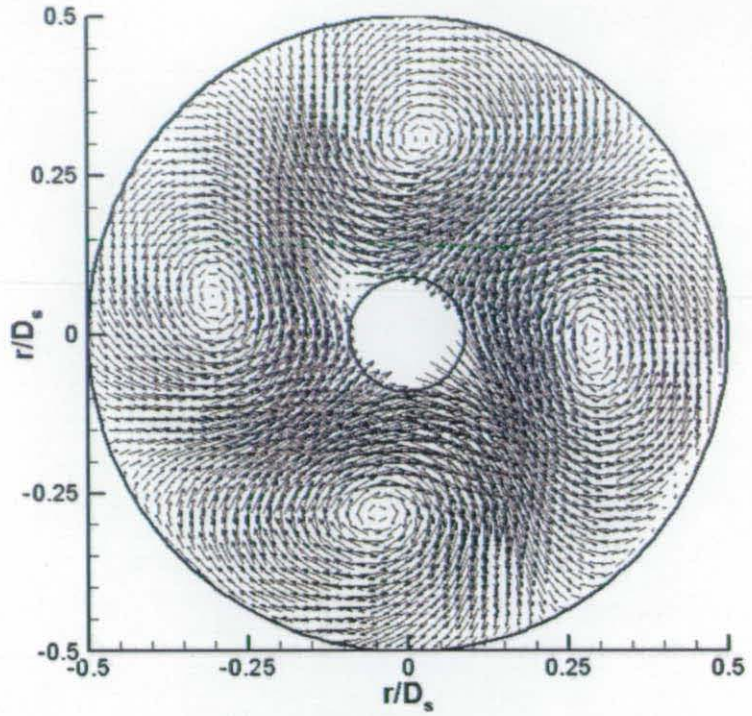

Figure 5.87. First POD Mode at $x/D_s=0$ (No-Jet Test Condition)

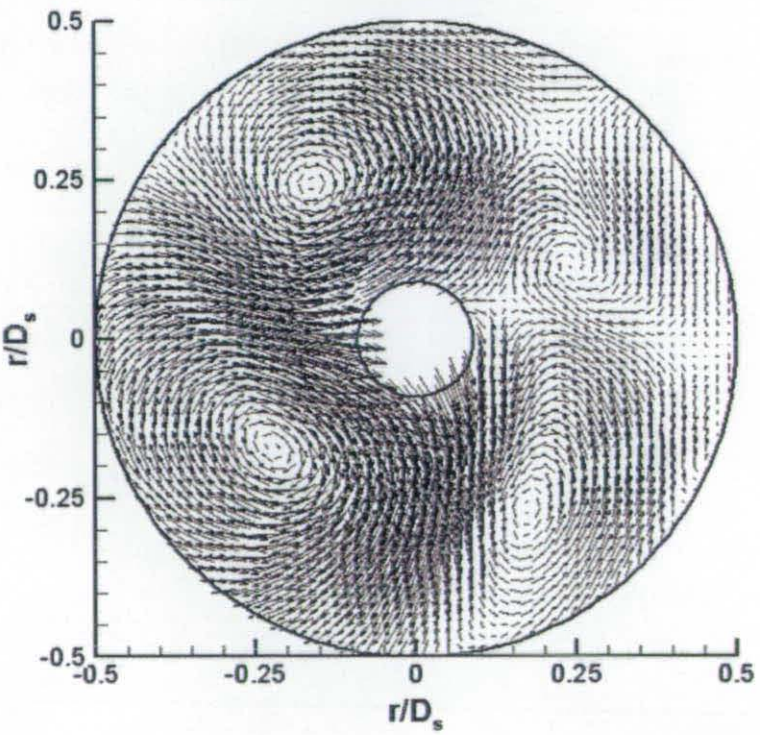

Figure 5.88. Second POD Mode at $x/D_s=0$ (No-Jet Test Condition)

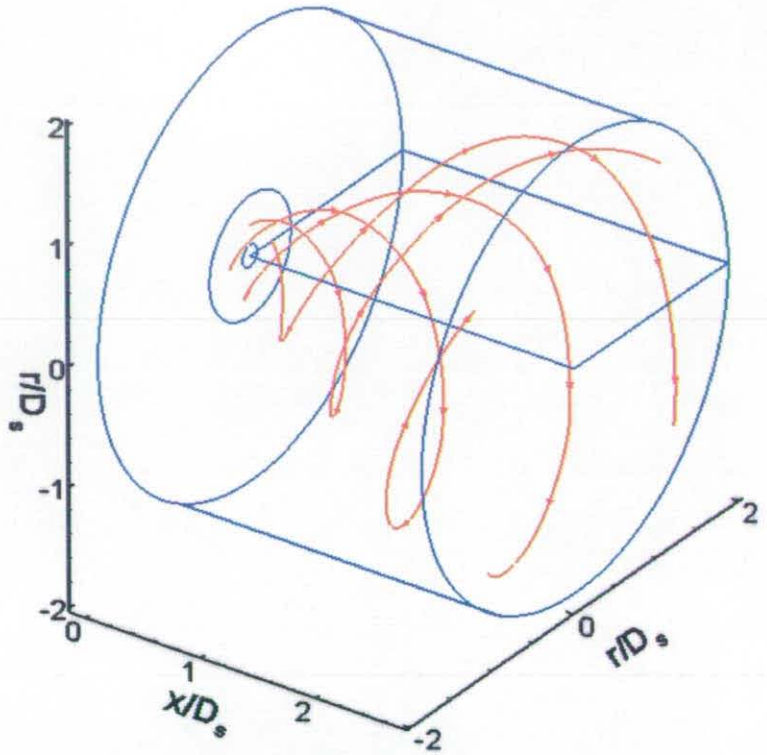

Figure 5.89. Stream-traces Representing the Mean Flow Paths of the Two-Strong and Two-Weak Counter-Rotating Vortex Pairs (No-Jet Test Condition)

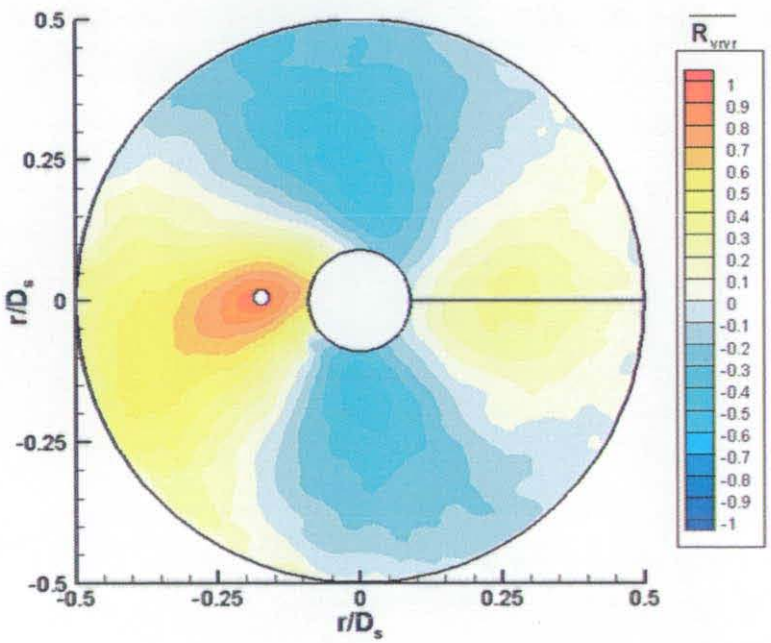

Figure 5.90. Radial Velocity Spatial Correlation Contours at $x/D_s=0$ (No-Jet Test Condition)

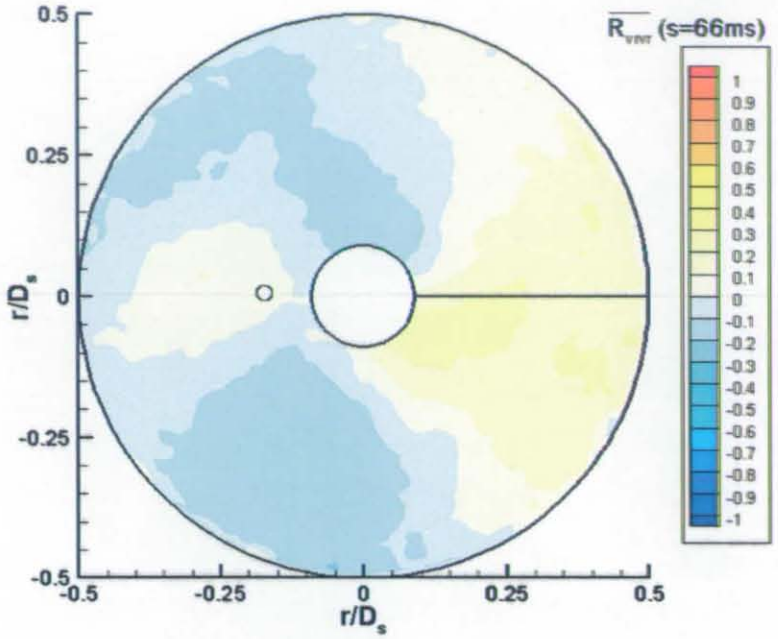

Figure 5.91. Radial Velocity Cross-Correlation Contours (s=66ms) at x/D_s=0 (No-Jet Test Condition)

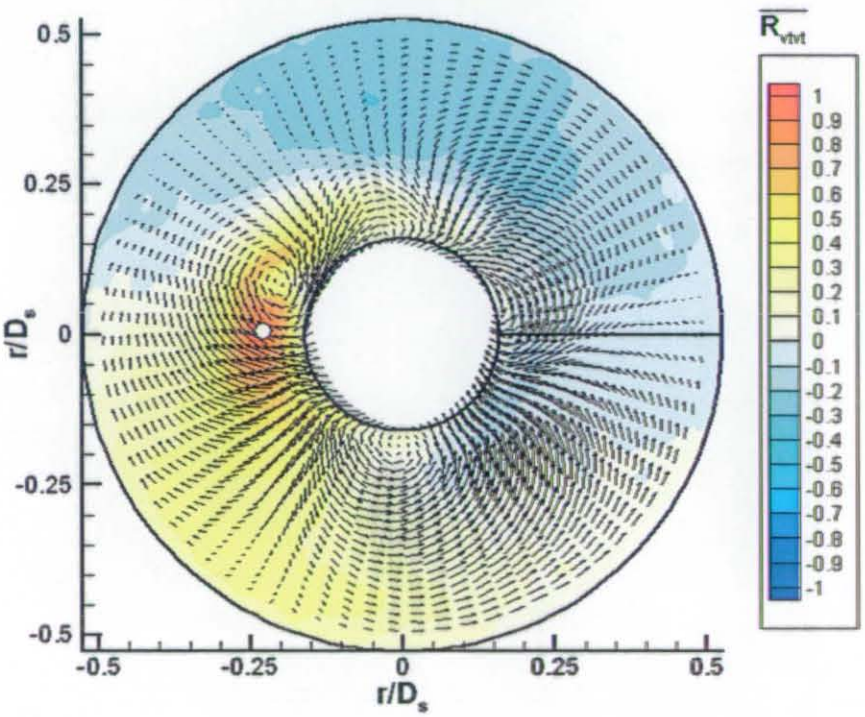

Figure 5.92. Circumferential Velocity Spatial Correlation Contours at x/D_s=-0.27 (No-Jet Test Condition)

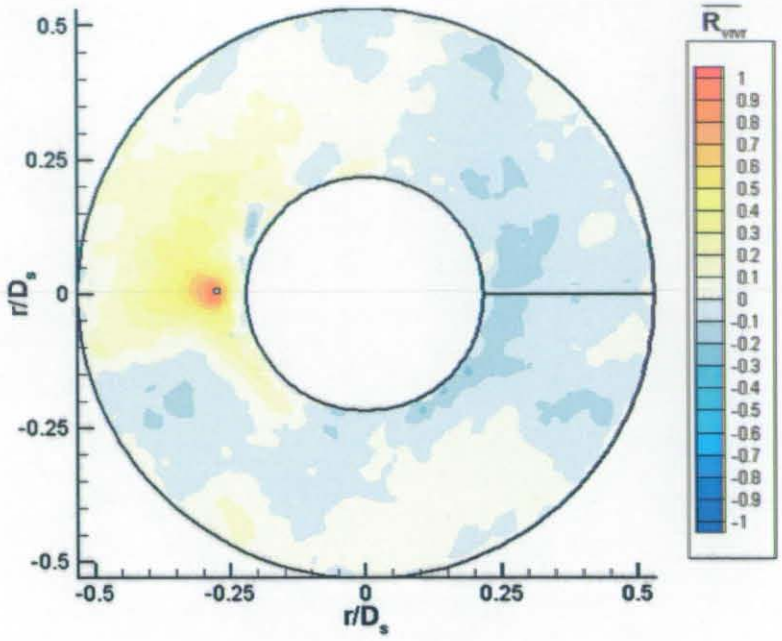

Figure 5.93. Circumferential Velocity Spatial Correlation Contours at x/D_s=-0.43 (No-Jet Test Condition)

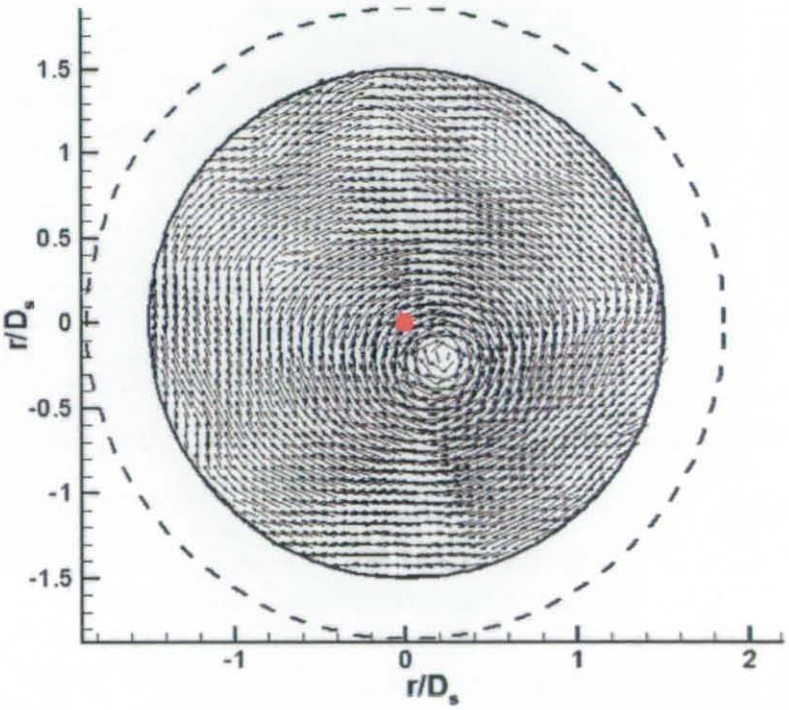

Figure 5.94. Instantaneous Velocity Vectors at x/D_s=2.65 (No-Jet Test Condition)

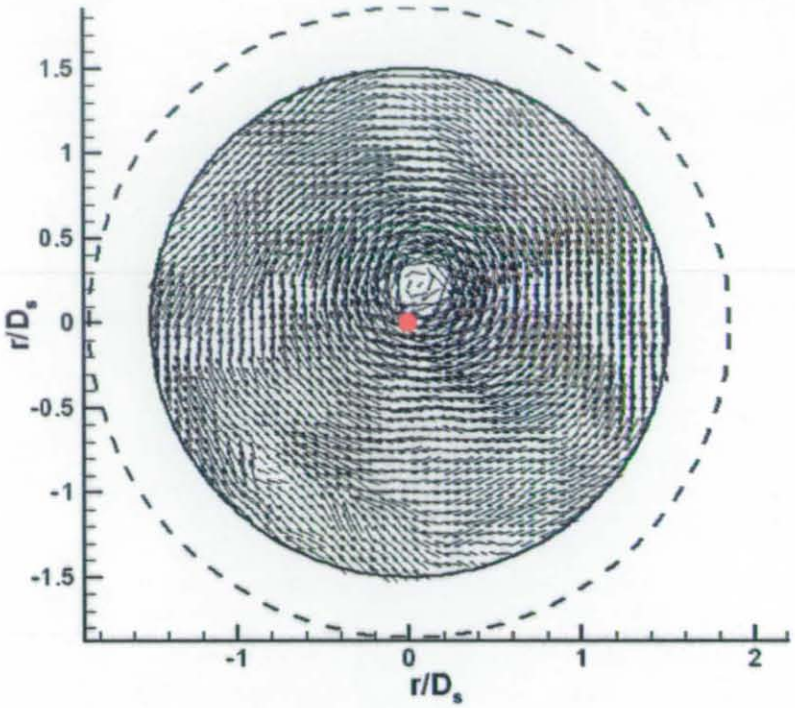

Figure 5.95. Instantaneous Velocity Vectors at x/D_s=2.65 (No-Jet Test Condition)

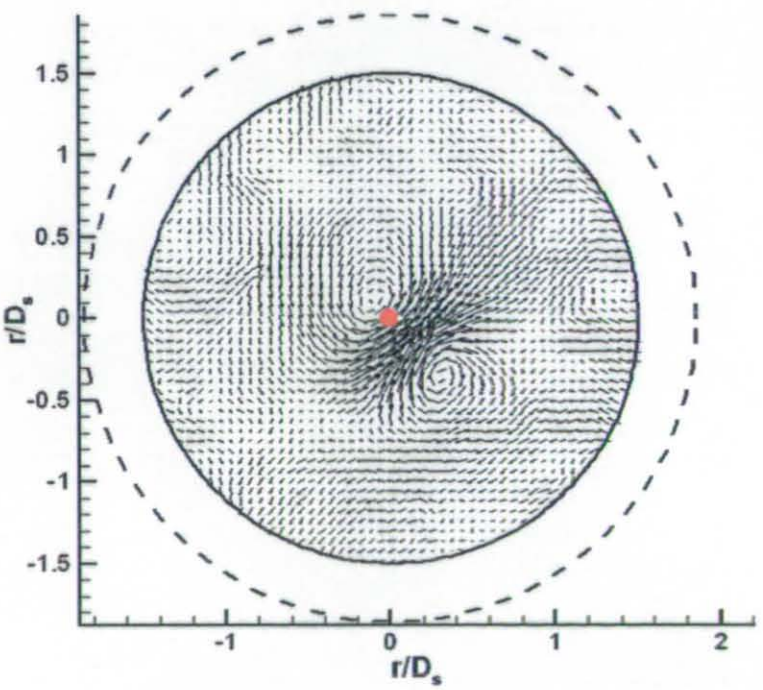

Figure 5.96. Reynolds Decomposed Velocity Field at x/D_s=2.65 (No-Jet Test Condition)

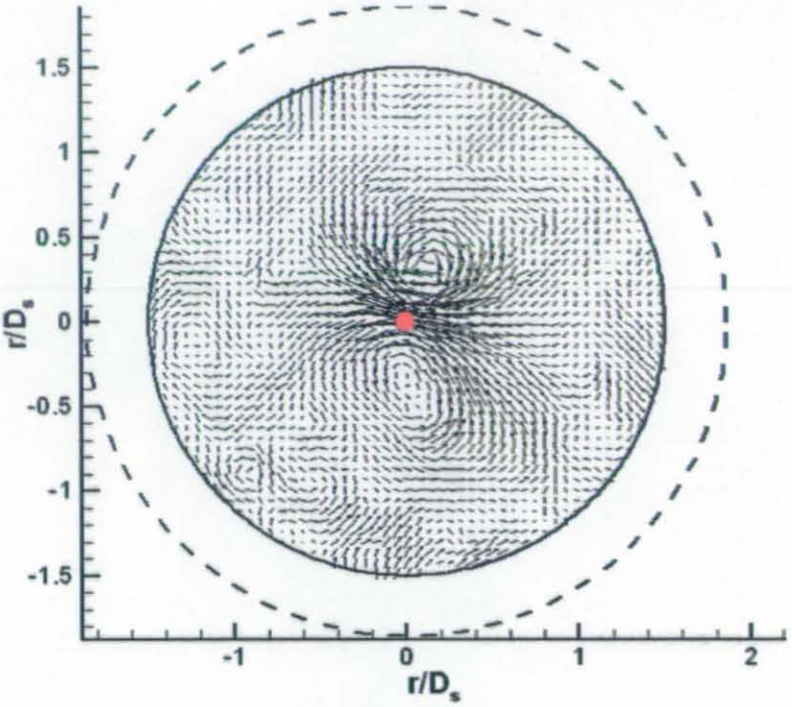

Figure 5.97. Reynolds Decomposed Velocity Field at x/D_s=2.65 (No-Jet Test Condition)

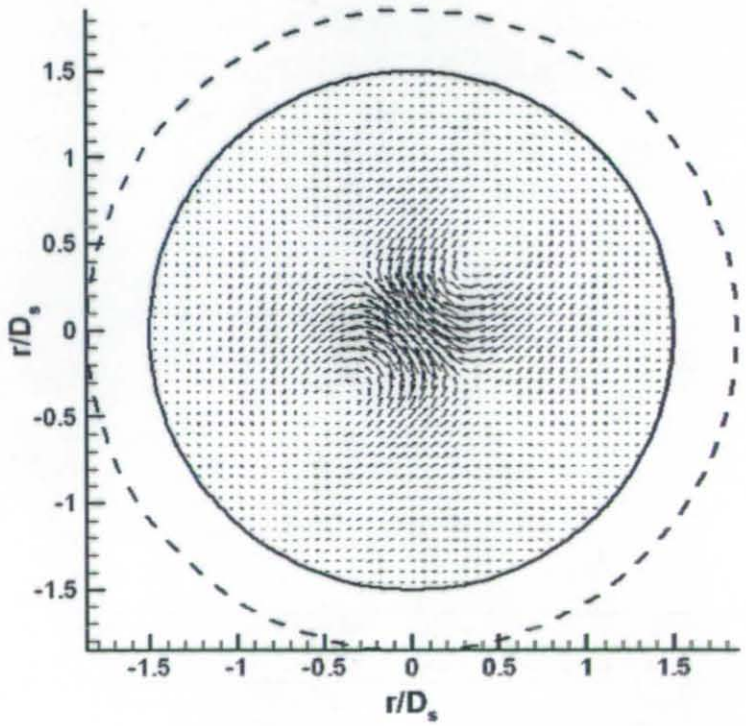

Figure 5.98. First POD Mode at x/D_s=2.65 (No-Jet Test Condition)

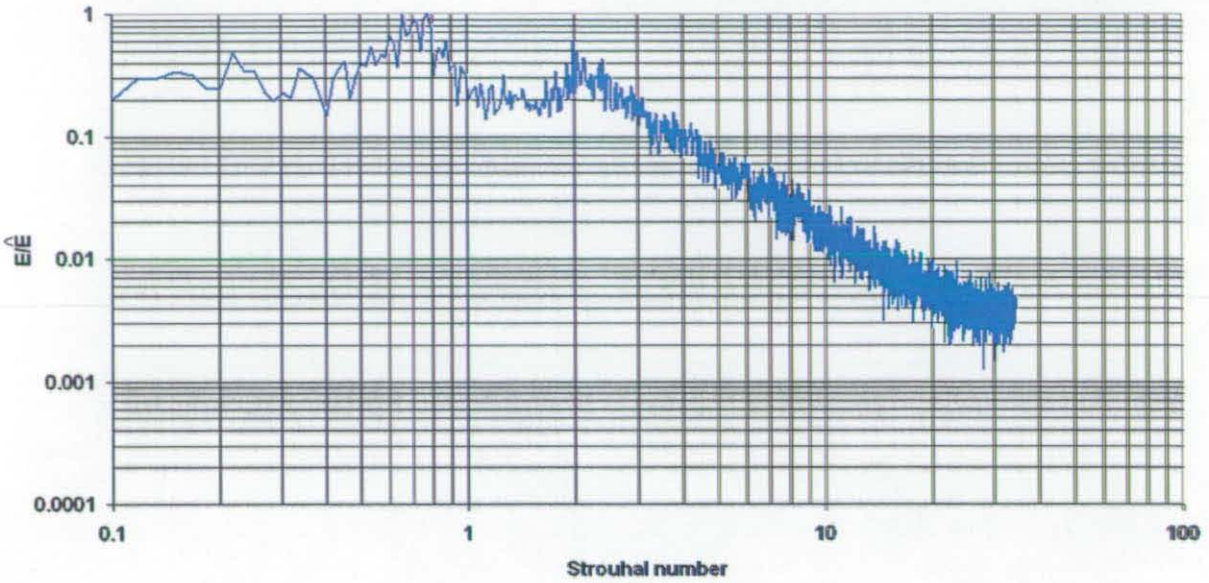

Figure 5.99. PSD Deduced from 1kHz HWA at Location (x=2.65,r=0.19,θ=0) (No-Jet Test Condition)

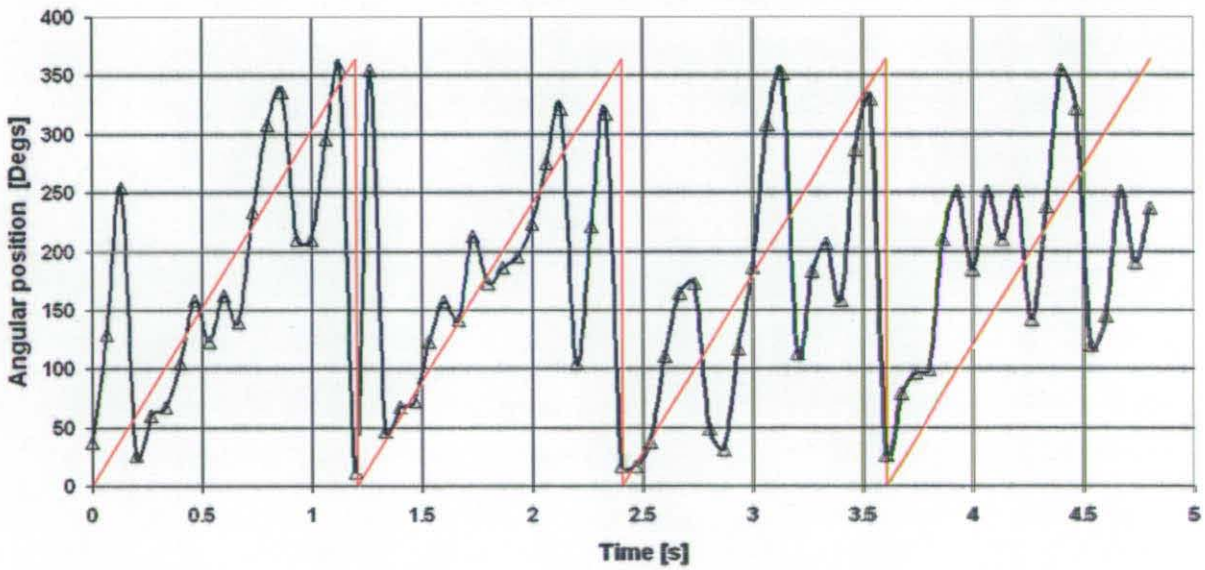

Figure 5.100. Angular Location of Aerodynamic Centre of Solid Body Rotation at x/D_s=2.65 (No-Jet Test Condition)

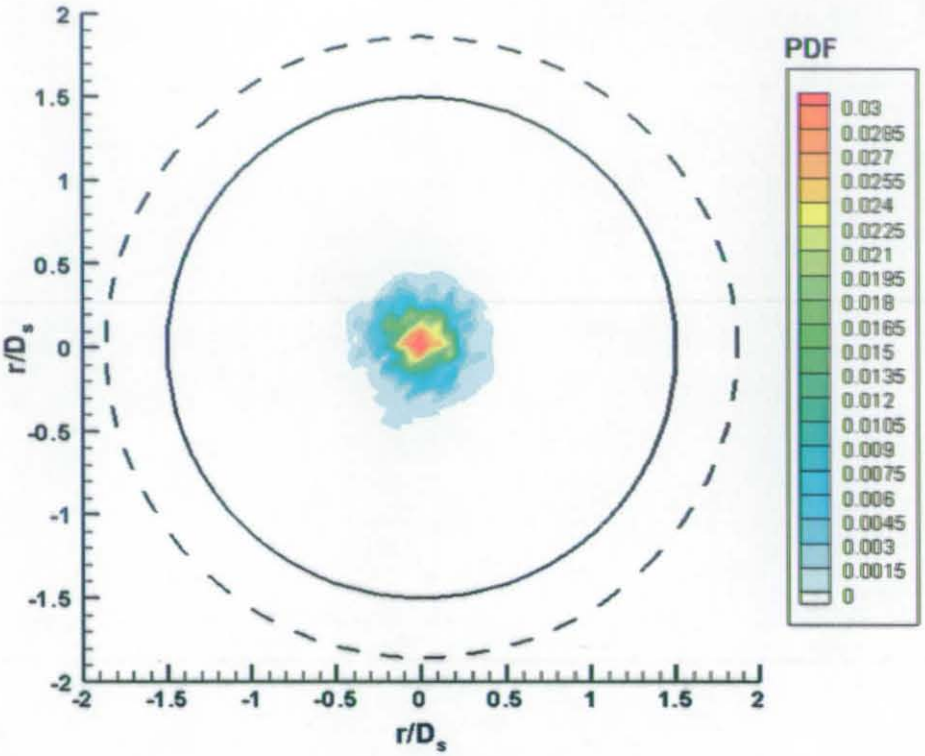

Figure 5.101. PDF Contours of the Location of the PVC at x/D_s=2.65 (No-Jet Test Condition)

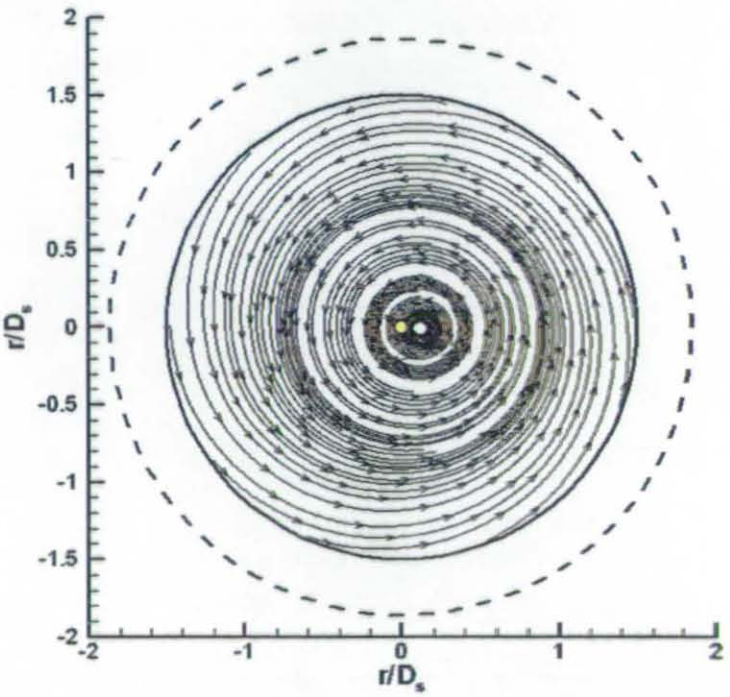

Figure 5.102. Streamlines of Rotationally Averaged Velocity Field at x/D_s=2.65 (No-Jet Test Condition)

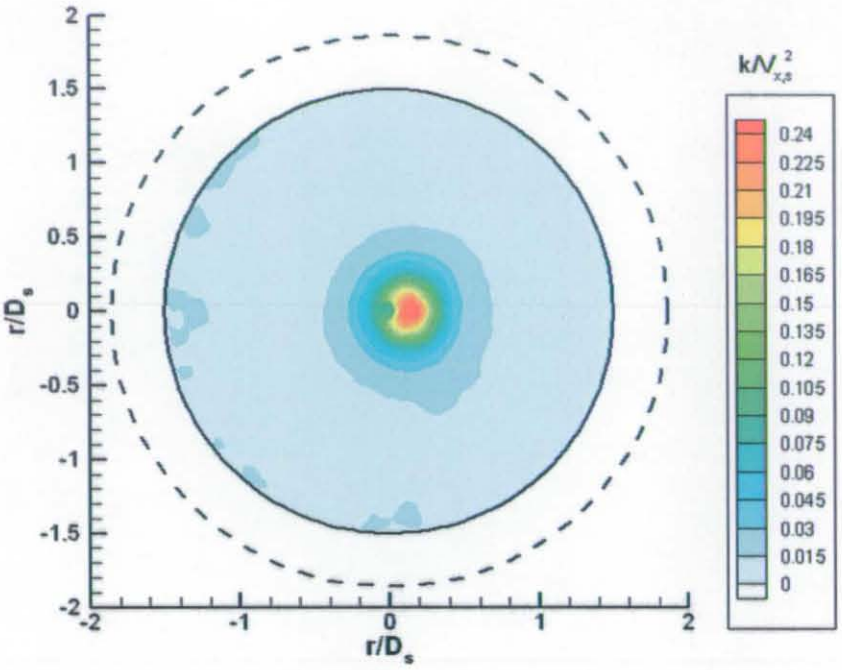

Figure 5.103. Rotationally Averaged Turbulent Kinetic Energy Contours at x/D_s=2.65 (No-Jet Test Condition)

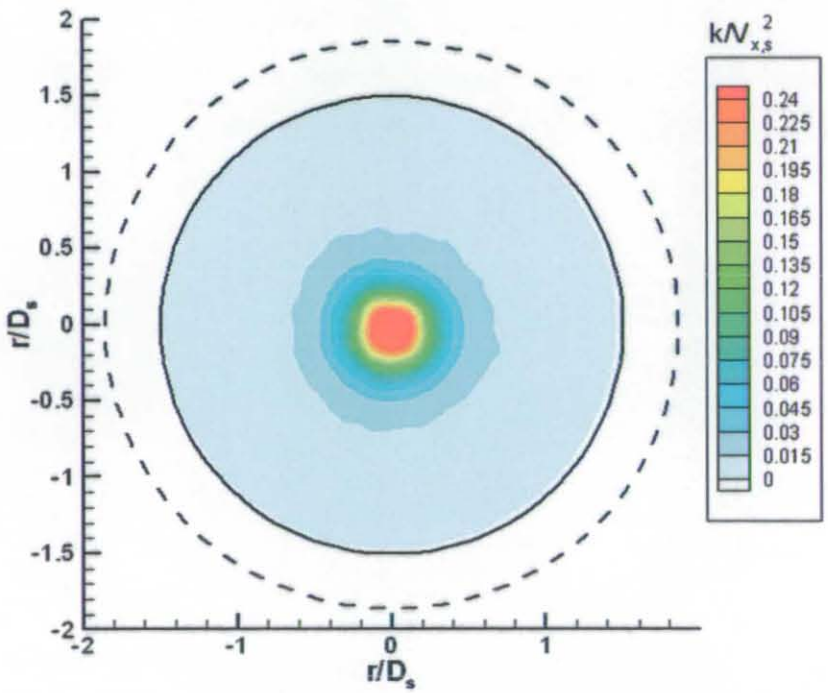

Figure 5.104. Turbulent Kinetic Energy Contours at x/D_s=2.65 (No-Jet Test Condition)

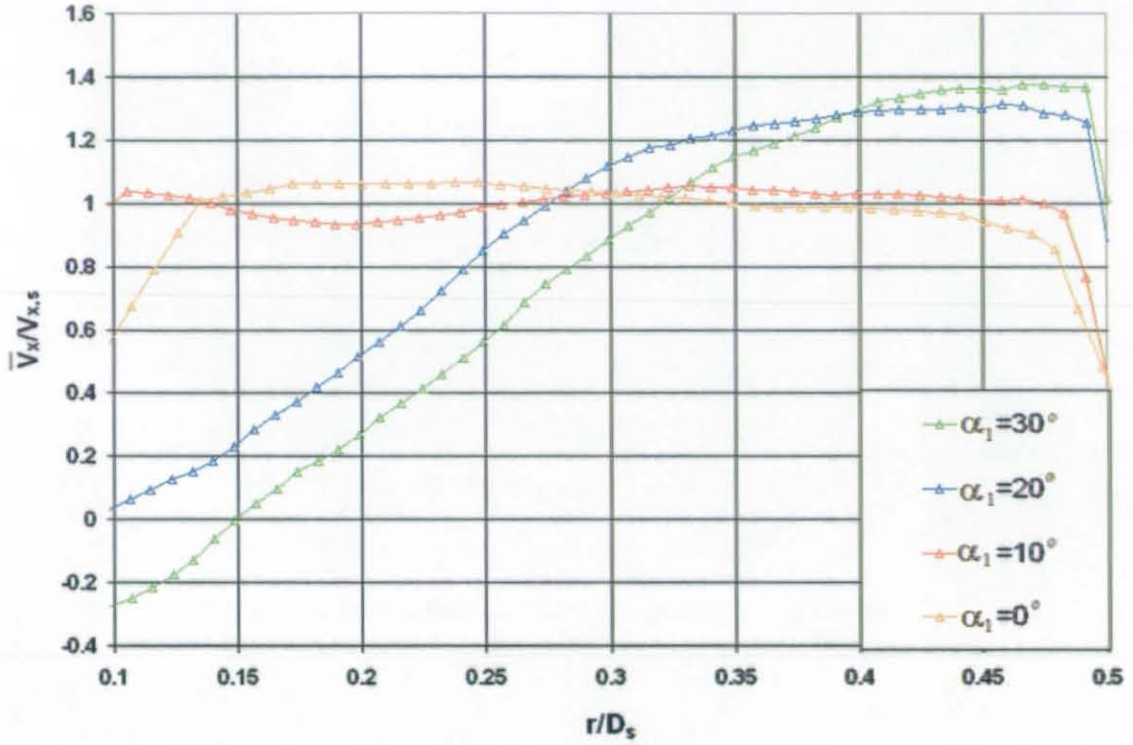

Figure 5.105. Mean Axial Velocity Profiles for Modular Swirler with Varying Slot Angle (Base Case Configuration)

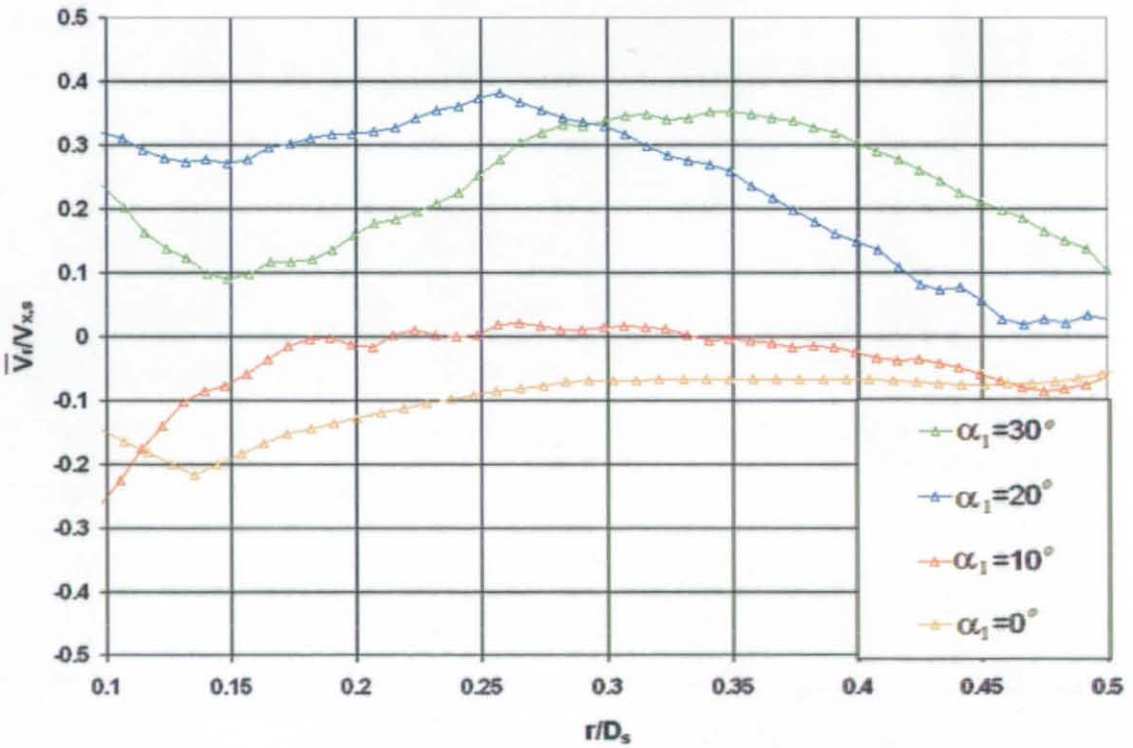

Figure 5.106. Mean Radial Velocity Profiles for Modular Swirler with Varying Slot Angle (Base Case Configuration)

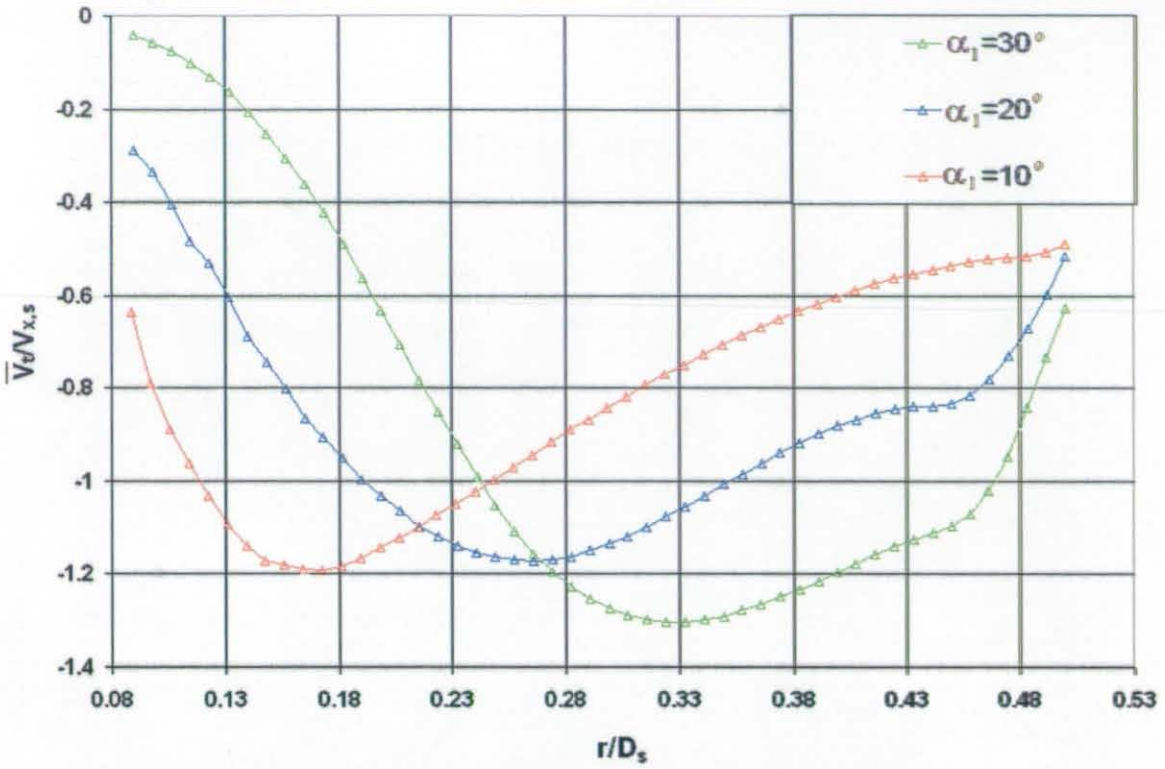

Figure 5.107. Mean Circumferential Velocity Profiles for Modular Swirler with Varying Slot Angle (Base Case Configuration)

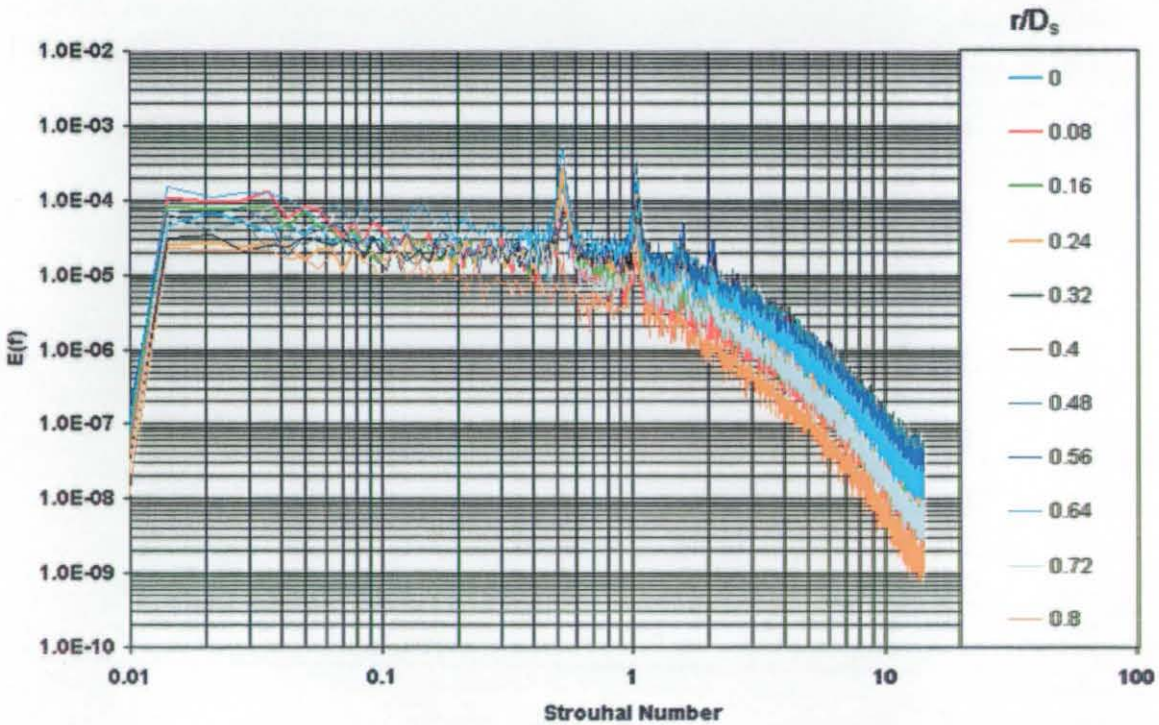

Figure 5.108. PSD Deduced from 25kHz HWA at x/D_s=0.27 with α_1=30° (Base Case Configuration)

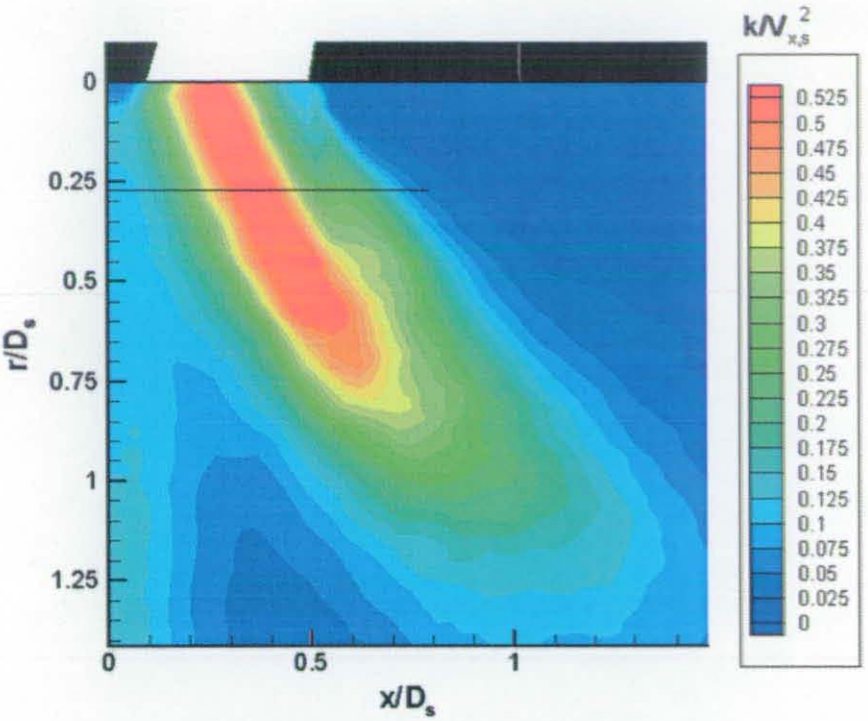

Figure 5.109. Turbulent Kinetic Energy Contours of Modular Swirler with α_1=30° (Base Case Configuration)

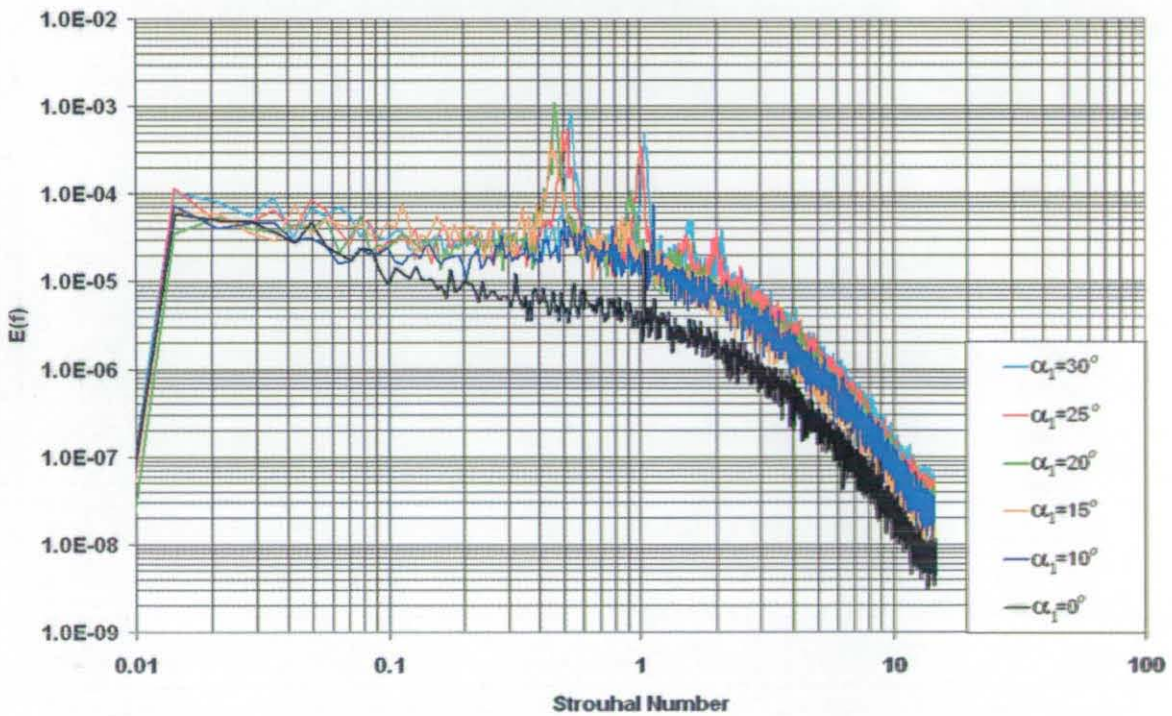

Figure 5.110. PSD Deduced from 25kHz HWA at x/D_s=0.27 of Modular Swirler with Varying Slot Angle (Base Case Configuration)

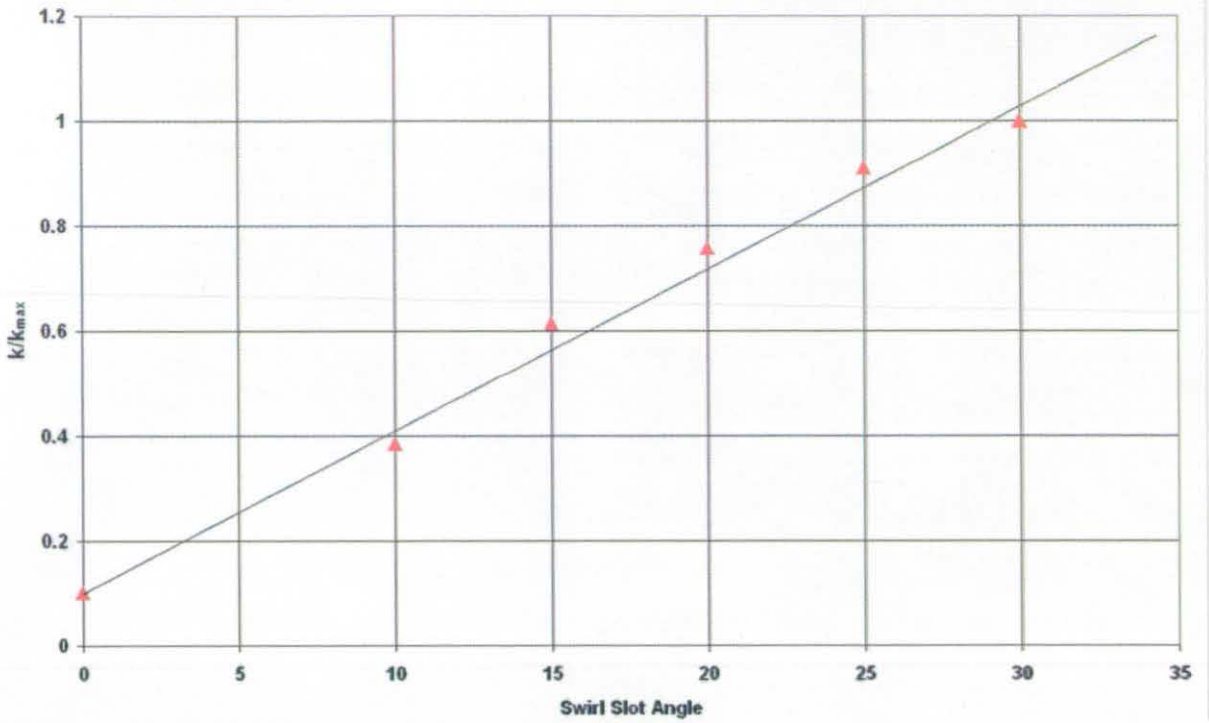

Figure 5.111. Turbulent Kinetic Energy Deduced From Integration of PSD (see Figure 5.110) for Modular Swirler (Base Case Configuration)

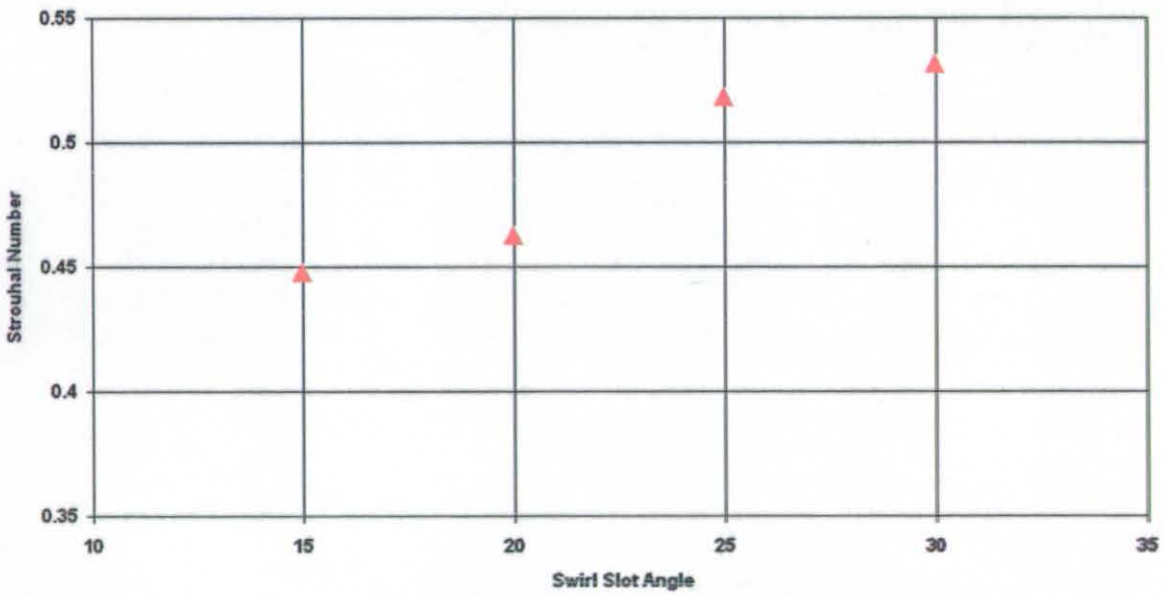

Figure 5.112. Peak Frequency at x/D_s=0.27 for Modular Swirler with Varying Slot Angle (Base Case Configuration)

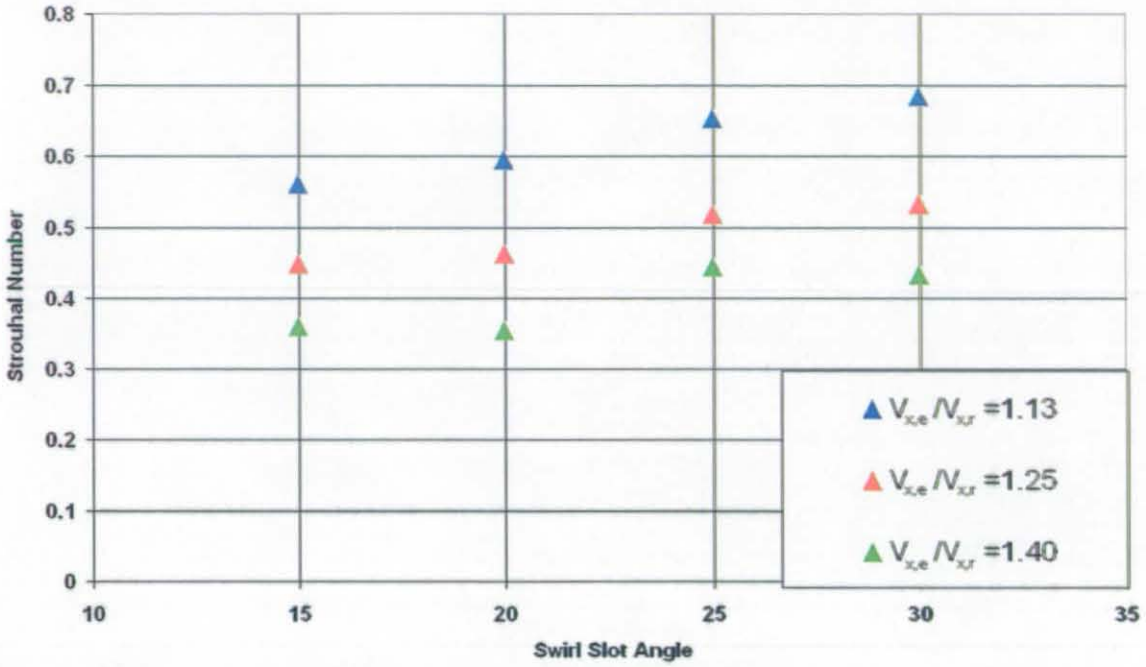

Figure 5.113. Effect of Bulk Average Axial Velocity Ratio on the Dominant Frequency at x/D_s=0.27 for Modular Swirler with Varying Slot Angle

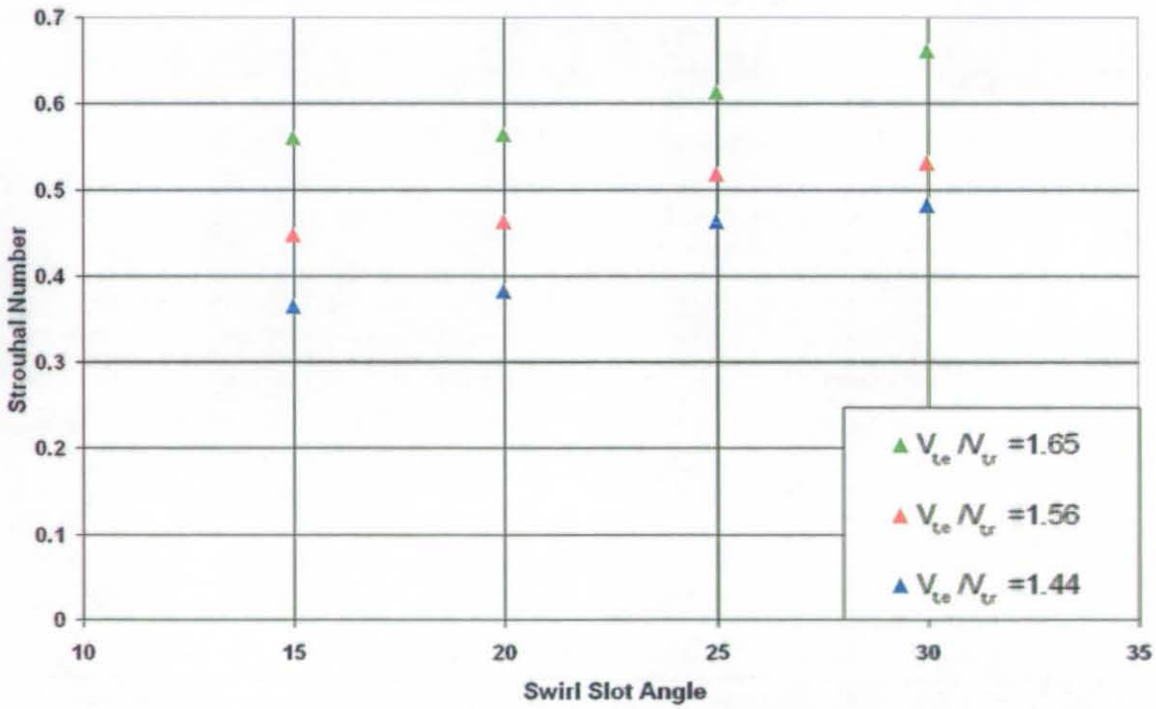

Figure 5.114. Effect of Bulk Average Circumferential Velocity Ratio on the Dominant Frequency at x/D_s=0.27 for Modular Swirler with Varying Slot Angle

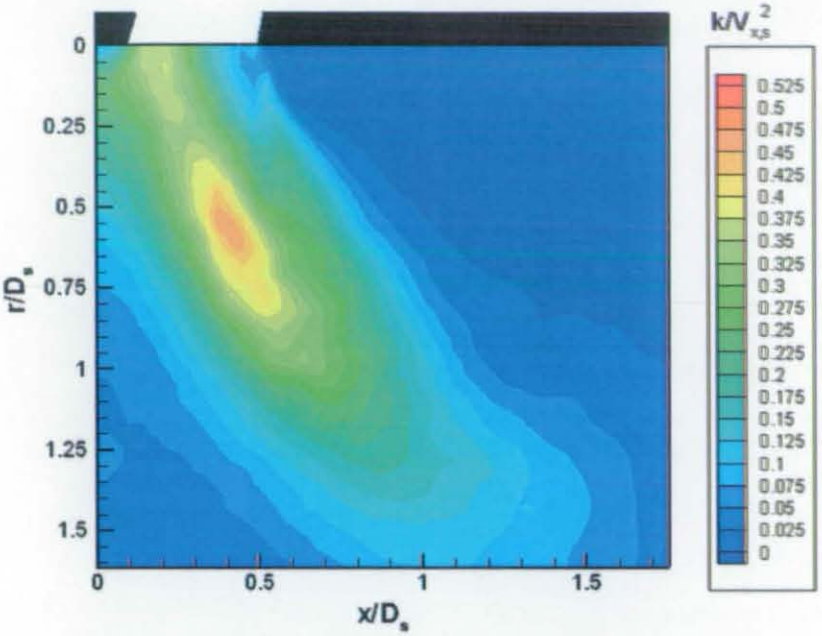

Figure 5.115. Turbulent Kinetic Energy Contours for Modular Swirler with α_1=20° (for Base Case Configuration)

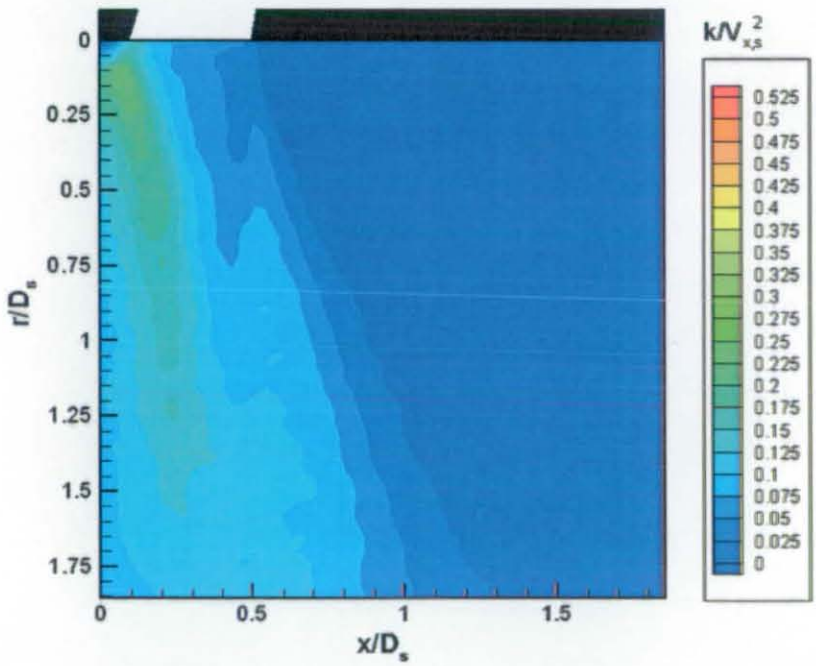

Figure 5.116. Turbulent Kinetic Energy Contours for Modular Swirler with α_1=10° (for Base Case Configuration)

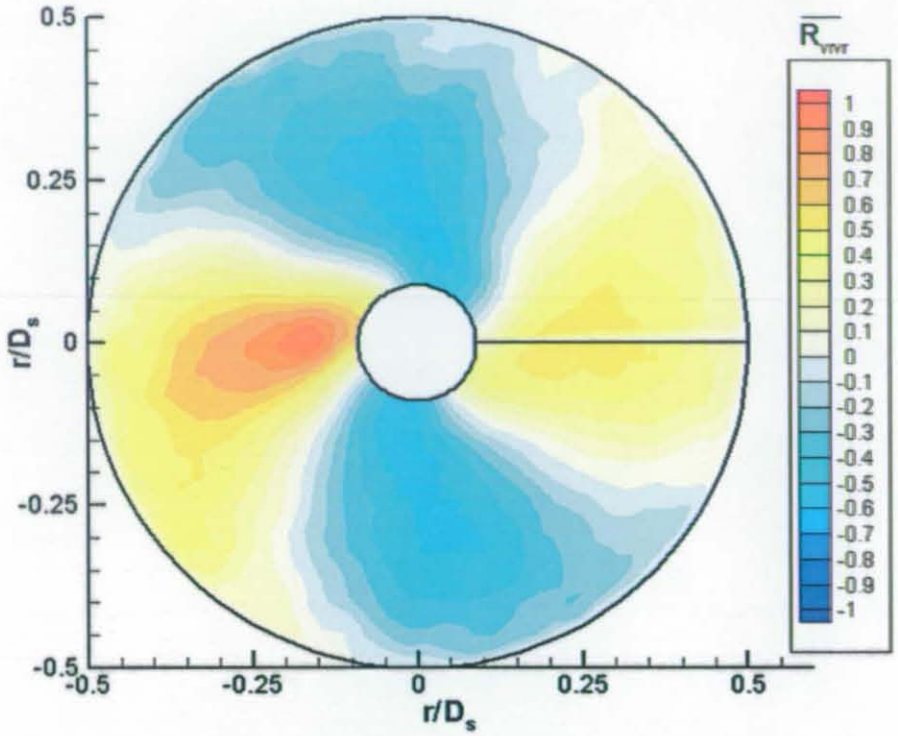

Figure 5.117. Radial Velocity Spatial Correlation Contours for Modular Swirl with α_1=30° at x/D_s=0 (Base Case Configuration)

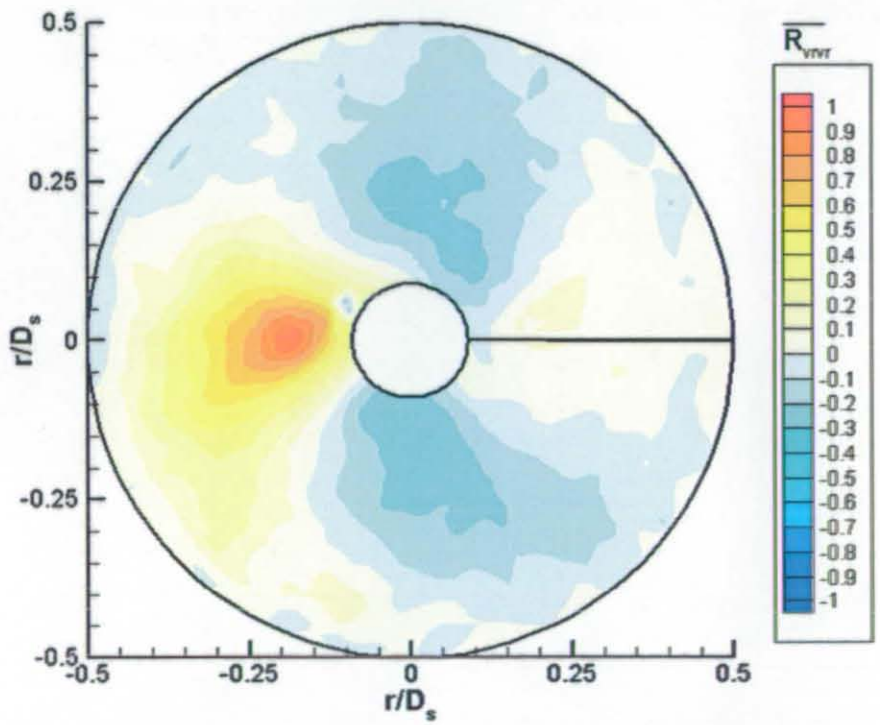

Figure 5.118. Radial Velocity Spatial Correlation Contours for Modular Swirl with α_1=20° at x/D_s=0 (Base Case Configuration)

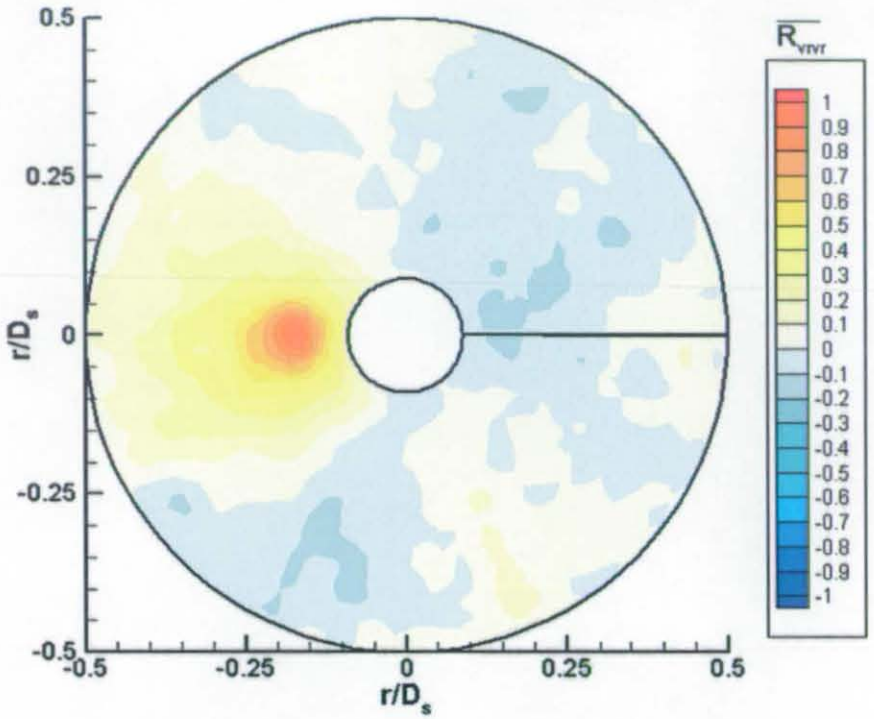

Figure 5.119. Radial Velocity Spatial Correlation Contours for Modular Swirl with α_1=10° at x/D$_s$=0 (Base Case Configuration)

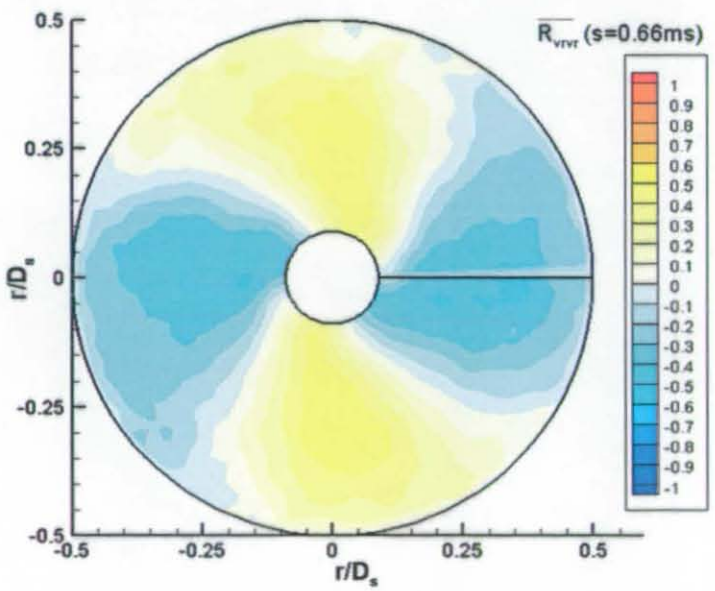

Figure 5.120. Radial Velocity Cross-Correlation Contours (s=66ms) for Modular Swirler with α_1=30° (Base Case Configuration)

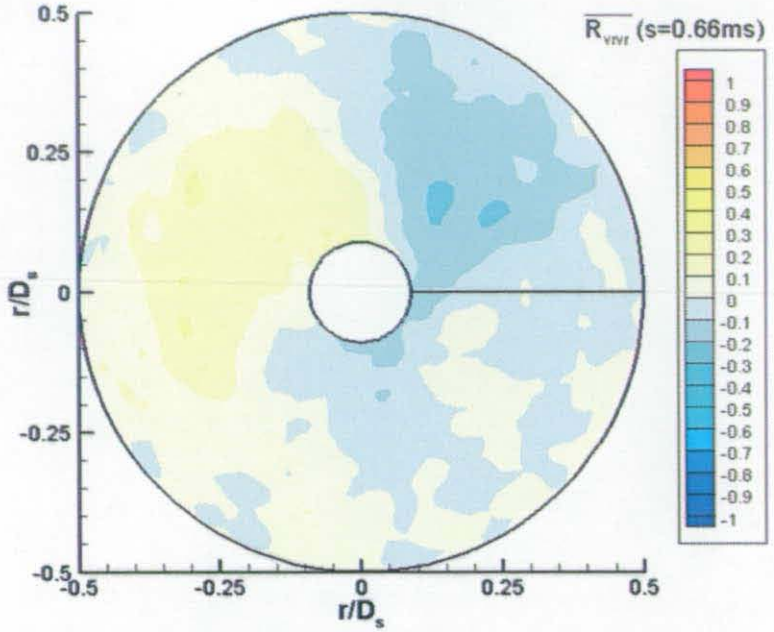

Figure 5.121. Radial Velocity Cross-Correlation Contours (s=66ms) for Modular Swirler with α_1=20° (Base Case Configuration)

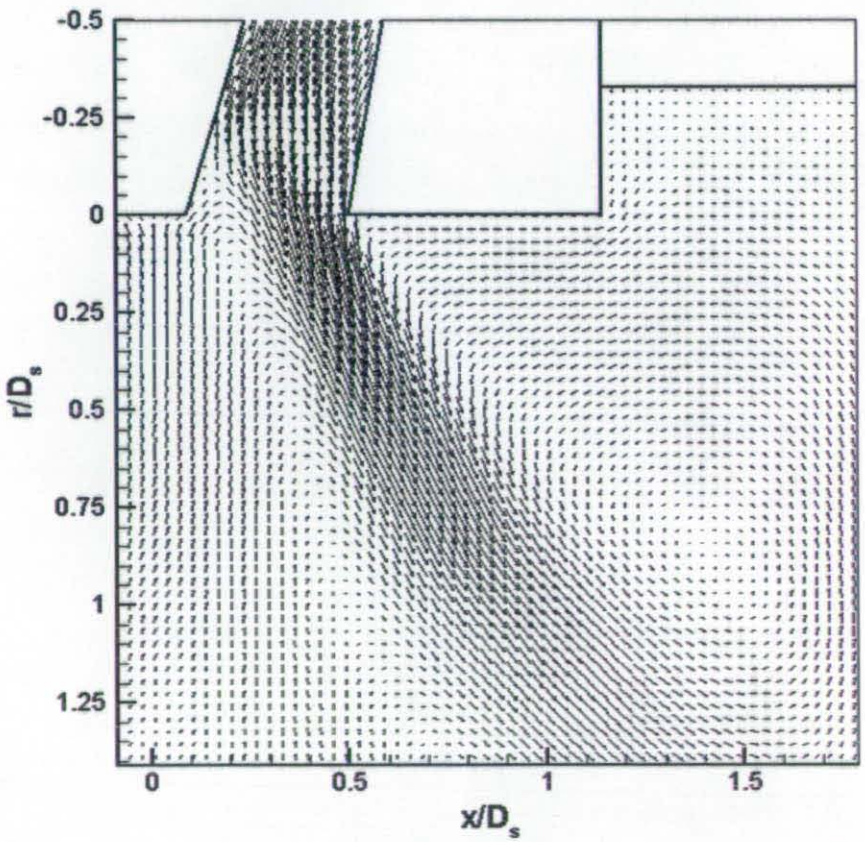

Figure 5.122. Mean Velocity Vectors for Modular Swirler with α_1=30° (Base Case Configuration)

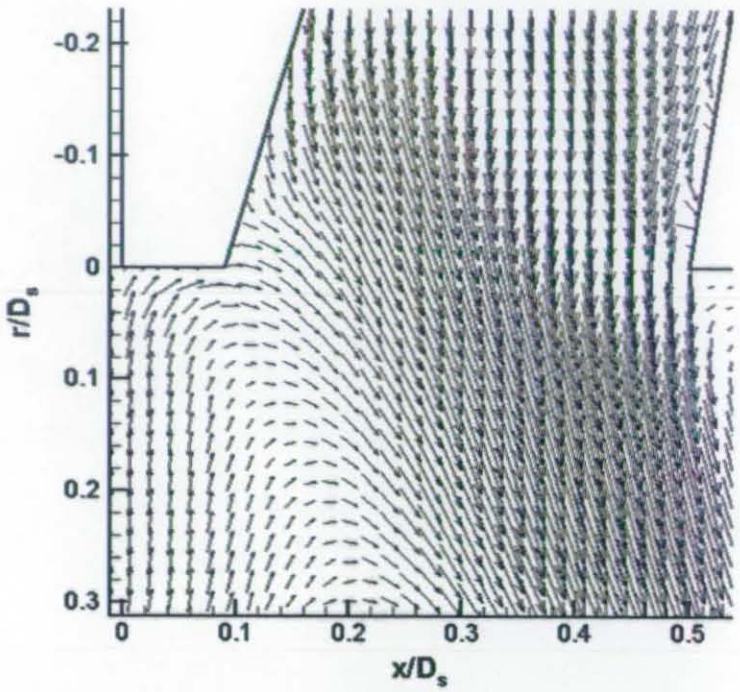

Figure 5.123. Mean Velocity Vectors for Modular Swirler with α_1=20° (Base Case Configuration)

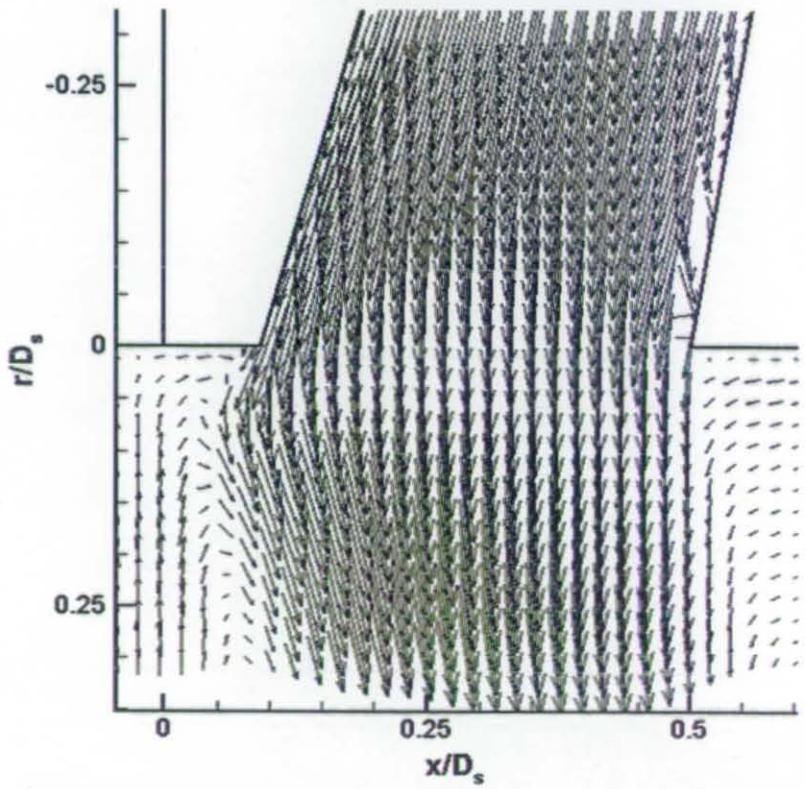

Figure 5.124. Mean Velocity Vectors for Modular Swirler with α_1=10° (Base Case Configuration)

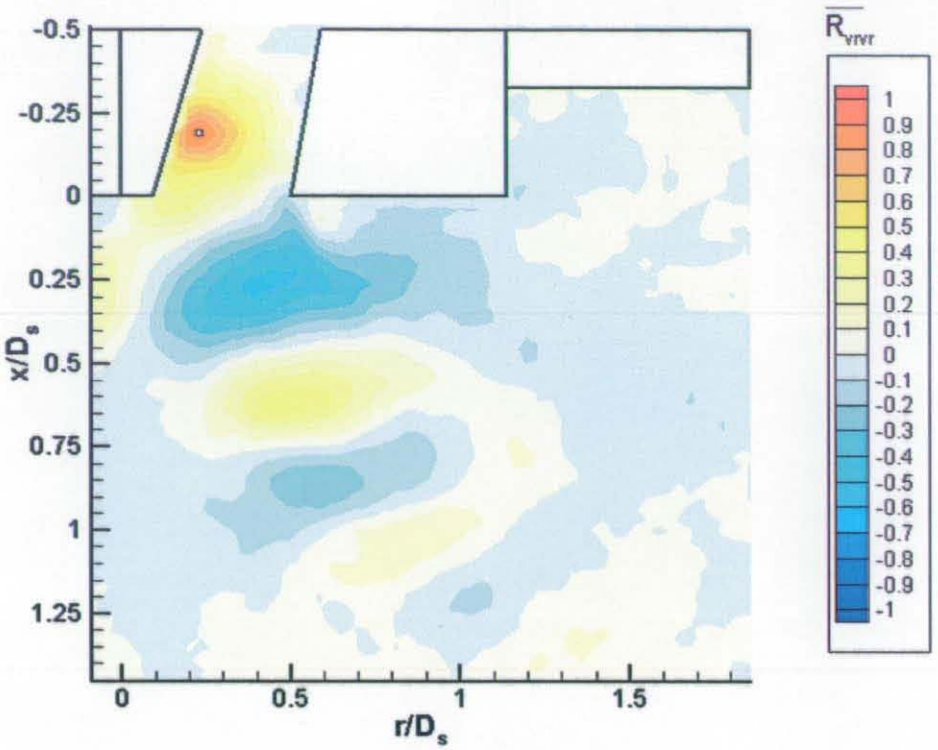

Figure 5.125. Radial Velocity Spatial Correlation Contours with α_1=30° (Base Case Configuration)

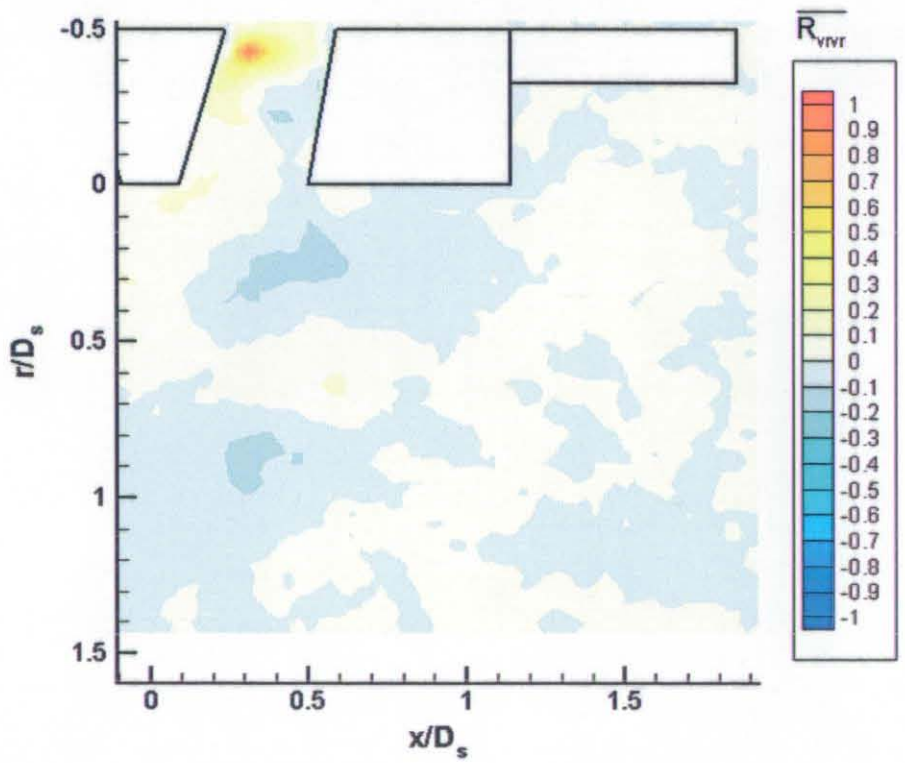

Figure 5.126. Radial Velocity Spatial Correlation Contours with α_1=30° (Base Case Configuration)

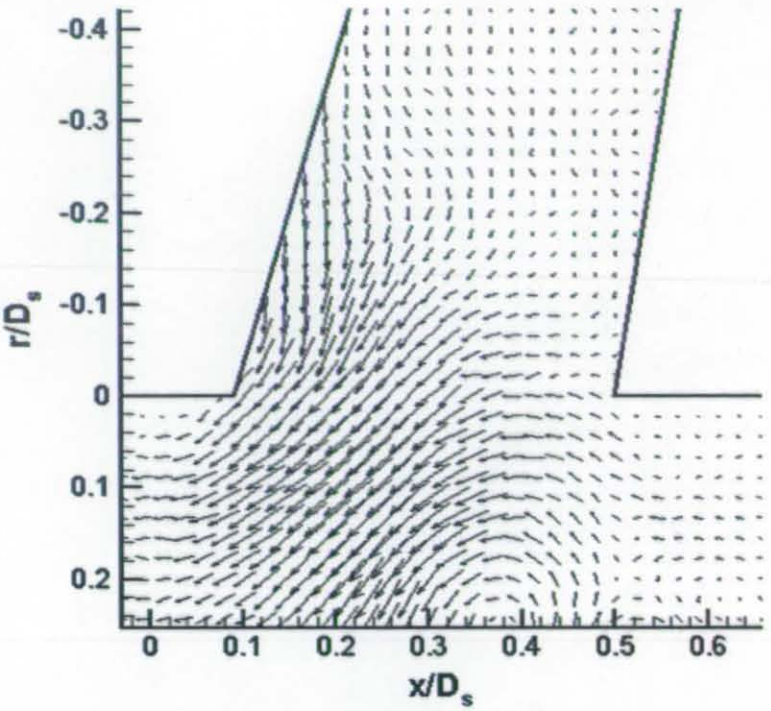

Figure 5.127. First POD Mode for Modular Swirler with α_1=30° (Base Case Configuration)

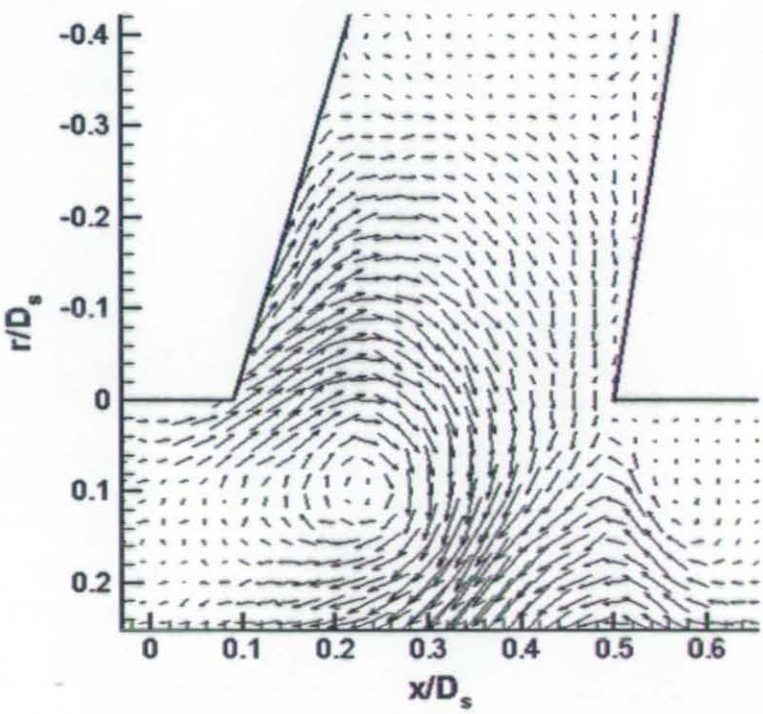

Figure 5.128. Second POD Mode for Modular Swirler with α_1=30° (Base Case Configuration)

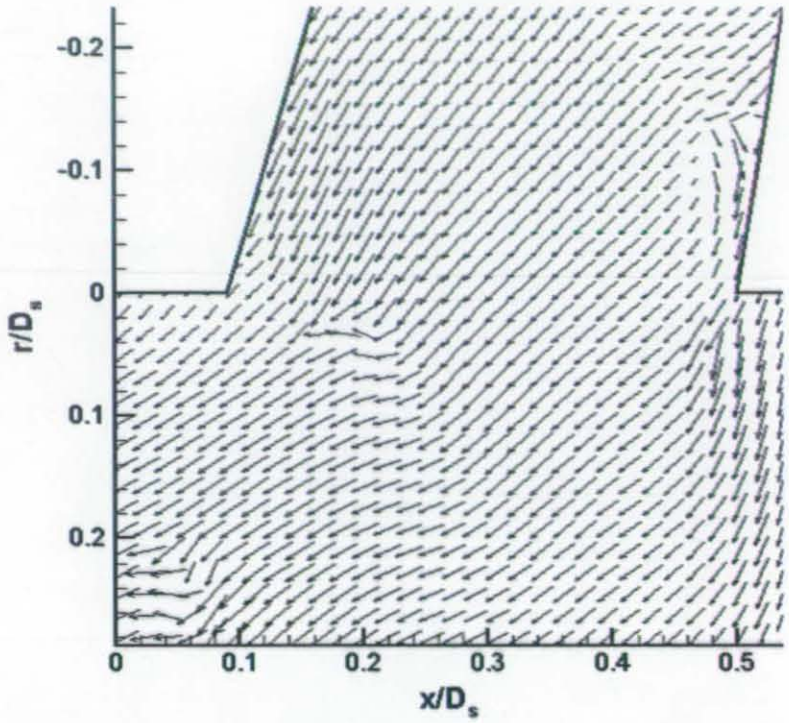

Figure 5.129. First POD Mode for Modular Swirler with α_1=20° (Base Case Configuration)

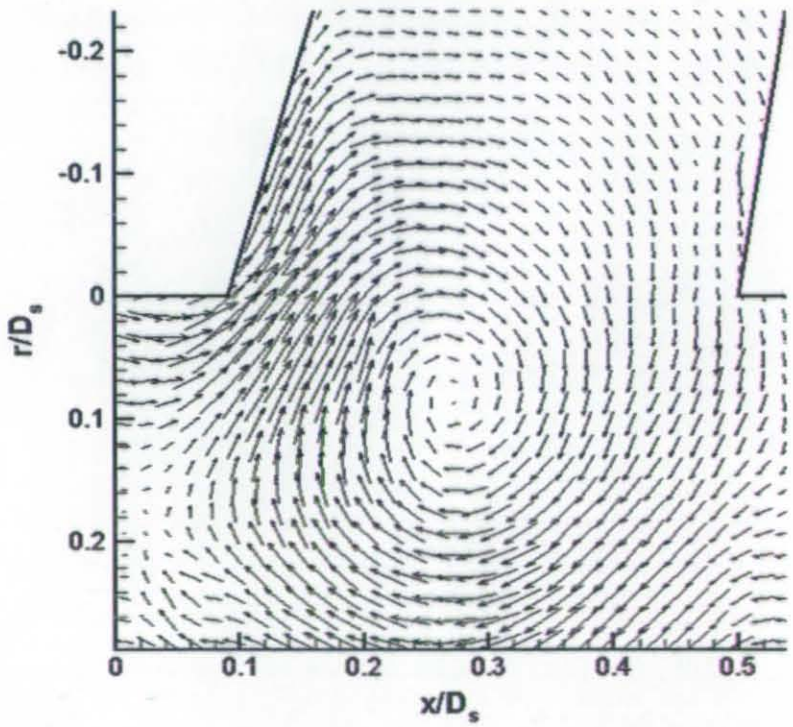

Figure 5.130. Second POD Mode for Modular Swirler with α_1=20° (Base Case Configuration)

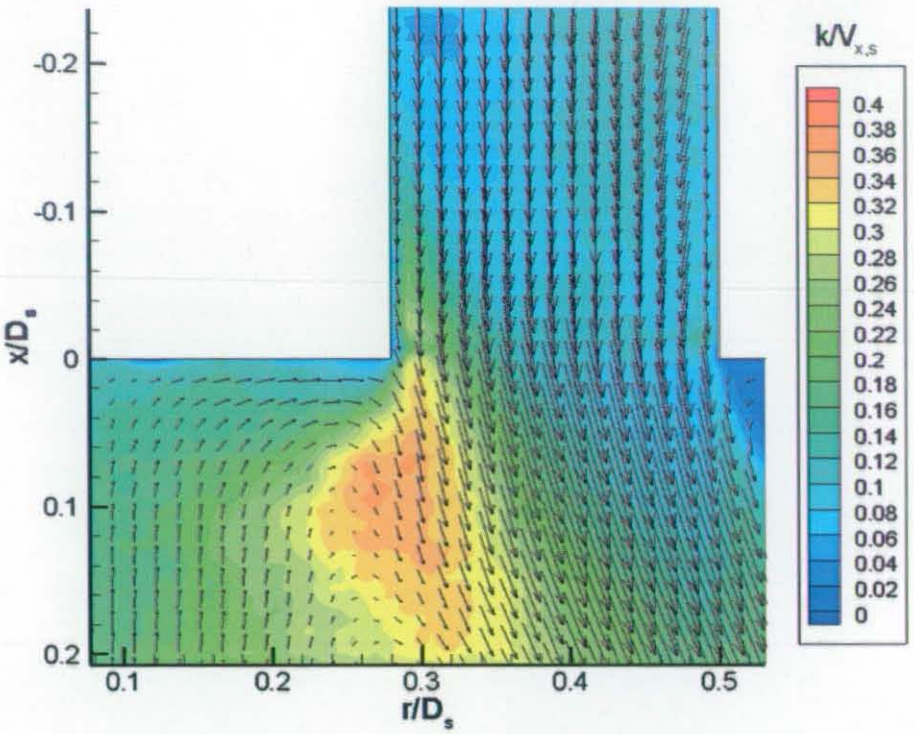

Figure 5.131. Mean Velocity Vectors Superimposed on Turbulent Kinetic Energy Contours for Modular Swirler with α_1=30° (Parallel Wall Configuration)

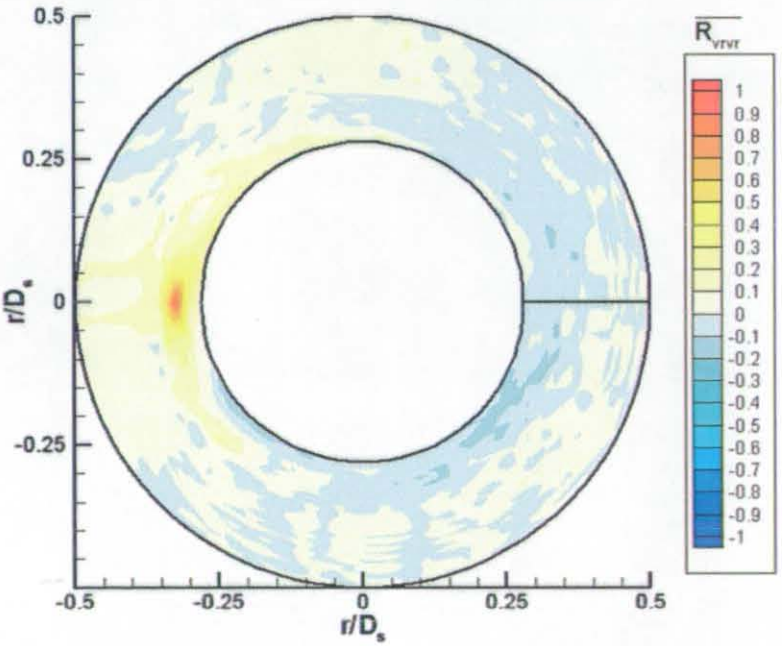

Figure 5.132. Radial Velocity Spatial Correlation Contours for Modular Swirler with α_1=30° (Parallel Wall Configuration)

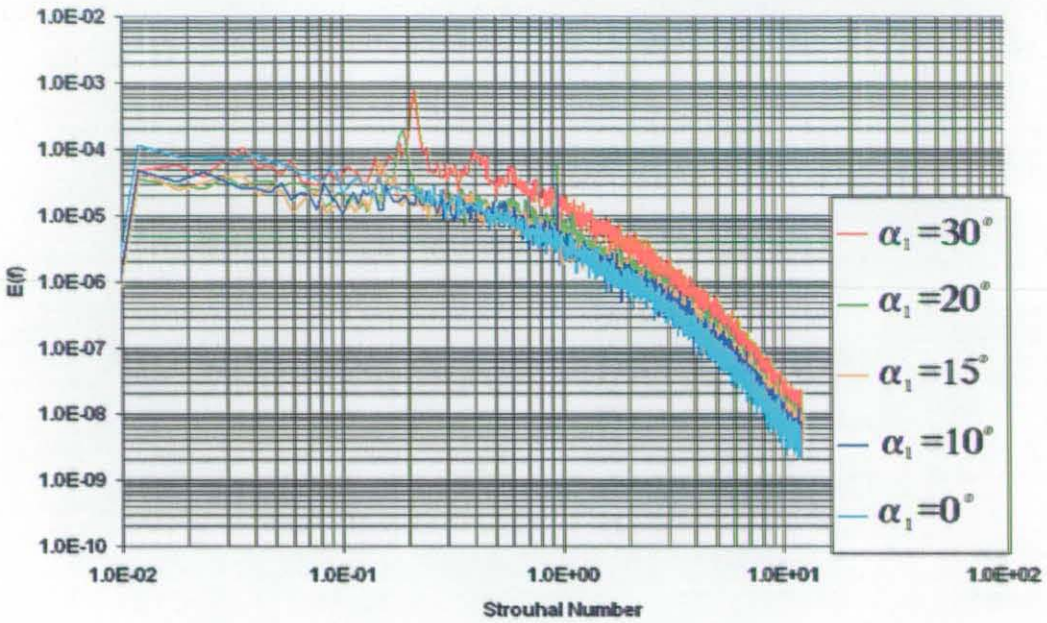

Figure 5.133. PSD Deduced from 10kHz HWA at x/D_s=0.27 for Modular Swirler (Parallel Wall Configuration)

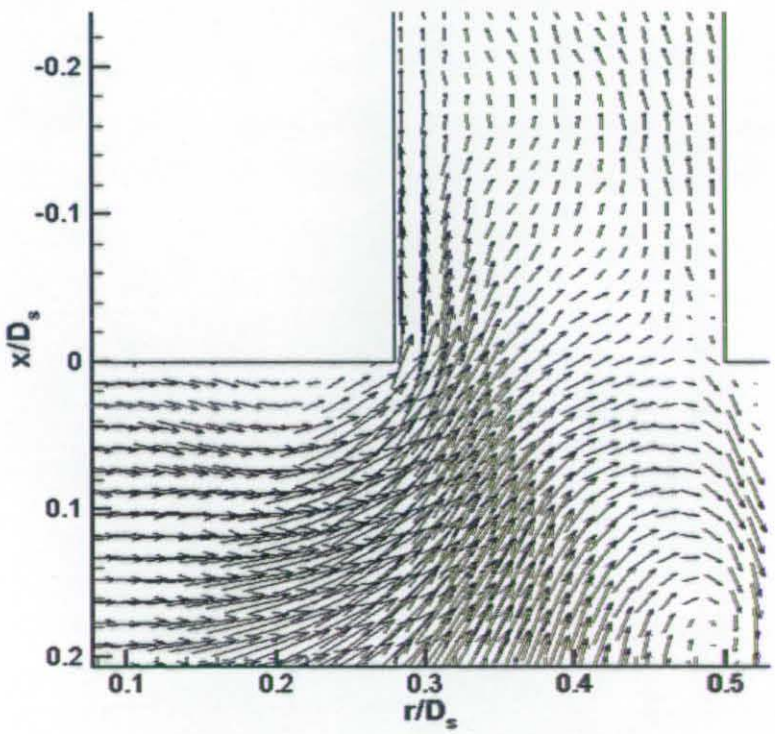

Figure 5.134. First POD Mode for Modular Swirler with α_1=30° (Parallel Wall Configuration)

6 SUMMARY REMARKS, CONCLUSIONS AND RECOMMENDATIONS

Summary Remarks and Conclusion

The primary objective of this thesis was to provide high quality benchmark data for the validation of LES codes, in a test case representative of the fuel injector component of a low emissions combustor. For this purpose a (datum) radial fed single swirling stream fuel injector was used, based on an industrial application Turbomeca geometry but modified to simplify CFD mesh generation. The Turbomeca geometry was particularly suitable for LES validation as in previous studies it was found to be *"susceptible to combustor oscillations"*, Lartigue *et al* (2004).

Single-phase isothermal measurements were made in order to focus on the aerodynamic characteristics. In order to maintain a representative flowfield the test conditions used were based on a combusting test case with the same fuel injector geometry. The most appropriate method for matching this test case was to maintain the correct axial momentum flux ratio between the swirl stream and the central jet at the fuel injector exit plane, denoted the main test condition. To assess the influence of the central jet on the flowfield a second test condition was then used without the presence of the central jet, denoted the no-jet test condition.

A pre-existing vertical flowing water rig was modified and a new airflow rig was designed to investigate the datum fuel injector. The design features common to both rigs included controlled and conditioned inlet and exit plane boundary conditions, excellent optical access to axial-radial and radial-circumferential planes and a downstream blockage to ensure a recovery of the radial pressure gradients before the exit manifold arrangement. Comparison of the axial momentum matched test condition in both air and water flow rigs showed non-dimensional profiles to be in excellent agreement, thus allowing for measurements to be compared from either rig with confidence. The rig chosen was based on the suitability to the measurement technique used.

The primary measurement techniques were based on LSI systems, to measure the velocity field using a Particle Image Velocimetry (PIV) methodology and the scalar field using a Planar Laser Induced Fluorescence (PLIF) methodology. LSI measurements were carried out in the water flow rig due to the improved quality of data collection relative to airflow measurements. PIV measurements are known to be susceptible to several error sources,

which in general are alleviated with increased image magnifications. Therefore, large measurement regions (essentially capturing the entire test section geometry) were used initially to assess the large-scale flow structure. This was followed by measurements with a succession of a smaller measurement regions (large image magnifications) optimised to match the local flow conditions in order to capture accurate statistics. This optimised data was then amalgamated onto one common grid and rotated to create a best representation 3D data set of the time-averaged statistics. LDA was used in water flow to validate the PIV measurements and HWA was used in airflow for high temporal resolution measurements at desired points of a radial traverse. For PLIF data the measurement region was chosen that was just large enough to assess the large-scale motions without being so big that optimisation became difficult or that a significant amount of image smearing occurred on the smallest scales of mixing.

The spatial and temporal resolution of the measurement techniques allowed for the use of several data reduction methods to extract information pertaining to the velocity and scalar fields. Classical single-point time-averaged statistics were calculated including mean velocity and Reynolds stress components as well as time and length scales via Auto-Correlation Functions (ACF). The calculation of Probability Density Functions (PDF) and Power Spectral Densities (PSD) allowed for alternative approaches to characterise the nature of single-point time-histories. The identification of large-scale turbulent structure embedded within the instantaneous velocity field was enhanced through the use of Singular Value Decomposition (SVD). Time-averaged representations of these structures were created through conditional averaging (analogous to phase locking) and rotational averaging. Finally, Proper Orthogonal Decomposition (POD) was used to identify the most energetic mode shapes corresponding to a set of instantaneous data and provide a method for partitioning the whole-field turbulent kinetic energy into a large-scale (coherent or periodic) contribution and a small-scale (turbulent) contribution.

The results showed that the swirl stream inner shear layer flow contained large-scale high-energy vortices. These vortices formed a two-strong two-weak rotating vortex pattern that was convected through the swirl stream along a helical flow path. Scalar measurements showed these vortices to entrain bursts of dyed fluid towards the vortex centres, therefore influencing the scalar mixing and transport processes. The internal fuel injector geometry or

the radial entry swirl slots were shown not to be the cause of the vortex formation. It was therefore postulated that the shear layer vortices formed due to an interaction of the forward flow of the swirl stream with the backflow (reverse flow) in the dump expansion chamber. It is believed that a "secondary" vortex breakdown of the helical mode instability type is superimposed on the "primary" vortex breakdown which causes the central recirculation in the main dump expansion chamber. As the Swirl number increases the central reverse flow strengthens and is able to penetrate further upstream, hence this interaction also moves upstream, possibly entering the fuel injector itself if the Swirl number is high enough. When the helical shear layer vortices were formed inside the fuel injector then they were much more coherent and energetic. Without the presence of a central jet a Precessing Vortex Core (PVC) was identified, this served to destabilise the swirl cone, which resulted in less coherent and energetic helical shear layer vortices.

By creating localised regions of high heat release due to the "bursts" of fuel (scalar) being entrained towards the vortex centres the inner shear layer vortices will be the cause of undesirable combustor oscillations. It is essential to create primary vortex breakdown in a combustor primary zone for flame stability reasons, so the formation of helical shear layer vortices is unavoidable (unless alternative methods of generating the central recirculation could be found). The problem is amplified in low-emissions fuel injectors as fairly long internal swirl stream passages are used to premix the fuel and air. If primary vortex breakdown penetrates into the fuel injector the shear layer vortices are formed inside the fuel injector. In this case the vortices appear much more energetic, thus creating much stronger combustor oscillations. Hence, careful design of the internal geometry is required such that the swirl number can remain high enough to ensure primary vortex breakdown but such that reverse flow does not enter the fuel injector body.

Recommendations for Further Work

Since the start of this project, LSI techniques have continued to develop. Newer systems utilise a dual camera configuration. This allows for "stereoscopic PIV" whereby all three velocity components can be instantaneously measured in a planar measurement region. Using stereoscopic PIV the highly three dimensional flowfield could be more fully investigated, in particular with regards to the formation mechanisms of the helical shear layer vortices. Duel camera configurations also allow for combined PIV and PLIF can be

achieved, therefore the scalar transport and mixing phenomena could be more fully investigated, in addition the ability to calculate the scalar fluxes would provide an even more comprehensive benchmark data set for LES validation.

Using duel camera LSI system configurations the modular swirler should be further investigated, especially the parallel wall test case, whereby increased swirl numbers should be used to create a flow separation off the inner wall. In this case much more coherent and energetic shear layer vortices should be observed. This would further validate the findings of this thesis. Measurements should then be taken using other generic low-emissions fuel injectors to observe if similar phenomena are observed. From the multiple configurations of the modular swirler and measurements using other fuel injector designs the overall recommendation for further work would be to develop effective design rules for low-emissions fuel injectors that allow the designer to design the fuel injector internal geometry such that a primary vortex breakdown in the combustor primary zone is ensured but the undesirable secondary (helical) vortex breakdown is suppressed.

REFERENCES

Adrian, R.J. (1991) – "Particle-Imaging Techniques for Experimental Fluid Mechanics", *Annual Reviews of Fluid Mechanics, Vol.23*

Adrian, R.J., Christensen, K.T. and Liu, Z.C. (2000) – "Analysis and Interpretation of Instantaneous Turbulent Velocity Fields", *Experiments in Fluids, Vol.29, pp.275-290*

Arcoumanis, C., McGuirk, J. J. and Palma, J.M.L.M. (1990) – "On the Use of Fluorescent Dyes for Concentration Measurements in Water Flows'' *Experiments in Fluids, Vol.10, pp.177–180*

Ahmed, S.A. (1997) – "Three Component Velocity Measurements of an Isothermal Confined Swirling Flow" *Proceedings of the Institution of Mechanical Engineers, Vol.211, Part G, pp.113-122*

Ahmed, S.A. (1998) - "Velocity Measurements and Turbulence Statistics of a Confined Isothermal Swirling Flow" *Experimental Thermal and Fluid Science, Vol.17, pp.256-264*

Anacleto, P.M., Fernandes, E.C., Heitor, M.V. and Shtork, S.I. (2001) – "Characteristics of Precessing Vortex Core in the LPP Combustor Model" *Proceedings of 2nd TSPF Symposium, Stockholm, Sweden*

Apte, S.V., Mahesh, K., Moin, P. and Oefelein, J.C. (2003) – "Large Eddy Simulation of Particle-Laden Flows in a Coaxial Combustor" *International Journal of Multiphase Flow, Vol.29, pp.1311-1331*

Behrouzi, P. and McGuirk, J.J. (1996) – "Capture of Unsteady Flow Features in Re-Ingestion Flows using a Laser-Induced Fluorescence Technique" *Proceedings of Optical Methods and Data Processing in Heat and Fluid Flow, City University, London, pp.429-438*

Benjamin, T.B. (1962) – "Theory of Vortex Breakdown Phenomenon" *Journal of Fluid Mechanics, Vol.14, pp.593-629*

Benjamin, T.B. (1967) – "Some Developments in the Theory of Vortex Breakdown" *Journal of Fluid Mechanics, Vol.28, pp.65-84*

Berkooz, G. Holmes, P. and Lumley, J.L. (1993) – ."The Proper Orthogonal Decomposition in the Analysis of Turbulent Flows". *Annual Reviews Of Fluid Mechanics, Vol.25 pp.539-575*

Beynon, J.D.E. (1976) – "Introduction to Charge-Coupled Devices", *Microelectronics and Reliability, Vol.15, No.4, pp.273-283*

Birch, N.T. (2000) – "2020 Vision: The Prospects for Large Civil Aircraft Propulsion" *The Aeronautical Journal, Vol.104, No.1038, pp.347-352*

Bolinder, J. (1999) –"Optimisation of PIV with Strong Velocity Gradients", *La Vision Gmbh, www.PIV.de*

Chanaud, R.C. (1965) – "Observations of Oscillatory Motion in Certain Swirling Flows", *Journal of Fluid Mechanics, Vol.21, pp.111-127*

Chigier, N.A. and Beer, J.M. (1972) – "Combustion Aerodynamics", *Applied Science Publishers, England*

Cizmas, P.G., Palacios, A., O'Brien, T. and Syamlal, M. (2003) – "Proper Orthogonal Decomposition of Spatio-Temporal Patterns in Fluidized Beds", *Chemical Engineering Science, Vol.58, pp.4417-4427*

Claypole, T.C. and Syred, N. (1980) – "Coherent Structures in Swirl Generators and Combustors" *Proceedings of the Symposium of Vortex Flows, Winter Meeting of ASME, Chicago, pp.47-56*

Colebrook, C.F. (1938) – "Turbulent Flow in Pipes", *Journal of the Inst. Civil Eng, Vol.11, pp.133.*

Coolen, M.C.J., Kieft, R.N., Rindt, C.C.M. and Van Steenhoven, A.A. (1999) – "Application of 2D LIF Temperature Measurements in Water using a Nd:YAG Laser" *Experiments in Fluids, Vol.27, pp.420-426*

Criminaldi, J.P. and Koseff, J. (2001) – "High Resolution Measurements of the Spatial and Temporal Scalar Structure of a Turbulent Plume", *Experiments in Fluids Vol.31, pp.90-102*

Dantec (1996) – "Streamline Users Guide", *Dantec Electronik, Denmark*

Dellenbeck, P.A., Metzger, D.E. and Neitzel, G.P. (1988) – "Measurements in Turbulent Swirling Flow through an Abrupt Axi-Symmetric Expansion" *AIAA, Vol.26, No.6, pp.669-681*

Di Mare, F., Jones, W.P. and Menzies, K.R. (2004) – "Large Eddy Simulation of a Model Gas Turbine Combustor" *Combustion and Flame, Vol.137, pp.278-294*

Dowling, A.P. and Hubbard, S. (2000) – "Instability in Lean Premixed Combustors" *Proceedings of the Institute of Mechanical Engineers, Vol.214, Part A, pp.317-332*

Durst, F., Melling, A. and Whitelaw, J.H. (1981) – "Principles and Practice of Laser Doppler Anemometry", *Second Edition, London; New York: Academic Press*

Elghobashi, S. (1994) – "On Predicting Particle-Laden Turbulent Flows", *Applied Scientific Research, Vol.52, pp.309-329*

Escudier, M.P. (1988) – "Vortex Breakdown: Observations and Explanations", *Prog. Aerospace Science, Vol.25, pp.189-229*

Escudier, M.P and Zehnder, N. (1982) – "Vortex-Flow Regimes" *Journal of Fluid Mechanics, Vol.115, pp.105-121*

Fincham A. and Delerce G. (2000) – "Advanced Optimisations of Correlation Imaging Velocimetry Algorithms" *Experiments in Fluids, Vol.29, pp.51-60*

Fingerson, L.M. and Menon, R.K. (1998) – "Basic Instruments: Laser Doppler Velocimetry" *Handbook of Fluid Dynamics, Springer-Verlag*

Froud, D., O'Doherty, T. and Syred, N. (1995) – "Phase Averaging of the Precessing Vortex Core in a Swirl Burner Under Piloted and Premixed Combustion Conditions" *Combustion and Flame, Vol.100, No.3 , pp.407-410*

Gad-el-Hak, M. (1998) – "Basic Instruments: Hotwire Anemometry" *Handbook of Fluid Dynamics, Springer-Verlag*

Golub, G.H. and van Loan, C.F. (1989) – "Matrix Computations" *The Johns Hopkins University Press. Second Edition*

Gouldin, F.C., Depsky, J.S. and Lee, S-L. (1985) – "Velocity Field Characteristics of a Swirling Flow Combustor", *AAIA Journal, Vol.23, No.1, pp.95-102*

Graftieaux, L., Michard, M. and Grosjean, N. (2001) – "Combining PIV, POD and Vortex Identification Algorithms for the Study of Unsteady Turbulent Swirling Flows" *Measurement Science and Technology, Vol.12, pp.1422-1429*

Grosjean, N., Grafieaux, L., Michard, M., Hubner, W., Tropea, C. and Volkert, J. (1997) – "Combining LDA and PIV for Turbulence Measurements in Un-Steady Swirling Flows", *Measurement Science and Technology, Vol.8, pp.1523-1532*

Guillard, F., Fritzon, R., Revstedt, C., Trägårgh, C., Aldén, M. and Fuchs, L. (1998) – "Mixing in a Confined Turbulent Impinging Jet Using Planar Laser-Induced Fluorescence", *Experiments in Fluids, Vol.25, pp.143-150*

Gupta, A.K. (1984) – "Swirl flows" *Abacus press, Kent, England*

Hall, M.G. (1967) - "A New Approach to Vortex Breakdown" *Proceedings of the Heat Transactions and Fluid Mechanics Institute, Univ. California, San Diego, pp.319-340*

Hall, M.G. (1972) - "Vortex Breakdown" *Annual Reviews of Fluid Mechanics', Vol.86, pp.313*

Hart, D.P. (2000) – "PIV Error Correction", *Experiments in Fluids, Vol.29, pp.13-22*

Harvey, J.K. (1962) – "Some Observations of the Vortex Breakdown Phenomenon" *Journal of Fluid Mechanics, Vol.14, pp.585-592*

Hinze, J.O. (1959) – "Turbulence: An Introduction to its Mechanism and Theory", *McGraw-Hill Book Company, Inc.*

Hollis, D., Spencer, A. and Carrotte, J.F. (2001) – "Statistical Analysis and Comparison of LDA and PIV Measurements for the Flow Over a Wall Mounted Obstacle", *9th Int. Conf of Laser Anemometry Advances and Applications, Limerick*

Hollis, D. (2004) – "Particle Image Velocimetry in Gas Turbine Combustor Flow Fields" *PhD Thesis, Loughborough University*

Holmes, P., Lumley, J.L. and Berkooz, G. (1996) – "Turbulence, Coherent Structures, Dynamical Systems and Symmetry", *Cambridge University Press*

Höest-Madsen, A. and Nielsen, A.H. (1995) – "Accuracy of PIV Measurements in Turbulent Flows", *ASME Laser Anemometry, FED, Vol.229*

Howard, L.N. and Gupta, A.S. (1962) – "On Hydrodynamic and Hydromagnetic Stability of Swirling Flows" *Journal of Fluid Mechanics, Vol.14, pp.463-476*

Hughes, N.J. (2003) – "Computational and Numerical Study of Multi-Stream Swirler", *PhD Thesis, Loughborough University*

ICAO (1981) – "International Standards and Recommended Practices" *Environmental Protection Annex 16 to the Convention on International Civil Aviation, Vol.2 (Aircraft Engine Emissions)*

IPCC (1999) – "Aviation and the Global Atmosphere" *IPCC Special Reports on Climate Change, Cambridge University Press*

Jamin, S. Schäfer, A., Moshe, B. and Waitz, I.A. (2004) – "Aviation Emissions and Abatement Policies in the United States: A City-Pair Analysis", *Transportation Research Part D: Transport and Environment, Vol.9, Issue 4, pp.295-317*

Janus, B., Dreizler, A. and Janicka, J. (2004) – "Flow Field and Structure of Swirl Stabilised Non-Premixed Natural Gas Flames at Elevated Pressure", *Proceedings of the ASME Turbo Expo, Power for Land and Sea, June 14-17, Vienna, GT-2004-53340*

Karrasso, P.S. and Mungal, M.G. (1997) – "PLIF Measurements in Aqueous Flows Using the Nd:YAG Laser" *Experiments in Fluids, Vol.23, pp.382-387*

Keane, R.D. and Adrian, R.J. (1990) – "Optimisation of Particle Image Velocimeters Part I: Double Pulsed Systems", *Measurement Science and Technology, Vol.1, pp.1202-1215*

Keane, R.D. and Adrian, R.J. (1991) – "Optimization of Particle Image Velocimeters Part II: Multiple Pulsed Systems", *Measurement Science and Technology, Vol.2, pp.963-974*

Keane, R.D. and Adrian, R.J. (1992) – "Theory of Cross Correlation Analysis of PIV Images" *Applied Science Res, Vol.49, pp.223-241*

Kerr, N.M. and Frasier, D. (1965) – "Swirl Effects of Axi-Symmetrical Turbulent Jets" *J. Inst. Fuel, Vol.38, pp.519-526*

Khezzar, L. (1998) – "Velocity Measurements in Near Field of a Radial Flow Swirler" *Experiments in Thermal and Fluid Science, Vol.16, pp.230-236*

Kihm, K.D., Chigier, N. and Sun, F. (1988) – "Laser Doppler Velocimetry Investigation of Swirler Flow Fields" *AIAA Journal of Propulsion, Vol.6, No.4, pp.364-374*

Kline, S.J. and Robertson, S.K. (1989) – "Quasi-Coherent Structures in the Turbulent Boundary Layer Part I: Status Report on a Community Wide Summary of the Data" *Proceedings of Zaric Memorial Conference, New York, pp.200-217,*

Koff, B.L. (1994) – "Aircraft Gas Turbine Emissions Challenge" *Transactions of the ASME, Journal of Engineering for Gas Turbines and Power, Vol.116, pp.474-477*

Kolmogorov, A.N. (1941) – "The Local Structure of Turbulence in Incompressible Viscous Fluid for Very Large Reynolds Numbers", *Dokl. Akad. Nauk. SSSR.30, pp.299-303*

Lartigue, G., Meier, U. and Bérat, C. (2004) – "Experimental and Numerical Investigation of Self-Excited Combustion Oscillations in a Scaled Gas Turbine Combustor", *Applied Thermal Engineering, Vol.24, No.11, pp.1583-1592*

LaVision GmbH (2001) – "PIV Flowmaster Manual"

Lefebvre, A.H. (1995) – "The Role of Fuel Preparation in Low-Emission Combustion" *ASME Journal of Engineering for Gas Turbines and Power, Vol.117, pp.617-653*

Leibovich, S. (1978) - "The Structure of Vortex Breakdown" *Annual Reviews Of Fluid Mechanics, Vol.10, pp.221-246*

Leibovich, S. and Stewartson, K. (1983) – "A Sufficient Condition for the Instability of Columnar Vortices" *Journal of Fluid Mechanics, Vol.126, pp.335-356*

Lemonine, F., Antoine, Y., Wolff, M. and Lebouche, M. (1999) – "Simultaneous Temperature and 2D Velocity Measurements in a Turbulent Heated Jet Using Combined Laser-Induced Fluorescent and LDA" *Experiments in Fluids, Vol.26, pp.315-323*

Li, H. and Tomita, Y. (1994) – "Characteristics of Swirling Flow in a Circular Pipe" *Transactions of the ASME, Vol.116, pp.370-373*

Lucca-Negro, O. and O'Doherty, T. (2001) – "Vortex Breakdown: A Review" *Prog. in Energy and Combustion Science, Vol.27, pp.431-481*

Lumley, J.L. (1967) – "The Structure of Inhomogeneous Turbulent Flows" *Atmospheric Turbulence and Radio Wave Propagation, Nauka, Moscow, pp.166-178,*

Lynn, P.A. (1973) – "An Introduction to the Analysis and Processing of Signals" *Macmillan Press, London*

M^{c}Greeham, W.F. and Schotsch, M.J. (1987) – "Flow Characteristics of Long Orifices with Rotation and Corner Radiusing" *ASME 87-GT-162*

Melton, L.A. and Lipp, C.W. (2003) – "Criteria for Quantitative PLIF Experiments Using High Powered Lasers", *Experiments in Fluids, Vol.35, pp.310-316*

Midgley, K.K., Spencer, A. and McGuirk, J.J. (2004) – "Unsteady Flow Structures in Radial Swirler Fed Fuel Injectors" *Proceedings of the ASME Turbo Expo, Power for Land and Sea, June 14-17, Vienna, GT-2004-53608*

Paul, P.H., van Cruyningen, I., Hanson, R.K. and Kychakoff, G. (1990) – "High Resolution Digital Flow Field Imaging of Jets" *Experiments in Fluids, Vol.9, pp.241-257*

Peckham, D.H. and Atkinson, S.A. (1957) – "Preliminary Results of Low Speed Wind Tunnel Tests on a Gothic Wing of Aspect Ratio 1.0", *Aeronautical Research Council, pp.508-526*

Pickering, C.J.D. and Halliwell, N.A. (1984) – "Speckle Photography in Fluid Flows, Signal Recovery in Two Step Processing", *Applied Optics, Vol.23, pp.1128-29*

Pope, S.B. (2000) – "Turbulent Flows", *Cambridge University Press*

Prandtl, L. (1921) – "Bermerkungen über die Enstehung der Turbulenz", *Z. Angew, Math. Mech. Vol.1, pp.431-436*

Prasad, A.K. (2000) – "Particle Image Velocimetry", *Current Science, Vol.79, pp.51-60*

Press, W.H., Flannery, B.P., Teukolsky, S.A. and Vetterling, W.T. (1992) – "Numerical Recipes in FORTRAN 77: The Art of Scientific Computing: Vol.1" *Cambridge University Press*

Pringsheim, P. (1949) – "Fluorescence and Phosphorescence" *Interscience Publishers, New York*

Raffel, M., Willert, C. and Kompenhaus, J. (1998) – "Particle Image Velocimetry", *Springer-Verlag*

Rayleigh, L. (1916) – "On the Dynamics of Revolving Fluids" *Proceeding of the Royal Society, London, No.93, pp.148-154*

Reid, C.R., Prausnitz, J.M. and Poling, E. (1986) – "The Properties of Gases and Liquids" *McGraw-Hill*

Reader-Harris, M.J. (1994) – "The Decay of Swirl in a Pipe" *International Journal of Heat and Fluid Flow, Vol.15, No.3, pp.212-217*

Richardson, L.F. (1922) – "Weather Prediction by Numerical Process", *Cambridge University Press*

Rink, K.K. and Lefebvre, A.H. (1989) – "Influence of Fuel Drop Size and Combustor Operating Conditions on Pollutant Emissions" *International Journal Of Turbo And Jet Engines, Vol.6, No.2, pp.113-122*

Rolls Royce (1995) – "The Jet Engine" *4th Edition, Rolls Royce Plc*

Sakakibara, J. and Adrian, R.J. (1997) – "Whole Field Temperature Measurements in Water Using Two-Color Laser-Induced Fluorescence", *TAM Report No.864 University of. Illinois*

Sarpkaya, T. (1971) – "Stationary and Travelling Vortex Breakdowns" *Journal of Fluid Mechanics, Vol.45, pp.545-569*

Sarpkaya, T. (1972) – "Vortex Breakdown in Swirling Conical Flows" *AIAA, Vol.9 pp.1792-1799*

Scott, C.J. and Bartlet, K.W. (1976) – "Decaying Annular Swirl Flow with Solid Body Rotation", *Transations of the ASME, Journal of Fluids Engineering, pp.33-39*

Schumann U. (2000) – "Aircraft Emissions", *Causes and Consequences of Global Environmental Change, Vol.3, pp.178-186*

Seaton, A., MacNee, W., Donaldson, K. and Godden, E. (1995) - "Particulate Air Pollution and Acute Health Effects", *Lancet, Vol.345, pp.176-178*

Selle, L., Lartigue, G., Poinsot, T., Koch, R., Schildmacher, K., Krebs, W., Prade, B., Kaufmann, P. and Veynante, D. (2004) – "Compressible Large Eddy Simulation of Turbulent Combustion in Complex Geometry on Unstructured Meshes" *Combustion and Flame, Vol.137, pp.489-505*

Shan, J.W., Lang, D.B. and Dimotakis, P.E. (2004) – "Scalar Concentration Measurements in Liquid-Phase Flows with Pulsed Lasers" *Experiments in Fluids, Vol.36, pp.268-273*

Solero, G. and Coghe, A. (2002) – "Experimental Fluid Dynamic Characterisation of a Cyclone Chamber" *Experiments in Thermal and Fluid Science, Vol.27, pp.87-96*

Spencer, A. (1998) – "Gas Turbine Combustor Port Flows", *Ph.D. Thesis, Loughborough University*

Spencer, A. and McGuirk, J.J. (2001) – "LDA Measurements of Feed Annulus Effects on Combustor Liner Port Flow" *ASME Journal of Fluids Engineering, Vol.123*

Stroud, K.A. (1995) – "Engineering Mathematics, Programmes and Problems: Fourth Edition" *Macmillan Press, London*

Syred, N., O'Doherty, T. and Froud, D. (1994) – "The Interaction of the Precessing Vortex Core and Reverse Flow Zone in the Exhaust of a Swirl Burner", *Proceedings of the Institution of Mechanical Engineers, Part A, Vol.208, pp.27-35*

Sirovich, L. (1987) – "Turbulence and Dynamics of Coherent Structures. Part I: Coherent Structures", *Quarterly of Applied Mathematics, Vol.45, No.3, pp.561-571*

Tecplot (1998) – "User Guide" *Amtec Engineering, Inc. Bellevue, Washington*

Walker, D.A. (1987) – "A Fluorescent Technique for Measurement of Concentration in Mixing Liquids" *Journal of Physics, Vol.20, pp.217-224*

Watson, J.D. and Crick, F.H.C. (1953) – "A Structure for Deoxyribose Nucleic Acid" *Nature, Vol.171, pp.737 1953*

Wang, S. and Rusak, Z. (1997) – "The Dynamics of a Swirling Flow in a Pipe and Transition to Axi-symmetric Vortex Breakdown" *Journal of Fluid Mechanics., Vol.350, pp.177-223*

Webster, D.R., Rahman, S. and Dasi, L.P. (2003) – "Laser Induced Fluorescence Measurements of a Turbulent Plume", *Journal of Engineering Mechanics, Vol.129, No.10, pp.1130-1137*

Westerweel, J. (1994) – "Efficient Detection of Spurious Vectors in Particle Image Velocimetry" *Experiments in Fluids, Vol.16, pp.236-247*

Westerweel, J (1997) – "Fundamentals of Digital Particle Image Velocimetry", *Measurement Science and,Technology, Vol.8, pp.1379-1392*

Westerweel, J., Hofmann, T., Fukushima, C. and Hunt, J.C.R. (2002) – "The Turbulent / Non-Turbulent Interface at the Outer Boundary of a Self Similar Turbulent Jet", *Experiments in Fluids, Vol.33, pp.873-878*

Wulff, A. and Hourmouziadis, J. (1997) – "Technology Review of Aero-Engine Pollutant Emissions" *Aerospace Science and Technology, Vol.8, pp.557-572*

Xia, J.L., Yadigaroglu, G., Lui, Y.S., Schmidli, J. and Smith, B.L. (1998) – "Numerical and Experimental Study of Swirling Flow in a Model Combustor", *Inst. J. Heat Mass Transfer, Vol.41, No.11, pp.1485-1497*

Yazdabadi, P., Griffiths, A.J. and Syred, N. (1994) – "Investigation into the Precessing Vortex Core Phenomenon in Cyclone Dust Separators" *Proceedings of the Institution of Mechanical Engineers, Part E, Vol.208*

Zhou, J., Adrian, R.J., Balachandar, S. and Kendall, T.M. (1999) – "Mechanisms for Generating Coherent Packets of Hairpin Vortices in Channel Flow", *Journal of Fluid Mechanics, Vol.387, pp.353-396*

Zhou, L.X., Li, T., Chen, T. and Xu, Y. (2000) – "Studies on the Effect of Swirl Numbers on Strongly Swirling Turbulent Gas Particle Flows using Phase Doppler Particle Anemometer" *Powder Technology, Vol.112, pp.79-86*

8 Appendix 1

The MOLECULES project (Modelling of Low Emissions Combustors using Large Eddy Simulation) was a collaborative research project including several European universities, research establishments and gas-turbine manufacturers. The overall project was divided up into several work-packages including LES methods and combustion model development. One work-package required the production of generic validation data for the LES calculations. The research work reported in this thesis is part of the generic validation tests component, tasked with producing validation data in strongly swirling flow representative of near-field fuel injector aerodynamics.

9 APPENDIX 2

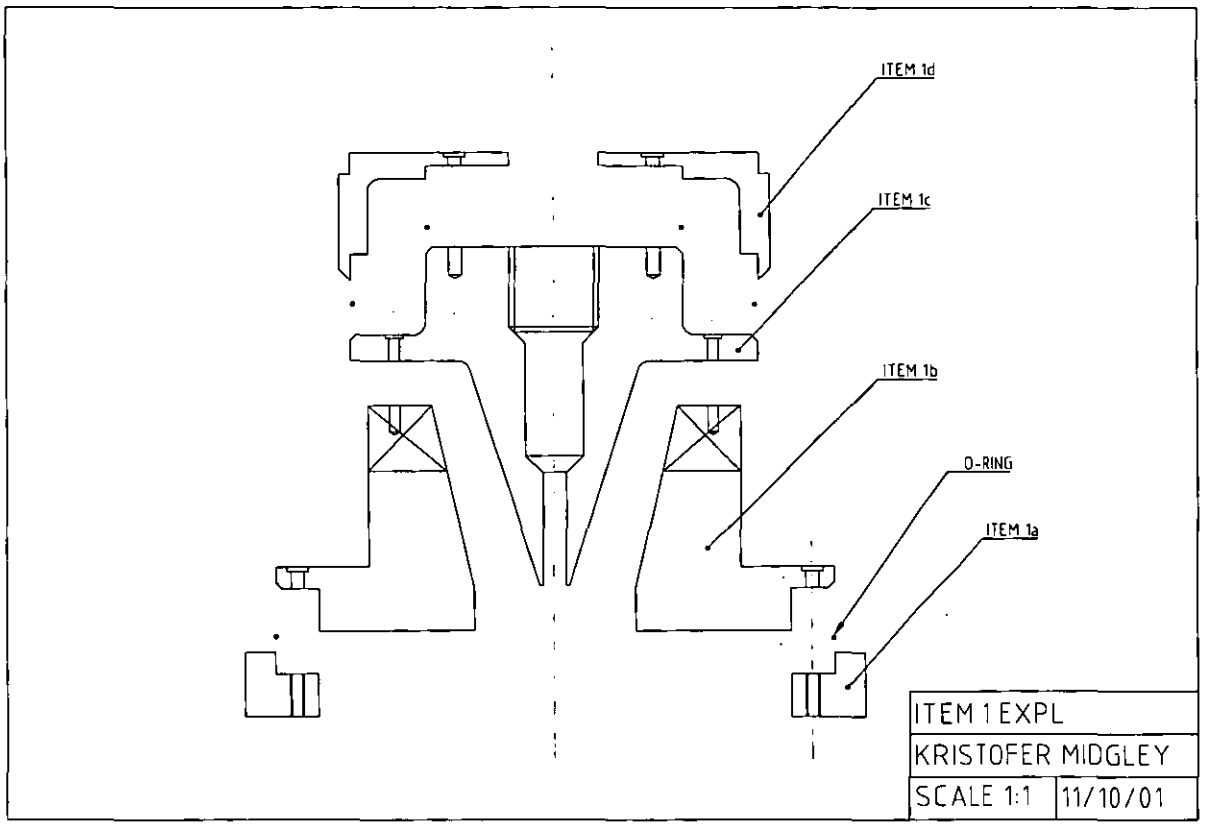
ITEM 1d
ITEM 1c
ITEM 1b
O-RING
ITEM 1a
ITEM 1 EXPL
KRISTOFER MIDGLEY
SCALE 1:1
11/10/01

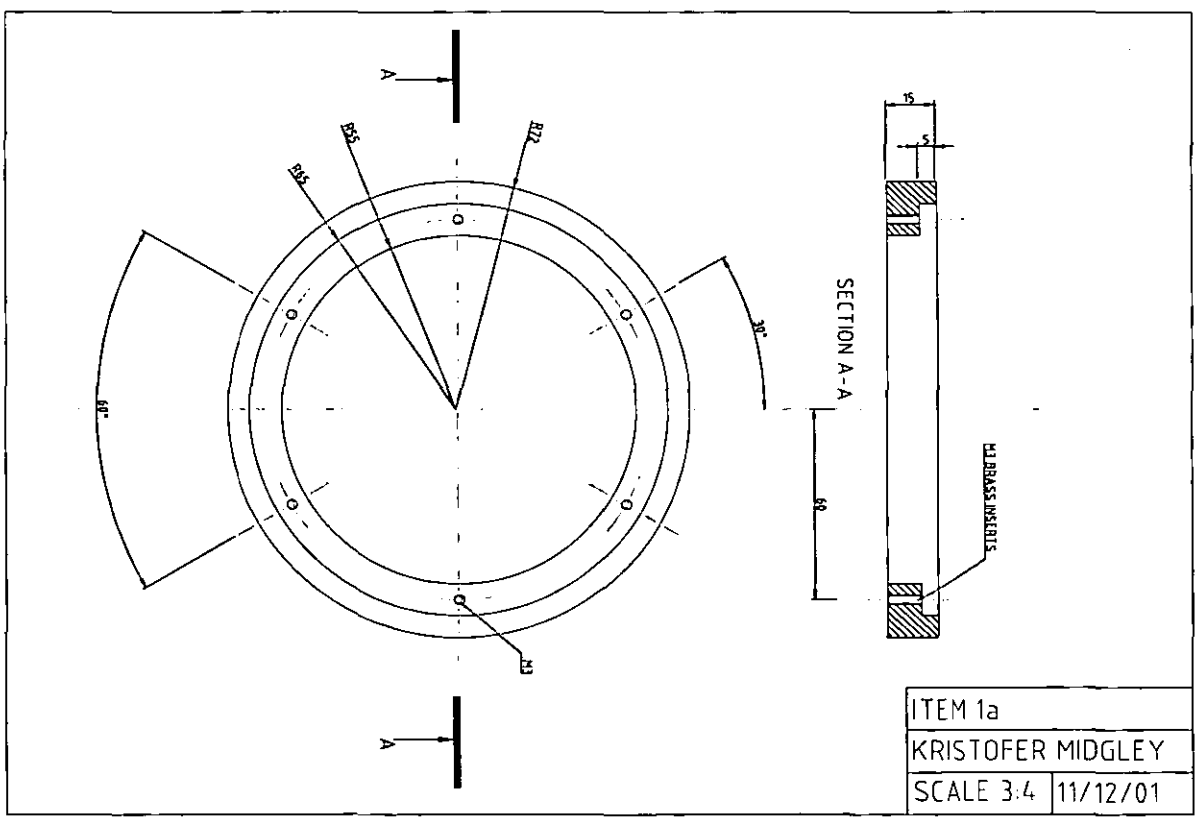
A
A
R22
R55
R65
30°
60°
R3
15
5
SECTION A-A
60
M3 BRASS INSERTS
ITEM 1a
KRISTOFER MIDGLEY
SCALE 3:4
11/12/01

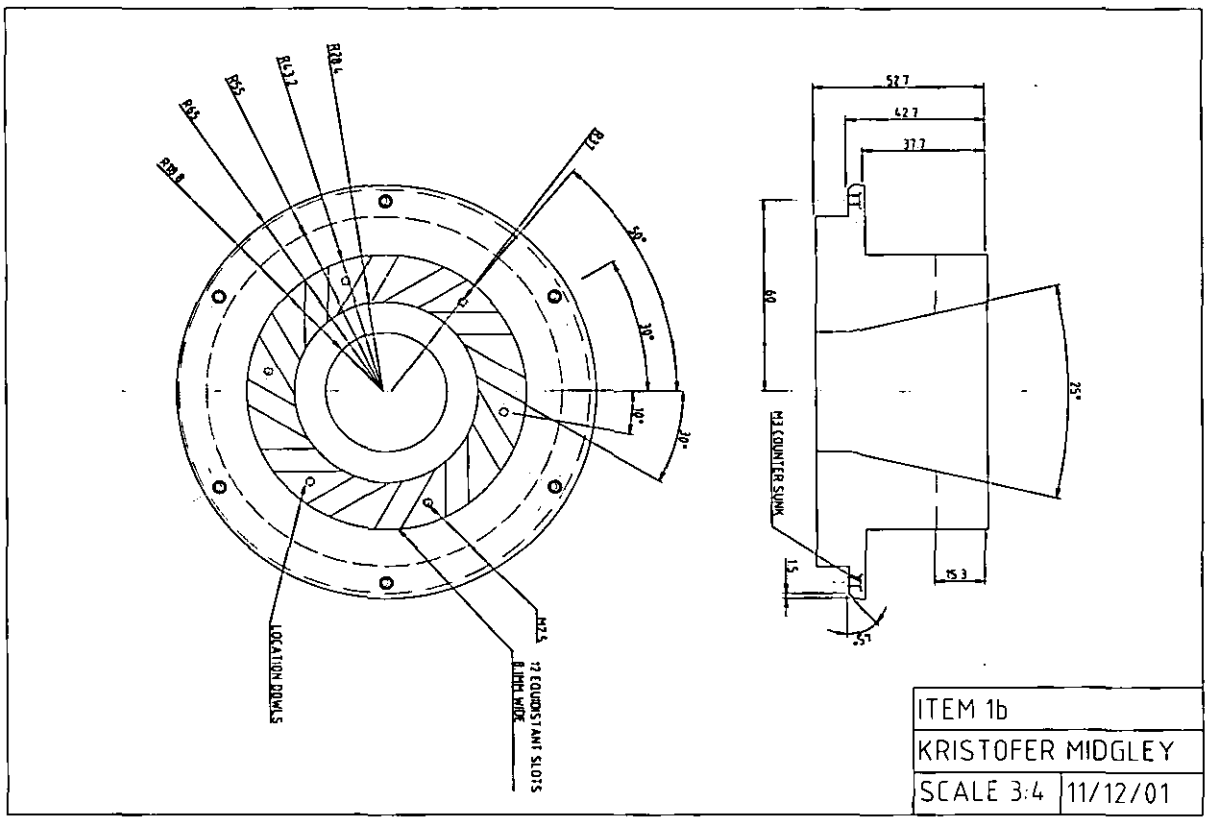

ITEM 1b	
KRISTOFER MIDGLEY	
SCALE 3:4	11/12/01

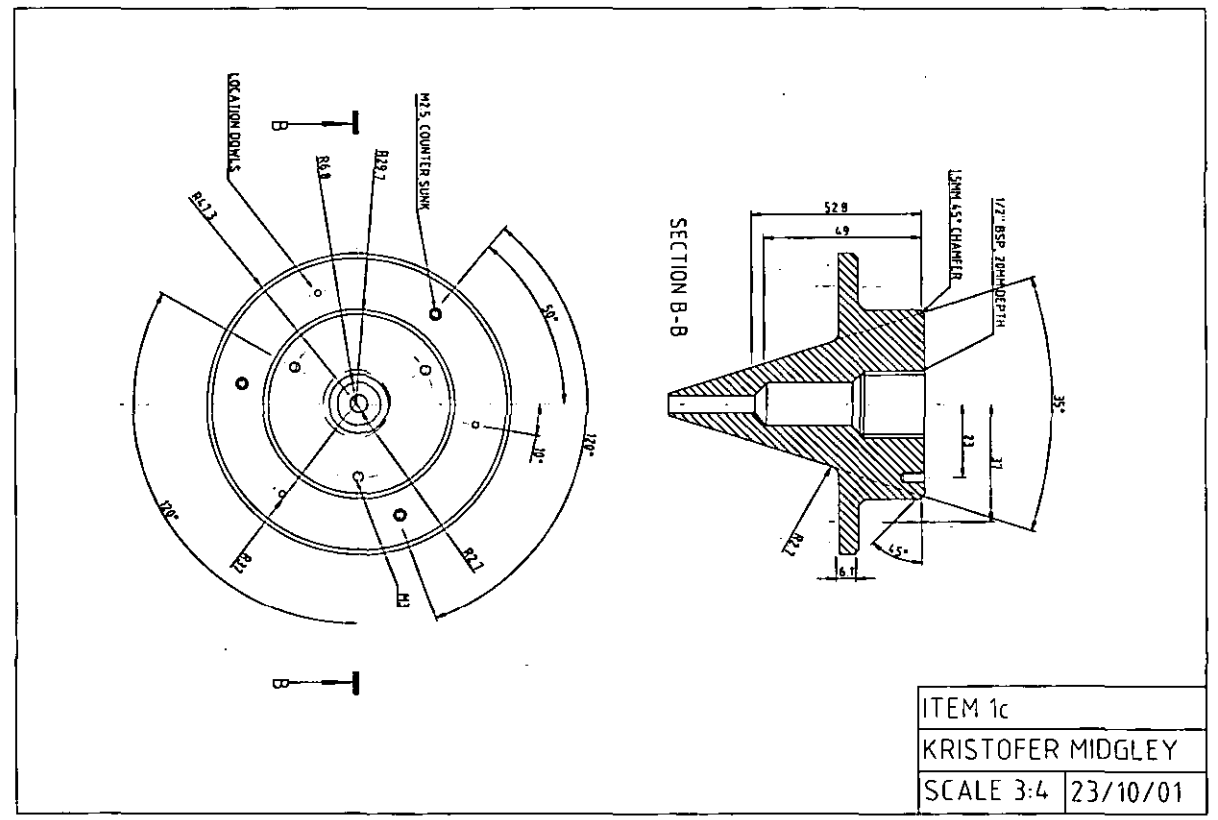

ITEM 1c	
KRISTOFER MIDGLEY	
SCALE 3:4	23/10/01

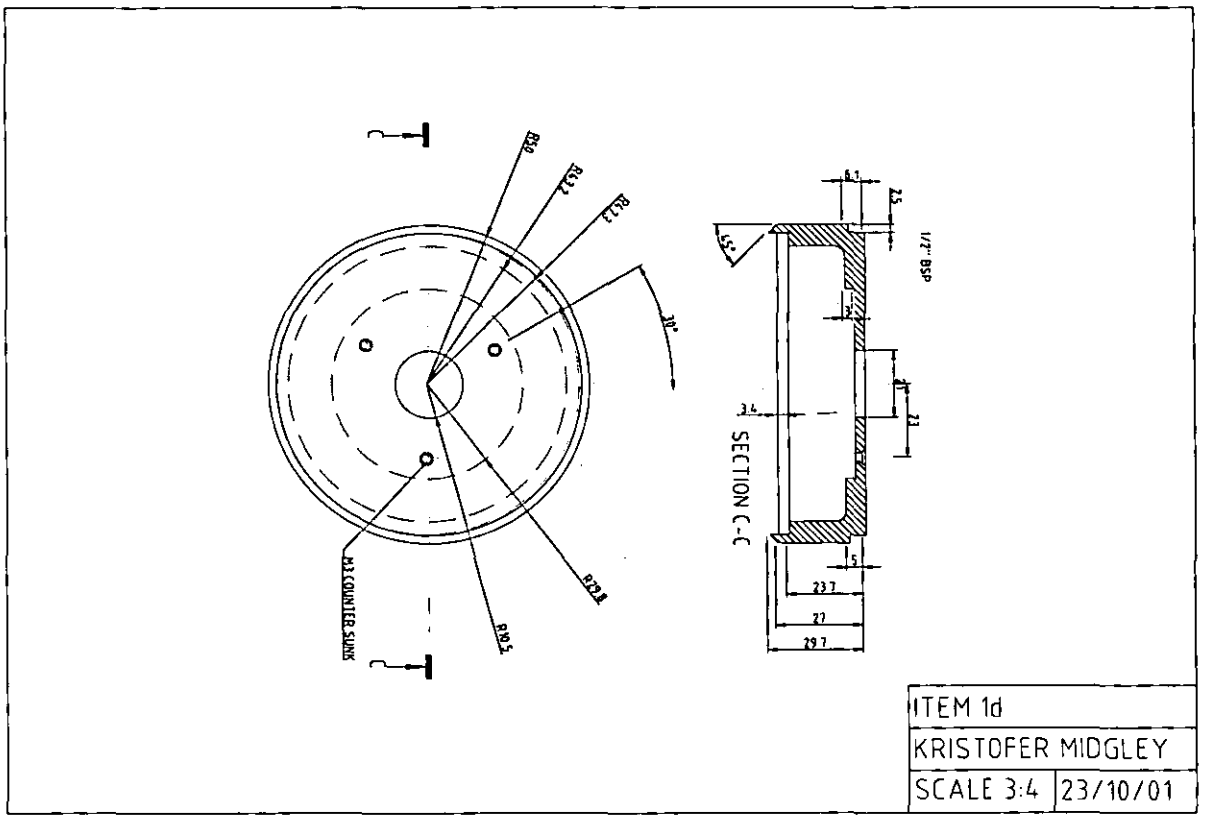
R30
R34.2
R31.3
30°
R29.8
R10.5
4X COUNTER SINK
SECTION C-C
45°
2.5
1/2" BSP
3.4
23
5
23.7
27
29.7
ITEM 1d
KRISTOFER MIDGLEY
SCALE 3:4
23/10/01